

Partonic Transport Model Application to Heavy Flavor

by

Weiyao Ke

Department of Physics
Duke University

Date: _____

Approved:

Steffen Bass, Supervisor

Berndt Müller

Christopher Walter

Robert Wolpert

Thomas Schäfer

Dissertation submitted in partial fulfillment of the
requirements for the degree of Doctor of Philosophy
in the Department of Physics
in the Graduate School of
Duke University

2019

ABSTRACT

Partonic Transport Model Application to Heavy Flavor

by

Weiyao Ke

Department of Department of Physics
Duke University

Date: _____

Approved:

Steffen Bass, Supervisor

Berndt Müller

Christopher Walter

Robert Wolpert

Thomas Schäfer

An abstract of a dissertation submitted in partial fulfillment of the
requirements for the degree of Doctor of Philosophy
in the Department of Department of Physics
in the Graduate School of
Duke University

2019

Copyright © 2019 by Weiyao Ke
All rights reserved

Abstract

Heavy-flavor particles are excellent probes of the properties of the hot and dense nuclear medium created in the relativistic heavy-ion collisions. Heavy-flavor transport coefficients in the quark-gluon plasma (QGP) stage of the collisions are particularly interesting, as they contain important information on the strong interaction at finite temperatures. Studying the heavy-flavor evolution in a dynamically evolving medium requires a comprehensive multi-stage modeling approach of both the medium and the probes, with an accurate implementation of the physical ingredients to be tested. For this purpose, I have developed a new partonic transport model (Linear-Boltzmann-plus-Diffusion-Transport-Model) LIDO and applied it to heavy quark propagation inside a QGP. The model has an improved implementation of parton in-medium bremsstrahlung and a flexible treatment of the probe-medium interactions, combining both large angle scatterings and diffusion processes. The model is then coupled to a high-energy event-generator, a hydrodynamic medium evolution and a hadronic transport model. Finally, applying a Bayesian analysis, I extract the heavy quark transport coefficients from a model-to-data comparison. The results, with uncertainty quantification, are found to be consistent with earlier extraction of the light-quark transport coefficients at high momentum and with first-principle calculations of the heavy flavor diffusion constant at low momentum.

Acknowledgements

This work was supported by the U.S. Department of Energy (DOE) grant number DE-FG02-05ER41367 and by National Science Foundation (NSC) grant number OAC-1550225. The computational resources were provided by the Open Science Grid (OSG) funded by DOE and NSF, and by the National Energy Research Scientific Computing Center (NERSC), which is the primary scientific computing facility for the Office of Science in the DOE.

Contents

Abstract	iv
Acknowledgements	v
List of Figures	x
List of Tables	1
1 Introduction	2
1.1 Quantum chromodynamics and nuclear matter	2
1.1.1 Asymptotic freedom and confinement	3
1.1.2 The phase-diagram of the QCD matter	4
1.2 Phenomenology of relativistic heavy-ion collision	7
1.2.1 Kinematics	7
1.2.2 Nuclear collision geometry	8
1.2.3 Particle production at low- p_T and collective flow	10
1.2.4 Probing sQGP using hard probes	12
1.2.5 Transport modeling of hard probes	16
1.2.6 Understanding QGP as a parameter inference problem	17
1.3 Outline of this Thesis	18
2 Bulk-medium evolution and initial conditions	19
2.1 A Hydrodynamics-based dynamical modeling	19
2.1.1 Relativistic hydrodynamic	19
2.1.2 Particularization and microscopic transport	21
2.1.3 Pre-equilibrium stage	22
2.2 Initial condition model	23

2.2.1	The original (boost-invariant) T _R ENTo model	23
2.2.2	Parametrizing the longitudinal dependence in T _R ENTo	25
2.3	Reverse engineering the 3D initial condition	27
2.3.1	Sensitive observables to the initial entropy deposition	28
2.3.2	Calibration of the 3D initial condition parameters	30
2.3.3	Prediction with the calibrated 3D initial condition	35
3	A transport model for hard partons in the QGP	43
3.1	The Boltzmann equation	44
3.1.1	The linearized Boltzmann equation and the diffusion limit . .	46
3.2	Hard parton transport in the incoherent limit	49
3.2.1	Hard/soft separation: elastic collisions	49
3.2.2	Hard/soft separation: inelastic collisions	50
3.2.3	The final incoherent transport equation and Monte-Carlo technique	52
3.3	The Landau-Pomeranchuk-Migdal effect: theory	55
3.3.1	Large medium	57
3.3.2	Thin medium: opacity expansion	61
3.3.3	Numerical solution for a general case	61
3.3.4	Mass effect in medium-induced branching	62
3.3.5	Treating multiple emissions	63
3.4	A modified transport model for the LPM effect	63
3.4.1	Modifying single particle evolution	64
3.4.2	Implementing mass effect	67
3.4.3	Implementing the running of α_s	68
3.5	Validating the modified transport approach	69

3.5.1	In a large and static medium	70
3.5.2	Branching in a finite / expanding medium	73
3.5.3	Heavy quarks and thermalization test	83
3.6	Comments on two other inelastic process implementations	86
3.6.1	The coherence factor approach	87
3.6.2	The “blocking radiation” approach	89
3.6.3	Energy loss comparison among the three approaches	90
4	A comprehensive heavy-flavor dynamical modeling framework	93
4.1	Initial production of heavy flavor	93
4.1.1	Factorization framework in proton-proton collisions	93
4.1.2	Production in the nuclear environment	95
4.1.3	Inclusive calculation versus Monte-Carlo event generator	96
4.2	Matching vacuum and medium-induced showers	97
4.2.1	Vacuum versus medium-induced shower phase-space	97
4.2.2	Visualizing the matching on the Lund diagram	100
4.3	Particles coupled to an evolving medium	101
4.4	Heavy-flavor hadronization and hadronic stage	103
4.4.1	The instantaneous approximation of hadronization	104
4.4.2	Hadronic rescattering	106
4.5	Benchmark calculation of observables	106
4.5.1	Open heavy flavor observables	106
4.5.2	A first comparison to data	108
5	Bayesian model-to-data comparison	116
5.1	Model evaluation	116
5.2	Data reduction	117

5.3	Model emulator	118
5.4	Bayes' theorem and Markov chain Monte Carlo	120
6	Results	122
6.1	Lessons from earlier extractions of \hat{q}_Q	122
6.2	Calibration using the improved transport model	127
7	Conclusion	141
A	Few-Body Matrix-Elements	145
A.0.1	2 \leftrightarrow 2 processes	145
A.0.2	2 \rightarrow 3 matrix-elements	146
	Bibliography	157
	Biography	180

List of Figures

- 1.1 The (partly projected) phase-diagram of the nuclear matter from reference [A^{+15g}] with the red dots from lattice calculation [BDH⁺¹²]. The horizontal variable is Baryon chemical potentail μ_B and the vertical variable is temperature T . The red and green trajectories indicates the reachable regions by the heavy-ion program at the LHC and RHIC. 5
- 1.2 The lattice equation of state for 2+1 flavor QCD taken from reference [B^{+14a}]. The rescaled pressure, energy density and entropy density as function of temperature at zero chemical potential are shown as red, blue and green bands. The dashed lines indicates non-interaction (Stephan-Boltzmann) limit and the solid lines show the expected values from a hadron resonance gas. The yellow band is the region of pseudo-critical temperature. 6
- 1.3 Illustration of the connections between final state particles and the formation of a dense medium and its geometry. Left: blue circles indicate the nuclei separated by a finite impact-parameter. An almond-shaped hot medium (red contour) is created in the overlapped region. The medium undergoes pressure driven expansion and creates a $\cos(2\phi)$ like modulation in the final particle distribution (denoted as colored histogram). Right: hard particles travel through the medium loses energy. On average, their final momentum (black arrow) are smaller than the original one (red arrow), and hard partons moving along the long-axis lose more energy than those moving along the short-axis direction. 9
- 1.4 The momentum anisotropy coefficient v_2 estimated from multi-particle correlation for charged particle from the ALICE collaboration [A⁺¹¹, A^{+16b}]. The hydrodynamic-based calculations [NEPT16, NHLO16] (lines) very well explains the centrality dependence of the second (red), third (blue) and fourth (green) order coefficients at different beam energies. 11
- 1.5 The nuclear modification factor $R_{AA}(p_T)$ of charged hadron (gray), D meson (red), B meson (blue), and b -decayed D meson (red), b -decayed J/ Ψ (purple) measured by the CMS collaboration [K^{+17a}, S^{+18a}, S^{+18c}, S⁺¹⁷] (figure from Matthew Nguyen). 14
- 1.6 The charged pion (red) and D meson momentum anisotropy measured by the ALICE Collaboration (black) and the CMS Collaboration (green). Left and right panels show the results for 10-30% centrality and 30-50% centrality respectively. 15

2.1	Two sample events for Pb-Pb collision (top row) and p+Pb collision (bottom row). The left column and the right column slice the initial entropy density at middle rapidity and the $x = 0$ plane respectively. The relative skewness parametrization is used with $\mu_0 = 1$, $\sigma_0 = 3$ and $\gamma_r = 6$	28
2.2	The posterior distribution of the observables after the fitting process. Blue and red stands for the results calibrated using the “relative skewness” and the “absolute skewness” ansatz respectively. From left to the right are charged particle pseudorapidity density in Pb-Pb collision, in p+Pb collision, and the rms of the a_1 coefficient in the two-particle pseudorapidity correlation decomposition. The lines in the right most figure shows that the rms a_1 is not very sensitive to the viscous effect in the hydrodynamic evolution.	31
2.3	The posterior probability distribution of the model parameters, the colors distinguish the use of “absolute skewness” (red) and “relative skewness” ansatz. The diagonals are single parameter distribution, the off-diagonals are two-parameter joint distributions.	33
2.4	The constrained functional form of the three-dimensional initial entropy deposition $s(T_A(\mathbf{x}_\perp), T_B(\mathbf{x}_\perp), \eta_s)$. T_A and T_B is varied from 0.2 to 2.4 fm^{-2} . Colors distinguish the results from using “absolute skewness” (red) and “relative skewness” ansatz.	34
2.5	Flow coefficients $v_2\{2\}$ (blue) and $v_3\{2\}$ (orange) are plotted as a function of centrality. The calculation uses a 3+1D viscous hydrodynamic-based model with constant $\eta/s = 0.17$ and 0.19 for “relative skewness” (solid) and “absolute skewness” (dashed) ansatz. $\zeta/s = 0$ and the switching temperature is $T_{\text{sw}} = 154 \text{ MeV}$. The initial condition parameters are selected from the high-likelihood region of the posterior.	36
2.6	Pseudorapidity dependent flow coefficients $v_2\{2\}$ (blue circle), $v_3\{2\}$ (green triangle) and $v_2\{4\}$ (orange diamond). Constant $\eta/s = 0.25$ and 0.28 are used for “relative skewness” (closed symbol) and “absolute skewness” (open symbol) ansatz. Data is taken from the ALICE Collaboration [A ⁺ 16g].	38
2.7	The $n = 2$ (blue) and $n = 3$ (orange) event-plane decorrelations obtained for “relative skewness” (lines with bands) and “absolute skewness” (lines with hatches) ansatz. The top and bottom plots uses different reference particle bins $3.0 < \eta_b < 4.0$ and $4.4 < \eta_b < 5.0$ respectively.	40

2.8	The symmetric cumulants (top row) and normalized symmetric cumulants (bottom row) obtained from the “relative skewness” (left column) and the “absolute skewness” (right column) ansatz. $SC(4, 2)$ (blue) and $SC(3, 2)$ (green) are shown as functions of centrality. The experimental measurements at mid-rapidity (black symbols) are taken from [A ⁺ 16e]. The calculations are performed at both mid-rapidity $ \eta < 0.8$ (solid lines) and forward/backward rapidity $2.5 < \eta < 3.5$ (dashed lines).	41
3.1	A schematic demonstration of the physics of in-medium parton bremsstrahlung. The hard parton “ <i>a</i> ” splits into two hard partons “ <i>b</i> ” and “ <i>c</i> ”. The hard partons (quarks or gluon) are denoted as straight lines. The hard system constantly interacts with the medium through gluon exchanges, denoted as the loop lines. One sums the squared amplitudes ($ \dots ^2$) over an arbitrary number (<i>m</i>) of interactions with the medium. Each amplitude has to include all the interference contribution. Finally, one does an ensemble average over the medium configurations.	55
3.2	A schematic demonstration of the “modified transport” approach. We seek for an approximation to the coherent process by an incoherent transport simulation with a multiplicative correction to the branching probability.	64
3.3	The $q \rightarrow q + g$ splitting rate simulated in an infinite box with $T = 0.5$ GeV. The quark energy is $E = 1$ TeV. $\alpha_s = 0.1$. In the top plot, the spectrum $dR/d\omega$ (red line) is fitted to a power function ω^λ in different gluon energy regions. The green dashed line is fitted in the Bethe-Heitler region $\omega < \omega_{BH} \approx 2\pi T$; the blue dash-dotted line is fitted in the LPM region $\omega > \omega_{BH}$. The middle plot compares to the simulation to NLL solution to the AMY equation, and their ratio is shown in the bottom plot	71
3.4	The rate of different channels $q \rightarrow q + g^*$, $g \rightarrow g + g^*$, and $g \rightarrow q^* + \bar{q}$ are plotted as functions of the daughter (labeled by “*”) parton energy. The mother parton has a energy $E = 1$ TeV. The medium temperature is $T = 0.5$ GeV. $\alpha_s = 0.1$. The simulations (thick dashed lines) are compared to the NLL solutions (thin solid lines).	72
3.5	Ratios of splitting rate dR/ω between the modified Boltzmann simulation and the NLL solution for $q \rightarrow q + g$ splitting. The quark energies are E is 10, 100, and 100 GeV from top to the bottom plot. And two coupling constants are used: $\alpha_s = 0.1$ (red solid lines) and $\alpha_s = 0.3$ (blue dashed lines). ω stands for the gluon energy. The horizontal dashed lines denote $\pm 10\%$ deviation from unity.	74

3.6	The same as figure 3.5, but $g \rightarrow g + g$	75
3.7	The same as figure 3.5, but $g \rightarrow q + \bar{q}$	76
3.8	Comparing the simulation with running coupling constant the NLL solution with running α_s prescription. The scale Q in the emission vertex and in the theoretical formula for the effective transport parameter \hat{q}_3 (equation 3.108) is chosen to be 1/2, 1 and 2 times of the scale $\sqrt{\langle k_\perp^2 \rangle}$ in equation 3.109. The ratio is shown in the bottom plot.	77
3.9	The path-length dependence of the simulated $q \rightarrow q + g$ emission rate $dR/d\omega$ compared to the direction calculation of formula 3.90 from [CHG10]. $\alpha_s = 0.3$. The quark energy is 16 GeV. The left and right columns have medium temperature $T = 0.2$ and 0.4 GeV respectively. The top and bottom rows show the differential rate at $\omega = 3$ and 8 GeV.	79
3.10	The same as figure 3.10, but the initial quark energy is 100 GeV, and is plotted for gluon at 5 (top), 10 (middle) and 50 (bottom) GeV. . .	81
3.11	Top plot: the simulated spectrum (diffusion plus diffusion-induced radiation only) using the parametric medium with expansion parameters $\nu = 0$ (static, black), 3/4 (green), 1 (Bjorken, blue), and 3/2 (orange). The analytic results are shown in symbols and simulations in lines. $\alpha_s = 0.3$. The expansion starts at $\tau_0 = 0.2$ fm/c with an initial temperature $T_0 = 1$ GeV. Bottom plot: the ratios between calculation (simulation) in an expanding medium to that in the static medium. . .	82
3.12	The mass dependence of the radiation spectrum $q \rightarrow q + g$, presented as the ratio of bottom $dR/d\omega$ over the light quark $dR/d\omega$, as functions of path length. The left and right columns use temperatures 0.2 and 0.4 GeV. Different rows (from top to bottom) plot cases for gluon energy $\omega = 5, 10, 20, 50$ (GeV).	84
3.13	The approach to thermal equilibrium for heavy flavor is quantified as the change of ΔS (defined in equation 3.121) as function of time.. The red dotted lines includes elastic processes only. The green dashed line further includes $2 \rightarrow 3$ and $1 \rightarrow 2$ processes. The blue solid lines turn on the detailed balance processes $3 \rightarrow 2$ and $2 \rightarrow 1$	85

3.14 Energy loss per unit path length dE/dx as a function of energy E , temperature T and coupling constant α_s . Each column corresponds to a value of the coupling constant $\alpha_s = 0.075, 0.15, 0.3$, and 0.6 (from left to right). Each row corresponds to a temperature of $T = 0.2, 0.4$, and 0.6 GeV (from top to bottom). dE/dx is divided by the expected scaling $\alpha_s^2 \sqrt{ET^3}$. The MC implementations in this work (red dashed lines) is compared to the “coherence factor” approach (green dash-dotted lines) and the “block radiation” approach (blue dotted lines). The analytic results are denoted as black solid lines.	90
3.15 Energy loss ΔE as a function of path length L , temperature T and coupling constant α_s . Each column corresponds to a coupling constant of value $\alpha_s = 0.075, 0.15, 0.3$, and 0.6 (from left to right). Each row corresponds to a temperature of value $T = 0.2, 0.4$, and 0.6 GeV (from top to bottom). ΔE is scaled by $\alpha_s E$ and L is scaled by an estimated critical path length $L_c^0 = \sqrt{E/\hat{q}_0}$, $\hat{q}_0 = C_A \alpha_s T m_D^2$. The MC implementations in this work (red dashed lines) is compared to the “coherence factor” approach (green dash-dotted lines) and the “block radiation” approach (blue dotted lines). The analytic results for a thin medium are denoted as black solid lines.	91
4.1 A schematic workflow of the heavy quark simulation. The left branch evolves the medium in the hydrodynamic based model, providing medium information (temperature, flow velocity) to the hard probe transport in the right branch. The hard and soft hadrons are evolved in the hadronic afterburner in the last step.	94
4.2 A schematic demonstration of the factorization theorem. Two incoming proton momenta are p_1 and p_2 . $f_{i,j}$ are the parton distribution function. $d\sigma$ is the perturbative matrix-element. f_H is the fragmentation function.	95
4.3 Top plot: a comparison of D -meson production in proton-proton collisions (blue) and in Pb-Pb collisions (red) with cold nuclear matter effect only. FONLL calculations are shown as lines and Pythia8 simulations are shown as symbols. Bottom plot: the ratio between the production in Pb-Pb collision (cold nuclear matter effect only) to the proton-proton baseline shows the nuclear shadowing effect.	98
4.4 Demonstration of the medium corrections to vacuum-like radiation with different formation time. The energy of the gluon is hold fixed, while the virtuality is decreasing from left to right.	98

4.5 Plotting the gluon radiations from a charm quark on the Lund diagram. The gluon emission has an energy ω with angle θ with respect to the heavy quark. The blue heat map in the left plot shows the distribution of vacuum-like emissions without medium effects. The heat map in right left plot shows the distribution of vacuum-like emissions with medium effects; while the red contour stands for the medium induced emissions. Emissions on the black dashed lines have $k_\perp^2 = \sqrt{2\omega\hat{q}}$. Emissions on the dashed-dotted lines have a formation time equals to the medium path-length. Finally, the dotted lines is the non-perturbative cut-off in Pythia $k_\perp = 0.4$ GeV.	101
4.6 Benchmark results using a fixed coupling constant $\alpha_s = 0.2$ (dashed), 0.3 (solid), and 0.4 (dash-dotted). The blue bands fill between the results using $\alpha_s = 0.2$ and 0.4. They are compared to the experimental data (black symbols) obtained by the ALICE Collaboration [A ⁺ 18a, A ⁺ 18b] and the CMS Collaboration [S ⁺ 18c, S ⁺ 18b].	109
4.7 Demonstrating the mass dependence of the observables using $\alpha_s = 0.4$. The D meson and B meson results are labeled by color black and blue respectively. Left plot: R_{AA} for 0-100% centrality. Right plot: v_2 for 10-30% centrality.	110
4.8 Benchmark results using a running coupling constant. The medium scale that stops the low- Q running is chosen at $Q_{\text{med}} = \mu\pi T = \pi T$ (dashed), $2\pi T$ (solid), and $4\pi T$ (dash-dotted). They are compared to the experimental data (black symbols) obtained by the ALICE Collaboration and the CMS Collaboration.	112
4.9 Effect of changing the switch scale between small- Q diffusion modeling and large- Q scattering modeling. $\mu = 2$ is used. The red solid lines used a switching scale at $Q_{\text{switch}}^2 = 4m_D^2$, and the blue dashed lines uses $16m_D^2$	113
4.10 Effect of changing the matching scale parameter R_v ($\Delta k_\perp^2 = R_v Q^2$) between the vacuum-like shower and the medium-induced shower. $\mu = 2$ is used. The red solid lines use $R_v = 1$, while the blue dashed lines use $R_v = 1000$, which leave the vacuum-like shower largely unmodified.	113
4.11 The impact of using the “local rate” approximation. The red solid lines use the default implementation; while the blue dashed lines perform the rescatterings in an imaginary infinite box using locally defined temperatures to mimic the “local rate” approximation.	114

6.1	The prior distribution of calculated observables compared to data. The colors labeled the use of EPPS (blue) and nCTEQ15np (green) nuclear PDF.	123
6.2	The 90% credible region of the posterior distribution of observables compared to data. The colors labeled the use of EPPS (blue) and nCTEQ15np (green) nuclear PDF.	124
6.3	Posteriors of single-parameter distributions (diagonal plots) and two-parameter joint distributions (off-diagonal plots). The colors labeled the use of EPPS (blue) and nCTEQ15np (green) nuclear PDF.	125
6.4	The 95% credible region of the heavy quark transverse momentum broadening parameter \hat{q} extracted using the model described in [KXB18]. The charm quark results are shown in red, and bottom results in blue. The difference coming from using different nuclear PDF has been marginalized into the uncertainty bands. Left plot: the temperature dependence at $p = 10$ GeV. Right plot: the momentum dependence at $T = 0.35$ GeV.	126
6.5	Comparison of the 95% credible region of the charm \hat{q} using different models. The red regions use the model described in [KXB18], while the shaded regions are obtained using the improved-Langevin model [CQB13a].	127
6.6	Left: the prior range of the transport parameter \hat{q} as function of temperature at different heavy quark energy. Right: the prior range of the longitudinal diffusion parameter \hat{q}_L , plotted as ratio $2\hat{q}_L/\hat{q}$	129
6.7	The prior distribution of the calculated observables at LHC energy compared to data.	131
6.8	The prior distribution of the calculated observables at RHIC energy compared to data.	132
6.9	Validation of the emulators performance. The top two plots shows the correlation between the calculated quantities (x variable) versus the emulated quantities (y variable). The bottom two plots compare the GP's estimated standard deviation σ of the prediction to the true deviation from the actual calculation. The dashed regions indicates where the true deviations have a larger than 3σ difference from the emulator's prediction.	133

6.10 The 90% credible region (blue bands) of the posterior distribution of the observables at the LHC energy. Black dashed lines are the median prediction.	135
6.11 The 90% credible region (blue bands) of the posterior distribution of the observables at the RHIC energy. Black dashed lines are the median prediction.	136
6.12 The single-parameter posterior distributions (diagonal plots) and two-parameter joint posterior distributions (off-diagonal plots).	137
6.13 Left plot: the scale dependence of the running coupling constant at $T = 0.3$ GeV. Right plot: the temperature dependence of running coupling evaluated at the cut-off scale $Q = \mu\pi T$. The red bands are generated using 90% credible region of the μ parameter; the gray bands are the prior distributions; and the black dashed lines are median predictions.	138
6.14 The 90% credible region of the charm quark transport coefficients (left plot) and of the longitudinal transport parameter (right plot) are shown in red. The prior range are shown in gray. The results are also compared to the previous JET Collaboration extraction of the light quark transport parameters at $p = 10$ GeV (black symbols).	139
6.15 The 90% credible region of the spatial diffusion constant defined in the zero momentum limit. Prior range is indicated by the gray band. The posterior of charm and bottom flavor are shown as red band and blue boundary receptively. It is compared to lattice QCD evaluation in references [BDGM12] (black boxes), [FKL ⁺ 15] (the black dot) and [DFK ⁺ 12] (red triangles).	140
7.1 This figure shows the main result of this dissertation. The 90% credible transport coefficient \hat{q}/T^3 extracted for the charm flavor is displayed on the two dimensional landscape of energy and temperature. The JET Collaboraton extraction of light quark transport coefficients at $p = 10$ GeV [B ⁺ 14b] (blue diamonds) and two lattice calculations of the momentum diffusion coefficient κ ($\hat{q} = 2\kappa$) [DFK ⁺ 12, BDGM12] are plotted for comparison.	142
A.1 Elastic processes: The first diagram corresponds to heavy quark (Q) - light quark (q, \bar{q}) scattering. The last three diagrams contribute to heavy quark (Q) - gluon (g) scattering.	146

A.2 Three diagrams A (Top), B (Bottom left), C (Bottom right) that contribute to the large angle scattering induced gluon splitting into quark-anti-quark pair in the forward region of the center-of-mass frame.	147
A.3 Three diagrams A (Top), B (Bottom left), C (Bottom right) that contribute to the large angle scattering induced a quark splitting into a quark and a gluon in the forward region of the center-of-mass frame.	151
A.4 Three diagrams A (Top), B (Bottom left), C (Bottom right) that contribute to the large angle scattering induced gluon splitting into two gluons in the forward region of the center-of-mass frame.	152

List of Tables

2.1	TRENTo p -parameter	25
2.2	Table	27
2.3	Three-dimensional initial condition parameters	30
2.4	A high likelihood parameter set	35
4.1	ALICE dataset	107
4.2	CMS dataset	107
6.1	Prior range of parameters	128

Chapter 1

Introduction

The fundamental theory of strong interaction – Quantum chromodynamics (QCD) – describes rich set of phenomena, from low energy vibrations of atomic nuclei to the production of energetic jets of particles with over trillion electron volts of energy on the Large Hadron Collider (LHC). Its force binds over 99% of the mass in the visible universe, yet its complexity has made it a subject very hard to approach both experimentally and theoretically. To understand its dynamics, people look for simplified scenarios to do experiments and examine our understandings. One such limit is the high energy limit, where the coupling constant of the strong interaction α_s becomes relatively small, known as asymptotic freedom [GW73, Pol73]. Theoretical tools such as perturbative QCD (pQCD) can be applied. Observations from high energy collisions have confirmed the success of perturbation theory [Owe87]. Another interesting aspect is to understand physical systems in the “many particle” (thermodynamic) limit. Instead of exciting a few fundamental particles and observing their evolution, one deposits a huge amount of energy into a tiny region, for example, by colliding heavy nuclei that excite a medium with thousands of particles. In this limit, one is more interested in the collective dynamics of the strong force. Features such as the structure of the equation-of-state (EoS), the medium transport coefficients, and the medium stopping power (opacity), etc, are also fundamental properties of the strong interaction. Applying tools from many body physics such as the finite temperature field theory, kinetic transport theory, and hydrodynamics, many facets of QCD have been revealed from data taken at particle colliders.

I shall briefly review the basic concepts of QCD and our current understanding of nuclear matter, in particular, the quark-gluon plasma (QGP). Then key experimental discoveries made by studying relativistic heavy-ion collisions are reviewed and I will show how different probes can be used to characterize the different transport properties of the QGP through a model-to-data comparison. This dissertation is an example of such practice: I developed a heavy-flavor transport model and combined it with an advanced statistical method to reverse engineer heavy quark transport coefficient from experimental data.

1.1 Quantum chromodynamics and nuclear matter

QCD describes the interaction of objects that carries “color” charges. Quarks (fermions) and gluons (bosons) are the elementary degrees of freedom. The QCD Lagrangian (with one flavor of quark) is,

$$\mathcal{L} = \bar{\psi}_i \left(i\gamma_\mu D_{ij}^\mu - m\delta_{ij} \right) \psi_j - \frac{1}{4} G_{\mu\nu}^a G^{\mu\nu,a}, \quad (1.1)$$

where ψ_i is the Dirac spinor of the quark field with color $i = 1, \dots, N_c$. There are three types of color charges $N_c = 3$ in the physical world.

$$D_{ij}^\mu = \partial^\mu - igT_{ij}^a A^{\mu,a} \quad (1.2)$$

is the covariant derivative, containing the interaction between quark field and the gluon field with coupling strength g . Here T_{ij}^a are the generators of the SU(3) group in the fundamental representation of the color space and they satisfy the commutation relation,

$$[T^a, T^b] = if^{abc}T^c \quad (1.3)$$

where f^{abc} are known as the structure constants of SU(3). The field tensor of the gluon field with color a is,

$$G^{\mu\nu,a} = \partial^\mu A^{\nu,a} - \partial^\nu A^{\mu,a} + gf^{abc}A^{\mu,b}A^{\mu,c} \quad (1.4)$$

The first term is the kinetic term, and the second term is the gluon field self-interaction (also with strength g), which is a unique feature of the non-Abelian gauge field. a, b and c label the color of the gluon field which forms a $N_c^2 - 1 = 8$ dimension ad-join representation in the color space.

1.1.1 Asymptotic freedom and confinement

Due to quantum fluctuations, the effective coupling strength g changes with the energy scale of a process. The rate of change of g with respect to the scale parameter is called the β -function,

$$\frac{\partial g}{\partial \ln \mu} = \beta(g), \quad (1.5)$$

which can be evaluated as a perturbation series of g at weak coupling. At leading order, the QCD β function with number of colors N_c and n_f flavors of quarks is,

$$\beta(g) = -\left(\frac{11}{3}N_c - \frac{2}{3}n_f\right)\frac{g^3}{16\pi^2}. \quad (1.6)$$

This β function is negative for QCD ($N_c = 3$) using realistic numbers of quark flavors $n_f = 2 \dots 6$, meaning the effective coupling constant decreases with increasing energy scale. This property is known as the asymptotic freedom of QCD because the interaction becomes small at asymptotically high energy, which also makes possible the use of perturbation theory at high energy.

Often, the strong coupling constant is defined as $\alpha_s = g^2/4\pi$. Using the leading order β -function, its scale dependence is

$$\alpha_s(Q^2) = \frac{4\pi}{\left(\frac{11}{3}N_c - \frac{2}{3}n_f\right)\ln\left(\frac{Q^2}{\Lambda^2}\right)}. \quad (1.7)$$

The integration constant has been absorbed into the QCD scale parameter Λ . Therefore, at least in perturbation theory, Λ becomes the only parameter of QCD. Its value is determined by anchoring $\alpha_s(\mu)$ to the experimental measurement at a fixed scale, for example, $\alpha_s(M_z) = 0.1185$ at the scale equal to the Z boson mass. The leading order Λ is then around 200 MeV.

The decrease of $\alpha_s(Q)$ is logarithmically slow at high energy, but it rises quickly with Q approaching Λ from above. Even before reaching this scale, the coupling constant is already too large for a reliable perturbative calculation. Near the Λ scale, QCD enters the non-perturbative region. At the long distances ($l \gtrsim 1/\Lambda$), only hadrons exist as colorless bound states of quarks and gluons. The fact that color is not directly observed at large distances is known as “color confinement” of QCD. To pull a quark out of the hadron, the color field becomes so strong that eventually more quark-anti-quark pairs populate the space in-between the pulled quark and the remnant and form new colorless hadrons.

Depending on its valence quarks (quarks that carry the net quantum number of the hadron) content, hadrons are generally categorized as baryons and mesons. Baryons have three valence quarks or anti-quarks, such as neutrons and protons. Mesons have a valence quark and an anti-quark, such as pions and kaons. Hadrons are also populated with sea-quarks and gluons that are constantly produced and annihilated as quantum fluctuations. The momentum of a hadron is mostly carried by the valence quarks. The sea quarks and gluons together share the remaining fraction of the total momentum, but their abundance at high energy is very important for the particle production in relativistic hadron / heavy-ion collisions.

Nowadays, the only reliable ab initio theoretical tool for solving non-perturbative QCD is lattice field theory, where the QCD Lagrangian is discretized on a finite lattice and studied on a computer.

1.1.2 The phase-diagram of the QCD matter

At zero temperature (T), protons and neutrons form bound states of atomic nuclei that are the building blocks of the ordinary matter. One can define the baryon chemical potential μ_b , which for ordinary matter is around 1 GeV, close to the proton mass. The region of ordinary nuclei is indicated as the white dot on the (partly conjectured) phase diagram in figure 1.1 [A⁺15g]. Increasing the temperature of the system, nucleons start to escape from the nuclear potential and other hadrons can be created from collisions and resonance formation and decay. This system is known as the hadron gas (cyan region in figure 1.1).

Because QCD has asymptotic freedom at high energy and confinement occurs at a low energy scale, a so-called deconfinement phase-transition exists when temperatures cross the QCD non-perturbative scale. At asymptotically high temperature, the weakening of the coupling should lead to the transition from the color confined hadronic matter to a system of deconfined quarks and gluons, termed the quark-gluon plasma (QGP). First principle lattice QCD calculations have studied this transition at zero baryon chemical potential with 2+1 flavors (up, down plus strange quark).

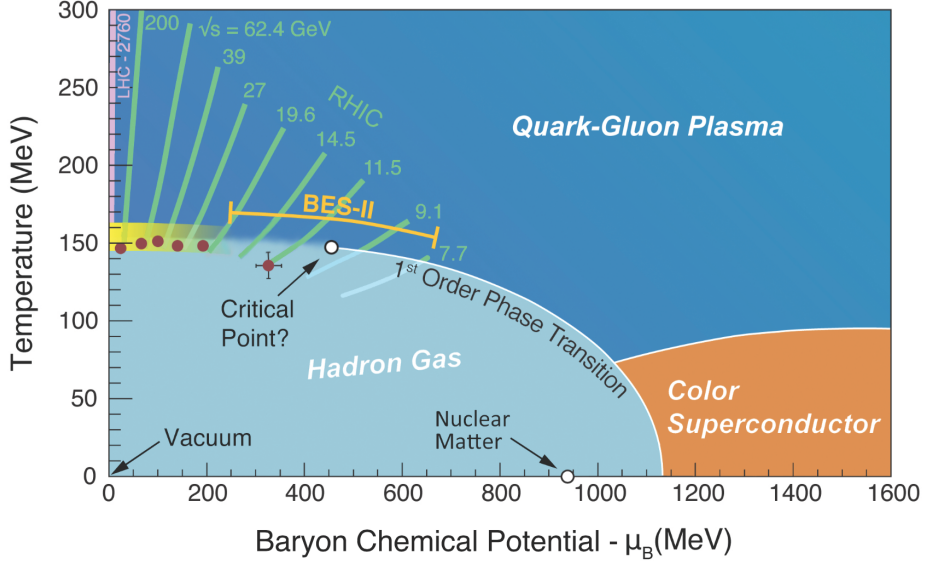


Figure 1.1: The (partly projected) phase-diagram of the nuclear matter from reference [A⁺15g] with the red dots from lattice calculation [BDH⁺12]. The horizontal variable is Baryon chemical potential μ_B and the vertical variable is temperature T . The red and green trajectories indicates the reachable regions by the heavy-ion program at the LHC and RHIC.

Figure 1.2 quotes the equation of state computed by the HotQCD Collaboration [B⁺14a]. It shows the pressure P , energy density (ϵ) and entropy density (s) of the system. These thermodynamic quantities are scaled by powers of temperature, so that the ratio can be loosely related to the effective number of degrees of freedom (DoF) of the system. The Stefan-Boltzmann limit (non-interacting gas of quarks and gluons) is denoted as the dashed lines in the up-right corner. It is observed that the effective number of DoF converges to the expectation from a hadron resonance gas model (solid lines) at low temperature and rapidly increases to a value close to the Stefan-Boltzmann limit in a narrow temperature window. This suggests a release of the quark and gluon degrees of freedom at high temperature. More dedicated studies indicate that this is not a real phase-transition at $\mu_b = 0$, and is referred to as a “cross-over” phase transition, where the thermodynamic quantities smoothly across this region of phase-diagram. Nevertheless, a pseudo critical temperature is defined to be $T_c \approx 150$ MeV, corresponding to 1.5 trillion Kelvin.

Moving towards a finite baryon chemical potential, the lattice approach runs into the fermion sign problem, though recent studies have been pushing the realm of lattice QCD into regions of small μ/T [GBB⁺17, B⁺17]. Effective models studies have suggested the existence of a first order phase transition at large μ_B/T and one may refer to [FH11] for a review. If true, the first-order coexistence line must end at a point on the phase-diagram at lower μ_b , beyond which the phase-transition is of the cross-over type. Such a point, called the critical end point (CEP), has attracted great interests from both the theoretical and the experimental community.

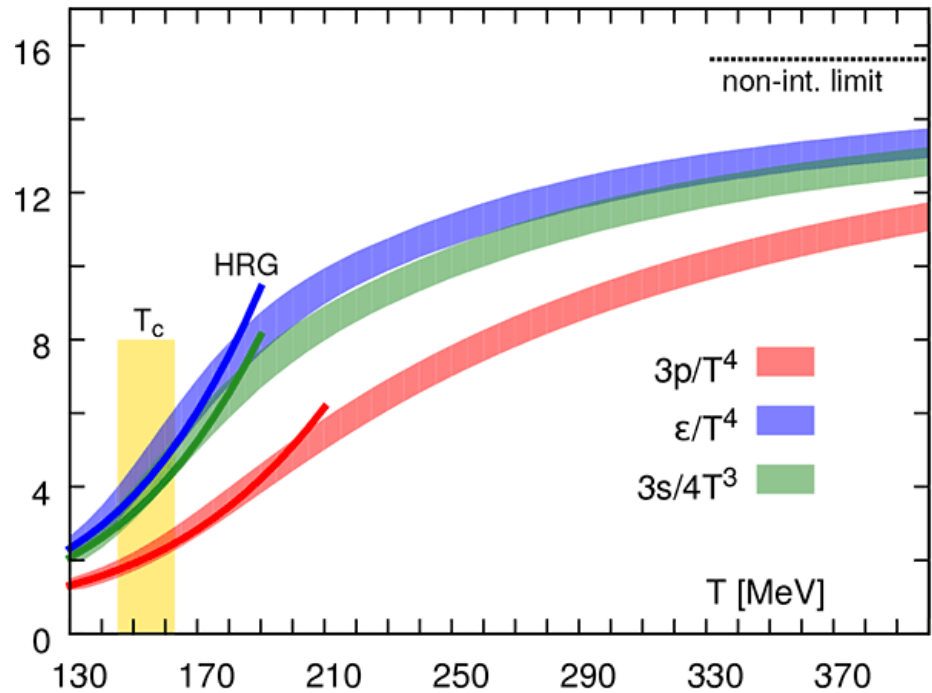


Figure 1.2: The lattice equation of state for 2+1 flavor QCD taken from reference [B⁺14a]. The rescaled pressure, energy density and entropy density as function of temperature at zero chemical potential are shown as red, blue and green bands. The dashed lines indicates non-interaction (Stephan-Boltzmann) limit and the solid lines show the expected values from a hadron resonance gas. The yellow band is the region of pseudo-critical temperature.

It is believed that the QCD high-temperature phase-transition occurred in the early universe around microseconds after “the Big Bang”, when its temperature drops down to the QCD scale. In “nowadays” universe, compact stars are “celestial laboratories” to test the QCD equation-of-state in the high density and low temperature region, providing an important physical input for simulating the recently discovered gravitational wave emission from neutron star mergers [A⁺17a]. In laboratories, we create hot and dense nuclear matter by colliding heavy nuclei at ultra-relativistic high energies. While the created matter is transient and tiny compared to the cosmic nuclear matter, we can study not only thermodynamic properties but also essential dynamical properties of QCD in these experiments.

1.2 Phenomenology of relativistic heavy-ion collision

Relativistic heavy-ion collisions are currently the only tool to access the high energy density QCD medium in laboratory. Since 2000, the Relativistic Heavy-ion Collider (RHIC) at the Brookhaven National Laboratory (BNL) has been colliding gold nuclei at 200 GeV. The Large Hadron Collider (LHC) started its heavy ion programs later, colliding lead nuclei at 2.76 TeV and 5.02 TeV. Since then, evidences have been pointing to the existence a new state-of-matter: the strongly coupled quark-gluon plasma (sQGP).

In this section, I shall introduce useful concepts and terminology used in heavy-ion collision physics. Then I will review a few important experimental observables and how they can help us understand the properties of the sQGP.

1.2.1 Kinematics

In ultra relativistic collisions, it is advantageous to use a new set of coordinates, related to the Cartesian coordinates by,

$$x_\perp = x_\perp \quad (1.8)$$

$$\tau = \sqrt{t^2 - z^2} \quad (1.9)$$

$$\eta_s = \frac{1}{2} \ln \frac{t+z}{t-z} \quad (1.10)$$

where the z direction aligns with the beam direction. τ is called the “proper time” and η_s is called the space-time rapidity. One advantage of using this set of coordinates is that τ and η_s transforms much simpler than t and z under a Lorentz boost (β_z) in the beam direction,

$$\tau' = \tau, \quad (1.11)$$

$$\eta'_s = \eta_s + \frac{1}{2} \ln \frac{1 + \beta_z}{1 - \beta_z} \quad (1.12)$$

Similarly, the four momentum p^μ is parametrized as

$$p_x = p_T \cos \phi \quad (1.13)$$

$$p_y = p_T \sin \phi \quad (1.14)$$

$$m_T = \sqrt{m^2 + p_T^2} \quad (1.15)$$

$$y = \frac{1}{2} \ln \frac{E + p_z}{E - p_z}. \quad (1.16)$$

p_T is transverse momentum relative to the beam (z) direction, ϕ is the azimuth angle of particle emission. m_T is referred as the transverse mass, and y is the rapidity of a particle. Besides, pseudorapidity is often used in experiments,

$$\eta = \frac{1}{2} \ln \frac{|p| + p_z}{|p| - p_z} = \frac{1}{2} \ln \frac{1 + \cos \theta}{1 - \cos \theta} \quad (1.17)$$

It has the merits that it is directly related to the polar angle θ of particle emission. When the transverse mass is small compared to p_z , the pseudorapidity is also a good proxy of rapidity.

1.2.2 Nuclear collision geometry

Nuclei are extended objects. The radius of heavy nuclei approximately scales like $A^{1/3}$ fm, where A is the atomic number; therefore, the collision geometry plays a far more important role than it is in the proton-proton collision. In the center-of-mass frame, nuclei “shrink” in the z direction by the factor $\gamma = (1 - v^2)^{-1/2} = E/M$ due to Lorentz contraction. γ is about 100 for gold nuclei at top RHIC energy and is larger than 2500 for lead nuclei at the LHC. As a result, the approaching nuclei takes a very short time to penetrate each other $t_L = 2R/\gamma$, while dynamics in the transverse direction can only propagate within a causal circle of $r < t_L$ that is much smaller than the nuclear radius.

Impact-parameter and centrality Defining the impact parameter \vec{b} as the transverse separation between the centers-of-mass of the two approaching nuclei, the initial deposition of the energy largely depends on \vec{b} . The collision geometry is a useful handle to study QGP dynamics; however, it is impossible to control b directly in high energy experiments. What is used as an approximate geometry indicator is the so-called centrality. Centrality is defined in different ways (detector response / multiplicity / transverse energy) and with different kinematic cuts, but the idea is that the nuclear collision geometry strongly correlates with the particle production activity. It is reasonable to anticipate that the average number of charged particles produced or the total transverse energy deposited within a certain detector’s acceptance is higher if the collision is more central (small impact parameter), and is lower for peripheral collision (large impact parameter). Of course the relation between centrality and impact-parameter is not exact, as dynamical fluctuations smear out the one-to-one correspondence. Correctly accounting for these fluctuations is particularly important for small collision systems, such as proton-lead and deuteron-gold collisions.

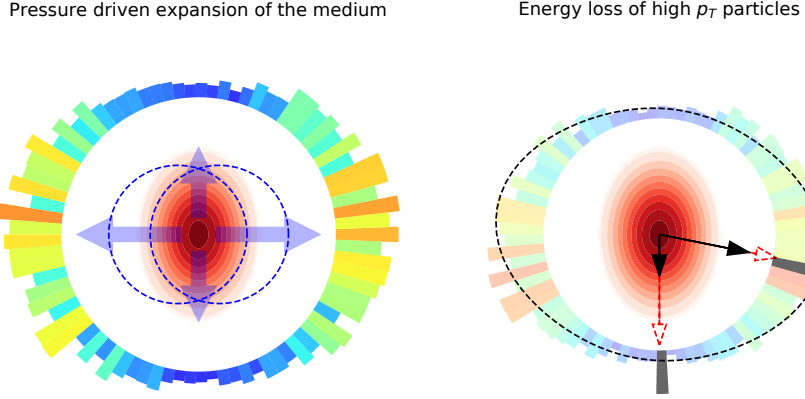


Figure 1.3: Illustration of the connections between final state particles and the formation of a dense medium and its geometry. Left: blue circles indicate the nuclei separated by a finite impact-parameter. An almond-shaped hot medium (red contour) is created in the overlapped region. The medium undergoes pressure driven expansion and creates a $\cos(2\phi)$ like modulation in the final particle distribution (denoted as colored histogram). Right: hard particles travel through the medium loses energy. On average, their final momentum (black arrow) are smaller than the original one (red arrow), and hard partons moving along the long-axis lose more energy than those moving along the short-axis direction.

Centrality selection Experimentally, a minimum-biased (a minimum set of event triggers) sample of recorded events are sorted according to the centrality definition, e.g., multiplicity. Then the events are binned by percentile. For example, the top 0–5% highest multiplicity events are associated with centrality class 0–5%. The collision geometry of a certain centrality class can then be studied through a model. Usually, the model is one of many variants of the Glauber model [MRSS07], which we shall explained it in detail in section 2). It computes the number of binary nucleon-nucleon (N_{bin}) collisions and number of participant nucleons (N_{part} , nucleons that suffers at least one binary collisions) at a given impact parameter. Experimentally, N_{part} is often used as the centrality estimator of the model as it is roughly proportional to the bulk particle production; while the cross-section of hard processes that involves large momentum transfer $Q \gg \Lambda$ scales like the N_{bin} . While this correspondence can be model dependent, the uncertainty can be quantified and model predictions can be validated by studying the production of colorless probes such as photon and weak-boson [A⁺12a, C⁺11, A⁺13a, A⁺16a, A⁺16f]. In particular, recent measurement of Z boson production in Pb-Pb collisions at $\sqrt{s} = 5.02$ TeV has reached a very high precision to constrain collision geometry models in the future [col17b].

1.2.3 Particle production at low- p_T and collective flow

Immediately after the nuclei pass through each other at $t \sim 2R/\gamma$, a huge amount of energy is deposited into the overlap area and entropy is produced, creating a fireball in the middle while the nuclear remnants recede. This highly excited fireball of fields undergoes complex dynamics and cools down rapidly due to its longitudinal and transverse expansion. Eventually, the system hadronizes, and the hadrons can have further interactions and may decay into other hadrons, photons and lepton that are measured by the detectors.

It is observed that the particles produced in relativistic nuclear collisions are distributed across a wide (pseudo)rapidity range, and have steep falling transverse momentum spectra [A^{+16d}]. The majority of the particles are soft hadrons with relatively small transverse momenta $p_T \lesssim 3$ GeV and their creation is a consequence of final state interactions. One of the most striking discoveries from the RHIC and the LHC heavy-ion programs is that these soft particles display a strong collectivity and the patterns can be described by viscous hydrodynamic-based models to a very high precision [DT08, SH08b, SJG10, PSB⁺⁰⁸, NEP16, BMB⁺¹⁶, Ber18]. This success of the hydrodynamic model reveals the strongly coupled nature of the matter produced with a temperature of several times T_c and it has been given the name strongly coupled quark-gluon plasma. This is in contrast to a weakly coupled gas of quarks and gluons that would not exhibit any collectivity.

One manifestation of collectivity is the momentum-space anisotropy or collective flow of the bulk medium. We decompose the charged particle spectra into a Fourier series of the azimuth angle,

$$E \frac{dN}{p_T dp_T d\phi dy} = \frac{1}{2\pi} \frac{dN}{p_T dp_T dy} \left(1 + 2 \sum_{n=1}^{\infty} v_n(p_T) \cos[n(\phi - \Psi_n)] \right). \quad (1.18)$$

The first term is an averaged yield, and subsequent terms in the sum encode the angular dependence. The $n = 1$ term is a shift of the center-of-mass momentum. From $n = 2$, v_n s are momentum anisotropy coefficients of $\cos(n\phi)$ modulations. If the particle production is simply an independent sum of elementary nucleon binary collisions, then the anisotropy would be zero after the average. However, experiments observe a surprisingly larger elliptic flow (v_2), triangular flow (v_3) and higher order v_n at both RHIC and LHC in nuclear collisions. Figure 1.4 shows the variation of the v_n as function of centrality from ALICE measurements [A⁺¹¹, A^{+16b}]. The v_2 coefficient first increases from central to mid-central collisions and slightly decreases at peripheral collisions, while v_3 , v_4 signals are smaller and varies slower with centrality.

In the hydrodynamic picture, a non-central collision deposits initial energy density in an almond shape and the initial fireball has a finite spatial eccentricity ϵ_2 (please refer to the left of figure 1.3 for an illustration). The energy density is higher in the middle and lower at the boundary, so a hydrodynamic pressure builds up and drives the transverse expansion of the fireball. Because the pressure gradient is larger in the short axis-direction and the long-axis direction, the matter flows in an isotropic way, creating the observed momentum space second-order anisotropy v_2 . The existence of

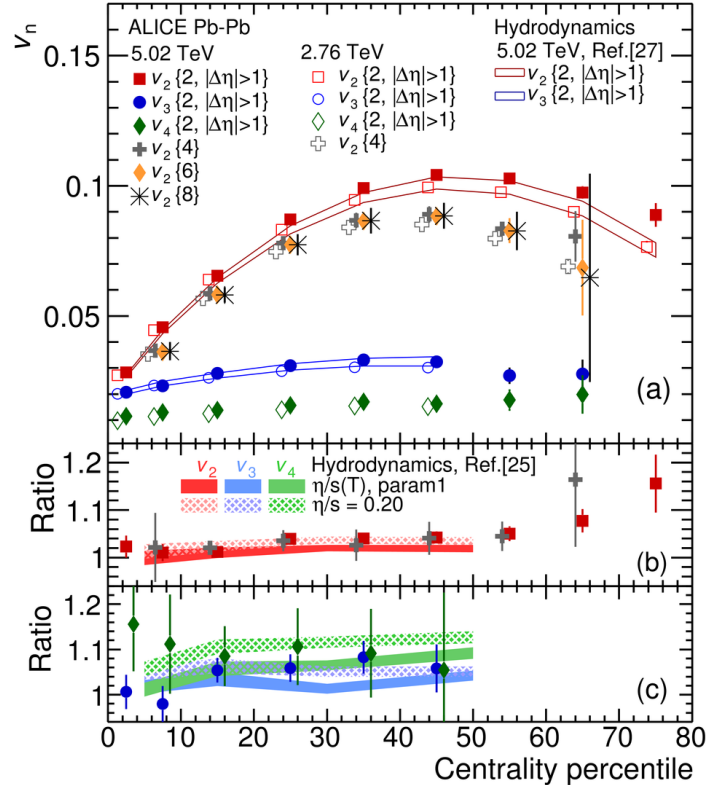


Figure 1.4: The momentum anisotropy coefficient v_2 estimated from multi-particle correlation for charged particle from the ALICE collaboration [A⁺¹¹, A^{+16b}]. The hydrodynamic-based calculations [NEPT16, NHLO16] (lines) very well explains the centrality dependence of the second (red), third (blue) and fourth (green) order coefficients at different beam energies.

higher order of flow harmonics and non-zero v_2 in the most central collisions is because nuclear configuration fluctuations, such as randomized nucleon positions, create all orders of eccentricity ϵ_n . In short, a hydrodynamic expansion transfer initial geometry eccentricities ϵ_n into final state momentum anisotropy v_n of the particle.

Extracting the QGP transport coefficients A relativistic ideal hydrodynamic model assumes an infinitely strong interaction that the medium always stays in local thermal equilibrium. A more sophisticated treatment is relativistic viscous hydrodynamics which accounts for deviations from the local thermal equilibrium due to large gradients in the expansion. The response of the hydrodynamic evolution to the gradients are characterized by the shear viscosity η and bulk viscosity ζ . The QGP shear viscosity and bulk viscosity are of fundamental importance. The shear viscosity to entropy ratio η/s is an indicator of the stong / weak coupling nature of the QGP. And the bulk viscosity to entropy ratio ζ/s is directly related to the scale-invariance breaking of QCD.

Dynamical quantities such as viscosity are extremely hard to compute from first principle, so currently, the determination of these numbers and their temperature dependence requires phenomenological extraction from experiments [MR04, Cha06, RR07, DT08, SH08a, LR08]. The flow harmonics v_n are particular sensitive to the viscous effects, as a finite viscosity dampens the development of anisotropic flows, reducing the transition efficiency from ϵ_n to v_n . Global comparisons of the state-of-the-art medium modeling to a collection of soft observables have corroborated the need of a small η/s that is likely to be slowly increasing with temperature and a non-vanishing ζ/s .

1.2.4 Probing sQGP using hard probes

Very occasionally, an initial collision involving large momentum transfer creates high- p_T particles in the system ($p_T \gtrsim 10$ GeV) that referred to as “hard” particles. By uncertainty principal, they can only be produced at the beginning of the nuclear collision on a time scale $\delta t \sim 1/p_T$, then they pass through and interact with the surrounding bulk medium. Hard particles can be used as self-generated probes of the system. Due to asymptotic freedom, the initial production of hard processes can be computed in the perturbative framework, granting a good theoretical control of its initial state. The final state interaction with the medium then modifies the initial production and leaves finger prints of the medium on the hard probes.

Jet and jet quenching Initial hard partons (gluons, quarks) undergoes complex QCD dynamics, radiating more partons which then hadronize into a collimated bunch of hadrons and decay products. This final collection of particles is observed in the detector as jets. In proton-proton collisions, perturbative calculations and Monte-Carlo simulations are able to explain the production cross-section of the jet and leading hadrons (the hardest hadron in the jet) reasonably well. In nuclear collisions, the initial parton and its radiative daughter partons interact with the medium, causing

energy loss and triggering medium-induced radiation. As a result, one expects the jet / leading parton yield at high- p_T to be reduced compared to the reference in proton-proton collisions (please refer to the right of figure 1.3 for an illustration). To focus on the difference caused by medium effects, the reference has to cancel out a naïve difference that simply rises because there are more effective nucleon-nucleon collisions in a nuclear collision. One defines the so-called “nuclear modification factor”,

$$R_{AA}(y, p_T) = \frac{\frac{dN_{AA}}{dydp_T}}{\langle N_{\text{coll}} \rangle \frac{dN_{pp}}{dydp_T}} = \frac{\frac{dN_{AA}}{dydp_T}}{\langle T_{AA} \rangle \frac{d\sigma_{pp}}{dydp_T}}. \quad (1.19)$$

It is the average N_{bin} “normalized” ratio between the yield in AA collisions and pp collisions. The number of binary collisions is sometimes replaced by the average nuclear overlapping function $\langle N_{\text{coll}} \rangle = \langle T_{AA} \rangle / \sigma_{pp}^{\text{inel}}$, and the yield is replaced by the inclusive cross-section for the proton-proton collision $\frac{dN_{pp}}{dydp_T} \rightarrow \frac{d\sigma_{pp}}{dydp_T}$. These two expressions are equivalent. The ratio is expected to be unity if there is no medium effect, though we do remind the readers that N_{coll} is not a directly observed quantity and has to be estimated in a model-dependent way.

At both RHIC and LHC, colored probes as measured by the R_{AA} of leading hadrons and jets are found to be significantly below unity in nuclear collisions, while the R_{AA} of color neutral probe such as Z -boson is consistent with unity [A⁺08, C⁺11, A⁺12a, A⁺13a, A⁺16a, A⁺16f, col17b]. These discoveries indicate the creation of a color deconfined medium that strongly modifies the hard parton propagation. The interaction strength between the hard parton and the medium is theoretically quantified as the jet transport coefficient \hat{q} , which is defined as the momentum broadening per unit path-length in the transverse direction of the propagation,

$$\hat{q} = \frac{d\langle p_\perp^2 \rangle}{dL} \quad (1.20)$$

The jet transport coefficient is another quantity of fundamental interest in heavy-ion collisions, and there has been a great effort in both first principle computation and phenomenological extraction [WGP95, Zak96, BDM⁺97a, Zak97, AMY03a, GVWZ03, KW03, JM05, CSS07, DH08, BGM⁺09, SGJ09, Maj09, MVL11, A⁺12b, ZSW11, OV11, KLRO⁺15, CLQW16, Kau18, C⁺17]. The hard parton / jet probes the medium at different scales at different stages of its evolution, and more sophisticated observables and theoretical tools are being constructed to answer more microscopic questions such as the actual degrees of freedom of the strongly coupled QGP. Future experimental upgrades might provide the precision to look into this problems [Col12, A⁺14c, WtSC14, A⁺15c, Col17a].

Heavy-flavor probes Heavy flavor is also the major focus of this work. Heavy quarks have masses well above the QCD non-perturbative scale. The charm quark ($M = 1.3$ GeV) and bottom quark ($M=4.2$ GeV) are the most relevant heavy quarks for the present study. The reason that the top quark ($M = 173$ GeV) is out of our discussion is due to its extremely short life time ($\sim 5 \times 10^{-25} \approx 0.15$ fm/c in its

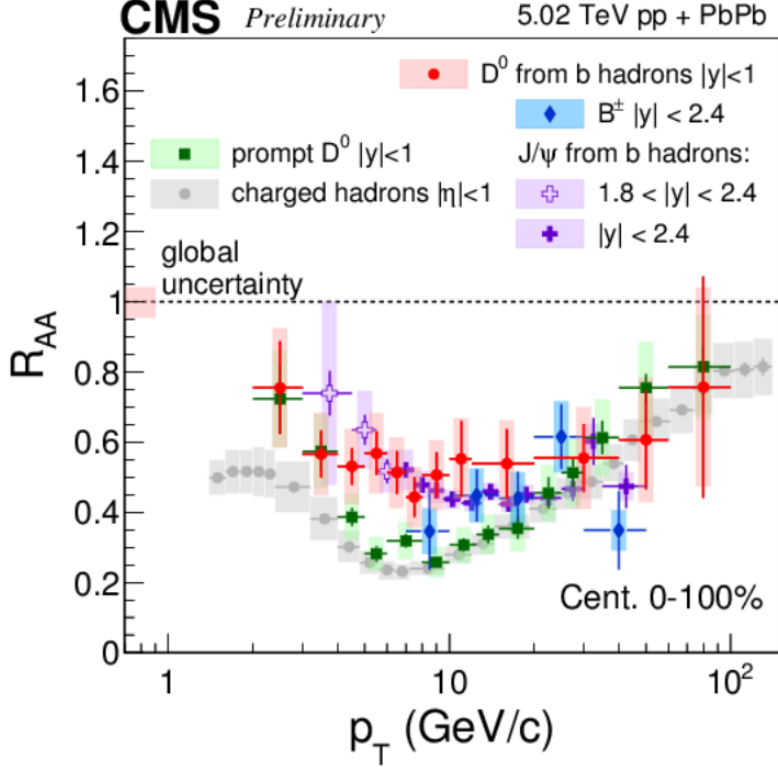


Figure 1.5: The nuclear modification factor $R_{AA}(p_T)$ of charged hadron (gray), D meson (red), B meson (blue), and b -decayed D meson (red), b -decayed J/Ψ (purple) measured by the CMS collaboration [K+17a, S+18a, S+18c, S+17] (figure from Matthew Nguyen).

rest frame) so it barely interacts with the QGP before it decays into, predominantly, bottom quarks. Though there has also been a proposal that takes the advantage of this short life-time to probe the temporal structure of the QGP evolution [AMSS18], we only focus on the charm and bottom flavor in this work.

A large mass guarantees a negligible thermal production contribution, at least for the present top LHC beam energies (there are estimates that thermal contribution can play a role for the future FCC collider [ZCGZ16]). Therefore, heavy flavors, regardless of p_T , are almost always created in initial hard processes. Moreover, the tiny population of heavy flavors in the collision also suppresses the chances that they annihilate / recombine with their anti-particles. Certainly heavy mesons have a long life time such that their decay vertices are outside of the fireball and can be resolved by experiments. Therefore, the number of heavy-flavor particles is almost conserved from the beginning to the end of the entire medium evolution including both the QGP phase and the hadronic phase.

Heavy flavors are of physical interests in many ways. The mass effects are negligible at high p_T where heavy flavors merge into the topic of the jet energy loss physics. At intermediate p_T , the mass effect is expected to suppress the medium-induced radiation, which dominates the energy loss of light quark. And there may

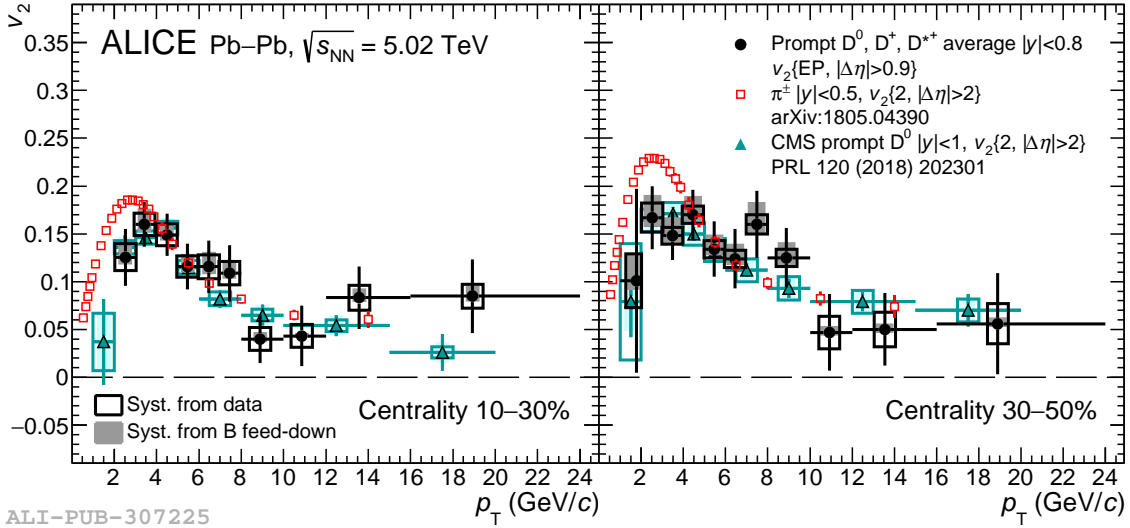


Figure 1.6: The charged pion (red) and D meson momentum anisotropy measured by the ALICE Collaboration (black) and the CMS Collaboration (green). Left and right panels show the results for 10–30% centrality and 30–50% centrality respectively.

be a competition between the collisional energy loss and radiation processes. Experimentally, these differences lead to a hierarchy in the amount of nuclear suppression. For example, figure 1.5 from the CMS collaboration shows a collection of R_{AA} measurements, for charged (mostly light) hadron, prompt D meson, prompt B meson and D and J/ Ψ from b -decays. All the R_{AA} tends to collapse onto the same trend at very high- p_T , while for p_T range around 5 to 20 GeV, despite the large uncertainty, there is a suggestive hierarchy of $R_{AA}(\text{light}) < R_{AA}(\text{charm}) < R_{AA}(\text{bottom})$. It would be interesting to study whether a theoretical framework can explain this difference quantitatively and distinguish different energy loss mechanisms.

Low- p_T heavy quark physics is even more interesting. In this region, collisional process dominates over radiative process, and the description of the heavy quark dynamics under the influence of medium “kicks” reduces to a succinct diffusion equation [MT05]. A spatial diffusion constant D_s controls the close-to-equilibrium dynamics, and can be related to the momentum diffusion by $D_s = 4T^2/\hat{q}(p \rightarrow 0)$. The large inertia $M \gg T$ delays its relaxation time $\tau_{\text{th}} \propto M/TD_s$ and one expects to find a different degree of thermalization for light, charmed, and bottom hadrons [Sve88, MT05, RR10, CQB13a]. For instance, looking at the low p_T momentum anisotropy of charmed meson shown in figure 1.6 [A⁺18a, S⁺18b]. The large v_2 of the charged pions below 3 GeV is due to the collective expansion. The charmed mesons also catch up a significant amount of flow ¹, though still less than the pion. To explains this amount of D meson v_2 , phenomenological studies suggests a D_s close to the lattice QCD calculations [HFR13, CQB13a, XBB⁺18, BDGM12, DFK⁺12, FKL⁺15], while leading order weakly coupled result [MT05] is inadequate . This finding sug-

¹As a remark, the finite v_2 of D meson at high p_T is not directly related to the flow phenomena, but as a result of anisotropic energy loss in a spatial eccentric medium

gests the importance of non-perturbative phenomenon in understanding the coupling between low momentum heavy quark and the medium.

Finally, the unique flavors of heavy quarks help to tag certain processes of interest. For example, the study of recombination hadronization mechanism, strangeness enhancement, and implementation of a selection bias on the quark / gluon-initiated jet ratio.

1.2.5 Transport modeling of hard probes

The understanding of jets and heavy-flavor in heavy-ion collisions needs a comprehensive non-equilibrium modeling effort. This includes initial production / DGLAP evolution, partonic propagation in the QGP, and eventually hadronic interaction. Transport equations are convenient tools to couple the microscopic hard probes propagation to the macroscopic medium evolution, though one has to be very careful with the multiple scales of the problem. For example DGLAP evolution brings the parton scale from p_T down to $O(\text{GeV})$. The probe-medium interactions happens at typical scales around temperature T and the screening mass $m_D \sim gT$, while the medium-induced radiation occurs at a momentum broadening scale of order $\hat{q}t$. Eventually, hadronization happens at scale Λ . Meanwhile, the medium evolution has another set of (time) scales, the hydrodynamization time $\sim 1 \text{ fm}/c$, the finite-size and life-time of the QGP fireball $\sim O(10) \text{ fm}/c$, and the expansion time scale τ_{ex} . Usually a separation of scales allows great simplification to theory calculations. For example, the Boltzmann transport equation requires a separation between the mean-free-path and the coherence time of the scattering. However, in realistic event simulations, treating regions of overlapping scales seems inevitable. We would like to develop in this thesis a new transport model to account for a few of these overlapping scale issues.

Heavy quark transport models In early days, the heavy quark measurements at RHIC energy did not extend to very high- p_T and the radiative energy loss is not as important as elastic ones. Therefore, early studies relied on non-equilibrium dynamics using a pure diffusion model [MT05, vHMRG08]. To include physics at high- p_T physics, a radiation improved diffusion model was then developed [CQB13a] and has been applied to the first Bayesian extraction of the heavy quark transport coefficients [XBB⁺18]. Apart from the diffusion-based models, Boltzmann and linearized Boltzmann models, including both elastic and inelastic interactions, has also been developed [SDM⁺17, CLQW18, KXB18]. Regarding the physical inputs, the Boltzmann-based model takes a weakly-coupled picture; the diffusion based model is more flexible, since the transport coefficient can be computed in both weakly coupled or strongly coupled approaches. Using different models, the extracted transport parameters D_s , \hat{q} have notable differences [B⁺18, XBM⁺19, C⁺18]. The major sources that leads to these differences are:

- Inclusion of radiative energy loss.

- Assumptions on the medium: close-to-equilibrium hydrodynamic medium, or non-equilibrium medium from a full partonic Boltzmann equation.
- Weakly coupled approach versus strongly coupled approach.
- More subtle differences such as Langevin versus Boltzmann dynamics, and the detailed treatment of the radiative processes.

To make progress, improved theoretical calculations and more accurate modeling is important; on the other hand, more subtle differences can be treated as intrinsic modeling uncertainty so that the extracted transport parameters are not over-interpreted (a finite theoretical uncertainty bands on D_s and \hat{q}).

1.2.6 Understanding QGP as a parameter inference problem

All the interesting dynamics of heavy-ion collisions last for $O(10)$ fm/ c , while we can only observe the collision remnants by detectors meters away. Therefore, the determination of any intrinsic properties of the QGP is essentially a parameter inference problem: given measurements, models, and parameters of QGP such as η/s , \hat{q} , what is the favored range of parameters to explain the data. Finally, by comparing the theoretical expectations and the phenomenological constraints of these parameters, one can evaluate the theoretical assumptions, which provide new information on the QGP.

This inversion from observables to parameters is not as simple as it appears, because of the following difficulties,

- The dynamical models are complex and computationally expensive.
- Models take multiple parameters or unknown functions that have infinitely many degrees of freedom.
- Global comparison to many experimental observables.
- The quantification of uncertainty: including experimental uncertainty, model uncertainty and theoretical uncertainty.

Most of these issues can be solved by a Bayes analysis for model parameter calibration, and its key ingredients will be explained in chapter 5. A remaining issue is the theoretical uncertainty, which is hard to quantify. Our solution to the theoretical uncertainty is two-fold. First, if there exist more than one theoretical assumptions without compelling reasons to disfavor either of them, then this difference should be propagated into the extracted model parameters. Including these uncertainty will certainly decrease the constraining power on the transport parameters, but it prevents biasing the estimated number from imposing a too strong assumption. Second, existing theoretical calculations are often worked out in certain idealized limits, while a dynamical modeling approach is much more complicated and may not closely follow the underlying theory. This will certainly obscure the interpretation of the extracted

parameters. Therefore, as an important practice for dynamical modeling, the model should be able to calibrate to theoretical calculations at least in those idealized limits, and then be generalized to the more complex scenario. We devoted chapter 3 to improve the accuracy of hard parton transport model.

1.3 Outline of this Thesis

In this thesis, I focuses on the extraction of the heavy quark transport coefficients from experiments using a newly developed transport model for hard parton propagation in a QGP. In chapter 2, I introduce a hydrodynamic-based medium for the medium evolution. As an application of this simulation framework, I review my project on reverse engineering a three-dimensional initial entropy deposition of the heavy-ion collision from experimental data. In chapter 3, we develop the transport model for hard parton (including heavy flavor) propagation inside the QGP. This model interpolates a small-angle diffusion picture and a large-angle scattering picture of the probe-medium interaction. I show the limitation of the semi-classical transport approach in implementing parton branching processes (radiation) at high energy, and demonstrate how to modify the semi-classical approach to treat it properly. Chapter 4 builds a comprehensive simulation workflow that couples the initial production and in-medium transport of heavy flavors to the bulk medium evolution. Benchmark calculations with simple guesses of parameters are compared to the experimental measurements. Chapter 5 is a brief description of the Bayes methodology of model parameter calibration. Applying the Bayes method, in chapter 6, a systematic model-to-data comparison is performed, extracting the heavy flavor transport properties. Finally, chapter 7 summarizes the work and discuss possible future improvements.

Chapter 2

Bulk-medium evolution and initial conditions

This chapter introduces a hydrodynamic-based model for the medium evolution in heavy-ion collisions. I will also review my project on applying this framework to the reverse engineering of the initial three-dimensional entropy deposition from experimental observables [KMBB17].

2.1 A Hydrodynamics-based dynamical modeling

2.1.1 Relativistic hydrodynamic

Relativistic hydrodynamics plays a center role in the modeling of heavy-ion collisions. It is relativistic as the flow velocity of the QGP fireball expansion can reach a significant fraction of the speed of light. It is a macroscopic description that propagates the energy-momentum tensor of the system without a detailed knowledge of the microscopic interaction. The first set of equations comes from energy-momentum conservation, which should always be satisfied,

$$\partial_\mu T^{\mu\nu} = 0. \quad (2.1)$$

$T^{\mu\nu}$ is the energy momentum tensor and $\partial_\mu = \partial/\partial x^\mu$. Here we have choose the metric as $g^{\mu\nu} = \text{diag}\{1, -1, -1, -1\}$.

Ideal hydrodynamics Ideal hydrodynamics assumes that the system relaxes to local thermal equilibrium much faster compared to other time scales. Then, $T^{\mu\nu}$ can be specified by given only the energy density e , pressure P , and flow velocity u^μ of a fluid element,

$$\partial_\mu T^{\mu\nu} = eu^\mu u^\nu - P(g^{\mu\nu} - u^\mu u^\nu). \quad (2.2)$$

Boosting into the co-moving frame of the fluid element, $T^{\mu\nu}$ reduces to the diagonal form $T^{\mu\nu} = \text{diag}\{e, -P, -P, -P\}$.

There are five unknowns e, P, u_x, u_y, u_z (u_t is determined by $u^2 = 1$), but the conservation laws 2.1 only provide four equations. A fifth equation is the equation of state (EoS) $P = P(e)$, relating pressure and energy density in the thermal equilibrium, which completes the ideal-hydrodynamic equations. Lattice QCD calculations have determined the 2+1 flavor QCD EoS to a high precision. Though it is not a prior that the lattice QCD EoS computed in an infinite matter in an infinite time is the right choice for describing a transient system with large gradients, using the lattice

input does result in reasonable agreement with the data. Moreover, there has been a study that tries to constrain the form of the EoS from experimental data and the “calibrated” EoS is very close to the Lattice calculation [PSSW15].

Viscous hydrodynamics and QCD transport coefficients A physical relaxation rate is always finite, and the system can be driven out of local thermal equilibrium by large gradients of the fast expanding fireball. Relativistic viscous hydrodynamics takes into account these off-equilibrium effect by including viscous corrections. The energy-momentum tensor deviates from the ideal one by a bulk viscous pressure Π , and a shear viscous tensor $\pi^{\mu\nu}$,

$$T^{\mu\nu} = u^\mu u^\nu e - (g^{\mu\nu} - u^\mu u^\nu)(P + \Pi) + \pi^{\mu\nu}. \quad (2.3)$$

The Π and $\pi^{\mu\nu}$ will then respond to the finite gradients of the fluid field. To first order in the gradient, they are given by the constitutive relations,

$$\pi^{\mu\nu} = 2\eta\sigma^{\mu\nu}, \quad (2.4)$$

$$\Pi = -\zeta\theta, \quad (2.5)$$

and the hydrodynamic equations are the relativistic version of the Naiver-Stokes equations. Here, $\sigma^{\mu\nu} = \partial^{(\mu}u^{\nu)}$, $\theta = \partial \cdot u$ are the fluid shear stress and expansion rate. The proportionality constants are known as the QCD shear (η) and bulk (ζ) viscosity, encoding dynamical information of the QCD medium. Their dimensionless ratio to the entropy density η/s and ζ/s are important indicators of the interaction strength and the scale-violation of the QCD matter and are of great physical importance. A significant effort is underway to either compute these quantities from first principles or effective models or extract these numbers from experiments [BMCS⁺15, BMB⁺16, AKBB18, Ber18, NNP⁺14].

Coming back to the hydrodynamic equations, it has been shown that one has to go to second order in the gradient expansion to render the viscous correction compatible with special relativity [Isr76]. Meanwhile, π and Π become dynamical quantities that relax to the Naiver-Stokes limit.

$$\begin{aligned} \tau_\pi \dot{\pi}^{\langle\mu\nu\rangle} + \pi^{\mu\nu} &= 2\eta\sigma^{\mu\nu} - \delta_{\pi\pi}\pi^{\mu\nu}\theta + \phi_7\pi_\alpha^{\langle\mu}\pi^{\nu\rangle\alpha} \\ &\quad - \tau_{\pi\pi}\pi_\alpha^{\langle\mu}\sigma^{\nu\rangle\alpha} + \lambda_{\pi\Pi}\Pi\sigma^{\mu\nu}, \end{aligned} \quad (2.6)$$

$$\tau_\Pi \dot{\Pi} + \Pi = -\zeta\theta - \delta_{\Pi\Pi}\Pi\theta + \lambda_{\Pi\pi}\pi^{\mu\nu}\sigma_{\mu\nu}. \quad (2.7)$$

The $\tau_\pi, \tau_\Pi, \delta, \phi, \lambda$ are known as second order transport coefficients. This complicated set of equations together with the conservation law and the EoS forms the viscous hydrodynamic equations. Nowadays, well tested numerical packages have been developed solving these equations in the context of heavy-ion collisions [SH08a, SQS⁺16, SJG10, KHB14].

Boost-invariance approximation and beyond In general, the hydrodynamic equations have to be solved in 3+1 dimensions. But a reduction to a 2+1 dimension is

possible, if a boost-invariant symmetry is assumed near mid-rapidity [MRSS07, DN07, STV12, NEP16, MBB15, CSG⁺16]. This symmetry is first proposed by Bjorken in [Bjo83]. It states that the system at different space-time rapidity behaves the same upto a longitudinal boost, and is termed “boost-invariance”. Then, the 2+1 dimensional solution obtained at one space-time rapidity ($\eta_s = 0$) can be boosted to get the solution at other η_s . As a result, particle emissions from such a fireball does not strongly depends on η_s .

The η_s -dependence cannot be detected but is related to the emitted particle rapidity / pseudo-rapidity for the reason below. Suppose that the Lorentz contracted nuclei interact at $z = 0$ and produce excitations that free-stream in the longitudinal direction, then for each of these excitations,

$$\frac{z}{t} = \frac{p_z}{E}. \quad (2.8)$$

This approximation provides the equivalence of η_s and y at early stages of the collision:

$$\eta_s = \frac{1}{2} \log \frac{t+z}{t-z} \sim y = \frac{1}{2} \log \frac{E+p_z}{E-p_z}. \quad (2.9)$$

Assume further that these initial excitations have small masses, then the rapidity can be approximated by pseudorapidity as $E \approx |p|$. Since the following hydrodynamics is boost-invariant, then emitted particle pseudo-rapidity should be flat. Experimentally, the event-averaged rapidity-distribution of charged particles dN_{ch}/dy in both proton-proton and symmetric nuclei-nuclei collisions at the RHIC and energy falls off at large rapidity but has a central plateau at least within $|y| < 2$.

However, since dN_{ch}/dy are event-averaged quantities, it being flat within $|y| < 2$ does not rule out event-by-event particle production fluctuation which break the boost-invariance, and these fluctuations can be different at different transverse locations. Moreover, asymmetric nuclear collision such as p-Pb, p-Au, d-Au, He-Au, etc clearly break the boost-invariance even on an event averaged level [A^{+14e}, A^{+14a}, A^{+13b}, C^{+13b}, C^{+13a}, K^{+15a}, K^{+15c}, K^{+16a}, A^{+15d}, A^{+15e}, A^{+18c}]. Therefore, the study of longitudinal fluctuation related observables or the search for hydrodynamic behavior in small collision system requires one to go beyond the boost-invariance set-up.

2.1.2 Particularization and microscopic transport

The longitudinal and transverse expansion cools down the system temperature. Density and relaxation rate also drop rapidly. Eventually the relaxation time is too long for the hydrodynamic approach to be applicable. At this point, it is proper to switch to a microscopic transport model. This switching is usually done near or below the pseudo-critical temperature $T_{sw} \lesssim T_c$ so that the energy momentum tensor can be particularized as an ensemble of hadrons, whose interactions are well known. If this matching is performed well above T_c , then we will have to deal with the problem of modeling quark / gluon dynamics and hadronization in the strong coupled regime

near T_c . Of course, whether hydrodynamics with lattice EoS and a hadronic transport model are both valid in the $T_{sw} \lesssim T_c$ region is another question.

The hydrodynamic $T^{\mu\nu}$ is usually particlized at a constant energy density / temperature hypersurface using the Cooper-Frye prescription [CF74]. The number of specie “a” particles emitted with momentum p from a hypersurface element i is computed from,

$$\Delta N_i^a(p) = \frac{g^a f^a(p) dp^3}{(2\pi)^3} \frac{p^\mu}{E} \Delta\sigma_{i,\mu}. \quad (2.10)$$

$f^a(p)$ is the phase space density, $\Delta\sigma_{i,\mu}$ is the four components of the surface element, which has a unit of a 3D volume, and g^a is the degeneracy of the specie. This distribution function should include both a thermal part and a viscous correction, $f = f_0 + \delta f$. There are more than one way to construct the viscous correction δf from e, P, n, Π and $\pi^{\mu\nu}$ based on different assumptions of the non-equilibrium corrections. In this work, we use a non-additive δf correction that has been developed in [PT10, Pra14] and implemented by [Ber18]. Please refer to these references for the original formulation and numerical implementation details.

The particlized hadronic system is then solved by the Ultra-relativistic Quantum Molecular Dynamics (UrQMD) model [B⁺98, B⁺99] until the system is dilute enough and interaction ceases (kinetic freezeout). The UrQMD model includes processes such as resonance decays, elastic and inelastic scatterings, and string formations and fragmentations.

2.1.3 Pre-equilibrium stage

At very early times of the collision, the system is off equilibrium. However, viscous hydrodynamic assumes a closeness to the local thermal equilibrium . (There are also recent efforts in understanding the effectiveness of hydrodynamics outside of its traditional range of applicability [Phy15, Rom18, Str19]). A successful prediction using an early onset of hydrodynamic evolution at $\tau_0 \lesssim 1\text{fm}/c$ suggests a fast hydrodynamization, though the mechanism is still under debate. There are different models of the pre-equilibrium stage available¹, including solving the classical Yang-Mills equation [STV12, SS16], applying partonic transport models [CBOP18], a collision-less Boltzmann equation (free-streaming) plus Landau matching [LSH15], and the linear response method of the effective kinetic approach [KMP⁺19].

Here we briefly introduce the free-streaming model [LSH15]. The initial energy density ($\tau = 0^+$) at mid-rapidity is thought to be carried by mass-less partons that propagate at the speed of light in the transverse direction. The initial distribution function is put into factorized form $f(x_\perp, p_\perp, \tau = 0) = n(x, \tau = 0) \times dN/dp_\perp^2$. The

¹Such a pre-equilibrium stage was not included in my study of the 3D initial condition, and the hydrodynamics starts at $\tau_0 = 0.6 \text{ fm}/c$ assuming local thermal equilibrium. For my later study of the heavy flavor transport, a 2+1D collision-less Boltzmann equation implemented by [Ber18] is used.

momentum distribution dN/dp_\perp^2 does not evolve with time as collisions are neglected, while the spatial density propagates as

$$n(\vec{x}, \tau) = \int n(\vec{x}', \tau = 0) \delta^{(2)}(\vec{x} - \vec{x}' - \tau) d\vec{x}'^2 \quad (2.11)$$

Then, the model assumes a sudden hydrodynamization at time τ_{hydro} , where the free-streamed

$$T^{\mu\nu}(x_\perp, \tau_{\text{hydro}}) = \int f(x_\perp, p_\perp, \tau = 0) \frac{p^\mu p^\nu}{E} dp^3 \quad (2.12)$$

is used for initializing the hydrodynamic equations by the Landau matching procedure [LSH15].

2.2 Initial condition model

Unlike the dynamical models that are governed by a few equations / laws with a few parameters, the initial condition model parameterizes many more unknowns. For different initial condition models, these unknowns can be the initial color density of the nuclear wave function, the effective size of a nucleon, the form factor of the nucleon-nucleon inelastic cross-section, and the amount of fluctuations in particle production / energy deposition, etc. There are two classes of initial condition models:

- Models that takes into account the particle production dynamics. Such as minijet production, strings productions and flux-tubes, coarse-grained hadronic transport models, and color-glass condensate (CGC) effective field theory based models.
- Parametric models. Models provide macroscopic initial conditions without a dynamical component. Such as the Monte-Carlo Glauber models and its extensions, and the T_RENTo initial condition model to be explained.

This section introduces the original boost-invariant T_RENTo model, and my work that extends the model to include longitudinal structure and fluctuations.

2.2.1 The original (boost-invariant) T_RENTo model

The original T_RENTo model is proposed as a flexible ansatz to investigate a family of entropy / energy deposition behaviors at mid-rapidity. First, the impact parameter \vec{b}_{AB} between the two colliding nuclei A and B is sampled at random. Then, nucleon positions inside each nucleus are sampled according to the Woods-Saxon distribution²,

$$\frac{df_N}{r^2 dr d\phi d \cos \theta} = \frac{1}{\exp\left\{\frac{r - R(1 + \beta_2 Y_{20}(\theta) + \beta_4 Y_{40}(\theta))}{a}\right\} + 1} \quad (2.13)$$

²The Woods-Saxon distribution is intended for heavy nuclei, for light nuclei such as Deuteron, Helium, Oxygen, the few-body wave function or pre-tabulated nuclear configurations are used for sampling

including the quadrupole and hexadecapole deformation of certain nuclei. The randomized nucleon position is critical to explain the odd order of flow harmonics observed in experiments [AR10].

The collision between the two nuclei is determined at the nucleon level. Every nucleon pair $\{i, j\}$ with i from nucleus A and j from nucleus B has a certain probability to collide inelastically. This probability at given nucleon-nucleon impact parameter $\vec{b}_{ij} = \vec{b}_{AB} + \vec{x}_{i,\perp} - \vec{x}_{j,\perp}$ is parametrized as,

$$P(b_{ij}; \sigma) = 1 - \exp[-\sigma T_{pp}(b_{ij})], \quad (2.14)$$

where $T_{pp}(b)$ is the overlap function between the z -integrated density of the nucleon T_p ,

$$T_{pp}(b) = \int d\vec{x}_\perp^2 T_p(\vec{x}_\perp - \vec{b}/2) T_p(\vec{x}_\perp + \vec{b}/2). \quad (2.15)$$

Assuming a 3D Gaussian shaped nucleon with width parameter w , T_p is

$$T_p(\vec{x}_\perp^2) = \frac{1}{2\pi w^2} \exp\left(-\frac{\vec{x}_\perp^2}{2w^2}\right). \quad (2.16)$$

w is treated as a tunable parameter. The σ parameter in equation 2.14 is the nucleon opacity parameter with units of an area. It is determined by fitting to the experimental measured proton-proton inelastic cross-section at a given beam energy,

$$\sigma_{pp}^{\text{inel}}(\sqrt{s}) = \int d\vec{b}^2 P(b; \sigma(\sqrt{s})). \quad (2.17)$$

We apply the probabilistic collision criteria of equation 2.14 to each pair of nucleons and sample the binary collisions. Nucleons that suffer at least one inelastic collision are called participants and the total number of binary inelastic collisions is denoted as N_{bin} . The minimum-biased event sample in the TRENTo model is defined as all events that have at least one binary collision.

The above procedure is similar to the that of a Monte-Carlo Glauber model in determine the nuclear inelastic cross-section [MRSS07]. Some experimental versions of the Glauber model use a black disk proton instead of a Gaussian profile. We found that this difference results in little change in the centrality dependence of N_{part} , but can greatly affect N_{bin} and may affect the computation of the hard probe nuclear modification factor.

The novel component of TRENTo is an ansatz that maps the participants to the energy / entropy density deposited at mid-rapidity. Defining the participant densities as a sum of the participants' thickness function,

$$T_{A,B}(\mathbf{x}) = \sum_{i \in \text{Parts}_{A,B}} w_i T_p(\mathbf{x} - \mathbf{x}_i). \quad (2.18)$$

The summation goes over all participants in nuclei A and B , and each contribution is modulated by a fluctuating weight w_i that follows a Γ -distribution. The fluctuation

Table 2.1: TRENTo p -parameter

$p \in \mathbb{R}$	$f(x, y)$	Entropy / energy production
$-\infty$	$\min\{x, y\}$	dominated by the thinner target
-1	$2xy/(x + y)$	the harmonic mean scaling
0	\sqrt{xy}	the geometric mean scaling
1	$(x + y)/2$	the arithmetic mean (participant) scaling
$+\infty$	$\max\{x, y\}$	dominated by the thicker target

has unit mean and variance $1/k$ and k is a free parameter. This weight accounts for the large multiplicity fluctuation in minimum biased proton-proton collisions. The entropy / energy density deposition at mid-rapidity is assumed to be a function of T_A and T_B only at each transverse location,

$$\frac{dS(\vec{x})}{d\eta dx_{\perp}^2} \text{ or } \frac{dE(\vec{x})}{d\eta dx_{\perp}^2} = f(T_A(\vec{x}), T_B(\vec{x})). \quad (2.19)$$

This simplification is possible because at $\tau = 0^+$, causality requires that the entropy production at one location cannot be correlated with the information at a different transverse location. Also, the partons that contribute to the bulk low- p_T particle production at high \sqrt{s} are predominately low energy gluons whose longitudinal wavelength is longer than the contracted proton radius in the z -direction; therefore, the entropy production should not be sensitive to the details of how the participants are aligned but only its z -integrated density. TRENTo parametrizes this mapping from T_A and T_B to the energy / entropy deposition using a “generalized mean” ansatz,

$$f(T_A, T_B; p) = \left(\frac{T_A^p + T_B^p}{2} \right)^{1/p}. \quad (2.20)$$

p is another tunable parameter. Some special values of p reduce the ansatz to well known averaging procedures as shown in table 2.1. This way the model is able to parametrize a class of entropy / energy production scheme and includes certain type of initial condition uncertainty. Through a global model-to-data comparison, this p parameter has been calibrated to be very close to 0, suggesting the data favors a mid-rapidity entropy / energy deposition that scales as $(T_A T_B)^{0.5}$. A similar scaling is also found in the EKRT initial condition model based on pQCD particle production and saturation physics [EKRT00].

2.2.2 Parametrizing the longitudinal dependence in TRENTo

The TRENTo model has been very successful describing obserables at mid-rapidity [MBB15, BMB⁺16, MBB18]. My work focuses on extending the parametrization to a rapidity-dependent initial condition, and seeks a reverse-engineered 3D entropy production from rapidity-dependent observables [KMBB17].

Boost-invariance can be broken if the initial participant density is asymmetric ($T_A(\mathbf{x}_{\perp}) \neq T_B(\mathbf{x}_{\perp})$); in addition, dynamical fluctuations can generate asymmetry as well. We listed what contributions are included and what are not in the model

- In asymmetric collisions like p-A and non-central A-A, the local thickness functions are imbalanced $T_A \neq T_B$.
- Even in central A - A collision, nuclear / nucleon configuration fluctuations also contribute to the asymmetry. It is included as the randomized nucleon position fluctuation and the γ -fluctuation of the nucleon thickness function.
- Initial stage dynamical fluctuation, initial flow in the z -direction are not included.

Therefore, the asymmetry in the extended T_{RENT}o model only comes from the imbalance between T_A and T_B . Take the following decomposition of $s(\mathbf{x}, \eta_s)$ at the hydrodynamic starting time τ_0 ,

$$s(\mathbf{x}, \eta_s)|_{\tau=\tau_0} \propto f(T_A(\mathbf{x}), T_B(\mathbf{x})) \times g(T_A(\mathbf{x}), T_B(\mathbf{x}), \eta_s). \quad (2.21)$$

f is the entropy production at midrapidity as explained above. g parametrize the rapidity-dependence and is always normalized such that $g(\eta_s = 0) = 1$, so that it reduces to the original model at mid-rapidity. We parametrize the g function in terms of rapidity and then transformed to the space-time rapidity.

$$g(\mathbf{x}, \eta) = g(y; T_A(\mathbf{x}), T_B(\mathbf{x})) \frac{J \cosh \eta_s}{\sqrt{1 + J^2 \sinh^2 \eta_s}}, \quad (2.22)$$

where the species-dependent factor J is replaced with an effective value $J \approx \langle p_T \rangle / \langle m_T \rangle$. To relate the asymmetry of $g(y)$ to the difference of T_A, T_B , we choose to parametrize the y -cumulents of g as functions of T_A and T_B . The $g(y)$ function is then reconstructed using its first few cumulants (mean μ , standard deviation σ , and skewness γ) by,

$$g(\mathbf{x}, y) = \mathcal{F}^{-1}\{\tilde{g}(\mathbf{x}, k)\}, \quad (2.23)$$

$$\log \tilde{g} = i\mu k - \frac{1}{2}\sigma^2 k^2 - \frac{1}{6}i\gamma\sigma^3 k^3 e^{-\frac{1}{2}\sigma^2 k^2} + \dots \quad (2.24)$$

where for the skewness term, we have included an exponential factor that systematically includes higher order cumulants to regulate the behavior of the function at large y . Numerically, we have found that within the range of $|y| < 3.3\sigma$, the reconstructed function has a good behavior and remains positive definite. The mean, standard deviation (width), and the skewness are parametrized as follows,

- For the mean parameter, we assume it is proportional to the center-of-mass rapidity of the local participant density $\mu = \mu_0 \eta_{\text{cm}}$,

$$\eta_{\text{cm}} = \frac{1}{2} \log \left[\frac{T_A e^{y_b} + T_B e^{-y_b}}{T_A e^{-y_b} + T_B e^{y_b}} \right] \quad (2.25)$$

where y_b is the beam rapidity.

- For the standard deviation, currently we leave it as a global parameter independent of the transverse location $\sigma = \sigma_0$, but only a function of the center-of-mass energy.

Table 2.2: Table

Model	mean μ	std. σ	skewness γ
Relative	$\frac{1}{2}\mu_0 \ln\left(\frac{T_A e^{y_b} + T_B e^{-y_b}}{T_A e^{-y_b} + T_B e^{y_b}}\right)$	σ_0	$\gamma_r \frac{T_A - T_B}{T_A + T_B}$
Absolute	$\frac{1}{2}\mu_0 \ln\left(\frac{T_A e^{y_b} + T_B e^{-y_b}}{T_A e^{-y_b} + T_B e^{y_b}}\right)$	σ_0	$\gamma_a(T_A - T_B)/T_0$

- For the skewness, there is not a preferred form, so we tested two parametrizations. And in the end, we will check whether the 3D initial condition extracted from data is sensitive to the different parametrizations schemes. These two choices are termed “relative skewness” and “absolute skewness”.
 - The “relative skewness” parametrization assume a skewness proportional to the relative difference of T_A and T_B ,

$$\mathcal{A}(T_A, T_B) = \gamma_r \frac{T_A - T_B}{T_A + T_B}, \quad (2.26)$$

- The “absolute skewness” parametrization assume a skewness proportional to the absolute difference of T_A and T_B ,

$$\mathcal{A}(T_A, T_B) = \gamma_a \frac{T_A - T_B}{T_0}. \quad (2.27)$$

And we put the unit for thickness function $T_0 = 1 \text{ fm}^{-2}$ to restore γ as a dimensionless parameter.

We have summarized the two parametrizations in table 2.2, and μ_0 , σ_0 , γ_r or γ_a , along with the effective Jacobian J are the four additional parameters introduced for the three-dimensional extended TRENTo model.

In figure 2.1, we show two sample events from a Pb - Pb collision (top plots) and a p - Pb collision (bottom plots) generated by TRENTo. The 3D initial entropy densities are sliced at mid-rapidity $\eta_s = 0$ (left plots) and at the $x = 0$ plane (right plots). The mid-rapidity results are identical to the one predicted in the original TRENTo model. The model is capable of generating fluctuating longitudinal structures that are local in the transverse plane, and breaking the boost-invariance both locally and globally. For the p - Pb event, there is a clear structure that one hot spot extends into the proton going side $\eta_s > 0$, while the participant clusters from the lead nuclei push the entropy production into the lead going side $\eta_s < 0$.

2.3 Reverse engineering the 3D initial condition

In the final section of this chapter, I apply the hydrodynamic-based simulation framework and the flexible TRENTo-3D initial condition model to reverse engineer the 3D entropy deposition at the onset of hydrodynamics at LHC energies.

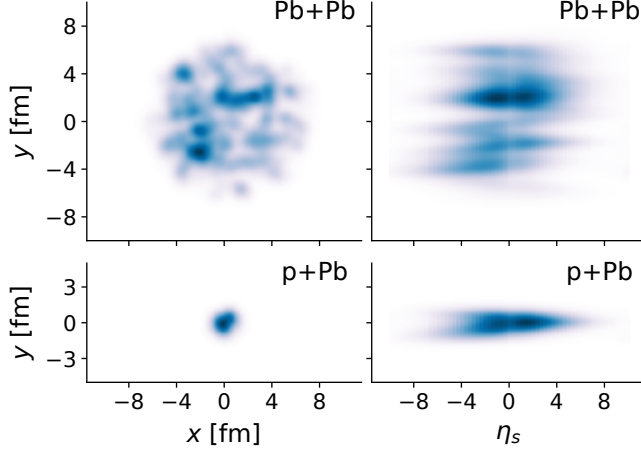


Figure 2.1: Two sample events for Pb-Pb collision (top row) and p+Pb collision (bottom row). The left column and the right column slice the initial entropy density at middle rapidity and the $x = 0$ plane respectively. The relative skewness parametrization is used with $\mu_0 = 1$, $\sigma_0 = 3$ and $\gamma_r = 6$.

Experimentally, one can only measure rapidity-dependent observables on an event averaged level, which already integrates the contribution of particle production over the transverse plane; while our parametrization in the TRENTo model only involves local functions of the participant density function. So it is a nontrivial task to infer the functional form of local entropy production $s(\mathbf{x}, \eta_s)$ from these “global” measurements. The statistical technique for the reverse-engineering is the Bayes analysis explained in chapter 5.

2.3.1 Sensitive observables to the initial entropy deposition

The single particle spectra The most direct observable is the charged particle pseudo-rapidity density $dN_{\text{ch}}/d\eta$ measured for different collision systems and centralities. The ALICE collaboration and the ATLAS collaboration has measured this quantity for both the Pb-Pb system ($-3.5 < \eta < 5.0$) and the p-Pb system ($|\eta| < 2.7$). $dN_{\text{ch}}/d\eta$ can very well constrain the global rapidity profile and the centrality dependence of the mode, while the limitation being that it is less sensitive to the amount of longitudinal fluctuations.

Two particle pseudo-rapidity correlation A good probe of event-by-event longitudinal fluctuations is the two-particle pseudorapidity correlation observable $C(\eta_1, \eta_2)$,

$$C(\eta_1, \eta_2) = \frac{\langle N(\eta_1)N(\eta_2) \rangle}{\langle N(\eta_1) \rangle \langle N(\eta_2) \rangle} \quad (2.28)$$

The long range part of $C(\eta_1, \eta_2)$ is sensitive to the initial state. This is because the correlation between particles separated by a large rapidity gap at proper time τ can only come from proper times before $\tau e^{-|\eta_1 - \eta_2|/2}$ due to causality. For example, if two

particles separated by four units of rapidity are emitted at a constant $\tau = 8 \text{ fm}/c$ hydrodynamic freeze-out hyper-surface and neglecting the long range correlation from the hadronic cascade, then any correlation must have come from before the proper time $8e^{-2} \approx 1 \text{ fm}/c$.

To see how $C(\eta_1, \eta_2)$ is related to the longitudinal fluctuation of the entropy deposition / particle production, decompose $dN_{\text{ch}}/d\eta$ for each event in a finite pseudo-rapidity window $[-Y, Y]$ using the normalized Legendre polynomials basis [BT13, JRZ16, col15],

$$\frac{dN}{d\eta} = \left\langle \frac{dN}{d\eta} \right\rangle \left[1 + \sum_{n=0}^{\infty} a_n T_n \left(\frac{\eta}{Y} \right) \right], \quad (2.29)$$

$$T_n(x) = \sqrt{n + \frac{1}{2}} P_n(x) \quad (2.30)$$

Where $\langle \frac{dN}{d\eta} \rangle$ is the reference multiplicity at mid-rapidity for a certain centrality. a_0 is the total multiplicity fluctuation and a_1 controls how the multiplicity distribution is tilted in rapidity in each event and so on. The two-particle correlation $C(\eta_1, \eta_2)$ measures the variance of these a_n coefficients. Define the normalized event-wise distribution $R(\eta) = dN/d\eta/\langle dN/d\eta \rangle$, then the correlator is,

$$C(\eta_1, \eta_2) = \langle R(\eta_1)R(\eta_2) \rangle \quad (2.31)$$

$$= 1 + \sum_{m,n} \langle a_m a_n \rangle T_{mn}(\eta_1, \eta_2), \quad (2.32)$$

$$T_{mn}(\eta_1, \eta_2) = \frac{T_n(\eta_1)T_m(\eta_2) + T_m(\eta_1)T_n(\eta_2)}{2}. \quad (2.33)$$

Therefore, $\langle a_m a_n \rangle$ can be extracted by projecting the two particle correlation on to the function T_{mn} .

Combinations like $\langle a_0 a_n \rangle$ simply reflect how the event-wise rapidity fluctuation correlates with the multiplicity fluctuation. These contributions are canceled to first order by another normalization to define C_N ,

$$C_N(\eta_1, \eta_2) = \frac{C(\eta_1, \eta_2)}{C_1(\eta_1)C_2(\eta_2)}, \quad (2.34)$$

$$C_{1,2}(\eta_{1,2}) = \int_{-Y}^Y C(\eta_1, \eta_2) \frac{d\eta_{2,1}}{2Y}. \quad (2.35)$$

Finally, C_N is directly related to the rapidity fluctuation itself,

$$C_N(\eta_1, \eta_2) \sim 1 + \frac{3}{2} \langle a_1^2 \rangle \frac{\eta_1 \eta_2}{Y^2} + \dots \quad (2.36)$$

We make use of the $\langle a_1^2 \rangle$ measurements to constrain the amount of linearly-tilting fluctuation in the initial condition model.

In addition to the initial condition fluctuation, short range correlation also contribute to the a_1 fluctuation [DMRS15]. The UrQMD hadronic afterburner is able to model certain type short range correlations coming from resonance decay and collisions, but jet-like correlations are hard to accounted for.

Table 2.3: Three-dimensional initial condition parameters

Parameter	Description	Range
$N_{\text{p+Pb}}$	Overall p+Pb normalization	140.0–190.0
$N_{\text{Pb-Pb}}$	Overall Pb-Pb normalization	150.0–200.0
p	Generalized mean parameter	-0.3–0.3 (with a prior)
k	Multiplicity fluct. shape	1.0–5.0
w	Gaussian nucleon width	0.4–0.6
μ_0	Rapidity shift mean coeff.	0.0–1.0
σ_0	Rapidity width std. coeff.	2.0–4.0
γ_0	Rapidity skewness coeff.	0.0–10.0 (rel) 0.0–3.6 (abs)
J	Pseudorapidity Jacobian param.	0.6–0.9

2.3.2 Calibration of the 3D initial condition parameters

The degrees of freedom of the initial condition model are,

- 1–2. Two normalization factors for Pb-Pb and p+Pb collisions at $\sqrt{s_{\text{NN}}} = 2.76$ TeV and 5.02 TeV beam energies. They are not fully independent as $N_{\text{p+Pb}} > N_{\text{Pb-Pb}}$ is always imposed in the parameter sweep.
3. The mid-rapidity entropy deposition parameter p .
4. The Γ -fluctuation variance parameter $1/k$.
5. The Gaussian nucleon width w , which determines the initial state granularity.
- 6–8. Three coefficients that modulate the local rapidity distribution's shift μ_0 , width σ_0 , and skewness γ_r or γ_a ,
9. An average Jacobian J for the conversion from rapidity to pseudorapidity.

The range of the parameters is shown in 2.3. One may notice that we did not use different width parameters for the rapidity distribution σ_0 for Pb-Pb and p-Pb collisions, because the beam rapidity changes less than 8% from 2.76 TeV to 5.02 TeV.

The dynamical model consists of a 3+1D relativistic hydrodynamics and a hadronic afterburner. The equation-of-state (EoS) is obtained by interpolating the state-of-the-art lattice-QCD EoS [B⁺14a] at high temperature (zero baryon density) to a hadron resonance gas EoS at low temperature [MS16b]. The energy density at which the hydrodynamic energy momentum tensor is particularized into hadrons is $\epsilon_{sw} = 0.322 \text{ GeV/fm}^3$ corresponding to a switching temperature close to the pseudo-critical temperature $T_{sw} \sim T_c = 0.154 \text{ GeV}$. As a remark, the relativistic hydrodynamics code vHLLE [KHB14] includes viscous corrections, but we used its ideal mode in the parameter extraction. This is because the parameter optimization process requires running the model on hundreds of different parameter sets. For each parameter set, thousands of minimum-biased events needed to be generated to control the statistical uncertainty, especially for the correlation observables. The full 3+1D viscous hydrodynamics is extremely time consuming, therefore we choose to run the

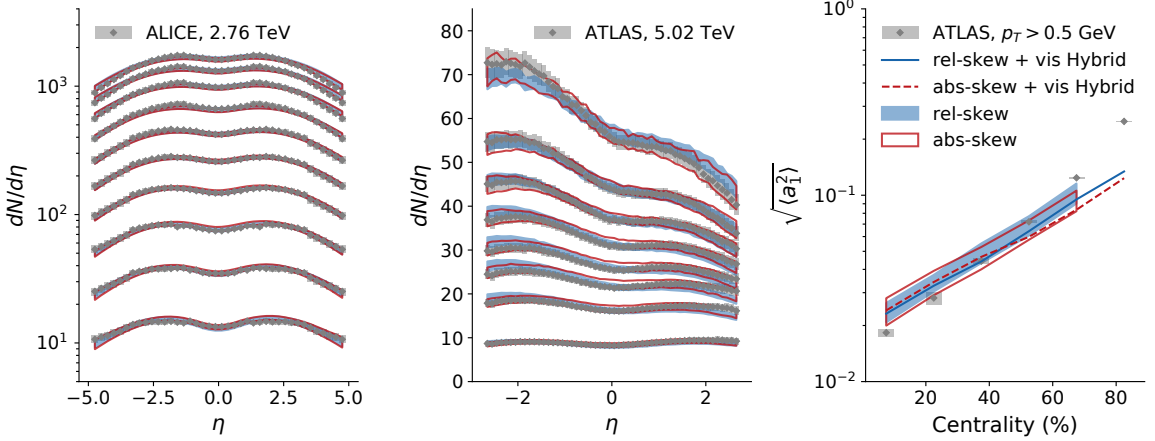


Figure 2.2: The posterior distribution of the observables after the fitting process. Blue and red stands for the results calibrated using the “relative skewness” and the “absolute skewness” ansatz respectively. From left to the right are charged particle pseudorapidity density in Pb-Pb collision, in p+Pb collision, and the rms of the a_1 coefficient in the two-particle pseudorapidity correlation decomposition. The lines in the right most figure shows that the rms a_1 is not very sensitive to the viscous effect in the hydrodynamic evolution.

hydrodynamic model in its ideal mode and on a rather coarse grid. The justification is that the rapidity distribution of the multiplicity and normalized two-particle correlations is less sensitive to the viscosity. In the end, as a validation of this procedure, we will be using a set of high-likelihood parameters and run the dynamical model with the viscous mode of the hydrodynamic model to see if other observables such as the anisotropic flows, and event-plane decorrelations can be described.

Four thousands Pb-Pb and ten thousands p-Pb events are generated at 100 sets of parameter values, then the Bayesian analysis makes inference on the probability distribution of the parameters by comparing to measurements. After the calibration, the $dN_{\text{ch}}/d\eta$ and a_1 fluctuations as function of centrality are compared to measurements in figure 2.2. The single particle distribution can be well reproduced by the calibrated initial condition plus dynamical evolution, while the correlation observables can be described up to 50% centrality. For more peripheral Pb-Pb collisions, the hydrodynamic model significantly underestimate the a_1 fluctuation. We understand this as a consequence of inadequate modeling of the short range correlation for peripheral collisions, as they are more important in low multiplicity events ($dN_{\text{ch}}/d\eta \sim 250$ and $N_{\text{part}} \sim 75$ at 50% centrality). In fact, the authors of [col15] compared the measurements to the HIJING event generator that is based on mini-jet production. It is found that these jet-like correlations agrees well with the a_1 fluctuation for peripheral collisions with $N_{\text{part}} \lesssim 80$, while it overshoots the data for more central collision. The hydrodynamic model and mini-jet production model provide a complementary picture to fully understand the rms a_1 : at larger centrality, mini-jet production dominates the fluctuation of the $dN_{\text{ch}}/d\eta$, while as multiplicity increases and the final state interactions are frequent, the event-by-event asymmetry in the single-particle

distribution dominates the rms a_1 .

Regarding the performance of different parametrizations of the skewness, the “relative” skewness ansatz does better in reproducing the uprising trend of rms a_1 , while the absolute skewness ansatz better describes the large $dN_{\text{ch}}/d\eta$ asymmetry in the top 1% p+Pb collisions. However, there is no strong evidence to favor any of them over the other. We will see later that this is because the two parametrizations, though take different forms, actually behave similar in terms of $ds/d\eta(\eta; T_A, T_B)$, for typical values of T_A and T_B of heavy nuclei.

The distribution of the calibrated parameters is shown in figure 2.3. The red and blue lines and color map correspond to results using the “absolute” and “relative” skewness respectively. The normalization parameters N_{PbPb} and N_{pPb} , mid-rapidity entropy deposition parameter p , nucleon thickness function fluctuation parameter k , the width of the rapidity distribution σ_0 and the effective Jacobian J have similar probability distributions between the two parametrizations. However, the distribution of the asymmetry related parameters μ_0 and γ_0 (anti-correlated), and nucleon width w are very different. This is because the Bayesian calibration looks for the high-likelihood region of the parameter space to explain the data, and the two different parametrizations can achieve this same goal by optimizing the parameter combinations differently. For the “relative” skewness one, the optimized parameters have a small shift of the mean μ and a large skewness γ ; for the “absolute” skewness one, they correspond to the region with a large μ but vanishing γ . This does not mean that there are “two models” explaining the same data, because both of them are an oversimplified parametrization of $ds/d\eta(\eta; T_A, T_B)$ with infinitely many degrees of freedom. Instead, we should treat them as an estimation of the systematic uncertainty in extracting the function form of the initial 3D entropy deposition $ds/d\eta(\eta; T_A(\mathbf{x}), T_B(\mathbf{x}))$. It is more instructive to see the probability distribution of $ds/d\eta$ it self, given different values of $T_A(\mathbf{x})$ and $T_B(\mathbf{x})$. In Fig. 2.4, we samples the calibrated parameter distributions and use them to draw the entropy density as function of rapidity at different values of T_A and T_B . Again, the red and blue colors represents “absolute” and “relative” skewness parametrizations; the lines shows the median prediction and the bands are one standard deviation uncertainties. In each row and each column, T_A and T_B varies from 0.2 fm^{-2} to 2.4 fm^{-2} . For references, the value of the thickness function at the center of a Gaussian proton with nucleon width 0.5 fm is about 0.6 fm^{-2} and is 0.2 fm^{-2} at 1.5 width away from its center; while the maximum nuclear thickness function of a Pb nucleus is about 2.2 fm^{-2} . Therefore, the chosen range of $T_{A,B}$ already cover the typical ranges and combinations for entropy production in a realistic heavy-ion collision. One observe that the functional form of the ds/dy between the two parametrization agrees within one standard deviation, with the deviations increasing as the asymmetry increases. Certainly, with sufficiently different T_A and T_B combinations, the two results will have totally different predictions; however, within the physical range of the thickness function, the two methods converges onto a similar behavior. We conclude that by applying the hydrodynamic-based model and a flexible 3D initial condition, the form of the local rapidity distribution as function of participant densities can be reverse engineered

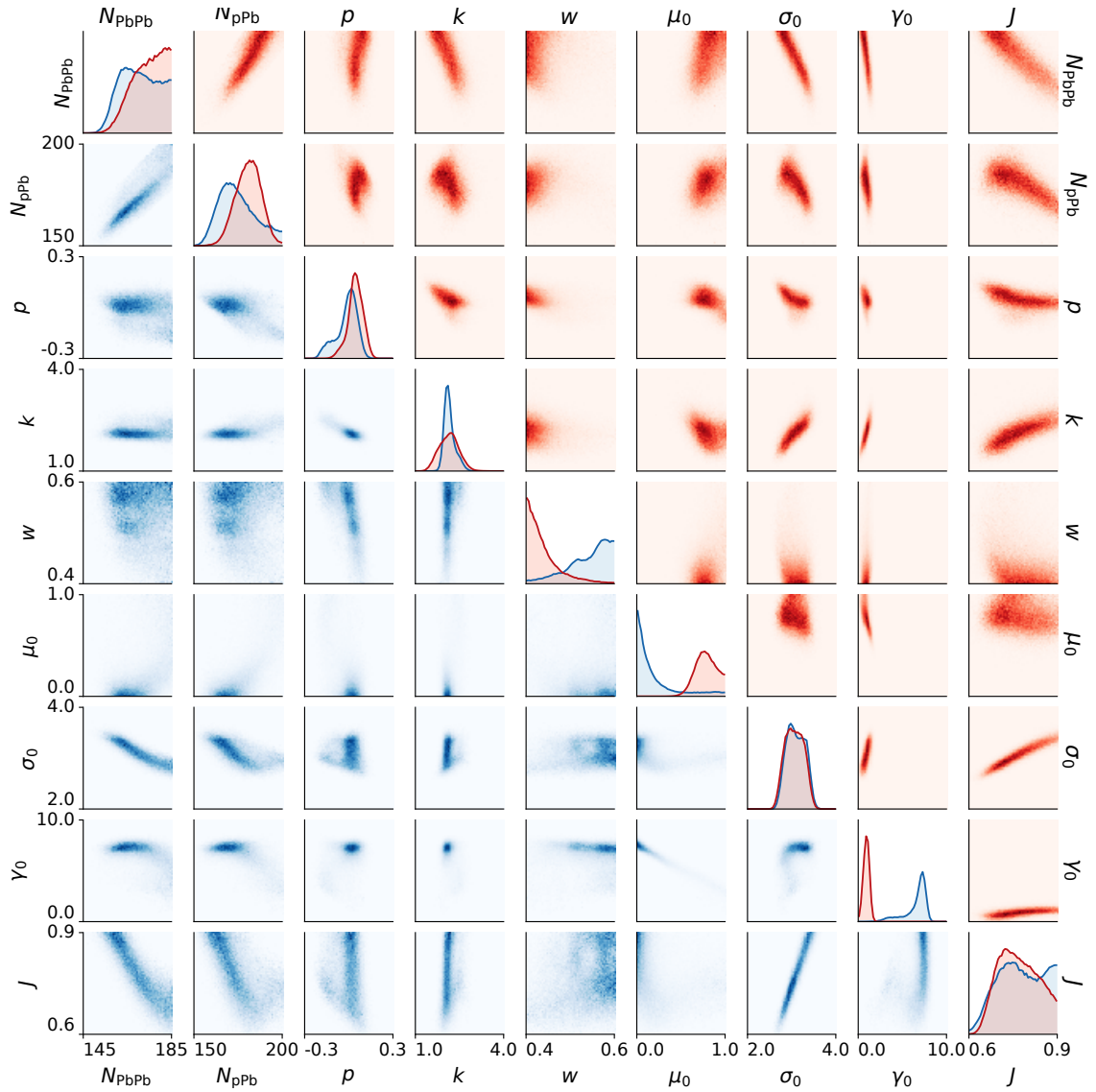


Figure 2.3: The posterior probability distribution of the model parameters, the colors distinguish the use of “absolute skewness” (red) and “relative skewness” ansatz. The diagonals are single parameter distribution, the off-diagonals are two-parameter joint distributions.

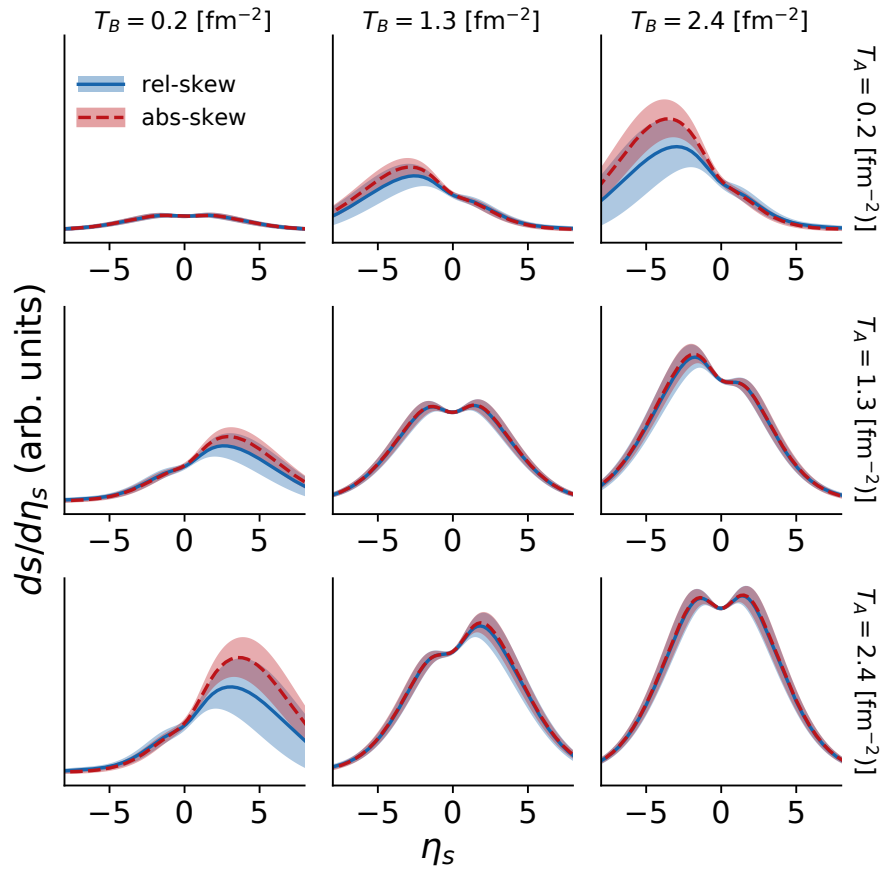


Figure 2.4: The constrained functional form of the three-dimensional initial entropy deposition $s(T_A(\mathbf{x}_\perp), T_B(\mathbf{x}_\perp), \eta_s)$. T_A and T_B is varied from 0.2 to 2.4 fm $^{-2}$. Colors distinguish the results from using “absolute skewness” (red) and “relative skewness” ansatz.

Table 2.4: A high likelihood parameter set

Parameter	rel-skew	abs-skew
$N_{\text{Pb-Pb}}$	150.0	154.0
p	0.0	0.0
k	2.0	2.0
w	0.59	0.42
μ_0	0.0	0.75
σ_0	2.9	2.9
γ_0	7.3	1.0
J	0.75	0.75

using single particle pseudo-rapidity distributions and two-particle pseudo-rapidity correlations.

2.3.3 Prediction with the calibrated 3D initial condition

The calibrated initial condition is useful in predicting other rapidity-dependent observables. Especially, because we have only used multiplicity based observables $dN_{\text{ch}}/d\eta$ and rms a_1 in the calibration, a prediction of azimuthal anisotropy related observables would provide an important validation of the initial condition. We choose a set of high-likelihood parameters shown in table 2.4. The selected validation / prediction observables are pseudo-rapidity dependent harmonic flows, event-plane decorrelations and the symmetric cumulants which quantify the correlation between different flow harmonics.

Mid-rapidity v_n The elliptic and triangular flow from two-particle correlation $v_2\{2\}$ and $v_3\{2\}$ are calculated at as function of centrality at mid-rapidity (figure 2.5) and as function of pesudo-rapidity at different centrality (figure 2.6). We are able to describe flow measured by ALICE [A⁺16b] at mid-rapidity with a shear viscosity $\eta/s = 0.17\text{--}0.19$ close to other phenomenological studies, though the bulk viscosity is not included in this study.

Rapidity-dependent v_n For the rapidity dependent flow figure 2.6, we used a larger $\eta/s = 0.25\text{--}0.28$. This inconsistency is because the ALICE measurement extrapolates the p_T range for the rapidity-dependent flow down to 0, while the mid-rapidity p_T cut is $0.2 < p_T < 5.0$ GeV. It would not be a problem for the model to describe both with the same transport parameters, if the p_T differential flow and p_T differential particle spectra are both reproduced. However, due to the lack of a systematic tuning of the model parameters including both shear and bulk viscosity, the current mean p_T is too high. Therefore, agreement with the p_T -integrated flow in one kinematic cut does not guarantee the agreement to measurements that extrapolate to $p_T = 0$. Since our primary interest is the η -dependence of the flow, we have chosen this larger-than-usual shear viscosity to match the $v_2\{2\}(\eta = 0)$ values to data. The

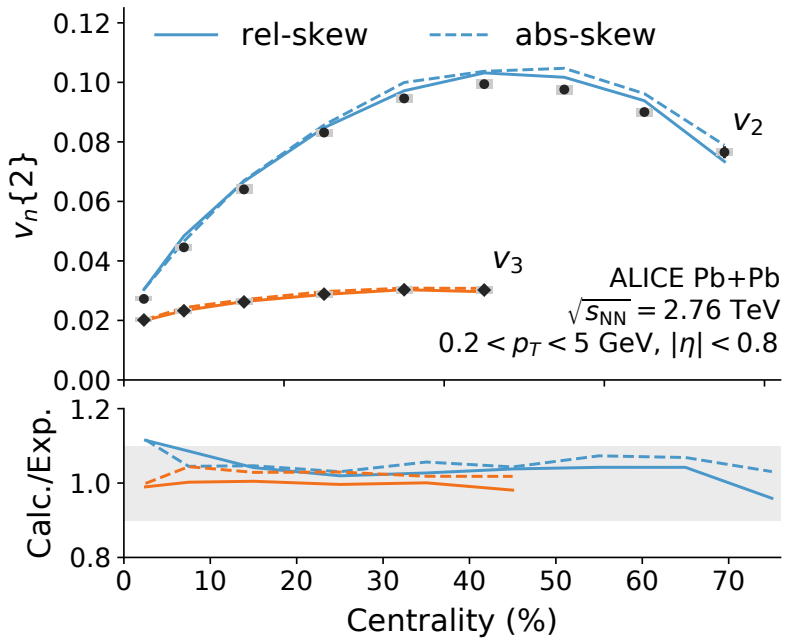


Figure 2.5: Flow coefficients $v_2\{2\}$ (blue) and $v_3\{2\}$ (orange) are plotted as a function of centrality. The calculation uses a 3+1D viscous hydrodynamic-based model with constant $\eta/s = 0.17$ and 0.19 for “relative skewness” (solid) and “absolute skewness” (dashed) ansatz. $\zeta/s = 0$ and the switching temperature is $T_{\text{sw}} = 154 \text{ MeV}$. The initial condition parameters are selected from the high-likelihood region of the posterior.

calculated $v_2\{2\}$, $v_3\{2\}$, and $v_2\{4\}$ gradually decrease from mid-rapidity to forward / backward rapidity, which is also the trend seen in the data. The shape of $v_3\{2\}$ is well described; but for $v_2\{2\}$ and $v_2\{4\}$ in the region $|\eta| > 2.0$, the data decreases faster than our predictions. There could be several reasons for this difference. It is possible that the current initial condition model produce enough fluctuations, but inadequate variance of the overlapping geometry as function of space-time rapidity. It is also showed in a study of at RHIC energies that the decreasing slope of $v_n(\eta)$ can be sensitive to the shear viscosity in the hadronic phase [DMRS15, BW10]. In our model, the transport properties of the system below T_c is all encoded in UrQMD and are not tunable. Moreover, we have assumed that hydrodynamization happens at a constant proper time hypersurface; while it is possible that a constant entropy density hypersurface is a better criteria, and as a result the matter at larger rapidity experiences a shorter period of pressure driven expansion. To systematically investigate all these effects, a future global parameter calibration including both initial condition parameters, transport parameters, and matching parameters is inevitable and is also feasible given the advances in the dynamical models and programming developments as well as more powerful computing resources.

Event-plane decorrelations The event-planes are defined as the phase angle of the anisotropic flow,

$$\Psi_n^{\text{EP}} = \frac{\text{atan}2(\langle \sin n\phi \rangle, \langle \cos n\phi \rangle)}{n}, \quad (2.37)$$

Due to longitudinal fluctuations, the event-planes separated by a rapidity gap decorrelate from each other. This decorrelation is important for observables that involve a large rapidity gap.

This event-plane decorrelation has been studied using initial conditions from a 3D extended Glauber model [BB16a] and A Multi-Phase Transport (AMPT) model [JH14, XLW13, PPQ⁺16]. Gluonic Yang-Mills dynamics in three-dimensions have also been used to study decorrelation at the initial stage level [SS16]. In our model, the geometry at forward and backward rapidity are dominated by the participant density of two different nuclei. And in between, the entropy production smoothly transit from one to another and so are the orientation of the energy density eccentricities that drive the flow of particles. The CMS collaborations quantifies the decorrelation by a three-bins factorization ratio [K⁺15c],

$$r_n(\eta^a, \eta^b) = \frac{V_{n\Delta}(-\eta^a, \eta^b)}{V_{n\Delta}(\eta^a, \eta^b)}, \quad (2.38)$$

$$V_{n\Delta}(\eta^a, \eta^b) = \langle\langle \cos(n\Delta\phi) \rangle\rangle, \quad (2.39)$$

where the double average runs over all particle pairs and all events. One of the rapidity bins is near η^b and the rest of the two bins are around $\pm\eta^a$. This ratio measures the decorrelation between two event planes separated by a larger rapidity gap $\eta^a + \eta^b$ relative to the decorrelation over a smaller gap $|\eta^a - \eta^b|$. In experiments, one would like to take the reference bin η^b farther from η_a to suppress the short

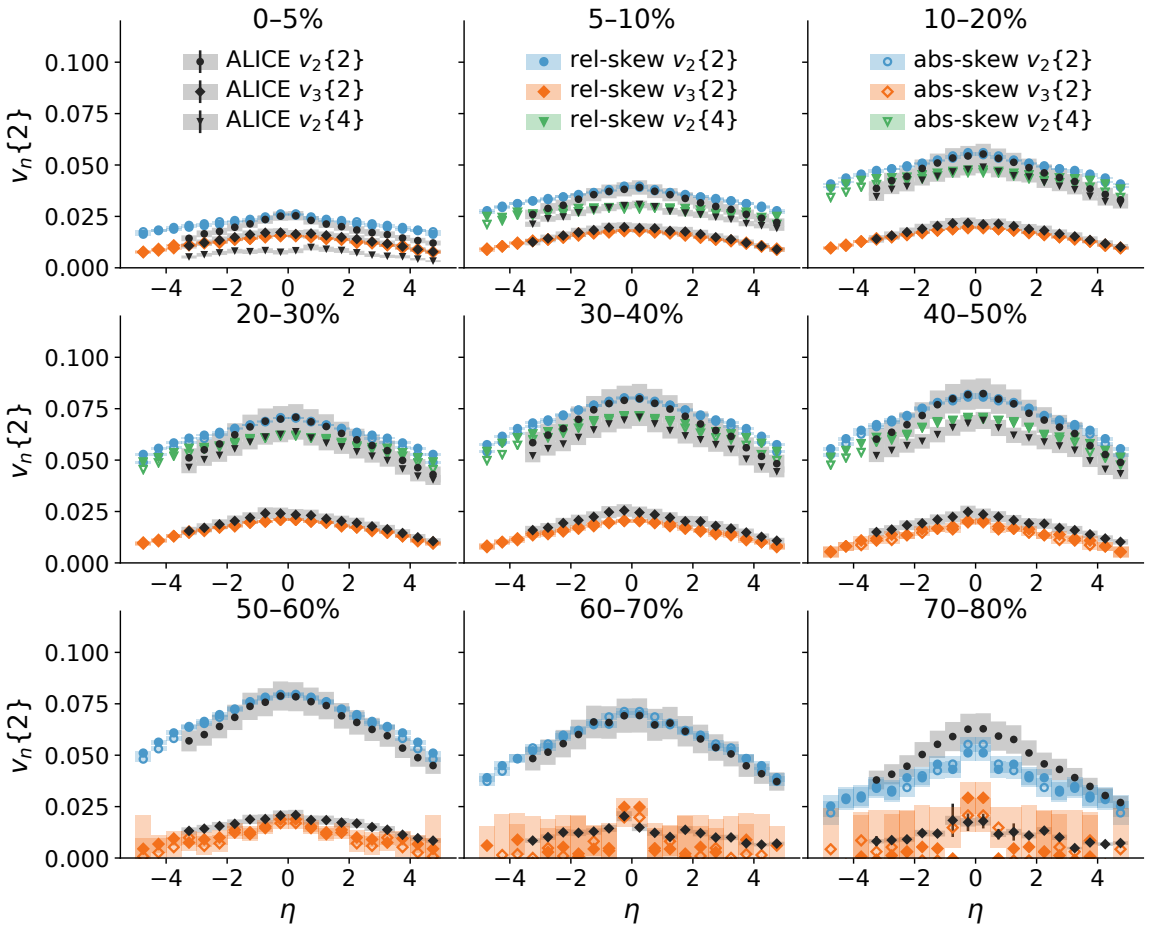


Figure 2.6: Pseudorapidity dependent flow coefficients $v_2\{2\}$ (blue circle), $v_3\{2\}$ (green triangle) and $v_2\{4\}$ (orange diamond). Constant $\eta/s = 0.25$ and 0.28 are used for “relative skewness” (closed symbol) and “absolute skewness” (open symbol) ansatz. Data is taken from the ALICE Collaboration [A⁺16g].

range correlations correlation. However, the way we build our model is to extend the mid-rapidity entropy deposition to finite rapidity, and this extension will eventually fail at sufficiently large rapidity because the model behavior in those region is not well constrained. In figure 2.7, we compare the model calculations to data with both a large $4.4 < \eta^b < 5.0$ (bottom) and a relative smaller $3.0 < \eta^b < 4.0$ (top). The predicted factorization ratios decreases linearly with the increasing rapidity gap. Using reference particles from $3.0 < \eta^b < 4.0$, the decorrelation is reproduced at larger centrality but not for central collisions. Because the $n = 2$ event-plane has a preferred direction defined by the impact parameter, while $n = 3$ event-plane does not, we observe that the $n = 2$ factorization ratio decorrelates slower than the $n = 3$ ratio, except for the most central collision when $n = 2$ event-plane is also dominated by fluctuations. Comparing to data with reference particles from $4.4 < \eta^b < 5.0$, the experimental data stays similar to the previous case except for central collisions, but the prediction is completely off. This is simply because the model fails on the details at large rapidity as we explained earlier. Given the present comparison, we conclude that the valid range of the model should be restricted to $|\eta| < 4.0$.

Symmetric cumulants Finally, we predict the symmetric cumulants (SC), which is a four particle correlation between different orders of anisotropic flows v_m and v_n [NDHH13, BCG⁺14].

$$\begin{aligned} SC(m, n) &= \langle\langle \cos(m\phi_1 + n\phi_2 - m\phi_3 - n\phi_4) \rangle\rangle \\ &- \langle\langle \cos[m(\phi_1 - \phi_2)] \rangle\rangle \langle\langle \cos[n(\phi_1 - \phi_2)] \rangle\rangle \\ &= \langle v_m^2 v_n^2 \rangle - \langle v_m^2 \rangle \langle v_n^2 \rangle. \end{aligned} \quad (2.40)$$

It is clear from the second equation that it measures the covariance between v_n^2 and v_m^2 . One can also define the normalized symmetric cumulants (NSC),

$$NSC(m, n) = \frac{SC(m, n)}{\langle v_m^2 \rangle \langle v_n^2 \rangle}. \quad (2.41)$$

These observables are interesting because they are robust against non-flow effects, and have been shown to be sensitive to the temperature dependence of the transport coefficients [A⁺16e]. Other analysis show that $SC(4, 2)$ probes the non-linear response of the hydrodynamic evolution, while $SC(3, 2)$ is more sensitive to initial conditions [ZZXS17].

The relative- and absolute-skewness calculations are arranged on the left and right of 2.8. Symmetric cumulants $SC(4, 2)$ (blue) and $SC(3, 2)$ (green) are displayed in the top plots, and $NSC(4, 2)$ (blue) and $NSC(3, 2)$ (green) in the bottom plots. Within each plot, black dots are ALICE measurements at midrapidity $|\eta| < 0.8$ [A⁺16e], which should be compared to the calculation shown in solid lines. The calculation shown in dashed lines are our predictions at forward/backward rapidity $2.5 < |\eta| < 3.5$,

$$\begin{aligned} SC'(m, n) &= \langle\langle \cos(m\phi_1 + n\phi_2 - m\phi'_3 - n\phi'_4) \rangle\rangle \\ &- \langle\langle \cos[m(\phi_1 - \phi'_2)] \rangle\rangle \langle\langle \cos[n(\phi_1 - \phi'_2)] \rangle\rangle, \end{aligned} \quad (2.42)$$

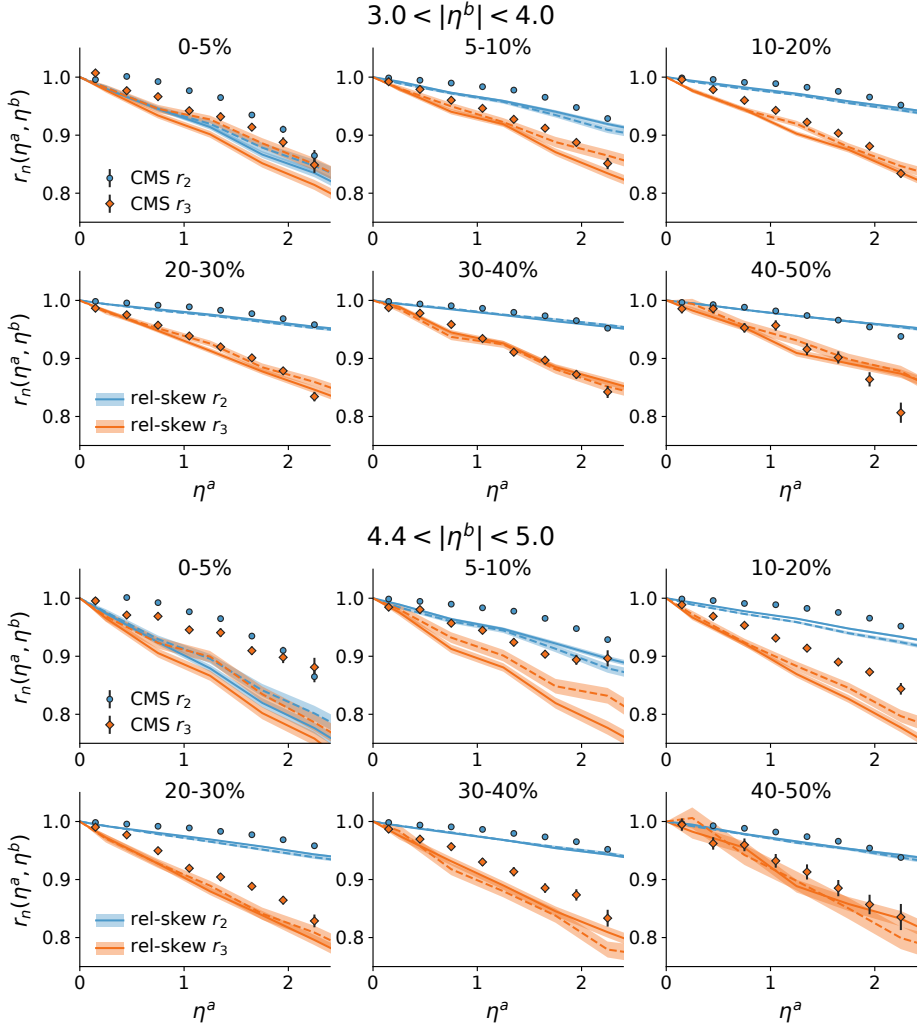


Figure 2.7: The $n = 2$ (blue) and $n = 3$ (orange) event-plane decorrelations obtained for “relative skewness” (lines with bands) and “absolute skewness” (lines with hatches) ansatz. The top and bottom plots uses different reference particle bins $3.0 < |\eta_b| < 4.0$ and $4.4 < |\eta_b| < 5.0$ respectively.

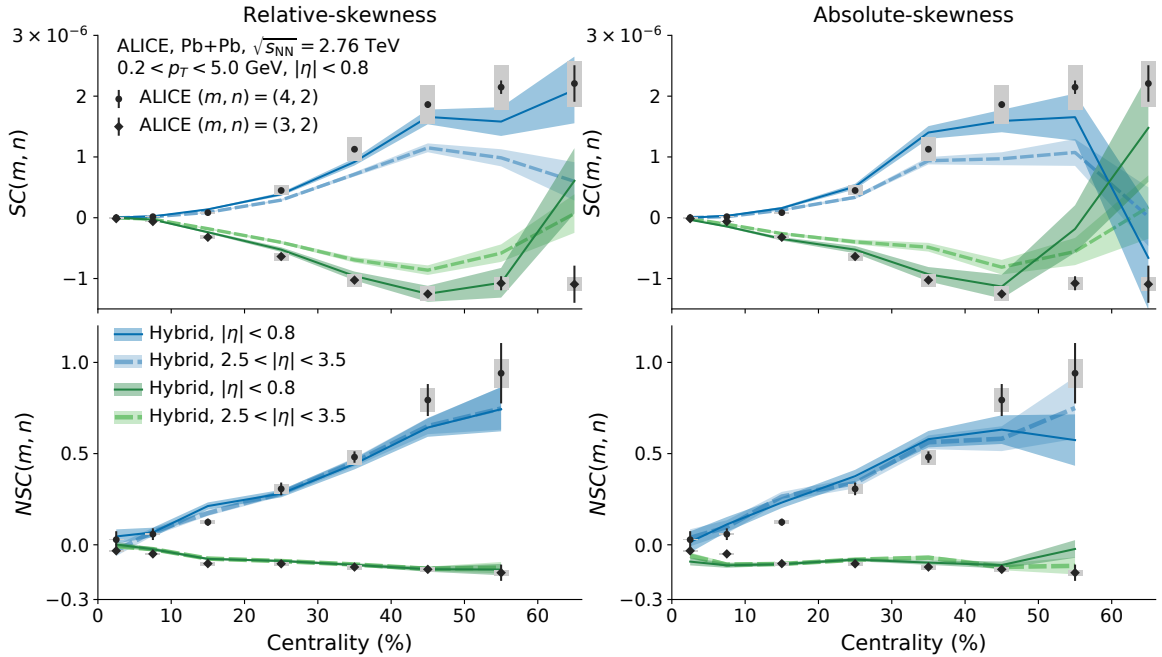


Figure 2.8: The symmetric cumulants (top row) and normalized symmetric cumulants (bottom row) obtained from the “relative skewness” (left column) and the “absolute skewness” (right column) ansatz. $SC(4, 2)$ (blue) and $SC(3, 2)$ (green) are shown as functions of centrality. The experimental measurements at mid-rapidity (black symbols) are taken from [A⁺16e]. The calculations are performed at both mid-rapidity $|\eta| < 0.8$ (solid lines) and forward/backward rapidity $2.5 < |\eta| < 3.5$ (dashed lines).

where the two of the particles (primed) are selected from the forward/backward rapidity bins, while the rest of the two still come from the mid-rapidity bin $|\eta| < 0.8$.

At mid-rapidity, the calculated (normalized) symmetric cumulants reproduce the trend of the measurements, and the “relative” skewed initial condition does a better quantitative job than the “absolute” skewed model. At forward and backward rapidity, though the magnitudes of both $SC(m, n)$ and v_n, v_m changed, the normalized symmetric cumulants remains the same as the one at mid-rapidity. This is a prediction that can be checked in future measurements to put further constraints on the three-dimensional initial condition model.

As a summary of this chapter, I have introduced the hydrodynamic-based medium evolution model that is very successful in describing the bulk observables. The sensitivity of the harmonic flows allows one to extract QCD transport coefficients using advanced statistical techniques. The initial condition for the dynamical model is still a large source of uncertainty in both data interpretation and parameter extraction. The TRENTo model was developed as a flexible ansatz for mid-rapidity entropy / energy deposition so that the initial condition and transport coefficients can be calibrated simultaneously to data. Finally, I discussed my work on extending the TRENTo initial condition to include rapidity dependence and the use of multiplicity observable

to reverse-engineer the functional form of initial 3D entropy deposition. The results can be used to predict more rapidity-dependent observables, and are useful to other studies involving a large rapidity range. Due to the simplicity of the modeling, and the lack of global fit of all parameters including both 3D initial conditions and transport coefficients, we cannot yet answer how the inclusion of longitudinal fluctuation quantitatively affects the extracted QCD transport coefficients, but it is an important question for a future precision analysis.

Chapter 3

A transport model for hard partons in the QGP

Hard partons are predominately created in perturbative scatterings at the earliest stage of relativistic heavy-ion collisions. The distribution of the hard partons gets modified by the medium and the final distribution carries information about the medium, as well as the hard-soft interaction properties.

Among the many ways of describing the in-medium evolution of hard partons, the transport approach has a unique advantage. Here, we refer to transport approach as a class of models that evolve the semi-classical particle distribution function of hard partons in real time. Transport models can be often formulated as simulations on the particle level, which provide easy coupling to local properties of a dynamically evolving and fluctuating medium, and an exclusive final state. Of course challenges exist when applying transport models to high energy collisions. First, there are different assumptions of the interactions between the hard partons and the medium to be made. Two commonly assumed extremes are:

- 1 A weakly coupled picture: the medium consists of perturbative quasi-particles (scattering centers) whose distribution is close to local thermal equilibrium. Hard partons scatter perturbatively with these well separated scattering centers. The dynamics is described by a Boltzmann equation.
- 2 Diffusion picture: interactions between the medium and the hard parton are frequent and soft, many-body effects and non-perturbative effects can be important. The effect of these interactions are modeled by a drag and a diffusion coefficient. The dynamics is solved using a Langevin equation.

These two commonly used approaches are not necessarily mutually exclusive, and can have overlapping range of validity. For example, the effect of soft momentum exchange processes in the perturbative calculation can be very well modeled by a diffusion equation [GMT16, DBPT19]. These different assumptions on the interaction between the medium and the hard probe are largely due to our inadequate theoretical tools in describing the QGP medium in the strongly coupled regime. On the one hand, this becomes the an uncertainty intrinsic to the transport approach, until one finds convincing way of calculating the dynamics of the strongly coupled QGP medium from first principles. On the other hand, experiments may be able to tell which assumption (or a combination of both) is preferred and answer the very question of how the sQGP participates in the jet-medium interactions.

A second difficulty is that semi-classical transport equations can be cumbersome in treating quantum coherence. Indeed, a quantum transition will always be bounded

by the uncertainty principle: a process with momentum scale Q can not be localized within a space-time extent of $1/Q$. While in the semi-classical transport model, one always specifies a local point in space-time where the interaction takes place. This is valid if the momentum scale Q is high enough that $1/Q$ is much smaller than the resolution of the transport model, e.g., characterized by the mean-free-path in the Boltzmann equation. However, the soft and collinear divergences of QCD bremsstrahlung (or more generally, parton branching and jointing) processes generate an abundance of small- Q events whose spatial extent can be much greater than the mean-free-path. This happens for certain phase space regions of both the vacuum parton shower and the medium-induced parton shower. For medium-induced branching, this is the QCD analog of the Landau-Pomeranchuk-Migdal (LPM) effect [Mig56, WGP95, Zak96], and the radiation pattern is changed qualitatively. When this happens, strictly speaking, the semi-classical transport equation is not the appropriate tool. However, considering the advantages of the transport formulation, we will develop a minimum set of modification to the semi-classical transport that can mimic some quantum effects of medium-induced branchings.

We start with an introduction of widely used transport equations: the (linearized) Boltzmann equation and the Langevin equation. Then, we combine these two approach into a hybrid one by introducing a cut-off distinguishing hard and soft momentum transfer processes and build the transport model in the incoherent limit. After that, we provide a brief review the theory of QCD in-medium parton branching processes at leading order, discussing its various approximations and also the numerical solutions in a simplified medium. With these theoretical insights, the main outcome of this chapter is developing a “modified Boltzmann” transport approach, treating the medium-induced parton branching with an approximate LPM effect. Finally, the simulations of the transport model are compared to theoretical expectations to validate the implementation in different regimes. We will show that the modified transport approach can reasonably describe the energy spectrum of the medium-induced splitting vertex for different channels $q \rightarrow q + g$, $g \rightarrow g + g$ and $g \rightarrow q + \bar{q}$. Treatment of the heavy quark masses effect, and running coupling are also investigated. For future references, in the very end, we make comparisons between two other Monte-Carlo approaches for medium-induced radiation with the present one and comment on potential problems.

3.1 The Boltzmann equation

The Boltzmann equation evolves the particles’ distribution function under the effect of localized collisions. By localization, it means that the time scale of the collision has to be much smaller than the mean free-path $\tau \ll \lambda$. Therefore, the collision probability can be evaluated using a local particle distribution function. It also allows one to include only few body collision processes, because the probability of interacting with an additional particle during this collision is small $P \approx \tau/\lambda \ll 1$. At weak coupling, we will see in the next section that this is indeed the case for elastic collisions or soft and large angle radiation. But for radiation with a large formation time, the

process becomes “non-local”. Accordingly, the Boltzmann formulation needs to be modified quite fundamentally for such processes. In this section, we only focus on local interactions.

With two-body to two-body (elastic) and two-body to three-body (inelastic, including the reverse process) processes, the Boltzmann equation for particle specie a takes the following form,

$$\frac{\partial f^a}{\partial t} + \vec{v} \cdot \frac{\partial f^a}{\partial \vec{x}} + \frac{\partial E}{\partial \vec{x}} \cdot \frac{\partial f^a}{\partial \vec{p}} = - \sum_{b,c,d} \mathcal{C}_a^{a+b \leftrightarrow c+d} - \sum_{b,c,d,e} \mathcal{C}_a^{a+b \leftrightarrow c+d+e} \quad (3.1)$$

On the left hand side, the distribution function $f^a(t, \vec{x}, p)$ undergoes transport with velocity $\vec{v} = \partial E / \partial \vec{p}$, and a potential force $\vec{f} = -\partial E / \partial \vec{x}$. On the right hand side of the equation, the $2 \leftrightarrow 2$ and $2 \leftrightarrow 3$ collision terms are functionals of the distribution functions. The summation of b, c, d, e iterates over all other particle species including a . Using the elastic process as an example and neglecting degeneracy of the internal quantum number for simplicity, the collision term can be separated into gain and loss terms,

$$\mathcal{C} = \mathcal{C}_{\text{loss}} + \mathcal{C}_{\text{gain}} \quad (3.2)$$

$$= \int_{bcd} f^a(p_1) f^b(p_2) [1 + \epsilon^c f^c(p_3)] [1 + \epsilon^d f^d(p_4)] \overline{|M|^2}(p_1, p_2; p_3, p_4) \quad (3.3)$$

$$- \int_{bcd} f^c(p_3) f^d(p_4) [1 + \epsilon^a f^a(p_1)] [1 + \epsilon^b f^b(p_2)] \overline{|M|^2}(p_3, p_4; p_1, p_2)$$

$$= \int_{bcd} \left\{ f^a(p_1) f^b(p_2) [1 + \epsilon^c f^c(p_3)] [1 + \epsilon^d f^d(p_4)] \right. \\ \left. - f^c(p_3) f^d(p_4) [1 + \epsilon^a f^a(p_1)] [1 + \epsilon^b f^b(p_2)] \right\} \overline{|M|^2} \quad (3.4)$$

Where the crossing symmetry of the matrix-elements has been used in the last line of the equation ($\overline{|M|^2}(p_1^a, p_2^b; p_3^c, p_4^d) = \overline{|M|^2}(p_3^c, p_4^d; p_1^a, p_2^b) = \overline{|M|^2}$), and the phase-space integral is

$$\int_{bcd} = \prod_{i \in b,c,d} \int \frac{dp_i^3}{2E_i(2\pi)^3} (2\pi)^4 \delta^4(p_a + p_b - p_c - p_d). \quad (3.5)$$

The $\epsilon = 0, -1, 1$ corresponds to classical, Fermi-Dirac, and Bose-Einstein statistics depending on the nature of the particle. The first term in the integration represents the loss of a particle of type “ a ” in the phase-space around point (x, p_1) due to elastic collision, and the second term represents the gain of a particle of type “ a ” due to the reverse process. The symmetry in the microscopic matrix-element is very important for the kinetic equation to satisfy detailed balance: the probability to transition from one microscopic state to another equals that of the reverse process. The detailed balance ensures the thermal equilibrium limit of the system. Assume the system evolves long enough in a box of finite volume and there is no spatial variance of the distribution function. Then the left side of equation 3.4 is zero, and the static solution has to satisfy the relation,

$$f^a f^b (1 + \epsilon f^c) (1 + \epsilon f^d) = f^c f^d (1 + \epsilon f^a) (1 + \epsilon f^b), \quad (3.6)$$

for the entire phase-space and every combination of particle species. Therefore, the following combination is conserved for each reaction channel.

$$\frac{f^a}{(1 + \epsilon^a f^a)} \frac{f^b}{(1 + \epsilon^b f^b)} = \frac{f^c}{(1 + \epsilon^c f^c)} \frac{f^d}{(1 + \epsilon^d f^d)} \quad (3.7)$$

The available conservation quantities are the four momentum; therefore, one solution to the previous equation is,

$$\frac{f^a}{(1 + \epsilon^a f^a)} = e^{-\beta\mu_a - \beta p \cdot u} \quad (3.8)$$

for every particle species with parameters μ, β and a four vector u ($u^2 = 1$). So the static solution of the distribution is

$$f^a(p) = \frac{1}{e^{\beta\mu_a + \beta p \cdot u} - \epsilon^a} \quad (3.9)$$

$$\mu_a + \mu_b = \mu_c + \mu_d \quad (3.10)$$

The first line is the thermal distribution (kinetic equilibrium), and the second line is the requirement for reaching chemical equilibrium. One can identify the β and μ parameter as the inverse temperature and chemical potential. The u vector is the flow velocity of the cell as can be seen from the average velocity,

$$\left\langle \frac{p^\mu}{M} \right\rangle = \frac{\int f(p) \frac{p^\mu}{M} dp^3}{\int f(p) dp^3} = \frac{\int f(p) \frac{p^\mu}{M} dp^3}{\int f(p) dp^3} = u^\mu \quad (3.11)$$

3.1.1 The linearized Boltzmann equation and the diffusion limit

Analytic solutions of the Boltzmann equations are almost impossible, even numerical solutions and simulations are highly non-trivial tasks. However, under certain circumstances, a linearization of the Boltzmann equation is possible and greatly simplifies both the analytic analysis as well as the numerical implementation.

Hard particles (jet partons, heavy flavors) either have a large momentum $p \gg T$ or a large mass $M \gg T$. In heavy-ion collisions, the hard cross-section drops fast with the increase of p_T and m_T , so hard partons are very rare in an actual event. Therefore the occupation number of hard partons is small $f_H \ll 1$. One can neglect the quantum statistics terms in the Boltzmann equation for them $1 + \epsilon f_H \approx 1$. Also, the collision terms with more than one uncorrelated hard particle in the initial state can also be neglected since these contributions are proportional to $f_H^2 \ll f_H$. Finally, we also assume that the response of the bulk of the particles to the hard particles is small, and shall neglect any collision terms that involve a hard parton in the Boltzmann equation for the bulk distribution function (recently studies show that such back reactions are important for the study of full jet observables [HCC⁺19], but

we only consider leading particles in this thesis). Under these approximations, one arrived at a set of equations that are linearized with respect to the hard parton:

$$\frac{df_H}{dt} = -\mathcal{C}_H[f_H, f_{\text{bulk}}], \quad (3.12)$$

$$\frac{df_{\text{bulk}}}{dt} = -\mathcal{C}[f_{\text{bulk}}]. \quad (3.13)$$

Here the collision term \mathcal{C}_H is linear with respect to f_H .

For the medium particles, the equations are still complex. But by observing that the time it takes for the low momentum bulk particles to reach local thermalization is much shorter than the relaxation time of the hard particles, a zeroth order approximation would be to use the local thermal distribution 3.9. The space-time evolution of the temperature T , chemical potential μ and flow velocity u can be obtained from a hydrodynamic simulation. Replacing the medium distribution function by the thermal one in 3.12, one arrives at a closed and linearized equation for the hard particles. Here we write down the equation assuming both classical statistics and the conservation of the hard parton's species, and only the elastic collision term is shown for simplicity,

$$\frac{df^H}{dt} = -\sum_b \int_{234} \left\{ f^H(p_1) f_{eq}^b(p_2) - f^H(p_3) f_{eq}^b(p_4) \right\} \overline{|M|^2} \quad (3.14)$$

$$= -\int \left\{ f^H(p_1) w(p_1; p_3) - f^H(p_3) w(p_3, p_1) \right\} \frac{dp_3^3}{2E_3(2\pi)^3}. \quad (3.15)$$

The $w(p; p')$ is the transition probability density for a particle with momentum p into momentum state p' ,

$$w(p; p') = \sum_b \int_{24} f_{eq}^b(p_2) \overline{|M|^2}(p, p_2; p', p_4) \quad (3.16)$$

Using local thermal solutions for the bulk particles is a strong assumption. The degree of local thermalization in realistic events is still an open question, especially at the early stage of the heavy-ion collision. Moreover, whether the system can be understood in terms of quasi-particle degrees of freedom is a different question. In an extreme weakly coupled system $g \ll 1$, one expects that the local pressure and energy density can be explained using fundamental degrees of freedom: quarks and gluons, with perturbative corrections [BIR01, SALS11, Su15]. But with a large g estimated from phenomenological studies, such a perturbative description may not be the most efficient way of understanding the bulk medium, and non-perturbative physics can play an essential role.

Interpreting the medium in terms of microscopic degrees-of-freedom seem to be a unavoidable step of the Boltzmann equations, however, it is possible to “integrate out” the microscopic details in the soft limit of interaction into a set of transport coefficients.

The Fokker Planck equation In the soft momentum transfer $q = p' - p$ limit $|q| \ll |p|$, the change in distribution function can be expanded to the second terms in q , and the linearized Boltzmann equation reduces to the Fokker-Planck type of equation,

$$\frac{df}{dt} = - \int \left\{ f(p) - \left[f(p) + \vec{q} \frac{\partial f}{\partial \vec{p}} + \frac{1}{2} \vec{q} \vec{q} \frac{\partial^2 f}{\partial \vec{p} \partial \vec{p}} \right] \right\} w(p', p) \frac{dp_3^3}{2E_3(2\pi)^3} \quad (3.17)$$

$$= - \int \left\{ \vec{q} \frac{\partial f}{\partial \vec{p}} - \frac{1}{2} \vec{q} \vec{q} \frac{\partial^2 f}{\partial \vec{p} \partial \vec{p}} \right\} w(p', p) \frac{dp_3^3}{2E_3(2\pi)^3} \quad (3.18)$$

$$= -\eta_D(p) \frac{\partial f}{\partial \vec{p}} + \frac{1}{2} B(p) \frac{\partial^2 f}{\partial \vec{p} \partial \vec{p}} \quad (3.19)$$

Where the vector function A and tensor function B are the first and second moments of the transition rate,

$$A_i(p) = \int w(p, p+q) q_i \frac{dp_3^3}{2E_3(2\pi)^3}, \quad (3.20)$$

$$B_{ij}(p) = \int w(p, p+q) q_i q_j \frac{dp_3^3}{2E_3(2\pi)^3}. \quad (3.21)$$

One remark is that although the form of the Fokker-Planck equation can be derived as the soft limit of the linearized Boltzmann equation, its range of applicability is different from the latter. This is because the transport coefficient is well defined in general regardless of whether one assumes quasi-particle type microscopic dynamics. Therefore in our model, we replace the soft sector of the Boltzmann equation with the Fokker-Planck equation so that the use of "medium quasi-particles" are restricted to hard momentum transfer processes.

Moments beyond second order are dropped in deriving the Fokker-Planck equation. This is justified if the interaction is frequent enough so that within the smallest time scale that is concerned, a statistical description of the effect of many interactions in terms of the first (mean) and the second moments (variance) is adequate. However, if the physical processes are rare, fluctuations contained in higher moments are very important and a diffusion equation is not a good approximation.

Transport coefficients and the Einstein relation The A and B functions have to satisfy a certain symmetry, as the only special direction after averaging over medium effects is the direction of motion. Therefore, $\vec{A} = \eta_D \vec{p}$ defines the drag coefficient η_D ; the tensor B can be decomposed into a transverse part and a longitudinal part, with the respective momentum diffusion coefficients κ and κ_L

$$B_{ij} = \kappa_L \frac{p_i p_j}{p^2} + \kappa \left(\delta_{ij} - \frac{p_i p_j}{p^2} \right) \quad (3.22)$$

One notices that the medium temperature does not show up explicitly in the equation,

$$\frac{df}{dt} = \frac{\partial}{\partial p_i} \left(\eta_D p_i + \frac{1}{2} \frac{\partial}{\partial p_j} B_{ij} \right) f \quad (3.23)$$

To guarantee the system has a thermalized solution, A , κ_{\parallel} and κ_{\perp} are not independent. Given a static and homogeneous medium at equilibrium with temperature T , $f = N \exp(-\beta E)$, the equation reduces to

$$0 = \frac{\partial}{\partial p_i} (\phi p_i f) \quad (3.24)$$

$$\phi = \eta_D - \frac{\kappa_{\parallel}}{2TE} + \frac{\partial \kappa_{\parallel}}{\partial p^2} + \frac{\kappa_{\parallel} - \kappa_{\perp}}{p^2}. \quad (3.25)$$

The Einstein relation $\phi = 0$ guarantees the existence of an equilibrium solution,

$$\eta_D = \frac{\kappa_{\parallel}}{2TE} - \frac{\partial \kappa_{\parallel}}{\partial p^2} - \frac{\kappa_{\parallel} - \kappa_{\perp}}{p^2} \quad (3.26)$$

This is where the temperature shows up explicitly in the Fokker-Planck equation.

3.2 Hard parton transport in the incoherent limit

In this section, we proceed to use a local and incoherent calculation of hard parton scatterings and will defer a detailed discussion on the inclusion of the LPM effect to the next section. The partonic processes are categorized into elastic (particle number conserving) and inelastic processes (particle number non-conserving). The inelastic processes are further divided into parton-splitting and parton-fusing contributions.

3.2.1 Hard/soft separation: elastic collisions

In a quasi-particle picture of the QGP, the hard parton collides with medium partons and transfers a certain amount of four momentum. These processes can be computed at leading order in the weakly coupled theory, where the collision cross-section is calculated using the dressed gluon propagator inside the medium [BT91],

$$D^{\mu\nu}(\omega, k) = \frac{\delta^{\mu 0}\delta^{\nu 0}}{k^2 - \Pi_L(\omega, k)} + \frac{\hat{P}_T^{\mu\nu}}{\omega^2 - k^2 - \Pi_T(\omega, k)} \quad (3.27)$$

where Π_T and Π_L are the self energies for the transverse and longitudinal modes. Due to the presence of the medium, the dressed propagator loses its Lorentz invariance and depends on the complicated functions Π_T and Π_L . The resulting cross-section formula will be equally complicated. Fortunately, it has been shown recently in [GMT16] that a simplification is possible at leading order in rewriting the elastic processes as large-angle scattering and small-angle diffusion. In such an approach, one chooses a scale Q_{cut} with a formal range of $gT \ll Q_{\text{cut}} \ll T$. For processes with momentum transfer to the medium larger than the cut-off (hard modes) the medium screening effect is neglected and vacuum matrix-elements are used. While for processes smaller than the cut-off (soft-mode), the propagator receives significant contributions from the screen effect. The soft processes happen frequently and only involve small momentum

transfers, satisfying the requirements of diffusion approximation. This separation allows the following modeling of the elastic interaction between hard partons and the medium,

$$\frac{df}{dt} = \mathcal{D}(Q_{\text{cut}})[f] + \mathcal{C}^{2\leftrightarrow 2}(Q_{\text{cut}})[f]. \quad (3.28)$$

Here, particles are continuously evolved by the diffusion process with their momentum occasionally changing by large- Q scatterings. Later we will verify that the cut-off dependence in the diffusion and scattering component indeed cancels for “physical observations” at sufficiently small coupling. The phenomenological value of g is actually very large, so the residue cut-off dependence may be significant. The advantage of the current formulation is that certain non-perturbative effects can also be modeled by a diffusion processes with an additional contribution to the transport coefficient.

Transport coefficients for soft modes The transverse and longitudinal transport parameters below the cut-off have been calculated in [GMT16],

$$\hat{q}_S = \int dq^2 \frac{\alpha_s m_D^2 T}{q^2(q^2 + m_D^2)} = g^2 C_R T m_D^2 \ln \left(1 + \frac{Q_{\text{cut}}^2}{m_D^2} \right). \quad (3.29)$$

$$\hat{q}_{S,L} = \int dq^2 \frac{\alpha_s m_\infty^2 T}{q^2(q^2 + m_\infty^2)} = g^2 C_R T m_\infty^2 \ln \left(1 + \frac{Q_{\text{cut}}^2}{m_\infty^2} \right) \quad (3.30)$$

$m_\infty^2 = m_D^2/2$ is the thermal mass of the gluon. The drag force is determined by the Einstein relation in equation 3.26,

$$\eta_D = \frac{\hat{q}_{S,L}}{2ET} - \frac{d\hat{q}_{S,L}}{dp^2} - \frac{2\hat{q}_{S,L} - 2\hat{q}_S}{2p^2} \quad (3.31)$$

Scattering rate for hard modes For the large- Q $2 \rightarrow 2$ scattering processes, the collision rates are computed by integrating the vacuum matrix-element,

$$R = \frac{d}{2E_1} \int \frac{d^3 p_2}{2E_2(2\pi)^3} f_0(p_2) 2\hat{s} \int_{-\hat{s}}^{Q_{\text{cut}}^2} \frac{d\sigma}{d\hat{t}} d\hat{t} \quad (3.32)$$

The integration is restricted to large momentum transfers above Q_{cut} and therefore we do not impose additional screening effects to regulate the matrix-element. In this work, the $2 \rightarrow 2$ matrix-element only includes the \hat{t} -channel contribution.

3.2.2 Hard/soft separation: inelastic collisions

Similarly, incoherent inelastic processes are divided into small- Q diffusion induced radiation / absorption ($1 \leftrightarrow 2$), and large- Q $2 \leftrightarrow 3$ processes.

Diffusion induced branching For the incoherent diffusion-induced splitting rate, we borrow the expression from [CLQW18] while stripping the time-dependent phase factor,

$$R_{1 \rightarrow 2} = \int dk_\perp^2 dx \frac{\alpha_s P(x) \hat{q}_S(Q_{\text{cut}})}{2\pi(k_\perp^2 + m_\infty^2)^2} \quad (3.33)$$

where a gluon thermal mass is added to screen the divergence. Because these processes are induced by processes with medium momentum transfer below the cut-off, Q_{cut} appears in the formula. For the reverse $2 \rightarrow 1$ processes, a similar reaction rate can be written down,

$$R_{2 \rightarrow 1} = \int e^{-\beta\omega} dk_\perp^2 dx \frac{\alpha_s P(x) \hat{q}_S(Q_{\text{cut}})}{2\pi(k_\perp^2 + m_\infty^2)^2}. \quad (3.34)$$

ω is the thermal parton's energy, and x is defined as the fraction of the thermal parton's energy to that of the final state hard parton. These expressions have to be used in the rest frame of the medium.

Large- Q $2 \leftrightarrow 3$ process Regarding the $2 \rightarrow 3$ matrix-element, in a previous study [KXB18], we used to employ an improved version of the original Gunion-Bertsch cross-section that works under the limits $k_\perp, q_\perp \ll \sqrt{s}$ and $xq_\perp \ll k_\perp$ [GB82, FUXG13, UFXG15]. In the present study, we keep improving the matrix-elements by following the derivation in [FUXG13] while relaxing the condition $xq_\perp \ll k_\perp$. Therefore the updated matrix-elements contain the correct vacuum splitting function in the collinear limit. We summarize the matrix-elements here and have attached a derivation in appendix A,

$$\overline{|M^2|}_{g+i \rightarrow g+g+i} = \overline{|M^2|}_{g+i \rightarrow g+i} P_{gg}^{g(0)} D_{gg}^g, \quad (3.35)$$

$$\overline{|M^2|}_{g+i \rightarrow q+\bar{q}+i} = \frac{C_F d_F}{C_A d_A} \overline{|M^2|}_{g+i \rightarrow g+i} P_{q\bar{q}}^{g(0)} D_{q\bar{q}}^g, \quad (3.36)$$

$$\overline{|M^2|}_{q+i \rightarrow q+g+i} = \overline{|M^2|}_{q+i \rightarrow q+i} P_{qg}^{g(0)} D_{qg}^q. \quad (3.37)$$

Index i represents a quark / anti-quark or a gluon. The two body matrix-elements that enter the $2 \rightarrow 3$ matrix-element are always required to be the t -channel contribution. $P_{bc}^{a(0)}(x)$ are vacuum splitting functions from parton a to partons b and c ,

$$P_{gg}^{g(0)} = g^2 C_A \frac{1 + x^4 + (1 - x)^4}{x(1 - x)}, \quad (3.38)$$

$$P_{qg}^{g(0)} = g^2 C_F \frac{1 + (1 - x)^4}{x}, \quad (3.39)$$

$$P_{q\bar{q}}^{g(0)} = g^2 \frac{N_f}{2} (x^2 + (1 - x)^4). \quad (3.40)$$

The D_{bc}^a contains the interference structure,

$$\begin{aligned} D_{qq}^g &= C_A(\vec{a} - \vec{b})^2 + C_A(\vec{a} - \vec{b})^2 \\ &\quad - C_A(\vec{a} - \vec{b}) \cdot (\vec{a} - \vec{c}), \end{aligned} \tag{3.41}$$

$$\begin{aligned} D_{q\bar{q}}^g &= C_F(\vec{a} - \vec{b})^2 + C_F(\vec{a} - \vec{b})^2 \\ &\quad - (2C_F - C_A)(\vec{a} - \vec{b}) \cdot (\vec{a} - \vec{b}), \end{aligned} \tag{3.42}$$

$$\begin{aligned} D_{qg}^q &= C_F(\vec{c} - \vec{a})^2 + C_F(\vec{c} - \vec{b})^2 \\ &\quad - (2C_F - C_A)(\vec{c} - \vec{a}) \cdot (\vec{c} - \vec{b}). \end{aligned} \tag{3.43}$$

with the vectors given by

$$\vec{a} = \frac{\vec{k}_\perp - x\vec{q}_\perp}{(\vec{k}_\perp - x\vec{q}_\perp)^2}, \vec{b} = \frac{\vec{k}_\perp - \vec{q}_\perp}{(\vec{k}_\perp - \vec{q}_\perp)^2}, \vec{c} = \frac{\vec{k}_\perp}{\vec{k}_\perp^2}. \tag{3.44}$$

3.2.3 The final incoherent transport equation and Monte-Carlo technique

Combining all these processes, we summarize the incoherent linearized-Boltzmann plus Langevin equation:

$$\frac{df}{dt} = \mathcal{D}[f] + \mathcal{C}_{1\leftrightarrow 2}[f] + \mathcal{C}_{2\leftrightarrow 2}[f] + \mathcal{C}_{2\leftrightarrow 3}[f]. \tag{3.45}$$

The distribution function undergoes soft diffusion and diffusion induced-radiation. Hard collisions with the medium are included as $2 \leftrightarrow 2$ and $2 \leftrightarrow 3$ collision terms. The next section is devoted to the inclusion of the LPM effect to such an incoherent transport equation. We now discuss the numerical techniques for simulating the above equation.

The Monte Carlo method starts from representing the distribution function by an ensemble of particle states,

$$f(t, x, p) \approx \sum_i \delta^3(x - x_i(t)) \delta^3(p - p_i(t)) \tag{3.46}$$

For linearized transport equations, it is sufficient to consider the dynamics of one such particle. Within a small time step Δt , a particle undergoes scattering with a certain probability. In between subsequent collisions, the particle is propagated by diffusion transport.

Order of operation In the presence of two types of operation: collision $\mathcal{C}[f_Q]$ and diffusion $\mathcal{D}[f_Q]$:

$$\frac{df}{dt} = (\hat{\mathcal{C}} + \hat{\mathcal{D}}) f_Q.$$

In principle, the order of operations on the particle should matter. But a different choice of ordering only results in an $O(\Delta t^2)$ change in the updated distribution function. This can be seen with the formal solution of the equation,

$$\begin{aligned} f_Q(x, p) &= \exp \left\{ \int_{x'}^x \gamma u \cdot dx \left(\hat{\mathcal{C}} + \hat{\mathcal{D}} \right) \right\} f_Q(x', p) \\ &\approx e^{\Delta t \hat{\mathcal{C}}} e^{\Delta t \hat{\mathcal{D}}} f_Q(x', p) + \mathcal{O}(\Delta t^2) \end{aligned} \quad (3.47)$$

The diffusion solver The Fokker Planck equation can be solved as an ensemble of particles governed by Langevin dynamics. The Langevin equation in the post-point discretization scheme is [HvHG⁺13],

$$\Delta \vec{x}_i = \frac{p}{E} \Delta t \quad (3.48)$$

$$\Delta \vec{p}_i = -\Gamma \vec{p}_i \Delta t + \sqrt{\overset{\leftrightarrow}{B}(p + \Delta p) \Delta t} \vec{\xi} \quad (3.49)$$

Γ is the Langevin drag term, and $\vec{\xi}$ is a unit-variance Gaussian random force. $\overset{\leftrightarrow}{B} = \hat{P}^{\parallel} \kappa_{\parallel} + \hat{P}^{\perp} \kappa_{\perp}$ are the diffusion coefficients in the tensor form. \hat{P}^{\parallel} and \hat{P}^{\perp} project any vector into the direction parallel and perpendicular to the direction of motion.

The diffusion coefficients are directly related to the one in the Fokker Planck equation $\kappa_{\parallel} = \hat{q}_L$, and $\kappa_{\perp} = \hat{q}/2$. While, the relation between the drag coefficient in the Fokker Planck equation η_D and the drag force Γ in the Langevin equation is discretization scheme dependent. In the post-step scheme, this relation is [HvHG⁺13],

$$p_j \Gamma = p_j A + \left(\sqrt{\kappa_{\parallel}} \hat{P}_{lk}^{\parallel} + \sqrt{\kappa_{\perp}} \hat{P}_{lk}^{\perp} \right) \frac{\partial}{\partial p_l} \left(\sqrt{\kappa_{\parallel}} \hat{P}_{kj}^{\parallel} + \sqrt{\kappa_{\perp}} \hat{P}_{kj}^{\perp} \right). \quad (3.50)$$

and reduces to,

$$\Gamma = \eta_D + \frac{d\kappa_{\parallel}}{dp^2} + \frac{2\sqrt{\kappa_{\parallel}\kappa_{\perp}} - 2\kappa_{\perp}}{p^2} \quad (3.51)$$

$$= \frac{\kappa_{\parallel}}{2TE} - \frac{1}{p^2} \left(\sqrt{\kappa_{\parallel}} - \sqrt{\kappa_{\perp}} \right)^2. \quad (3.52)$$

The Einstein relation between η_D and diffusion coefficient is used in the last step.

The scattering solver For two-body scattering, neglecting quantum statistics, the collision rate in the rest frame of the medium is,

$$R_a(p) = \sum_{b,c,d} \frac{1}{2E_a} \int \frac{dp_b^3}{(2\pi)^3 2E_b} f_0(p_b) \int d\Phi_m |M^2|_{ab \rightarrow cd} \quad (3.53)$$

A similar expression can also be obtained for $2 \leftrightarrow 3$ processes. For a short amount of time Δt , the probability to have no collision is $P_0 = \exp(-\Delta t R)$. The number of independent multiple collisions satisfies a Poisson distribution with mean $N = \Delta t R$. For a particle based simulation, one always needs to ensure that Δt is small enough

$(\Delta t \ll 1/R)$ so that effectively there is at most one collision happening within the time step. Once a collision is sampled to happen, the full final state can be obtained by further sampling each scattering channel and the momentum phase-space differential rates.

The multi-dimensional phase-space sampling is performed sequentially for the initial state and final state phase-space. For $2 \rightarrow 2$ and $2 \rightarrow 3$ body processes, we rewrite the integrated rate in the fluid cell rest frame as,

$$R_{2m}(E_1, T) = \frac{d}{\nu} \frac{1}{2E_1} \int \frac{e^{-\beta E_2} dp_2^3}{(2\pi)^3 2E_2} \int d\Phi_m \overline{|M|^2}. \quad (3.54)$$

If vacuum matrix-elements are used, the nested integration is a Lorentz invariant quantity, and we can choose to calculate it in the center-of-mass frame of the two-body collision,

$$\begin{aligned} \int d\Phi_m \overline{|M_{22}|^2} &= 2E_1 2E_2 v_{\text{rel}} \sigma \\ &= 2(s - M^2) \sigma_{\text{CoM}}^{22}(\sqrt{s}, T) \\ &= F_{2m}(\sqrt{s}, T) \end{aligned} \quad (3.55)$$

where σ is the cross-section of the process. In practice, the values of the integrated rates and cross-sections are tabulated. The sampling of initial state p_2 determines the center-of-mass energy of the process $s = (p_1 + p_2)^2 = 2(E_1 E_2 - p_1 p_2 \cos \theta_{12})$. Subsequently we sample the momentum-transfer q -differential cross-section with \sqrt{s}, T as inputs, and final states are reconstructed given the initial state and q . The sampling of the $3 \rightarrow 2$ body process is more difficult due to the larger number of parameters to specify the initial state kinematics,

$$R_{32}(E_1, T) = \frac{d}{\nu} \int \frac{e^{-\beta E_2} dp_2^3}{(2\pi)^3 2E_2} \frac{e^{-\beta k} dk^3}{(2\pi)^3 2k} \int d\Phi_2 \overline{|M|^2}. \quad (3.56)$$

The Lorentz invariant nested integral is a function of the initial state 3-body kinematics and temperature,

$$\int d\Phi_2 \overline{|M|^2} = F_{32}(\sqrt{s}, \sqrt{s_{12}}, \sqrt{s_{1k}}, T). \quad (3.57)$$

Where $s = (p_1 + p_2 + k)^2$ is the center of mass energy, $s_{12} = (p_1 + p_2)^2$ and $s_{1k} = (p_1 + k)^2$. This requires a four-dimensional table for the value of F_{32} and a five-dimensional initial state sampling. The tabulation of a high-dimensional rate and cross-section tables can be made manageable if a proper approximating function $A(x, y, \dots)$ is proposed that captures the limiting behavior of the target function $T(x, y, \dots)$. Tabulating the ratio of T/A would be extremely efficient and accurate with a moderate size table.

The sequential sampling breaks the original $m+n$ body phase-space sampling into two lower dimensional samplings. But as one should notice, the prerequisite is that the integration over the final state momentum of the matrix-element can be written into

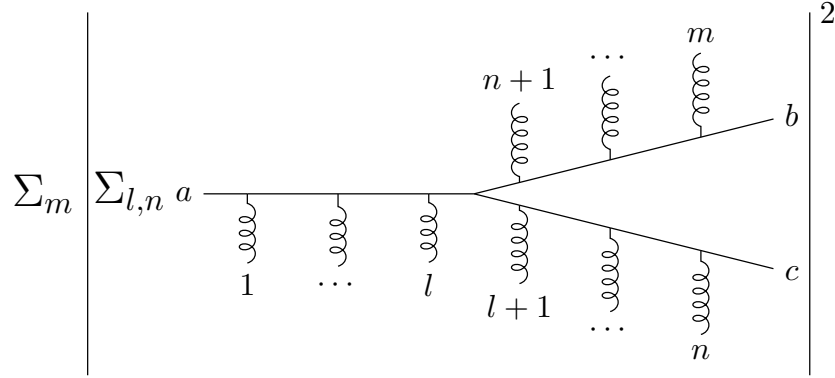


Figure 3.1: A schematic demonstration of the physics of in-medium parton bremsstrahlung. The hard parton “*a*” splits into two hard partons “*b*” and “*c*”. The hard partons (quarks or gluon) are denoted as straight lines. The hard system constantly interacts with the medium through gluon exchanges, denoted as the loop lines. One sums the squared amplitudes ($| \dots |^2$) over an arbitrary number (*m*) of interactions with the medium. Each amplitude has to include all the interference contribution. Finally, one does an ensemble average over the medium configurations.

a Lorentz invariant form and therefore only depends on the Mandelstam variables. This appealing feature is broken by the inclusion of either quantum statistics or in-medium propagators in the matrix-elements. Because quantum statistics introduces factors like $1 \pm f(p \cdot u)$ to the final momentum integral and the in-medium propagator is not Lorentz invariant, resulting in a F_{nm} that depends on the relative velocity between the collision system and the medium rest frame. This significantly increases the dimension and complexity of the problem. Fortunately, the separation of hard and soft modes allows one to use vacuum matrix-elements at large momentum transfer.

3.3 The Landau-Pomeranchuk-Migdal effect: theory

In the last section, all the processes were treated as instantaneous, however, a process actually takes a finite amount of time for its final states to loose coherence. For elastic collisions, this time is $1/m_D \sim 1/gT$ which is still short compared to the mean-free-path $\lambda \sim 1/g^2T$, provided a sufficiently small g . For inelastic process, the light-cone energy difference between the initial and final states is,

$$\delta E = \frac{k_\perp^2}{2k} + \frac{p_\perp^2}{2p} - \frac{p'^2_\perp}{2p'} = \frac{[(1-x)\vec{k}_\perp - x\vec{p}_\perp]^2}{2x(1-x)E} \quad (3.58)$$

By the uncertainty principal, the coherence time for such a transition is on the order of $\tau_f = 1/\delta E$, termed the “formation time” of the radiation. In this region of phase

space $k_\perp^2, p_\perp^2 < g^2 x(1-x)ET$, the average number of collisions during the radiation becomes a relatively large number $N = \tau_f/\lambda > 1$, so the picture of radiation being induced from independent scattering centers breaks down. It has been shown that these multiple scatterings should be resummed [Zak96, Zak97, BDM⁺97b] (please refer to figure 3.1 for a schematic demonstration), and the leading order resummed radiation probability is,

$$\begin{aligned} \frac{dP_{bc}^a}{d\omega} &= \frac{\alpha_s P_{bc}^{0,a}(x)}{x^2(1-x)^2 E^2} \Re e \int_0^\infty dt_1 \int_{t_1}^\infty dt_2 \\ &\quad \nabla_{\mathbf{b}_1} \cdot \nabla_{\mathbf{b}_2} \{G(t_2, \mathbf{b}_2; t_1, \mathbf{b}_1) - G_0(t_2, \mathbf{b}_2; t_1, \mathbf{b}_1)\} |_{\mathbf{b}_1, \mathbf{b}_2 \rightarrow 0} \end{aligned} \quad (3.59)$$

$P_{bc}^{0,a}(x)$ is the vacuum splitting function, and x is the energy fraction carried by the daughter b . Inside the double time integral, G is the propagator of the following Hamiltonian for the transverse dynamics of the splitting system,

$$\hat{H} = \frac{-\nabla_{\mathbf{b}}^2 + m_{\text{eff}}^2}{2x(1-x)E} - i\Gamma_3(\mathbf{b}) \quad (3.60)$$

$$\begin{aligned} \Gamma_3(\mathbf{b}) &= \frac{C_a - C_b + C_c}{2} \Gamma_2(\mathbf{b}) + \frac{C_a - C_c + C_b}{2} \Gamma_2(x\mathbf{b}) \\ &\quad + \frac{C_b + C_c - C_a}{2} \Gamma_2((1-x)\mathbf{b}) \end{aligned} \quad (3.61)$$

and G_0 is the free propagator. The variable \mathbf{b} is the Fourier transformation dual of the transverse momentum, and is usually referred to as the impact-parameter (not to be confused with the other use). m_{eff}^2 is a combination of both parton bare masses and thermal masses. Finally, the interaction $\Gamma_3(\mathbf{b})$ encodes the transverse broadening of the three body system $a \rightarrow b + c$ [Zak97]. It has three two-body contributions $\Gamma_2(\mathbf{b})$. The vacuum piece G_0 is subtracted from G so that this formula only computes the medium-induced radiation. The two gradient operators at time t_1 and t_2 come from the action of the radiation vertices, meaning this transition receives coherence contribution from t_1 to t_2 . If one neglects the mass term, G can be rewritten as $G_0 - iG_0\Gamma_3G$ so that,

$$\begin{aligned} \frac{dP_{bc}^a}{d\omega} &= \frac{\alpha_s P_{bc}^{0,a}(x)}{x^2(1-x)^2 E^2} \Re e \int_0^\infty dt_1 \int_{t_1}^\infty dt_2 \\ &\quad \nabla_{\mathbf{b}_1} \cdot \nabla_{\mathbf{b}_2} [G_0(-i\Gamma_3)G](t_2, \mathbf{b}_2; t_1, \mathbf{b}_1) |_{\mathbf{b}_1, \mathbf{b}_2 \rightarrow 0}, \end{aligned} \quad (3.62)$$

$$= \frac{\alpha_s P_{bc}^{0,a}(x)}{x^2(1-x)^2 E^2} \Re e \int_0^\infty dt_1 \int_{t_1}^\infty dt_2 F(t_2; t_1). \quad (3.63)$$

$F(t_2, t_1)$ is a short notation for term under the integration.

The interaction potential $\Gamma_2(\mathbf{b})$ depends on the assumption of the probe-medium interaction. For example, in a weakly coupled theory, a compact results is obtained at leading order [AGZ02],

$$\Gamma_2(\mathbf{b}) = \frac{1}{\pi} \int \frac{d\mathbf{q}_\perp^2}{(2\pi)^2} \frac{g^2 T m_D^2 (1 - e^{i\mathbf{b} \cdot \mathbf{q}_\perp})}{q_\perp^2 (q_\perp^2 + m_D^2)} \quad (3.64)$$

There are two systematic ways to investigate the properties of the medium-induced radiation computation in equation 3.60. In a method called the opacity expansion [Wie00, GLV00], the propagator is solved in a perturbation series of the number of interaction Γ_3 . Another approach which studies the solution assuming soft interactions (small- q) and approximates the collision kernel by a harmonic oscillator $\Gamma_2(b) \approx \frac{1}{4}\hat{q}b^2$ [BDM⁺97b, BDMS98, BDM⁺97a]. This is also known as the leading-log $1/\ln(N)$ approximation, where N can be interpreted as the “number” of coherent collision within the formation time. Taking the residue potential $\Gamma(b) - \frac{1}{4}\hat{q}b^2$ as a perturbation, improvements at the next-to-leading-log level has also been investigated in [AD08, MT19].

Though this leading order calculation has been written in this compact form, it is not trivial to include its effect (even approximately) in the semi-classical Boltzmann simulation. One can clearly see this problem by observing that it requires a finite time interval $t_1 \rightarrow t_2$ to compute the splitting rate at time t_1 , while the Boltzmann equation has only one time variable. We will devote the next section to an approximated solution to this problem. For the rest of this section, we shall elaborate the details of the current understanding in the opacity expansion and harmonic oscillator (deep-LPM) regime, which greatly facilitates the discussion of the next section.

3.3.1 Large medium

For a large and static medium that approaches the infinite medium limit, further simplification is possible. The problem becomes a “static” one, and a branching rate Γ can be defined as the branching probability per unit time. This limit is known as the AMY equation [AMY02, AMY03a, AMY03b],

$$\frac{d\Gamma_{a \rightarrow bc}}{dx} = \frac{1}{2E\nu_a} \frac{\alpha_s d_a P_{a \rightarrow bc}(x)}{x^2(1-x)^2} \int \frac{d^2\vec{k}}{(2\pi)^2} \vec{k} \cdot \Re e \vec{F}$$

where we have dropped the Bose enhancement and the Pauli blocking factors of the outgoing partons from the original formula. The vector valued wave-function $\vec{F}(\vec{h}; p, x)$ satisfies the following integral equation [AMY02],

$$2\vec{k} = i \frac{\vec{F}(\vec{k})}{\tau_f(k)} + g^2 \mathcal{C}_3[\vec{F}]$$

\vec{k} , and $\tau_f(k)$ is the transverse scale and the formation time of the branching. \mathcal{C}_3 is the Γ_3 operator in the momentum representation,

$$\begin{aligned} \mathcal{C}_3[f] &= \int_{\mathbf{q}} \mathcal{A}(q_\perp^2) \left\{ \frac{C_b + C_c - C_a}{2} (f_{\mathbf{p}} - f_{\mathbf{p}-\mathbf{q}}) \right. \\ &\quad \left. + \frac{C_a + C_c - C_b}{2} (f_{\mathbf{p}} - f_{\mathbf{p}+x\mathbf{q}}) + \frac{C_a + C_b - C_c}{2} (f_{\mathbf{p}} - f_{\mathbf{p}+(1-x)\mathbf{q}}) \right\} \end{aligned} \quad (3.65)$$

$$\mathcal{A}(q_\perp^2) = \frac{g^2 m_D^2 T}{q^2 (m_D^2 + q^2)} \quad (3.66)$$

The exact solution can be solved numerically. Here, we investigate this formula in two extreme regimes: the incoherent limit (Bethe-Heitler regime) and the deep-LPM regime.

The Bethe-Heitler regime: The quantum interference can be neglected if the formation time is sufficiently short. In such cases the amplitude under the double time integral has a delta-function like time structure, and the transition probability has a nice interpretation of integrating the localized branching rate over a single time variable. But the kinematic range for short formation times is very limited. The condition $\tau_f \ll \lambda$ translates to $\omega \ll T$. For such case, one may solve for F by treating F/τ_f as a large quantity [GMT16]. The leading equations are then,

$$2\vec{k}\tau_f(k) = -\Im\vec{F} \quad (3.67)$$

$$\Re\vec{F} = -g^2\tau_f(k)\mathcal{C}_3[\Im\vec{F}] \quad (3.68)$$

Take a quark splitting into a quark and a gluon as an example and neglecting the thermal masses, the resulting rate is then proportional to

$$\begin{aligned} R \propto & 2g^2 \int dk^2 \int dq^2 \mathcal{A}(q_\perp^2) \left\{ \frac{C_A}{2} \frac{\vec{k}}{\vec{k}^2} \cdot \left[\frac{\vec{k}}{\vec{k}^2} - \frac{\vec{k} - \vec{q}}{(\vec{k} - \vec{q})^2} \right] \right. \\ & \left. + \frac{2C_F - C_A}{2} \frac{\vec{k}}{\vec{k}^2} \cdot \left[\frac{\vec{k}}{\vec{k}^2} - \frac{\vec{k} + x\vec{q}}{(\vec{k} + x\vec{q})^2} \right] + \frac{C_A}{2} \frac{\vec{k}}{\vec{k}^2} \cdot \left[\frac{\vec{k}}{\vec{k}^2} - \frac{\vec{k} + (1-x)\vec{q}}{(\vec{k} + (1-x)\vec{q})^2} \right] \right\} \end{aligned} \quad (3.69)$$

though, this expression looks very different from the cross-section formula that we used in the incoherent rate of the Boltzmann equation, they are actually equivalent upon the integration of dk^2 . We provide a detailed explanation of this connection between the Bethe-Heitler approximation of the AMY rate equation and the incoherent rate computed with $2 \rightarrow 3$ cross-section in appendix A.

In the high energy limit $E \gg T \gg \omega$ so that $x \ll 1$, this rate can be approximated by its $x \rightarrow 0$ limit,

$$\frac{dR}{dx} = \frac{4E\alpha_s d_a P(x)}{\nu_a} \int \frac{dk^2}{(2\pi)^2} \int \frac{dq^2 \mathcal{A}(q_\perp^2)}{(2\pi)^2} \sum_{\pm} \frac{C_A}{2} \frac{\vec{k}}{\vec{k}^2} \cdot \left[\frac{\vec{k}}{\vec{k}^2} - \frac{\vec{k} \pm \vec{q}}{(\vec{k} \pm \vec{q})^2} \right] \quad (3.70)$$

$$= \frac{2C_A E \alpha_s d_a P(x)}{\nu_a} \int \frac{dk^2}{(2\pi)^2} \int \frac{dq^2 \mathcal{A}(q_\perp^2)}{(2\pi)^2} \left[\frac{\vec{k}}{\vec{k}^2} - \frac{(\vec{k} - \vec{q})}{(\vec{k} - \vec{q})^2} \right]^2 \quad (3.71)$$

where in the second step, the k integration of the term with the "+" sign has been shifted to an integration over $k - q$ to render the expression into the complete square form. This form is known as the Gunion-Bertsch approximation [GB82] of inelastic $2 \rightarrow 3$ scattering, whose improved form [FUXG13, UFXG15] has been employed in existing full Boltzmann simulations of the partonic transport equation [XG05, UFXG10]. To understand the physical meaning of the above expression, we can proceed to integrate and regulate the soft divergence with a screening mass whenever needed. Eventually we have,

$$\frac{dR}{dx} \propto \alpha_s P(x) \times \alpha_s C_A T \propto \frac{\alpha_s P(x)}{\lambda_g} \quad (3.72)$$

Where the second factor $\alpha_s C_A T$ can be interpreted as the inverse of the gluon-mean-free path. Now the physical meaning becomes clear: in the incoherent limit, a certain amount of radiation $\alpha_s P(x)$ is triggered every mean-free-path from interactions with the collision centers.

To summarize the Bethe-Heitler regime, the total number of branchings can be viewed as contributed by an incoherent sum of $2 \rightarrow 3$ processes localized at time t . And such contributions can be easily incorporated into the Boltzmann equation given the incoherent branching rate. However, the validity range for this approximation is at best $xE \sim$ a few times of the temperature.

The deep-LPM region (leading-log behavior): another useful approximation considers the limit τ_f being so large that many collisions contribute coherently to the branching. $\tau_f \gg \lambda$ corresponds to the region when the daughter parton's energy is large $\omega, E - \omega \gg T$. As a result, the transverse momentum k of the branching should be large compared to the average momentum transfer to each scattering center q . In this limit, a diffusion approximation to the \mathcal{C}_3 operators is possible. The finite difference between $F(k)$ and $F(k + O(q))$ is expanded in \vec{q} . The zeroth order cancels and the first order \vec{q} contribution vanishes due to the symmetric q integration. Keeping only second order terms in \vec{q} , the AMY equation is simplified to a diffusion type equation but with a complex diffusion constant and a source term [AD08]

$$-\frac{1}{4} \nabla_{\vec{k}}^2 \vec{F} + i \frac{k^2 + m_{\text{eff}}^2}{2x(1-x)E\hat{q}_3} \vec{F} = \frac{2\vec{k}}{\hat{q}_3}. \quad (3.73)$$

This approximation of the original collision operator is also known as the harmonic oscillator approximation. \hat{q}_3 is the effective transport parameter,

$$\hat{q}_3(x, Q_0^2) = \alpha_s T m_D^2 \ln \left(1 + \frac{Q_0^2}{m_D^2} \right) C_{abc}(x). \quad (3.74)$$

This is obtained by doing the \mathbf{q} integration of the expanded collision operator upto a cut-off scale Q_0 , below which the small- q approximation is considered to be valid. The effective transport parameter also depends on the color structure of the splitting,

$$C_{abc}(x) = \frac{C_b + C_c - C_a}{2} + x^2 \frac{C_a + C_c - C_b}{2} \quad (3.75)$$

$$+ (1-x)^2 \frac{C_a + C_b - C_c}{2} \quad (3.76)$$

Taking the momentum fraction of the “ b ” particle to zero $x \rightarrow 0$, this color factor goes to C_b ; similarly, $x \rightarrow 1$ which corresponds to “ c ” particle taking a vanishing fraction of the total energy, the color factor approaches C_c . Therefore, in these extreme limits $x \rightarrow 0$ or 1 , the effect transport parameters looks like the daughter with softer momentum. With finite $x, 1-x$, the color factor becomes a combination of the colors of the whole splitting system.

Neglecting the thermal mass, the solution to the this diffusion equation can be obtained analytically [AD08],

$$\vec{F} = i4x(1-x)E^2 \frac{\vec{k}}{k^2} \left[\exp \left(\frac{-i^{1/2}k^2}{\sqrt{2x(1-x)E\hat{q}_3}} \right) - 1 \right] \quad (3.77)$$

And the radiation rate can be obtained accordingly,

$$\frac{dR_{bc}^{a,\text{LL}}}{dx} = \frac{\alpha_s P_{bc}^{a(0)}}{\pi\sqrt{2}} \sqrt{\frac{\hat{q}_3(x, Q_0^2)}{2x(1-x)E}} \propto \frac{\alpha_s P(x)}{\langle \tau_f \rangle} \quad (3.78)$$

Such a result is often referred to as the leading-log (leading in $1/\ln(N)$) solution. An interesting scale $\sqrt{2x(1-x)E\hat{q}_3}$ shows up in this calculation which governs the typical transverse momentum of the splitting, or equivalently $\sqrt{\hat{q}_3/2x(1-x)E}$ which governs the rate at which the splitting happens. A simple interpretation for these scales is: during $\tau_f \sim 2x(1-x)E/k_\perp^2$, many soft interactions contribute to the broadening of k_\perp^2 . In a diffusion approximation, the variance $\langle k_\perp^2 \rangle$ is linearly proportional to the diffusion constant and time, $\langle k^2 \rangle \sim \hat{q}_3 \tau_f$. Combined with the expression of formation time, one arrives at the above typical transverse momentum and typical formation time.

Compared to the naïve “incoherent expectation” in equation 3.72, the actual radiation rate is reduced by a factor of $\lambda_{\text{el}}/\langle \tau_f \rangle$ on average. Therefore, in the deep-LPM regime, instead of triggering radiation every mean-free-path, many collision centers contribute coherently and trigger radiation every τ_f which scales as $\lambda\sqrt{\omega/T}$. Considering that this approximation only works for $\omega \gg T$, we combine this result with the Bethe-Heitler regime and summarize the radiation pattern in a large medium as,

$$\frac{dR_{bc}^a}{dx} \sim \frac{\alpha_s P_{bc}^{a(0)}(x)}{\max\{\lambda, \tau_f\}} \quad (3.79)$$

This simple idea will be the foundation for modeling of the parton branching processes in section 3.4.

The deep-LPM region (next-to-leading-log level): The previously introduced leading-log result has both a simplicity and a clear physical interpretation in explaining what happens in the deep-LPM region $\ln(N) \sim \ln(xE/T) \gg 1$. Together with the Bethe-Heitler (incoherent) limit at $xE \lesssim T$, one can already develop a pretty good understanding in an infinite medium.

One thing that still deserves a detailed discussion is the upper bound Q_0 introduced in the q -integration in the leading-log approximation. This cut-off scale, as a result of the small- q simplification of the full model, is generally unknown and brings an uncertainty to the approximation at this level. This issue has been studied at the next-to-leading-log (NLL) level by treating the large- q part of the collision kernel as a perturbation to this approximation. The authors of [AD08] and more recently authors of [MT19] have found that a reasonable choice of Q_0 is the order of k_\perp^2 itself. A self-consistent determination of Q_0 is also possible by requiring a minimal contribution from the NLL correction. The NLL result, takes a similar structure as the leading-log solution, but with the unknown Q_0 replaced by its NLL improved value Q_1 ,

$$Q_1^2 \approx \sqrt{\omega\hat{q}} \approx \sqrt{\omega\alpha_s C_R m_D^2 T \ln \frac{Q_0^2}{m_D^2}} \quad (3.80)$$

or a self-consistent determination as in [AD08],

$$\begin{aligned} Q_1^2 &= \sqrt{2x(1-x)E\alpha_s T m_D^2} \\ &\times \left(\frac{C_b + C_c - C_a}{2} \ln \frac{2\xi Q_1^2}{m_D^2} + \frac{C_a + C_c - C_b}{2} x^2 \ln \frac{2\xi Q_1^2}{x^2 m_D^2} \right. \\ &\left. + \frac{C_a + C_b - C_c}{2} (1-x)^2 \ln \frac{2\xi Q_1^2}{(1-x)^2 m_D^2} \right)^{1/2} \end{aligned} \quad (3.81)$$

with $\xi \approx 9.1$ a constant. This suggests that the optimal choice of the scale is on the order of the branching transverse momentum itself $\langle k^2 \rangle = \sqrt{2x(1-x)E\hat{q}_3}$, but with an improved logarithmic factor. It has been shown that using this self-consistent Q_1 , the approximation is very close to the numerical solution of the full model when $\omega \gg T$ [AD08].

3.3.2 Thin medium: opacity expansion

For a thin and dilute medium, there is only a few effective collisions that contributes. In such cases, a systematic expansion over L/λ has been developed and is known as the opacity expansion [Wie00, GLV00, DH08]. This can be obtained by solving the propagator with an perturbation series of the interaction potential Γ_3 . At leading order in the opacity expansion and applying soft approximation $x \ll 1$, the radiation rate is [DH08],

$$\frac{dR}{dx} \propto g^2 P(x) C_A \int \frac{d\vec{q}^2 d\vec{k}}{(2\pi)^4} \frac{g^2 T m_D^2}{q^2(q^2 + m_D^2)} \frac{\vec{k} \cdot \vec{q}}{(\vec{k} - \vec{q})^2 k^2} \left[1 - \cos \left(\frac{(\vec{k} - \vec{q})^2 t}{2xE} \right) \right] \quad (3.82)$$

It has a notable time-dependent $1 - \cos(\omega t)$ modulation due to interference from the production point at $t = 0$ to the first interaction with medium at time t . Therefore, this is an important finite-size effect for the radiation spectrum in a thin medium and the associated energy loss of the leading parton. The finite size effect is important for phenomenological studies, because the QGP fireball from nuclear collisions is far from an “infinite” medium.

3.3.3 Numerical solution for a general case

To go beyond the above approximation and investigate how the different limiting regimes are connected, one has to use a numerical approach. We follow the approach described in [CHG10] to solve the propagator G in momentum space. Neglecting the thermal mass term, the momentum space representation of the splitting rate is,

$$\frac{dR_{bc}^a(t)}{dx} = \frac{P_{bc}^{a(0)}(x)}{2\pi x(1-x)E} \Re e \int \frac{d\mathbf{p}^2}{(2\pi)^2} \int_0^t d\tau e^{\frac{-i\tau}{\tau_f(p)}} \vec{p} \cdot \vec{\Psi}(\vec{p}, \tau) \quad (3.83)$$

with the time evolution of the vector-valued wave function solved in the interaction picture with the initial condition,

$$\frac{\partial \vec{\Psi}}{\partial \tau} = -e^{\frac{-i\tau}{\tau_f(p)}} \mathcal{C}_3 \left[e^{\frac{i\tau}{\tau_f(p)}} \vec{\psi}(\vec{p}, \tau) \right] \quad (3.84)$$

$$\vec{\Psi}(\vec{p}, \tau = 0) = \mathcal{C}_3 \left[\frac{i\vec{p}}{p^2 + m_{\text{eff}}^2} \right] \quad (3.85)$$

The \mathcal{C}_3 operation involves a finite difference and two-dimensional integration over the transverse momentum p . Fortunately the integration over the azimuthal angle of p can be performed analytically at least for the leading order collision kernel with fixed coupling constant. Reparametrizing the vector function into a vector part times a rotational invariant function $\vec{\Psi} = \vec{p}/(p^2 + m_{\text{eff}}^2)^2 \Phi(p^2)$, the evolution equation for the scalar function Φ is,

$$\begin{aligned} \frac{\partial \Phi(p^2)}{\partial \tau} = & -\alpha_s T \sum_n c_n \int dq^2 \left\{ \frac{\Phi(p^2)}{|p^2 - q^2|} - \frac{\Phi(p^2)}{\sqrt{(p^2 + q^2 + m_n^2)^2 - 4p^2 q^2}} \right. \\ & \left. - e^{i\tau \frac{p^2 - q^2}{2x(1-x)E}} \frac{\Phi(q^2)}{2p^2} \frac{(p^2 + m_{\text{eff}}^2)^2}{(q^2 + m_{\text{eff}}^2)^2} \left[\frac{p^2 + q^2}{|p^2 - q^2|} - \frac{p^2 + q^2 + m_n^2}{\sqrt{(p^2 + q^2 + m_n^2)^2 - 4p^2 q^2}} \right] \right\} \end{aligned} \quad (3.86)$$

$$\begin{aligned} \Phi(\tau = 0) = & i \sum_n c_n \int dq^2 \left\{ \frac{p^2 + m_{\text{eff}}^2}{|p^2 - q^2|} - \frac{p^2 + m_{\text{eff}}^2}{\sqrt{(p^2 + q^2 + m_n^2)^2 - 4p^2 q^2}} \right. \\ & \left. - \frac{(p^2 + m_{\text{eff}}^2)^2}{2p^2(q^2 + m_{\text{eff}}^2)} \left[\frac{p^2 + q^2}{|p^2 - q^2|} - \frac{p^2 + q^2 + m_n^2}{\sqrt{(p^2 + q^2 + m_n^2)^2 - 4p^2 q^2}} \right] \right\}. \end{aligned} \quad (3.87)$$

Here, the summation goes over the different pieces of the three-body collision kernel, where the original integration variable \vec{q} has been shifted to $\vec{p} - \vec{q}$, $\vec{p} + x\vec{q}$, and $\vec{p} + (1-x)\vec{q}$ accordingly. The color factors c_n are $c_1 = (C_b + C_c - C_a)/2$, $c_2 = x^2(C_a + C_c - C_b)/2$, $c_3 = (1-x)^2(C_a + C_b - C_c)/2$, and m_n^2 terms are $m_1^2 = m_D^2$, $m_2^2 = x^2 m_D^2$, $m_3^2 = (1-x)^2 m_D^2$. The azimuthal integration over ϕ_q has been performed and q^2 integrates from zero to infinity. One may notice that one of the denominators $|q^2 - p^2|$ can vanish. But as q^2 tends to p^2 , the subtracted term in the second line approaches the expression in the first line, and therefore leaves the function to be integrated finite. Now, the problem has been reduced to an initial value problem of a 1+1 D first order differential-integral equation, and can be solved quite efficiently using finite difference and numerical quadrature methods.

3.3.4 Mass effect in medium-induced branching

For radiation in the vacuum, the heavy quark mass is a natural regulator for the collinear divergence,

$$\frac{dP}{dx dk_\perp^2} = \frac{\alpha_s P(x) k_\perp^2}{(k_\perp^2 + x^2 M^2)^2} = \frac{\alpha_s P(x)}{k_\perp^2} \left(\frac{\theta^2}{\theta^2 + \theta_M^2} \right)^2 \quad (3.88)$$

Compared to light quark, the radiation off a heavy quark is suppressed within a typical angle $\theta_M = M/E$. This is often referred to as the “dead-cone” (mass) effect [DKT91].

Inside a medium, the situation is more complicated [DK01, ASW04, AJMS12, ZWW04]. The mass not only changes the propagator, but also shorten the formation time

$$\tau_f = \frac{2x(1-x)E}{k_\perp^2 + m_{\text{eff}}'^2}, m_{\text{eff}}'^2 = (1-x)m_\infty^2 + x^2M^2 \quad (3.89)$$

These two competing features together contribute to the mass correction.

In principle, the formula discussed in this section also applies to heavy quarks once the effective mass m_{eff}^2 is replaced by $m_{\text{eff}}'^2$, though corrections like M/p are dropped. When $M/p \gtrsim g$, further corrections may be important, but this is also the region when elastic energy loss starts to dominate the radiative energy loss for heavy quark [MT05].

3.3.5 Treating multiple emissions

The formula that has been discussed in this section only computes the probability of a single bremsstrahlung. In reality, the averaged number of emissions obtained with this formula can be greater than one, so one has to find a strategy to include multiple emissions. There has been two major approaches used to resum multiple emissions. The first one is the modified DGLAP evolution approach for high virtuality partons [Wan02, CM17]. The single medium-induced emission probability is added to the vacuum splitting function, and then one applies the DGLAP evolution as in proton-proton collisions, but using the so-called modified splitting function. At low virtuality, the parton’s in-medium dynamics is more conveniently described as a time evolution. And the rate equation is used to generate multiple emissions in the course of time [AMY03a, JM05, SGJ09]. The problem that naturally arises is how to interface these two techniques in a realistic event, where an initial highly virtual parton transits to an in-medium transport parton. We shall discuss our tentative solution in the next chapter.

3.4 A modified transport model for the LPM effect

In this section, we shall investigate the approximated inclusion of the LPM effect in a particle based Boltzmann transport simulation, termed “a modified Boltzmann transport”. The approach is designed to work in a large medium and interpolates the deep-LPM region and the Bethe-Heitler region, with certain finite size behavior. The inclusion of the running coupling effect and mass effect for the study of heavy-flavor is discussed.

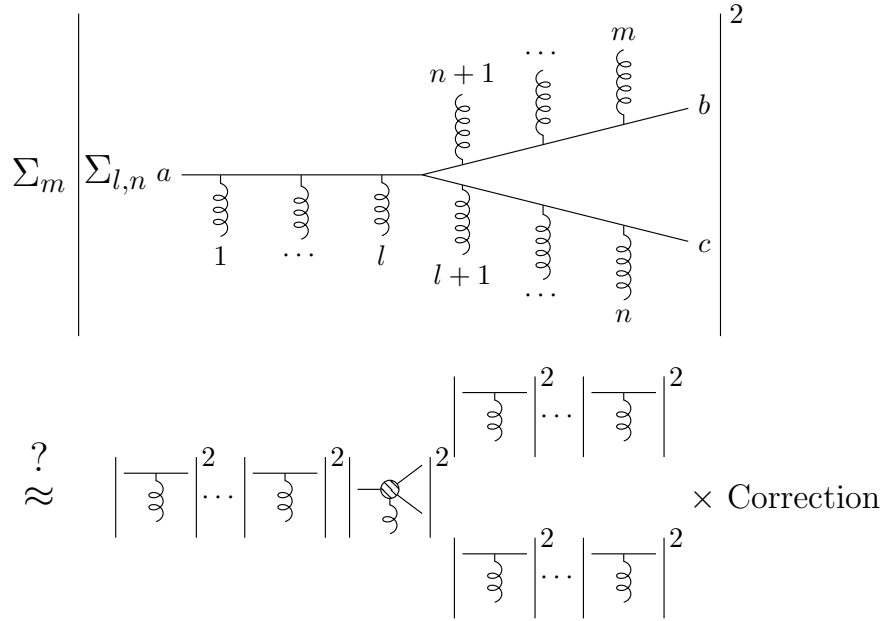


Figure 3.2: A schematic demonstration of the “modified transport” approach. We seek for an approximation to the coherent process by an incoherent transport simulation with a multiplicative correction to the branching probability.

3.4.1 Modifying single particle evolution

To see how to approximate the branching using a modification to the Boltzmann equation, we first go back to the branching probability formula introduced previously [CHG10],

$$\frac{dP_{bc}^a}{dx} = \int_0^\infty dt \frac{g^2 P(x)}{2\pi x(1-x)} \int_t^\infty dt' F(t', t), \quad (3.90)$$

$$F(t', t) = \Re e \int \frac{dp^2}{(2\pi)^2} e^{-it'/\tau_f} \vec{p} \cdot \Psi(\vec{p}, t'). \quad (3.91)$$

We have abbreviate the transition amplitude by the notation $F(t', t)$ for convenience, but always keep in mind this is a quantity that depends on E, ω, g and complete medium properties along the path of the parton, including temperature and fluid velocity profiles $T(t), u^\mu(t)$. The obstacle towards the Boltzmann formulation is the double time integral that is the signature of the quantum transition, which also suggests a fundamental change to the semi-classical approach.

If the time-dependent wave-function is expanded in a series of the collision operator, then this transition amplitude includes the superposition of an arbitrary number of multiple-interaction with the medium. Though multiple scatterings of the branching partons are also present in the Boltzmann simulation, the difference is that the Boltzmann multiple-scatterings are independent from the branching processes; therefore, they only broaden the relative transverse momentum *without* changing the

branching probability. From the leading-log approximation, we see that the branching probability should be reduced by a factor $\sim \lambda/\tau_f$. Our modified approach follows this simple observation, and can be summarized as follows (please also refers to figure 3.2 for a schematic demonstration),

1. Assume an incoherent branching processes is generated at $t = t_0$. Do not treat the daughter partons as immediately independent.
2. Both mother and daughter partons receives elastic broadening from interacting with the medium, which also changes the formation time of the branching.
3. Evolve the branching system until $t - t_0 > \tau_f$. Then, reject this branching process with an acceptance probability that is proportional to λ/τ_f , which corrects for the fact that these multiple scatterings should contribute coherently.
4. Branching partons for those accepted processes are treated as independent objects from this point, rejected partons are discarded without causing any physical effect.

Now we shall explain this scheme in detail. Formally, this method can be understood as replacing the transition amplitude $F(t', t)$ by an average over an ensemble (N) of branching systems using the following ansatz,

$$F(t', t) \rightarrow \frac{1}{N} \sum_{i=1}^N \frac{b}{\tau_i(t)} \delta(t - t' - a\tau_i(t)). \quad (3.92)$$

Each copy “ i ” that evolves under the incoherent Boltzmann dynamics will have a certainty probability to have a certain $\tau_i(t)$ at time t . The δ -function expresses that the branching that starts at time t' is thought to be formed at time $t + a\tau_f$. The additional factor b/τ_f corrects the probability, accounting for the difference between coherent and incoherent calculation. This ansatz of representing a two-point function using information at t and t' of an ensemble of particles follows the same spirit as the Monte-Carlo solver of the traditional Boltzmann equation to discretize a function by an ensemble of particles. This is indeed a crude proxy of the actually two-point function, and its validity has to be examined by comparing its prediction with the theoretical calculations. Finally, a and b are dimensionless factors whose forms shall be determined later and will be tuned to achieve an optimal level of agreement to theoretical calculations.

Plug this simplified ansatz for $F(t, t')$ into the branching probability,

$$\frac{dP_{bc}^a}{dx} = \frac{1}{N} \sum_i \int_0^\infty dt \frac{g^2 P(x)}{2\pi x(1-x)} \frac{b}{\tau_i} \quad (3.93)$$

$$= \frac{1}{N} \sum_i \int_0^\infty dt \frac{g^2 P(x)}{2\pi x(1-x)\tilde{\lambda}} \frac{b\tilde{\lambda}}{\tau_i(t = t' + \tau_i)}. \quad (3.94)$$

$$= \frac{1}{N} \sum_i \int_0^\infty dt \frac{dR_{\text{incoh}}}{dx} \frac{b\tilde{\lambda}}{\tau_i(t = t' + \tau_i)}. \quad (3.95)$$

In the second line, we divided and multiplied back an effective mean-free-path $\tilde{\lambda} = m_D^2/\hat{q}_g$. In doing so, the first factor is interpreted as the incoherent branching rate R_{incoh} , while the second factor is simple the acceptance factor for incoherent branching samples we introduced before. The formation time can be determined self-consistently for each branching copy as it is evolved under the influence of elastic broadening. It is determined at the time when

$$t - t' < \tau_f(t). \quad (3.96)$$

This iterative approach for determine τ_f was first developed and implemented by [ZSW11]. In the deep-LPM region where the number of rescattering is large, such a procedure reproduces the expected scaling of the average formation time $\langle \tau_f \rangle \propto \sqrt{\omega/\hat{q}}$. This approach also generalizes to a medium with a varying temperature profile as the re-scatterings are performed locally as they probe the medium. In cases where the formation time is short so that the acceptance probability is bigger than unity, the acceptance is set to one and the incoherent rate is recovered in the Bethe-Heitler regime. Therefore, this approach naturally provides an interpolation of the deep-LPM regime for energetic branchings and the Bethe-Heitler regime for soft branching in a large medium.

Now we will determine the form of parameters a and b with guidance from the theory in the deep-LPM region. In the leading-log formula, the average inverse formation time is $\langle \tau_f^{-1} \rangle \sim \sqrt{\hat{q}_3/2x(1-x)E}$. One notice that the effective \hat{q}_3 is different from the \hat{q} of a daughter parton, where we perform momentum broadening. \hat{q}_3 is related to the gluon \hat{q} by the process- and x -dependent factor C_{abc} that has been defined before. For this reason, we chose the a parameter to be the color combination for each branching channel.

$$a \rightarrow a_{abc}(x) = \frac{C_A}{C_{abc}(x)} \quad (3.97)$$

From the previous theory discussion, we know that there is a logarithmic ambiguity in the cut-off scale Q_0 in \hat{q}_3 , which can be determined at the NLL level to be the same order as the branching transverse momentum. We need to address what the Q_0 scale is in the Boltzmann simulation and how to improve on that. Because the large- Q part of the elastic rescattering also uses vacuum two-body matrix-elements, the upper bound of the momentum transfer integration is cut-off by the center-of-mass energy \sqrt{s} of each independent collision,

$$s = (p_1 + p_2)^2 = 2E_1 E_2 (1 - \cos(\theta)) \quad (3.98)$$

where p_1 and p_2 are the four momenta of the hard parton and the medium parton. Since at high energy, the cross-section evolves slowly with \sqrt{s} , we can define the average \sqrt{s} by simply averaging p_2 over the thermal distribution,

$$2p_1 \frac{\int p_2^3 e^{-p_2/T} (1 - \cos \theta) dp_2 d\cos \theta}{\int p_2^2 e^{-p_2/T} dp_2 d\cos \theta} = 6ET. \quad (3.99)$$

Therefore, the average Q_0^2 from the independent transport simulation is $6ET$, compared to the NLL choice of $\sqrt{\hat{q}\omega}$. The predictions from such a simulation would systematically deviate from theory predictions in a logarithmic manner, varying energy, temperature and coupling constant. To use the correct scale, we define a scale-dependent acceptance probability to correct the naïve choice of $Q_0 \sim \sqrt{6ET}$ with a b parameter,

$$b = 0.75 \sqrt{\frac{\ln(\hat{Q}_1^2)}{\ln(\hat{Q}_0^2)}}. \quad (3.100)$$

with \hat{Q}_1^2 and \hat{Q}_0^2 given by,

$$\hat{Q}_1^2 = 1 + \frac{\sqrt{2x(1-x)E\hat{q}}}{m_D^2} \approx 1 + \frac{\tau_f}{\tilde{\lambda}} \quad (3.101)$$

$$\hat{Q}_0^2 = 1 + \frac{6ET}{m_D^2} \quad (3.102)$$

The 0.75 is a constant determined when the simulation is tuned to theoretical calculations in the next section, and it will be the same throughout the entire work. The origin of this logarithmic ambiguity comes from the perturbative large- q^2 tail the vacuum \hat{t} -channel matrix-element, based on a perturbative argument. However, if one assumes the absence of such a slowly decaying tail in q^2 , such as in non-perturbative physics motivated coupling between the hard parton and the medium, the logarithmic part in the b -parameter is not necessary.

3.4.2 Implementing mass effect

Heavy quark's large mass $M \gg T$ and unique flavor make it an excellent probe and we would like to apply the aforementioned approach to study heavy flavor as well. Of course, both the theory and the method described should only work in the limit that the parton energy is still large compared to the heavy quark mass. In the region $p \lesssim M/g$ at weak coupling, the $M/E \ll 1$ assumption breaks down and the elastic energy loss starts to dominate over radiate processes.

Considering that heavy quarks introduce a mass correction to the Fermion propagator, the most *naïve* change is to include the mass effect in both the formation time and also the few-body matrix-elements,

$$\tau_f = \frac{2x(1-x)E}{k_\perp^2} \rightarrow \frac{2x(1-x)E}{k_\perp^2 + x^2M^2} \quad (3.103)$$

and

$$\overline{|M|^2}_{2\leftrightarrow 2}(m=0) \rightarrow \overline{|M|^2}_{2\leftrightarrow 2}(m=M) \quad (3.104)$$

$$\overline{|M|^2}_{2\leftrightarrow 3}(m=0) \rightarrow \overline{|M|^2}_{2\leftrightarrow 3}(m=M) \quad (3.105)$$

For elastic scatterings, this replacement using the massive version of the two-body matrix-element is justified because subsequent elastic collisions are incoherent in the weak coupling limit. For inelastic scatterings, again the problem arises from the coherence over multiple scattering centers. At high energy, a heavy quark acquires an average transverse momentum $\hat{q}\tau_f$ larger than the typical transverse momentum of the few body matrix-element $|M|^2_{2\leftrightarrow 3}$. As a result, the mass-effect should be less important compared to the scale $\hat{q}\tau_f$ than comparing to the transverse momentum acquired from a single collision center. To solve this problem in the simulation, we choose to use the dead-cone approximation for the radiation off a heavy quark. The $2 \rightarrow 3$ and $1 \rightarrow 2$ branching of the heavy quark is sampled from the massless calculation, while the formation time is determined using the massive formula. The key change is that the acceptance probability is modified by the dead-cone factor,

$$\frac{b\lambda}{\tau_f} \rightarrow \frac{b\lambda}{\tau_f} \left(\frac{k_\perp^2}{k_\perp^2 + x^2 M^2} \right)^2. \quad (3.106)$$

Note that the k_\perp here is the branching transverse momentum after the elastic momentum broadening, and on average $\langle k_\perp^2 \rangle = \langle k_{0,\perp}^2 \rangle + \langle \tau_f \hat{q} \rangle$, where $\langle k_{0,\perp}^2 \rangle$ is the average transverse momentum sampled from the the $2 \rightarrow 3$ matrix-element. One may question the accuracy of approximating the massive version of the complicated multiple scattering matrix-element using a dead-cone approximation. We will compare the radiation spectrum off the heavy quark to the exact solution for heavy quark in the next section.

3.4.3 Implementing the running of α_s

There are two places in the transport model where the running of the strong coupling constant might be important: the coupling between the hard parton and the medium, and the coupling constant for the branching vertices. These two processes often happens at different scales.

For elastic interactions, the scale would be the \hat{t} -channel momentum transfer, the typical scale is on the order of the screening mass $|\hat{t}| \sim m_D^2$. Using leading order running of α_s $n_f = 3$ and $\Lambda = 0.2$ GeV,

$$\alpha_s(Q^2) = \frac{4\pi}{9 \ln(Q^2/\Lambda^2)} \quad (3.107)$$

the coupling constant will blow up with the scale getting close to the non-perturbative scale Λ^2 , and applying a leading order perturbative calculation to such regions is problematic. In a medium, we introduce a minimum scale in the running coupling, proportional to the temperature $Q_{\text{med}} = \mu\pi T$, to regulate the leading order running formula. Of course, regulating α_s to a finite number using such a medium scale does not necessarily improve the accuracy of using the leading order calculation in this temperature range. For example $\alpha_s(2\pi T)$ ranges from 0.28 to 0.45 ($g \sim 1.9 - 2.4$) for temperature decreasing from $T = 0.4$ GeV to T_c , which are extremely large values, considering that the next-to-leading-order correction to the probe-medium

correction is $O(g)$ ¹. Following [AD08], the elastic collision couplings are evaluated at the \hat{t} -channel momentum transfer q_\perp^2 . This involve both the α_s in the large- q matrix-element ($2 \leftrightarrow 2$, and the elastic matrix-element factorized in $2 \leftrightarrow 3$) as well as the α_s in the soft transport coefficients \hat{q}_S and $\hat{q}_{S,L}$.

Unlike the coupling between hard parton and the medium, the scale for the splitting process is much harder than the screening mass. In a static medium, this is because that splitting with a short formation time (compared to the mean-free-path) involves a large transverse momentum $k_\perp^2 > 2x(1-x)E/\lambda \sim m_D\omega/T$, while splitting with longer formation time receives multiple scattering contribution and the average k_\perp^2 scales like $\sqrt{2x(1-x)E\hat{q}} \sim m_D^2\sqrt{\omega/T}$. Therefore for splitting where both the daughter patrons are hard $xE, (1-x)E \gg T$, the running of the splitting vertex coupling is under better control than the probe-medium coupling. The running of the splitting vertex is included in the theory by changing the \hat{q}_3 in the NLL formula to its running version [AD08],

$$\hat{q}_3^{\text{running}} \approx \frac{4\pi}{9} (g^2(m_D^2) - g^2(Q_0^2)) 1.27T^3 C_{abc}(x), \quad (3.108)$$

and then evaluate the splitting α_s around an averaged scale (note that k_\perp^2 in the simulation fluctuates a lot),

$$\langle k_\perp^2 \rangle \sim m_D^2 \sqrt{E/T \ln(E/T)} \quad (3.109)$$

For transport simulations, the running of splitting vertex requires a two-step implementation. First, the α_s for the splitting vertex in the few body matrix-element is evaluated at k_\perp^2 . Next, at the end of the elastic broadening for each splitting processes, the acceptance probability is multiplied by a running coupling factor

$$p_{\text{running}} = p \times \frac{\alpha_s(k_{\perp,t_0+\tau_f}^2)}{\alpha_s(k_{\perp,t_0}^2)}. \quad (3.110)$$

Where k_{\perp,t_0}^2 is the transverse momentum when the splitting is generated from the few-body processes, while $k_{\perp,t_0+\tau_f}^2$ is the final transverse momentum including the elastic broadening, and is on average greater than k_{\perp,t_0}^2 .

3.5 Validating the modified transport approach

In this section, we compare the simulation of the “modified Boltzmann transport” to theoretical calculations introduced in the previous sections for different parton energy, coupling constants, and medium temperatures that are relevant for phenomenological applications. Such a model validation is important as it tells us whether the model is

¹As a remark, in the final model-to-data comparison, we try to parametrize the non-perturbative contribution by a diffusion processes in our model to prevent the attempt to explain the coupling to sQGP in a pure perturbative framework.

a good proxy of the underlying theory and quantifies the theoretical uncertainty when applying the model to phenomenological studies and transport parameter extraction.

We first compare the splitting rate $dR/d\omega$ that comes out of the modified Boltzmann simulation to the NLL approximation in the infinite medium limit. Then, we apply the model to a finite and expanding medium, outside of the region where this approach is designed for. Nevertheless, a good qualitative agreement with theoretical calculation of the finite size effect is achieved. In the end, the mass effect implementation is also validated.

3.5.1 In a large and static medium

In practice, to define a Monte-Carlo transport simulation in an infinite medium limit and an eikonal limit of parton propagation, an ensemble of partons of a certain species is initialized at a fixed energy E_0 and will be let to propagate in the “+z” direction. Each time when a parton scatters elastically or splits, its splitting kinematics $(\omega, k_\perp, t_0, \tau_f)$ is recorded, then the mother parton’s energy is reset back to its initial value (a test in the eikonal limit). For elastic re-scatterings in the implementation of the LPM effect, the parton’s energy is re-scaled back to the value before scatterings without changing its direction. The system is evolved for a sufficiently long time t_{\max} , and only branchings that takes place within $[t_{\min}, t_{\max}]$ are analyzed to focus on the infinite time behavior of the simulation.

We start with the $q \rightarrow q+g$ channel. The differential rate $dR/d\omega$ for a 1 TeV quark propagating through a medium of $T = 0.5\text{GeV}$ with coupling constant $\alpha_s = 0.1$ is shown in figure 3.3. The vertical axis is the differential branching rate $dR/d\omega$, and the horizontal axis is the energy of the final state gluon ω . To better understand our result, we have put three “landmark” energy scales in the upper plot, which are the initial parton energy E , an estimate of the Bethe-Heitler energy $\omega_{\text{BH}} \sim \hat{q}_g \lambda_g^2 \sim 2\pi T$, and the screening mass $m_g = m_D/\sqrt{2}$. In the LPM regime $\omega_{\text{BH}} < \omega$, the spectrum falls off as a power law with fitted exponent -1.50 (the blue dash-dotted line), and in the Bethe-Heitler regime above the screening mass $m_g < \omega < \omega_{\text{BH}}$, the fitted power law exponent is close to -1 (the green dotted line). These exponents are in good agreement with the theoretical expectation that $dR_{\text{BH}}/d\omega \propto \omega^{-1}$ and $dR_{\text{LPM}}/d\omega \propto \omega^{-3/2}$ from equations 3.72 and 3.78. The screening mass regulates the soft divergence of the spectrum below m_g . One may notice a tiny increase of the spectrum when $\omega \rightarrow E$, this is region where the gluon takes a larger fraction of the initial quark’s energy.

In the middle plot, we compare the NLL solution to directly simulated results. As a remark, we have tuned the prefactor in the b -parameter to be 0.75 by comparing to this theory prediction at $\alpha_s = 0.1$, $E = 1\text{TeV}$, $T = 0.5\text{GeV}$ for the $q \rightarrow q + g$ channel. For the rest of the comparison with different coupling, parton energy, temperature, and channels, this parameter will **not** be further tuned. The simulation agrees with the NLL solution very well when $\omega \gg \omega_{\text{BH}}$ where the formula is valid. The bottom plot shows the ratio between the simulation and the theory, a level of $\pm 10\%$ agreement in the deep-LPM region is achieved in the static case.

Next, we compare the simulation with all the three channels in figure 3.4. The

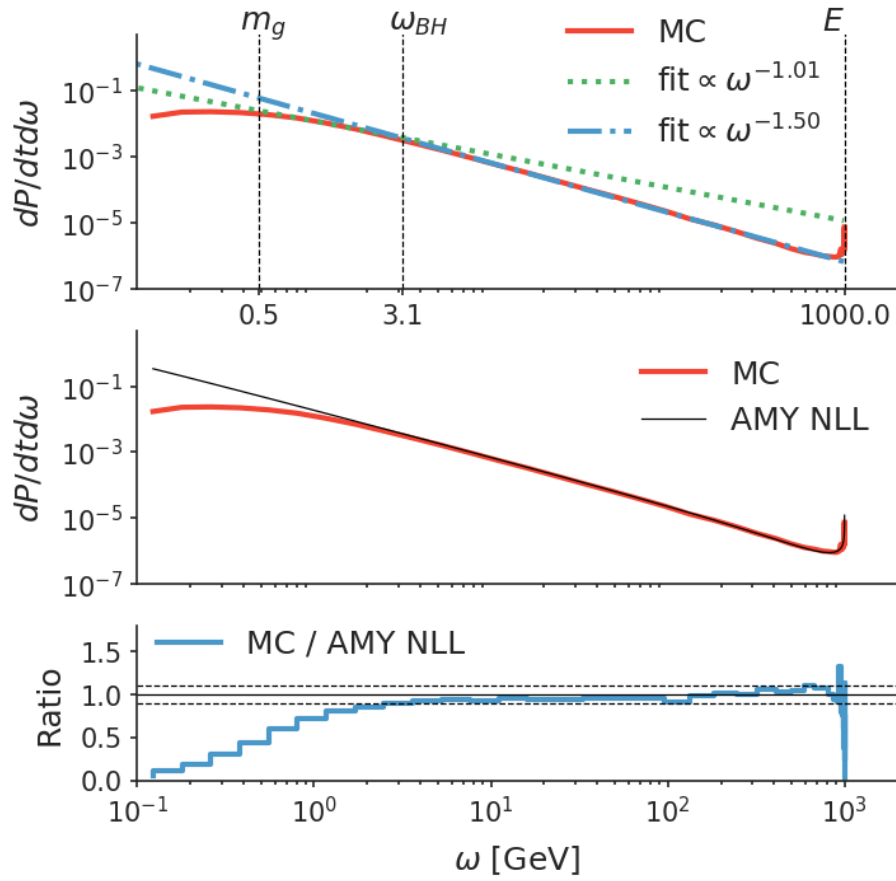


Figure 3.3: The $q \rightarrow q + g$ splitting rate simulated in an infinite box with $T = 0.5$ GeV. The quark energy is $E = 1$ TeV. $\alpha_s = 0.1$. In the top plot, the spectrum $dR/d\omega$ (red line) is fitted to a power function ω^λ in different gluon energy regions. The green dashed line is fitted in the Bethe-Heitler region $\omega < \omega_{BH} \approx 2\pi T$; the blue dash-dotted line is fitted in the LPM region $\omega > \omega_{BH}$. The middle plot compares to the simulation to NLL solution to the AMY equation, and their ratio is shown in the bottom plot

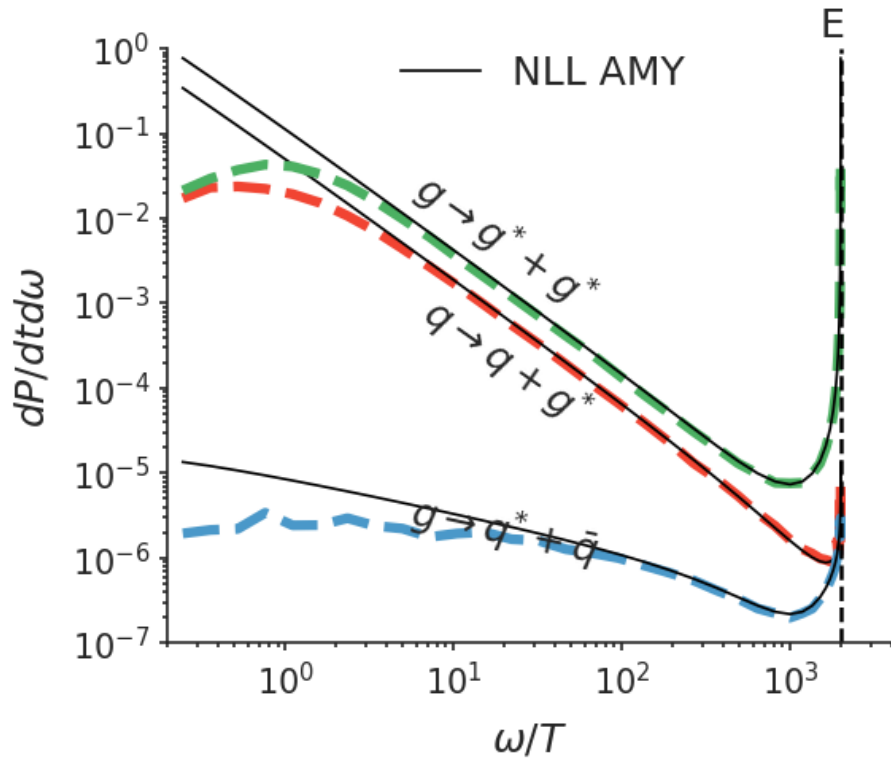


Figure 3.4: The rate of different channels $q \rightarrow q + g^*$, $g \rightarrow g + g^*$, and $g \rightarrow q^* + \bar{q}$ are plotted as functions of the daughter (labeled by "*" parton energy. The mother parton has a energy $E = 1$ TeV. The medium temperature is $T = 0.5$ GeV. $\alpha_s = 0.1$. The simulations (thick dashed lines) are compared to the NLL solutions (thin solid lines).

setup is the same as the figure 3.3. The red, green and blue lines correspond to the differential branching rate of processes $q \rightarrow q + g^*$, $g \rightarrow g^* + g^*$ and $g \rightarrow q^* + \bar{q}$; the thin black lines are the NLL solution to the AMY equation. The “ $*$ ” sign denotes the final state parton whose energy is ω . For the case of two final state gluons, both are taken into account in the simulation as they are identical particles. We have discussed the feature for the $q \rightarrow q + g$ process in the previous paragraph. The spectral shape of the $g \rightarrow g + g$ process is very similar to the quark splitting channel in the range $\omega \ll E$, with a higher value. The rate is symmetric with respect to $\omega = E/2$ due to its symmetric final states (though it is hard to tell from this double-log plot), so at large ω , the rate goes up again. The spectrum of $g \rightarrow q + \bar{q}$ is also symmetric with respect to $\omega = E/2$, though its final state consists of two different particle, but the splitting function is symmetric. We see that the simulation achieves a good agreement with the NLL solution in the deep-LPM region $\omega/T > 10$.

Next, we validate the simulation for different values of the coupling constant and parton energies. We choose both a relative small coupling $\alpha_s = 0.1$ ($g \approx 1.1$) and a value closer to the phenomenology coupling $\alpha_s = 0.3$ ($g \approx 1.9$), and vary the energy from 10, 10^2 , to 10^3 GeV. The ratios between the simulation and the NLL solutions are shown in figure 3.5, 3.6 and 3.7. From these systematic comparisons, one sees that the simulation reproduces the correct scaling in the LPM region, although this region shrinks due to the decrease of the parton energy. The overall performance of the modified Boltzmann transport in describing the inelastic processes in a large medium is good and under control. One remaining problem is that the systematic deviation for the $g \rightarrow q + \bar{q}$ channel is bigger than the other two channels, as we did not include the backward region in its $2 \rightarrow 3$ matrix-elements.

Finally, we validate the running coupling calculation in Fig. 3.8 using the $g \rightarrow g + g$ channel. The theory curves (black lines) are obtained combining Eq. 3.78 and Eq. 3.108. Different line styles correspond to the variation of the Q_0 value around an initial guess $m_D(E/T \ln(E/T))^{1/4}$ by a factor of 2 above and below. For this 1 TeV parton, the scale Q_0 is actually very large and the running of α_s is rather slow, which explains why the theory curve is not very sensitive to a factor of 4 change in Q_0 . The simulation was performed using the running coupling prescription described in section 3.4. The overall shape of the spectrum in the deep LPM region is again well described by the modified Boltzmann simulation.

3.5.2 Branching in a finite / expanding medium

We have made clear before that this approach is designed for interpolating between the Bethe-Heitler region and the deep-LPM region in a large medium, and looking at validation in the previous section, it indeed works very well. However, the medium created in heavy-ion collisions is never in the large and static limit, its finite life time and spatial extension, local hot spot fluctuations and the fast radial expansion can all have a significant impact on the hard parton propagation. Therefore, we need to investigate how our approach would behave in a few more complex scenarios: a finite medium and expanding medium, before applying the model to realistic phenomeno-

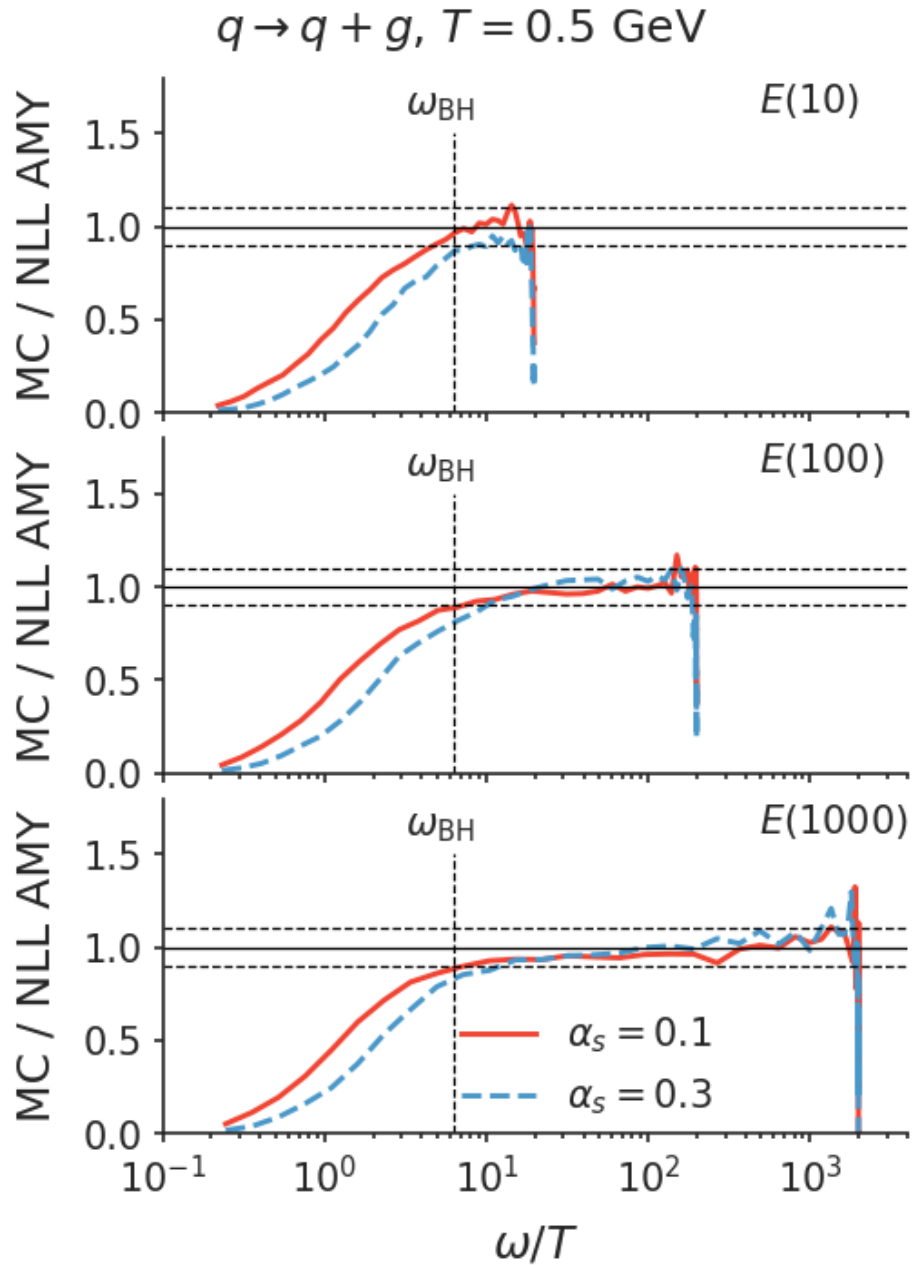


Figure 3.5: Ratios of splitting rate dR/ω between the modified Boltzmann simulation and the NLL solution for $q \rightarrow q + g$ splitting. The quark energies E is 10, 100, and 1000 GeV from top to the bottom plot. And two coupling constants are used: $\alpha_s = 0.1$ (red solid lines) and $\alpha_s = 0.3$ (blue dashed lines). ω stands for the gluon energy. The horizontal dashed lines denote $\pm 10\%$ deviation from unity.

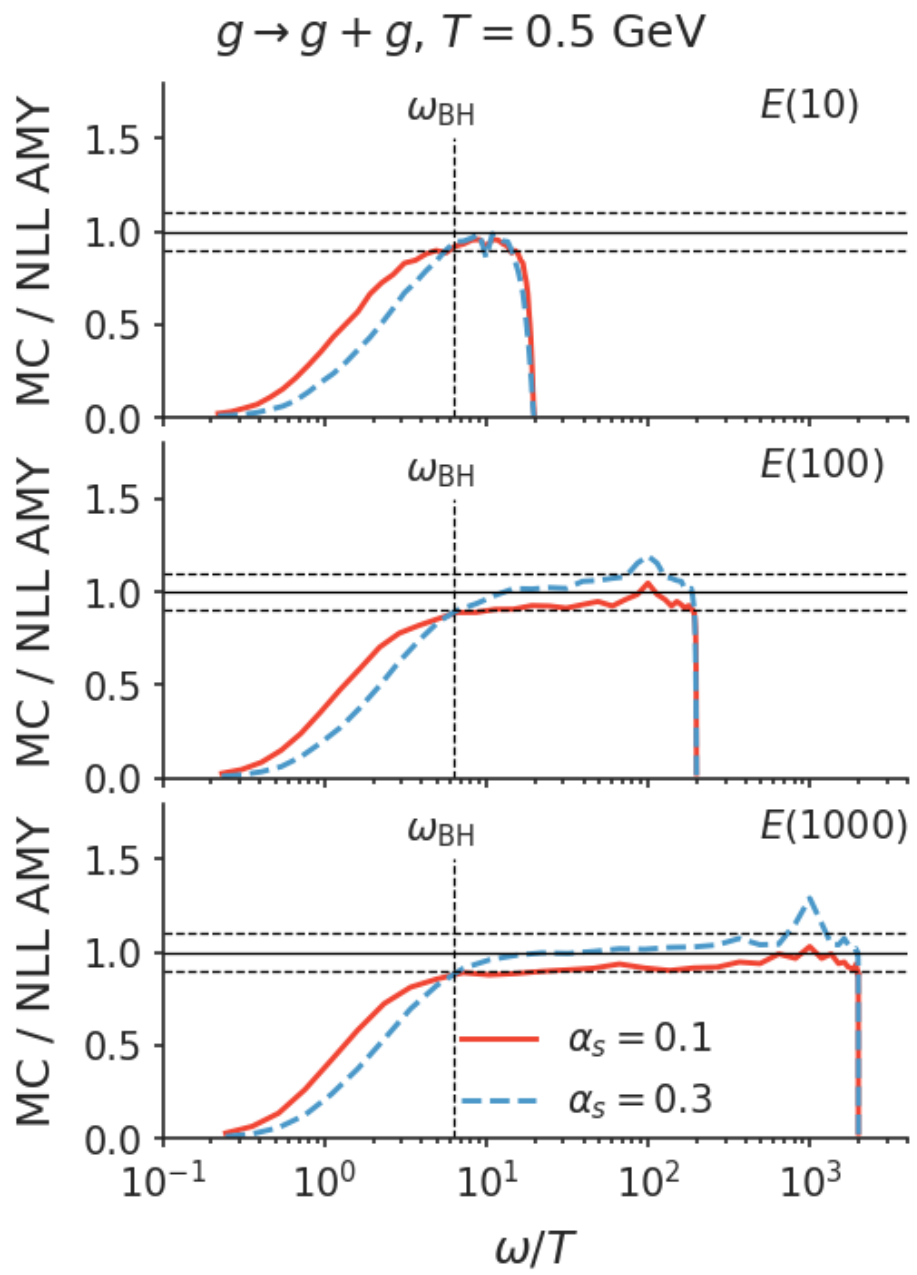


Figure 3.6: The same as figure 3.5, but $g \rightarrow g + g$.

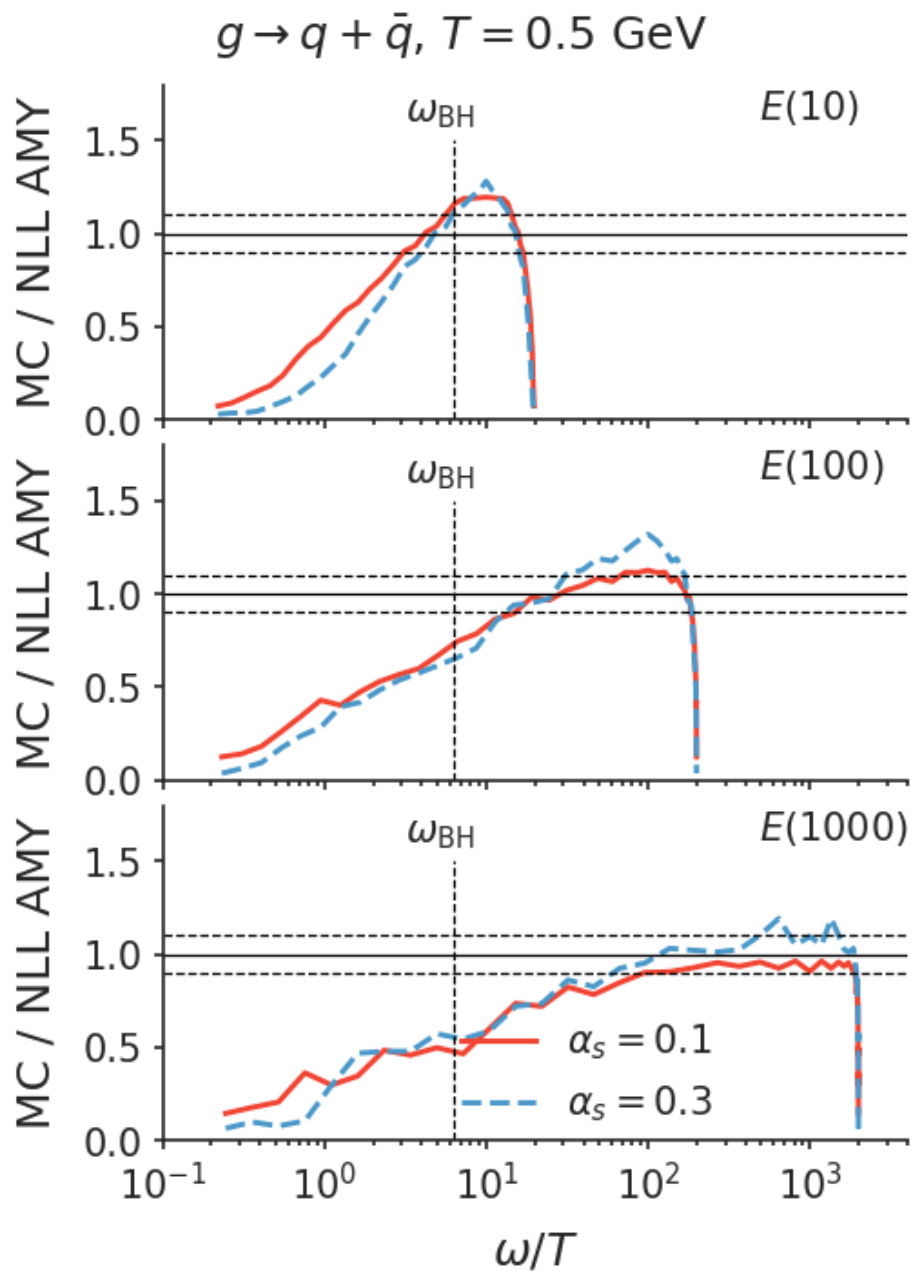


Figure 3.7: The same as figure 3.5, but $g \rightarrow q + \bar{q}$.

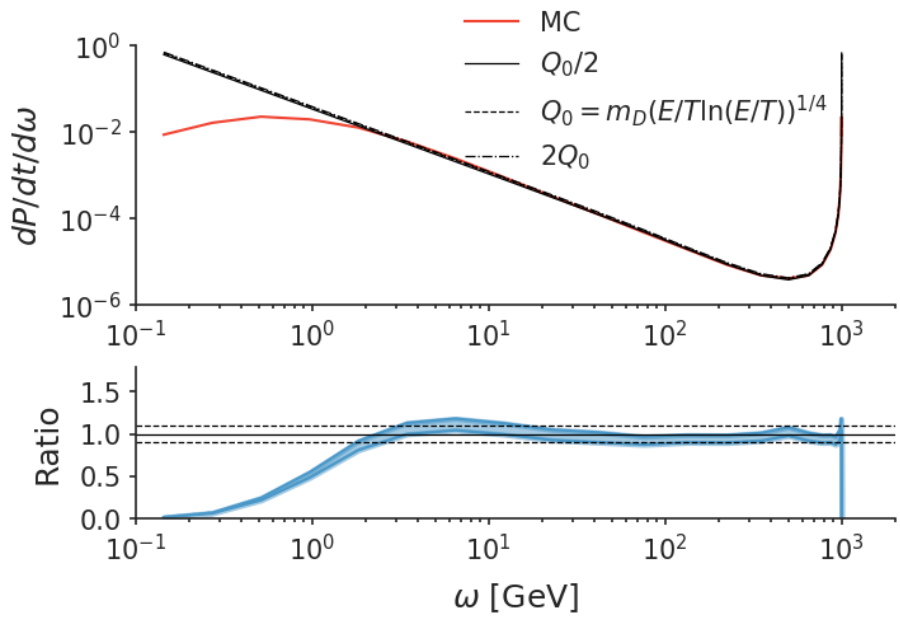


Figure 3.8: Comparing the simulation with running coupling constant the NLL solution with running α_s prescription. The scale Q in the emission vertex and in the theoretical formula for the effective transport parameter \hat{q}_3 (equation 3.108) is chosen to be $1/2$, 1 and 2 times of the scale $\sqrt{\langle k_\perp^2 \rangle}$ in equation 3.109. The ratio is shown in the bottom plot.

logical scenarios.

A semi-infinite medium Consider a semi-infinite medium with a static temperature profile,

$$T = \begin{cases} 0, & z < 0 \\ T_0, & z > 0 \end{cases} \quad (3.111)$$

with hard partons being created at $z = 0$ and propagating into the medium. Deep inside the medium, the medium induced radiation should be asymptotically close to the calculation in an infinite medium. At the boundary, there is a complicated interference between medium scatterings centers and the hard production vertex. For a thin medium where the path length is short compared to the formation time, these interference terms can be worked out in the “opacity expansion”, or by analyzing the propagator G with a semi-infinite temperature profile. This boundary effect results in a path length dependence of the medium induced branching rate that starts from zero at $t = 0$ and gradually approaches the asymptotic value in a large medium. The resulting parton energy loss rate is significantly reduced due to this effect: it scales quadratic with the path length $\Delta E \propto L^2$ near the boundary; while it transits to $\Delta E \propto L$ deep inside the medium.

It is true that our approach is designed for a large medium, but it also displays certain finite size effect. Remember that the branchings in the modified transport approach take a finite amount of time, and those branchings that become independent at time t are actually initiated by a $2 \rightarrow 3$ processes from a wide range of scattering centers in the past $t' = t - \tau_f$. Therefore, if the medium is semi-infinite, and there were no scattering centers before $t' = t - \tau_f < 0$, then the medium-induced contribution to the branchings at time t will be reduced. This reduction gets weaker and weaker when the condition $t - \tau_f > 0$ can be satisfied by more and more induced branchings and eventually, when $t \gg \langle \tau_f \rangle$, this boundary effect dies off in the simulation. Of course, we cannot achieve full quantitative agreement with the theory at $L \lesssim \tau_f$ since the interference pattern is not implemented. We would like to investigate if our simulation of the boundary effect can qualitatively mimic the interference physics that happens near the boundary.

In Figure 3.9, the differential rate obtained from simulation is compared to the numerical solution of the full leading order calculation for a finite medium. The horizontal axis is the time of travel by the hard parton (path length divided by the speed of light), and each subplot shows how the branching rate changes as a function of time with different medium temperatures ($T = 0.2$ GeV on the left, $T = 0.5$ GeV on the right) and for different branching parton energy ($\omega = 3$ GeV at the top, $\omega = 8$ GeV at the bottom). The theory curves are taken from reference [CHG10] for a 16 GeV parton with coupling constant $\alpha_s = 0.3$, and the red lines are our simulation. The theory curve first increases linearly and then turn over to a constant value in the large medium limit for $t \gg \sqrt{2x(1-x)E/\hat{q}_3}$. The simulation, as expected, reproduces the large time limit of the rate. Moreover, we find that the current implementation

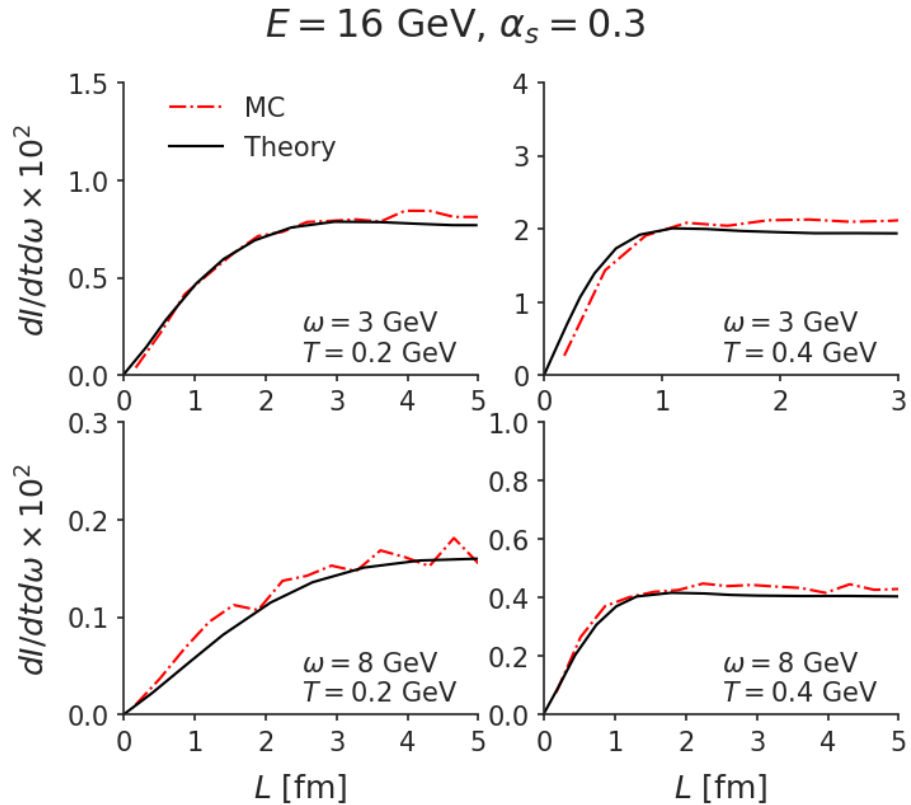


Figure 3.9: The path-length dependence of the simulated $q \rightarrow q + g$ emission rate $dR/d\omega$ compared to the direction calculation of formula 3.90 from [CHG10]. $\alpha_s = 0.3$. The quark energy is 16 GeV. The left and right columns have medium temperature $T = 0.2$ and 0.4 GeV respectively. The top and bottom rows show the differential rate at $\omega = 3$ and 8 GeV.

also predicts the qualitative ‘‘turn over’’ of the spectra at finite path length. The original paper only published this calculation for a 16 GeV quark. To validate if this qualitative agreement also holds at higher parton energies, we implemented the numerical approach of [CHG10] and compute the theoretical curves for $E = 100$ GeV partons. The comparison between simulation and numerical solutions are shown in figure 3.10 and again, we find qualitative agreement with the theoretical finite size effect.

An expanding medium Fast radial expansion is another important feature of the medium in heavy-ion collisions. It causes the temperature to decrease drastically in the early stages of the expansion and introduces another time scale in which the medium temperature changes notably. Assume a simplified power-law changing temperature profile

$$T(\tau; \nu)^3 = T_0^3 \left(\frac{\tau_0}{\tau} \right)^{2-1/\nu}. \quad (3.112)$$

The ν parameter controls the rate of expansion. $\nu = 1/2$ is the static medium limit, and $\nu = 1$ is the Bjorken flow. We can define the following medium expansion time, over which the transport parameter changes significantly,

$$\tau_{\text{ex}} = \left(\frac{d \ln(T^3)}{d\tau} \right)^{-1} = \frac{\tau}{2 - 1/\nu}. \quad (3.113)$$

The larger the ν parameter is, the smaller the expansion time scale. With $\tau_0 \sim 1$ fm/c, the expansion time scale can be short enough that energetic branchings already probe the changing temperature profiles within their formation time $\tau_f > \tau_{\text{ex}}$. One consequence of this fast changing of temperature is that, for these branchings $\tau_f > \tau_{\text{ex}}$, the transition probability over a finite amount of time can not be well approximated by integrating rates that are calculated in an infinite box defined by the local temperature,

$$\frac{dP(t_1, t_2)}{d\omega} \neq \int_{t_1}^{t_2} \frac{dR_\infty(T(t))}{d\omega} dt, \quad (3.114)$$

where the rate R_∞ is obtained by solving the branching rate in the infinite medium setup. This approach is employed in transport models like MARTINI and TEQULIA [JM05, SGJ09, DBPT19]. Our approach takes the change of the medium temperature (and also flow velocity) into account. This is because the rescattering procedure that determines amount of suppression is performed along the trajectory of the hard partons and therefore naturally includes the effect of the cooling of the medium. The typical formation time determined by the rescattering procedure is also changed by the expansion. Recall that in a static medium the dimensionless combination that enters the leading-log formula is $t/\tau_f \sim t\sqrt{\omega/\hat{q}}$, but with a \hat{q} that is decreasing with temperature. The self-consistent determination of the formation time requires the

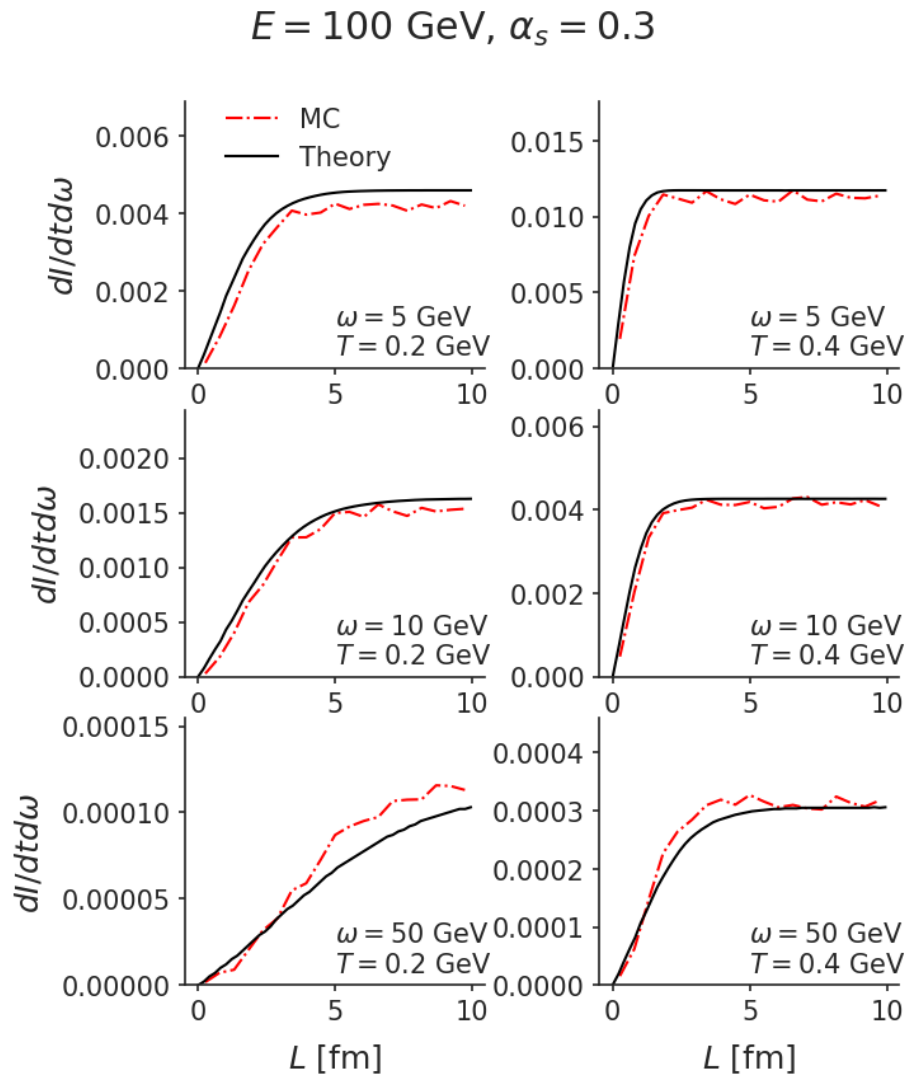


Figure 3.10: The same as figure 3.10, but the initial quark energy is 100 GeV, and is plotted for gluon at 5 (top), 10 (middle) and 50 (bottom) GeV.

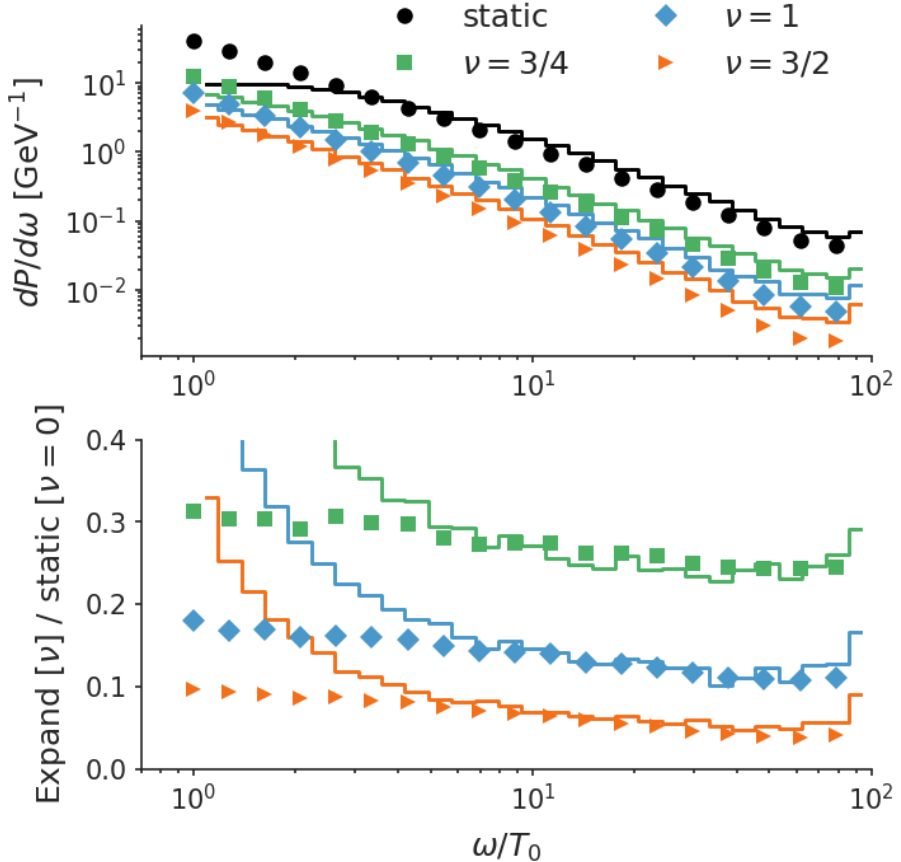


Figure 3.11: Top plot: the simulated spectrum (diffusion plus diffusion-induced radiation only) using the parametric medium with expansion parameters $\nu = 0$ (static, black), $3/4$ (green), 1 (Bjorken, blue), and $3/2$ (orange). The analytic results are shown in symbols and simulations in lines. $\alpha_s = 0.3$. The expansion starts at $\tau_0 = 0.2$ fm/c with an initial temperature $T_0 = 1$ GeV. Bottom plot: the ratios between calculation (simulation) in an expanding medium to that in the static medium.

following relation to hold on average,

$$t_2 - t_1 = \frac{2x(1-x)E}{k_\perp^2(t_1) + \int_{t_0}^t \hat{q}(\tau) d\tau}, \quad (3.115)$$

$$\hat{q}(\tau) = \hat{q}(\tau_0) \left(\frac{\tau_0}{\tau} \right)^{2-1/\nu} \quad (3.116)$$

Comparing to theoretical calculations, we utilize a result obtained in the BDMPS framework [BDM⁺97b, BDMS98]. Using the power-law decreasing temperature pro-

file, the obtained branching probability for the $q \rightarrow q + g$ splitting is [BDMS98],

$$\frac{dP}{d\omega} = \frac{\alpha_s}{2\pi E} P_{q \rightarrow qg}(x) \Re e \int_{\tau_0}^{\tau_0+L} \frac{dt_f}{t_f} \int_{\tau_0}^{t_f} \frac{dt_i}{t_i} \frac{1}{\nu^2} [I_{\nu-1}(z_i)K_{\nu-1}(z_f) - I_{\nu-1}(z_f)K_{\nu-1}(z_i)]^{-2} \Big|_{\omega=xE}^{\omega=\infty}, \quad (3.117)$$

$$z_{i,f} = 2i\nu \sqrt{\frac{\hat{q}_g(1-x+C_F/C_A x^2)}{2(1-x)\omega}} \tau_0 \left(\frac{t_{i,f}}{\tau_0}\right)^{1/2\nu}. \quad (3.118)$$

This result recovers the static BDMPS result [BDM⁺97b] when $\nu = 1/2$. One potential problem of comparing the formula to our simulation is that this BDMPS calculation works in the multiple-soft limit (leading log). Therefore, we used only the diffusion-induced radiation in the simulation and deactivate the large- Q $2 \rightarrow 3$ scattering part. Also as mentioned before, in the absence of the perturbative tail in the collision kernel, $b = 0.75$ is used without the logarithmic correcting factor in equation 3.100. In addition, we will not try to make a direct comparison to the spectra (top of figure 3.11), but focus more on the ratio between the expanding calculation/simulation over the static calculation/simulation instead (bottom of figure 3.11). This ratio reflects the change of the shape of the spectra due to the dropping of the temperature.

The simulation uses a medium with initial temperature $T_0 = 1$ GeV at $\tau_0 = 0.2$ fm/c and lasts until $\tau = 20$ fm/c using four different expansion rates $\nu = 1/2, 3/4, 1, 3/2$. These choices correspond to a static medium, a slowly expanding medium, Bjorken flow, and a faster-than-Bjorken expansion. We find that when $\omega \gg T_0$, the degree of change in the radiation spectra is well reproduced by the modified transport simulations.

3.5.3 Heavy quarks and thermalization test

Finally, we check the model performance for heavy quarks. The theory curves are obtained by solving the exact equation with a effective mass term,

$$m_{\text{eff}}^2 = (1-x)m_g^2 + x^2 M^2 \quad (3.119)$$

which includes both the thermal mass of the gluon and the current mass of the heavy quark. We present the comparison between the simulation and the theory in terms of the ratio between the differential branching rate of the heavy quark (charm mass at 1.3 GeV, bottom mass at 4.2 GeV) and the light quark. In figure 3.12 for the bottom quark case, the horizontal axis is the path-length, and the vertical axis is the ratio. Different rows have different radiated gluon energies, and different columns has medium temperatures at 0.2 GeV (left) and at 0.4 GeV (right) respectively. The initial bottom quark energy is 100 GeV and the coupling is $\alpha_s = 0.3$. We see that the dead-cone approximation agrees better with the theory calculation at larger x and larger path-length. Deviations observed at small path length are understood as the limitation of our implementation to the large medium, and should be better treated by

$$E = 100 \text{ GeV}, \alpha_s = 0.3$$

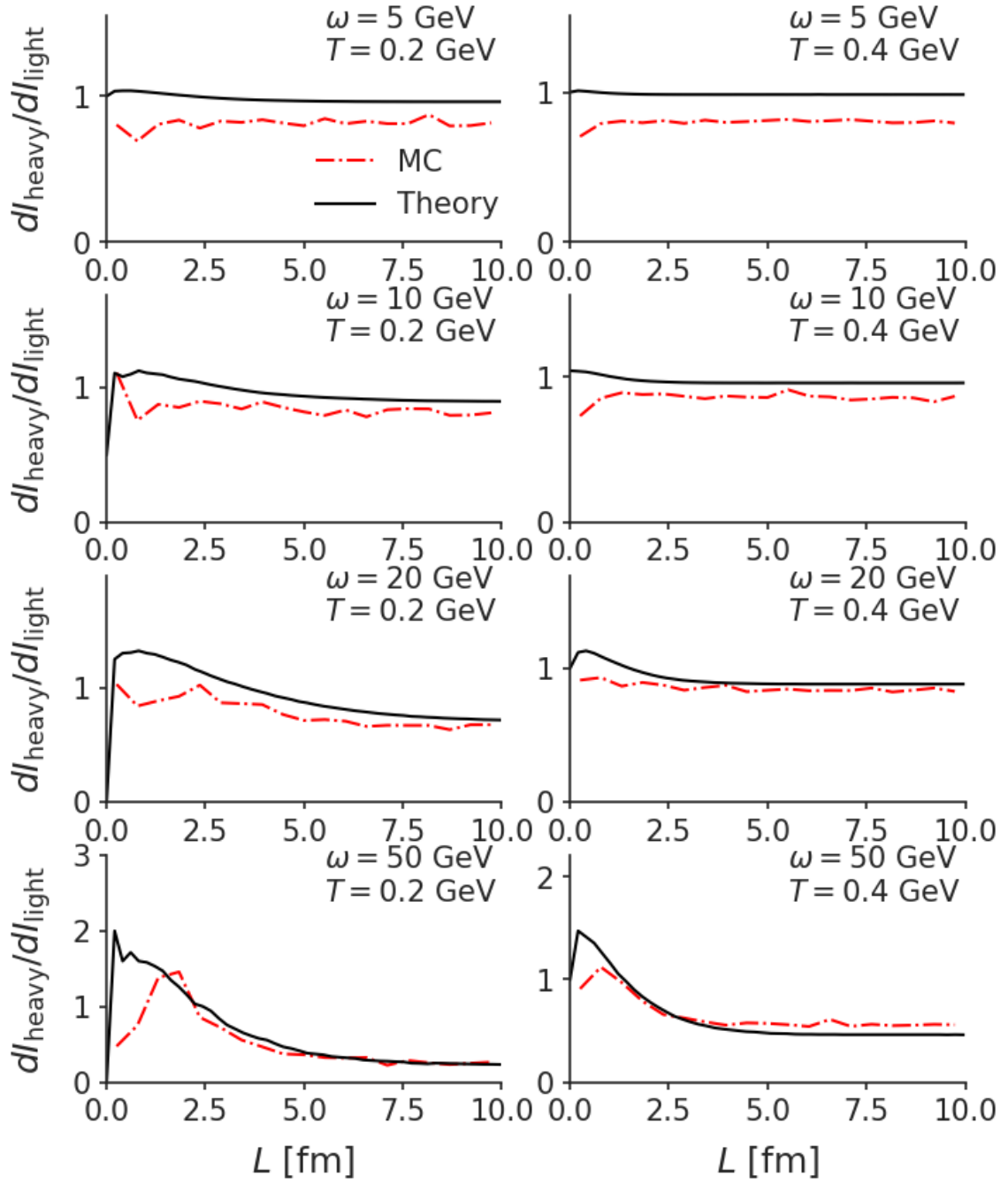


Figure 3.12: The mass dependence of the radiation spectrum $q \rightarrow q + g$, presented as the ratio of bottom $dR/d\omega$ over the light quark $dR/d\omega$, as functions of path length. The left and right columns use temperatures 0.2 and 0.4 GeV. Different rows (from top to bottom) plot cases for gluon energy $\omega = 5, 10, 20, 50$ (GeV).

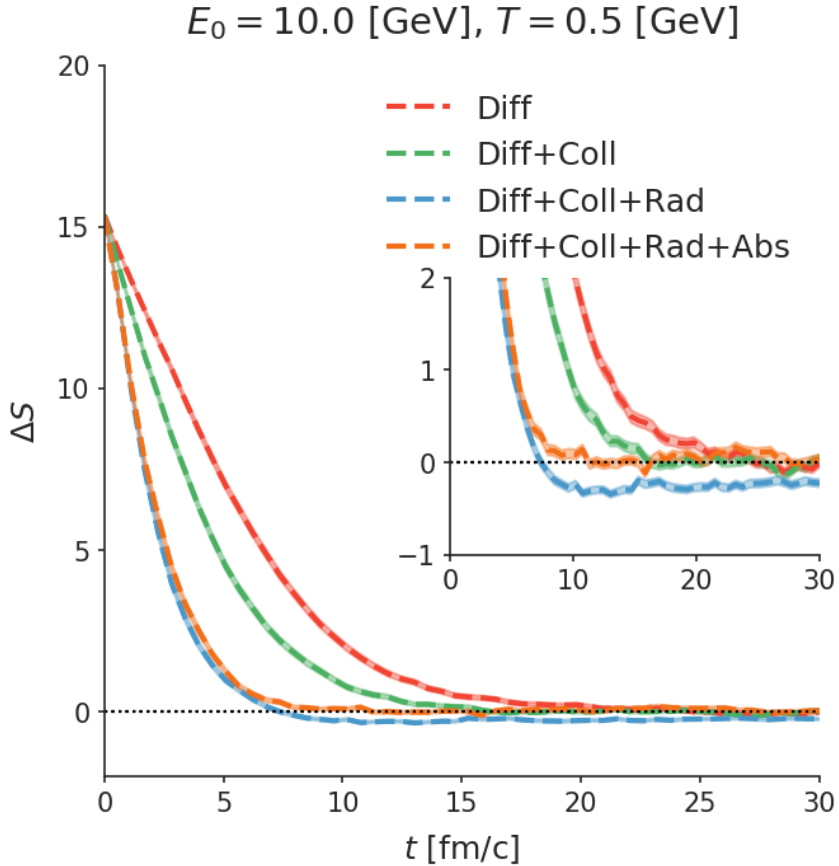


Figure 3.13: The approach to thermal equilibrium for heavy flavor is quantified as the change of ΔS (defined in equation 3.121) as function of time.. The red dotted lines includes elastic processes only. The green dashed line further includes $2 \rightarrow 3$ and $1 \rightarrow 2$ processes. The blue solid lines turn on the detailed balance processes $3 \rightarrow 2$ and $2 \rightarrow 1$.

the opacity expansion. The deviation at small x is interesting, particularly, since the theory almost predicts an identical heavy quark radiation spectra as the light quark. This absence of a dead cone at small- x is already observed in early works studying heavy quark energy loss in both the opacity expansion and the BDMPS framework [ASW04]. This means that the treatment of the mass effect is not as simple as the dead-cone approximation and should be improved in the future.

Thermalization of heavy quarks Due to a heavy quark's large mass, it takes a longer time to thermalize and the low- p_T end of the heavy quark production in the heavy-ion collisions can carry information on non-equilibrium dynamics. To extract the degrees of thermalization, one has to make sure the correct thermal limit is achieved in the transport model, given sufficient time. This is trivial for large-angle elastic scatterings and diffusion processes as long as the correct Einstein relation is

imposed. The $n \rightarrow n + 1$ body radiative process is approximated by an initial $2 \rightarrow 3$ or $1 \rightarrow 2$ process and a sequence of elastic interactions; therefore, in principle the $n + 1 \rightarrow n$ absorption processes need to be treated on the same footing to restore the detailed-balance in the modified-Boltzmann equation. This can be done but is overly complicated. Here we argue that close to a few times of temperature, the LPM effect is not that strong and an incoherent implementation of the absorption is enough to study the bulk of particles close to thermal distribution.

We define a quantity ΔS to measure the approach to thermal distribution $f_0 = e^{-E/T}$ for an ensemble of heavy quarks,

$$\Delta S = -\langle \ln f_0 \rangle - S_0 \quad (3.120)$$

$$= -\frac{1}{N} \sum_i \ln f_0(E_i) - \frac{\int dp^3 f_0 \ln(f_0)}{\int dp^3 f_0} \quad (3.121)$$

Where the first term is the ensemble average of the function $-\ln f_0$, and the subtracted term is proportional to the entropy of distribution f_0 . Note that the quantity is zero if the ensemble is thermalized. If the system is approaching a thermal distribution with an effective temperature such that $f = e^{-E/T'}$, then ΔS is

$$\Delta S = \frac{\int dp^3 E/T e^{-E/T'}}{\int dp^3 e^{-E/T'}} - S_0 = \frac{T' - T}{T} \quad (3.122)$$

which is a measure of the deviation of the effective temperature from the thermal bath temperature.

Using this definition, we plot ΔS as a function of time for 1000 heavy quark that are initialized at 10 GeV. The temperature of the thermal bath is 0.5 GeV and we used a fixed $\alpha_s = 0.3$. Under the influence of diffusion (red) and diffusion plus large-angle elastic collisions (green), ΔS decreases from a large value until fluctuating around zero after 25 fm/c (red) and 15 fm/c (green). Now, adding the radiative processes (blue), ΔS reaches a value below zero, which is a false equilibrium. Only after the balancing processes of parton absorption are also included (orange), the correct thermal equilibrium limit is restored. We also found that the absorption process only sets in when the ensemble is close enough to the thermal distribution, as the blue line and the orange line are almost overlapping until ΔS drops to 0.3. This is because the absorbed gluon follows the thermal distribution in the medium while phase-space for a high energy parton $E \gg T$ to absorb a low energy gluon is very limited $x < T/E$, compared to radiation processes where the value of x is not restricted by the Boltzmann factor $e^{-xE/T}$.

3.6 Comments on two other inelastic process implementations

I find it beneficial to discuss two other inelastic process implementations for the reader's reference. They are termed as the "coherence factor" approach and the

“blocking radiation” approach. I have used the previous approach in my earlier studies [KXB18], but it is the problems I encountered in this method that later motivated the development of the “modified Boltzmann transport” method. I shall show in this section that in the deep-LPM region, the “coherence factor” approach still qualitatively agrees with the power counting of the LPM suppression λ_{el}/τ_f , though it only includes the effect of one medium scattering center and the method can be logarithmically dependent on the infrared cut-off. The “blocking radiation” approach, however, does not reproduce the power counting of the LPM suppression. These two approaches, together with the “modified Boltzmann” approach will be compared later using the “energy loss” of a fixed energy quark. First, we introduce these two approaches.

3.6.1 The coherence factor approach

This approach is first implemented in the improved Langevin equation [CQB13a], using the single medium-induced radiation probability from the higher-twist calculation [Maj12, WG01] and a prescription for multiple emissions. The higher-twist formula of medium-induced radiation is derived for a high virtuality parton, including the interference of the hard production vertex and one medium scattering center. The single radiation rate reads,

$$\frac{dN_g}{dx dk_\perp^2 dt} = \frac{\alpha_s P(x) \hat{q}_g}{\pi k_\perp^4} 2 \left(1 - \cos \frac{t - t_0}{\tau_f} \right), \quad \tau_f = \frac{2x(1-x)E}{k_\perp^2} \quad (3.123)$$

Here the radiation rate is time-dependent (t) due to the interference with the hard production at time t_i . Note that the interference factor cancels the collinear divergence. The only divergence comes from soft emission $x \rightarrow 0$. This divergence is not a problem for computing more physical quantities such as the energy loss, as it will be balanced by gluon absorption processes. However, in order to apply the rate formulation, an infrared cut-off $x > x_c$ has to be introduced.

The advantage is that if there is only one radiation, then sampling of the time dependent rate indeed reproduces the higher-twist calculation. However, the ambiguity arises from the way it handles multiple emissions. For example, one can compute the average number of emission by integrating this formula along the trajectory of the hard parton and then samples the fluctuating number of emissions with a Poisson distribution. But of course, this would assume the parton energy is not significantly changed during the process, and it is not clear how the presence of more than one scattering center would change this picture. Here we would like to discuss another method in dealing with multiple emission using the higher-twist formula in a time evolution manner [CQB13a]. The algorithm goes as follows:

1. Choose an infrared cut-off for the gluon energy $x_c \propto T/E$, and a small enough time step Δt , so that the average number of emissions is much smaller than 1 to suppress multiple emissions within Δt ,

$$\langle N_g \rangle = \Delta t \int_{x_c}^1 dx \int dk_\perp^2 \frac{dN_g(t - t_0)}{dx dk_\perp^2 dt} \ll 1. \quad (3.124)$$

2. Sample N according to a Poisson distribution with $\langle N_g \rangle$. For $\langle N_g \rangle \ll 1$, it is sufficient to sample the two leading cases of $N = 0, 1$, as the probability to have more than 1 emission is negligible ($P_{N>2} = 1 - e^{-\langle N_g \rangle} - e^{-\langle N_g \rangle}/\langle N_g \rangle = O(\langle N_g \rangle^2) \ll P_1 \ll P_0$).
3. If $N = 0$ then propagate the parton to the $t + \Delta t$. If $N = 1$, then sample the emission gluon's x , and \vec{k}_\perp by the differential rate. *Meanwhile, t_0 is set to t* , so that the next emission's probability will be accumulated from zero again.
4. Proceed to the next time step.

We found that the key step here is resetting the clock $t_0 = t$ for the parton after every emission. As a result, from the second emission onwards, the $t - t_0$ that appears in the interference factor is measuring the time difference between two medium scattering centers. Therefore, we will not interpret this procedure as the higher-twist rate (interference between initial hard vertex and one medium collision center) starting from the second emission; instead we understand it as an ansatz, from the second emission onwards, to treat medium-induced emission in a large medium, as it does not require any information on the production vertex.

Considering that it only includes one medium scattering center in the trigger of the radiation, one wonders if this approach reproduces any in-medium radiation features predicted by theory. It is not immediately clear what this iterative procedure predicts unless one performs explicit simulations. To make a process, by pondering on the meaning of the “clock resetting” step, we find that the typical $\Delta = t - t_0$ between two emissions is a time scale within which the emission probability reaches order one,

$$1 \sim \int_{t_0}^t dt \int_{x_c}^1 dx \int dk_\perp^2 \frac{dN_g(t - t_0)}{dx dk_\perp^2 dt}. \quad (3.125)$$

With this key observation, after a few step of algebra, we are able to isolate the qualitative features of this approach. Taking the soft approximation $P(x) \sim 2/x$, $\tau_f \sim 2xE/k_\perp^2$, and performing the time integral first, then the k_\perp integral with limits from 0 to xE .

$$1 \sim 4\alpha_s \hat{q} \Delta t \int_{x_c}^1 \frac{dx}{x} \int \frac{dk_\perp^2}{k_\perp^4} \left(1 - \frac{\sin(\Delta t/\tau_f)}{\Delta t/\tau_f} \right) \quad (3.126)$$

$$= \alpha_s \hat{q}_g \Delta t^3 \int_{\frac{\Delta t E x_c}{2}}^{\frac{\Delta t E}{2}} \frac{du}{u^2} \frac{u^2 \text{Si}(u) - 2u + \sin(u) + u \cos(u)}{u^2} \quad (3.127)$$

$$= \frac{\alpha_s \hat{q}_g \Delta t^3}{3u^3} \left(u^3 \text{Ci}(u) - 3u^2 \text{Si}(u) \right. \quad (3.128)$$

$$\left. - u^2 \sin(u) + 3u - \sin(u) - 2u \cos(u) \right|_{\frac{\Delta t E x_c}{2}}^{\frac{\Delta t E}{2}}$$

This final integral of x (reparametrized by $u = xE\Delta t/2$) would have been logarithmic divergent if we had not cut it at x_c at the lower bound. The result has the following

expansion at small u : $\frac{1}{18}(6\ln(u) + 6\gamma_E - 17)$ and decays to 0 at infinity. A good proxy is therefore to use the small- u expansion but cut-off the upper bound of u at its zero, finally

$$1 \sim \frac{\alpha_s \hat{q} \Delta t^3}{3} \ln \frac{2}{x_c E \Delta t} \propto (g^2 T \Delta t)^3 \ln \frac{2}{x_c E \Delta t} \quad (3.129)$$

Now, it is clear that this procedure of implementing multiple emission inside the medium resets the clock in the interference factor every $1/g^2 T$ up to a certain logarithm dependence on the infrared cut-off, which is the order of the elastic collision mean-free-path. Put this estimated Δt back into the interference factor $2(1 - \cos(\Delta t/\tau_f))$, one indeed finds that the radiation spectrum will be strongly suppressed if the formation time is much greater than $\Delta t \sim \lambda_{el}$.

This suppression certainly mimics some property of the in-medium LPM effect, but is introduced by a very different mechanism. Recall that the LPM effect is the suppression of the single particle emission rate through multiple collisions with the medium, without any information about how subsequent emissions are correlated. While the interference factor approach mimics the effect of the LPM suppression through correlation between subsequent emissions. This will introduce several problems:

1. The correlation between subsequent emissions is in fact physics beyond leading order and requires new types of diagrams to be computed.
2. As we have seen, this procedure is affected by the choice of the infrared cut-off. Though its dependence is very weak, it is still a dependence that we try to avoid.

3.6.2 The “blocking radiation” approach

This is another approach we found in the literature [CSM12]. I would like to show that this approach is more problematic than the previous one, because it suppresses radiation with $\tau_f > \lambda_{inel}^{incoh}$ but not $\tau_f > \lambda_{el}$.

In this approach, the splitting is also first generated through an incoherent processes at time t_0 , and then the self-consistently determination the formation time by elastic broadening. But its LPM suppression is introduced by requiring that no other radiation is allowed from this radiator within the time from t_0 to $t_0 + \tau_f$. This clearly introduces a correlation between subsequent emission, while the LPM effect concerns only the one particle emission rate. While in our approach, the suppression is implemented by accepting the process with probability $\sim \lambda_{el}/\tau_f$, and more importantly, other emissions are unaffected by the current “imaginary splitting” as most of them would be rejected without causing any physical effect.

A closer investigation reveals bigger problems. This “blocking radiation” approach effectively reduces every τ_f/λ_{inel} incoherent emission to one, resulting only in an overall reduction of the radiation spectrum without changing its shape. And the

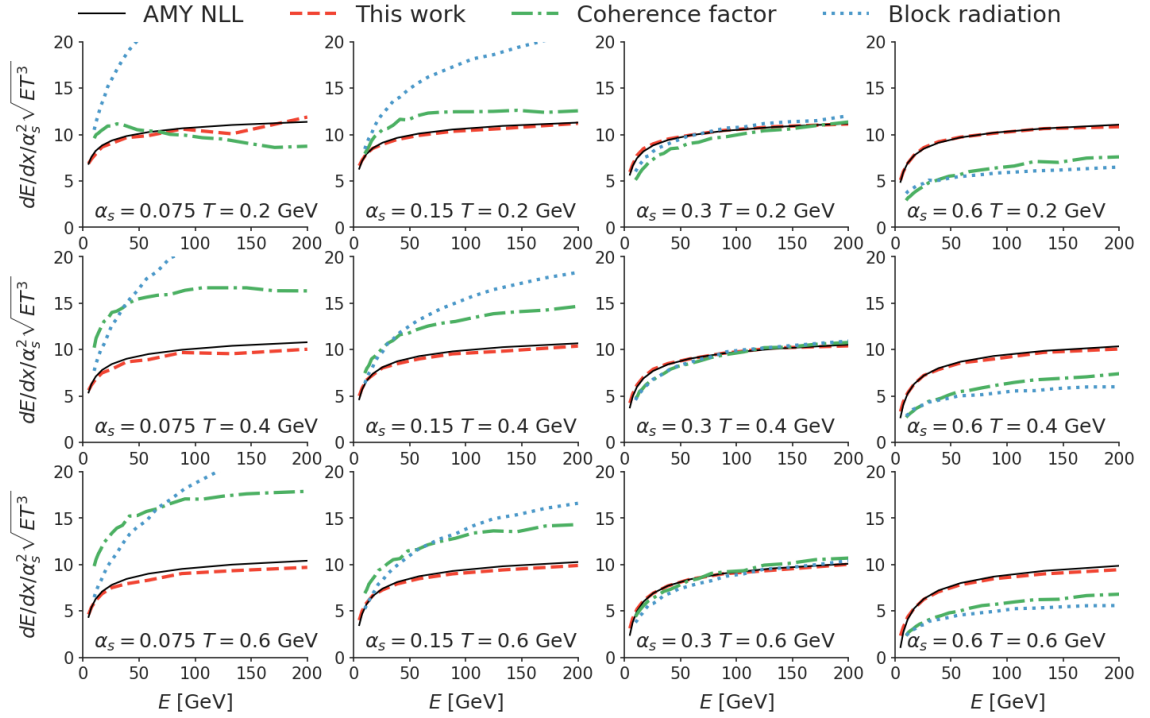


Figure 3.14: Energy loss per unit path length dE/dx as a function of energy E , temperature T and coupling constant α_s . Each column corresponds to a value of the coupling constant $\alpha_s = 0.075, 0.15, 0.3$, and 0.6 (from left to right). Each row corresponds to a temperature of $T = 0.2, 0.4$, and 0.6 GeV (from top to bottom). dE/dx is divided by the expected scaling $\alpha_s^2 \sqrt{ET^3}$. The MC implementations in this work (red dashed lines) is compared to the “coherence factor” approach (green dash-dotted lines) and the “block radiation” approach (blue dotted lines). The analytic results are denoted as black solid lines.

suppression factor λ_{inel}/τ_f is different from the expected one. This is in fact an order of α_s wrong as the mean-free-path of the incoherent radiation rate contains one more power of α_s than λ_{el} .

3.6.3 Energy loss comparison among the three approaches

In Figure 3.14, we show the calculation of energy loss per unit path length dE/dx of a quark in an “infinitely large” medium. Technically, dE/dx is measured after an evolution time long enough ($L \gg L_c$) that finite size effects have faded away. The results presented are normalized by $1/(\alpha_s^2 \sqrt{ET^3})$ in anticipation of the scaling $dE/dx \propto \alpha_s^2 \sqrt{ET^3}$. For each column, we double the value of α_s and for each row, the temperature is increased by 0.2 GeV. Within each subplot, the parton energy varies from 10 GeV to 200 GeV. Different Monte Carlo implementations of the LPM effect are shown in colored lines, AMY NLL results are shown as black bands (we only integrate ω above the Debye mass to calculate the AMY energy loss). Without

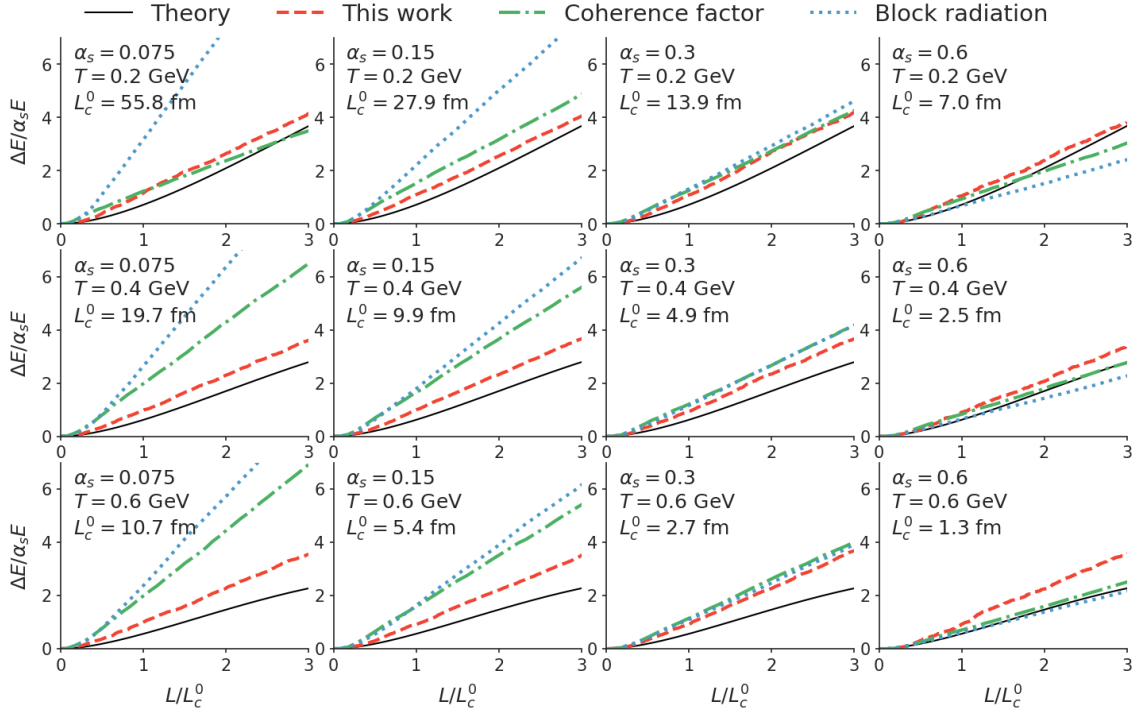


Figure 3.15: Energy loss ΔE as a function of path length L , temperature T and coupling constant α_s . Each column corresponds to a coupling constant of value $\alpha_s = 0.075, 0.15, 0.3$, and 0.6 (from left to right). Each row corresponds to a temperature of value $T = 0.2, 0.4$, and 0.6 GeV (from top to bottom). ΔE is scaled by $\alpha_s E$ and L is scaled by an estimated critical path length $L_c^0 = \sqrt{E/\hat{q}_0}$, $\hat{q}_0 = C_A \alpha_s T m_D^2$. The MC implementations in this work (red dashed lines) is compared to the “coherence factor” approach (green dash-dotted lines) and the “block radiation” approach (blue dotted lines). The analytic results for a thin medium are denoted as black solid lines.

a surprise, the “modified approach” approach (red-dashed lines) reproduces the energy, temperature, and coupling constant dependence of AMY NLL energy loss very well. The “coherence factor” approach (blue-dash-dotted lines) has a similar energy and temperature dependence to that of the theoretical baseline; however, it systematically deviates from the baseline for different values of the coupling constant in a logarithmic manner. For the “block radiation” approaches, the deviations from the baseline regarding their α_s -dependence are even bigger and the energy dependence also gets worse, which is not surprising as we have discussed its problems.

Next we examine the path-length (L) dependence of the energy loss ΔE of a quark with an initial energy of $E = 200$ GeV in a finite medium in Figure 3.15. Again, each column uses a different coupling constant and each row uses a different temperature. The path length within each subplot is varied up to four times L_c^0 . Here $L_c^0 = \sqrt{E/\hat{q}_0}$ with $\hat{q}_0 = C_A \alpha_s T m_D^2$ estimating the critical path length below which one expects a clear non-linear path-length dependence. All three implementations show the non-linear increase of ΔE as function of L . The “modified Boltzmann” approach stays close to the theory calculations when $L < L_c^0$ for all cases, while the other two approaches deviate systematically as α_s is varied, similar to our previous findings for the energy-loss in the infinite matter case.

Chapter 4

A comprehensive heavy-flavor dynamical modeling framework

The dynamical modeling framework for heavy flavor particles is summarized in the flow chart in figure 4.1. The soft initial condition model provides both the initial energy density of the medium and the location of the hard particle production vertices in the transverse plane, while pQCD based calculations provide the momentum space distribution of the hard partons. The left branch of this flow chart – the hydrodynamic-based medium evolution model – has been discussed in chapter 2. We briefly review the RHS of the flow chart – the multi-stage model for heavy-flavor evolution. The hard production model is introduced in section 4.1. The initially produced partons are highly virtual and undergo the DGLAP evolution (vacuum shower) that bring down the virtuality; eventually at some point this evolution will be matched to the in-medium transport calculations. There is a complication regarding vacuum-like parton showers in a medium, since certain vacuum parton branchings will occupy the same space-time volume as the medium and also receive medium corrections. Another obstacle is that multiple emissions are treated very differently between vacuum-like showers and medium-induce showers. For the vacuum evolution, the “time” variable is the virtuality scale with the space-time information integrated out, while the transport model evolves the systems in real time, with virtuality integrated out below a certain scale. Significant progress has been made in both theory and design of event-generators to solve this problem [MTST12, MTT18, C⁺17, Kau18, P⁺19, CIMS18, CIMS19]. In section 4.2.1, we discuss a possible prescription to interface the two types of showers in our simulation. Section 4.3 contains details of coupling the transport model to a dynamically evolving medium with large longitudinal expansion. The heavy flavor hadronization model and hadronic rescatterings are introduced in section 4.4. The hadronization routine applies a previously used implementation [CQB13a] of the high- p_T fragmentation plus low- p_T recombination model for heavy hadrons production [OKLY09]. Finally, in section 4.5, the model is benchmarked using a few values of fixed coupling constant and running coupling constants, before being systematically calibrated to data in the next chapter.

4.1 Initial production of heavy flavor

4.1.1 Factorization framework in proton-proton collisions

In the proton-proton collision, hard processes can be computed using pQCD-based techniques. The foundation of this calculation is the factorization framework as

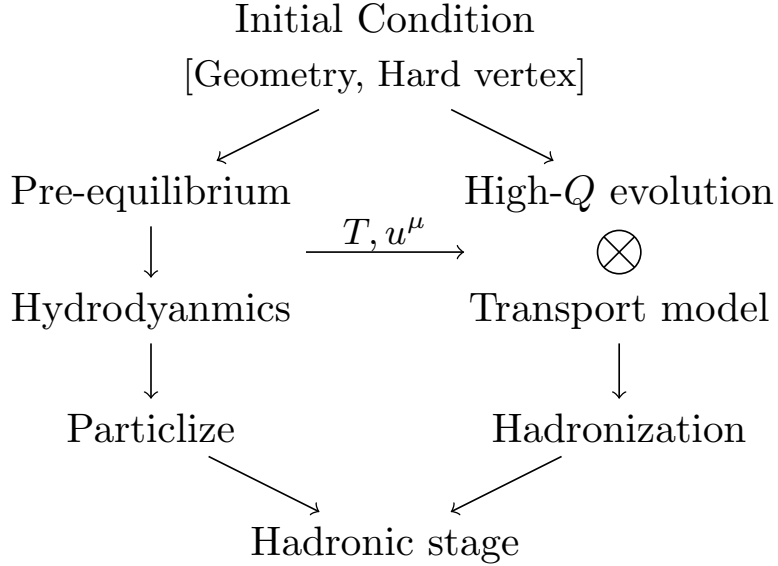


Figure 4.1: A schematic workflow of the heavy quark simulation. The left branch evolves the medium in the hydrodynamic based model, providing medium information (temperature, flow velocity) to the hard probe transport in the right branch. The hard and soft hadrons are evolved in the hadronic afterburner in the last step.

schematically demonstrated in 4.2. The incoming proton is a composite object and there is a certain ‘‘probability’’ of finding a parton $i(j)$ carrying $x_i(x_j)$ fraction of the momentum of the proton $p_1(p_2)$. This ‘‘probability’’ is known as the parton distribution function (PDF) $f_i(x, Q^2)$. It not only is a function of x , but also depends on the scale Q^2 at which the proton is probed. The probing scale is required to be much larger than the non-perturbative scale. Because $\alpha_s(Q^2)$ is small due to asymptotic freedom, the process of partons i and j scattering into partons k and l is computable in perturbative QCD. The final state partons eventually produce a bunch of hadrons, which is a non-perturbative process. The parton fragmentation function is defined as the probability to find a certain hadron H carrying a fraction x_H of the parton’s momentum. Combing these pieces together, the cross-section for the inclusive production of the hadron H can be written as [Fie89],

$$\frac{d\sigma_{p+p \rightarrow H+X}}{dy d\mathbf{p}_T^2} = \frac{1}{\pi} \int dx_i dx_j f_i(x_i, Q^2) f_j(x_j, Q^2) \frac{d\sigma_{ij \rightarrow kl}}{dt} \frac{1}{z_k} D^H(z_k, Q^2). \quad (4.1)$$

Although the parton distribution function f and the parton fragmentation function D are essentially non-perturbative objects, they parametrize universal long-distance physics and can be extracted from independent experiments at certain scales Q_0^2 . Moreover, the evolution from their ‘‘definition’’ scale Q_0^2 to the process scale Q^2 can be described by the DGLAP evolution equation [GL72, AP77, Dok77] based on perturbative QCD to increase the predictive power of the factorization formula.

The DGLAP evolution takes into account that the initial high-virtuality parton i (or j) could have come from a splitting process of a parton with lower virtuality

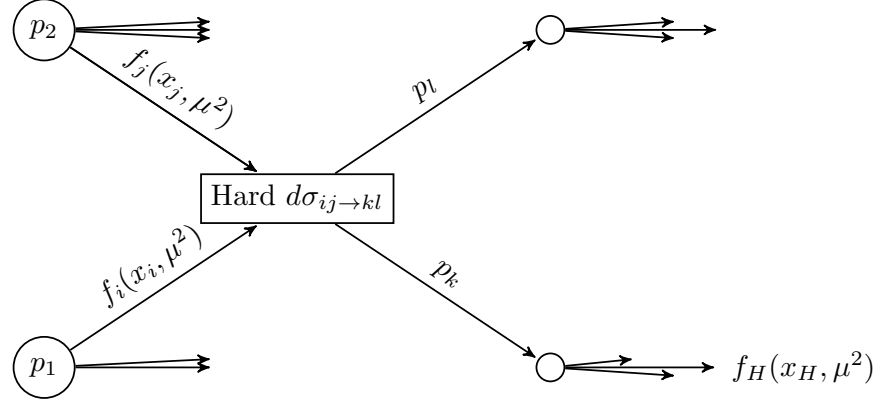


Figure 4.2: A schematic demonstration of the factorization theorem. Two incoming proton momenta are p_1 and p_2 . $f_{i,j}$ are the parton distribution function. $d\sigma$ is the perturbative matrix-element. f_H is the fragmentation function.

parton i' (or j'). Similarly, the final state high virtuality parton k (or l) could also split into a low virtuality parton k' (or l') before it turns into a hadron. Though each splitting causes an additional power of α_s , it is also magnified by a potentially large factor $\ln(Q^2/\mu^2)$ when Q^2 is much greater than the scale where the f , D are defined. The same argument also applies to partons i', j', k', l' . The DGLAP equations systematically resum contributions including an arbitrary number of parton splittings and evolve the scale from μ^2 to the hard scale Q^2 . Moreover, a very useful parton-shower picture can be built from this process with a probabilistic interpretation of the DGLAP evolution. Using Monte Carlo techniques, one can even mimic the production of the exclusive final state from the sequence of parton branching processes.

4.1.2 Production in the nuclear environment

The above framework explains very well the hard production process in proton-proton collisions. In a nuclear environment, there are several differences. First, the parton distribution functions inside a nucleus differ from a simple superposition of the nucleon PDFs. The ratio between the nuclear PDF and proton PDF generally deviates from unity. In particular, this ratio for small x gluons is significantly below one, known as the “nuclear shadowing” effect. This ratio increases and becomes larger than one at larger x , termed as the “anti-shadowing” region. The difference between the nuclear PDF and proton PDF belongs to the category of “cold nuclear matter” (CNM) effect, in contrary to the “hot nuclear matter” effect from the QGP medium. The CNM effect has to be included to correctly interpret the experimental data, though the current level on uncertainty on the nuclear PDF is still large.

4.1.3 Inclusive calculation versus Monte-Carlo event generator

In the course of my study, I have tried using both an inclusive cross-section calculation as well as a Monte-Carlo event generator to initialize the heavy quark production. The inclusive calculation directly applies the factorization theorem and computes the inclusive spectra of heavy quark / hadron production spectrum; while the event generator used the probabilistic picture of the DGLAP evolution to build an exclusive final state.

Initialization from an inclusive calculation of heavy flavor production We use a FONLL (Fixed-Order-Next-to-Leading-Log) calculation to generate the inclusive production cross-section of heavy flavors [CGN98]. The FONLL program is a combination of fixed order (NLO) massive matrix-elements and a massless resummation program. It computes the single inclusive differential cross-section of heavy quark / hadron production $d^2\sigma/dydp_T$. Using $d^2\sigma/dydp_T$, heavy quark's initial momentum is sampled.

This has the advantage of being a first principle calculation when applied to proton-proton collisions. The main disadvantage is the lack of an exclusive partonic final state. This causes several problems,

1. Limitation to the study of open-heavy flavor. For full jets, one needs the exclusive partonic final state. For quarkonia, the momentum correlations among the $Q-\bar{Q}$ pairs are important.
2. We cannot generate a space-time picture of the parton shower to implement medium modifications to parton evolution. Therefore, in this initialization routine, we have always assumed that the vacuum-like evolution is complete at time $\tau = 0^+$.

Initialization from Monte-Carlo event generator We used Pythia (version 8.235) as the hard parton generator [SAC⁺15, SMS06]. Pythia implements leading order (LO) matrix-elements for hard QCD processes, including LO production of heavy flavor particles, $g + g \rightarrow Q + \bar{Q}$ and $q + \bar{q} \rightarrow Q + \bar{Q}$. A parton shower including initial state radiation (ISR) and final state radiation (FSR) is generated around the hard vertex. At high energy, the LO production of heavy flavor is only a fraction of the total heavy flavor cross-section, the remainder are created in the parton showers via the so-called “gluon splitting” and “flavor creation” processes. The former correspond to a situation where the heavy flavor pair originates from a final state gluon splitting; and the latter produces the pair in initial state gluon splitting and is put-on shell by the hard scattering. These contributions also mimic certain pair correlations with non back-to-back angular correlations.

This initialization method is not a first principle approach. Also, the generation of full parton showers at LHC energy can be slow, but the benefits are enormous,

- Though the parton shower in Pythia is evolved as a function of virtuality Q^2 , an approximate space-time picture can be reconstructed by defining the formation time to be $2x(1-x)E/Q^2$ for each branching. Then, it is easy to determine which splitting happened inside the medium and receives medium modifications.
- It allows an initialization of full jet and the study of quarkonia transport.

A comparison of the proton-proton baseline and the CNM effect We checked whether the pythia event generator predicts a similar proton-proton baseline compared to the first principle approach FONLL. In the upper plot of figure 4.3, we compare the p_T differential cross-section of $p+p \rightarrow c$ from FONLL (lines) and Pythia simulations (symbols), and for Pb+Pb collision (red) and p+p collision (blue) at the LHC energy $\sqrt{s} = 5.02$ TeV. For proton-proton collisions, we use the CT10 parton distribution function [LGH⁺¹⁰]. The nuclear PDF uses the EPS09 parametrization [EPS09].

Though the absolute value of the cross-sections compared between FONLL and Pythia are different, the interesting observables are always ratios between nuclear collisions and the proton-proton baseline where the normalization cancels, or other dimensional-less observables such as the momentum-space anisotropy of heavy mesons. Therefore, we focus more on the shape of the spectra between the two calculation, which agree very well. The ratio of initial charm spectra in Pb+Pb collisions and p+p collisions estimates the magnitude of the cold-nuclear matter effect on the nuclear modification factor R_{AA} (without the hot QGP effect). FONLL and Pythia simulations predict consistent modulation: the initial production AA spectra of charm quark at low- p_T is suppressed compared to the pp spectra, due to the shadowing effect of the small- x gluon. At higher p_T , the ratio increase and slightly shoots over unity, because partons from anti-shadowing contribute more at larger- x .

4.2 Matching vacuum and medium-induced showers

4.2.1 Vacuum versus medium-induced shower phase-space

The fate of vacuum-like showers in the hot-medium is complicated and there has not been a lot of phenomenological studies [C⁺¹⁷, CIMS18, CIMS18, CIMS19]. The prescription that we build in this section is by no means exact, but follow the reasoning from a recent work [CIMS18]. The general idea is to identify different regions of phase-space of radiation, and apply different means of computation (DGLAP / transport) to different regions based on how much medium-modification it would have received.

Considering a vacuum splitting of a hard parton that enters the medium at $z = 0$. The vacuum splitting has a formation time of $\tau_f \sim 2x(1-x)E/k_\perp^2$. It is very likely that the radiated gluon (or the quark) interacts with one or more scattering centers (labeled by “i”) in the medium at time t_i . Whether these interactions contribute coherently to

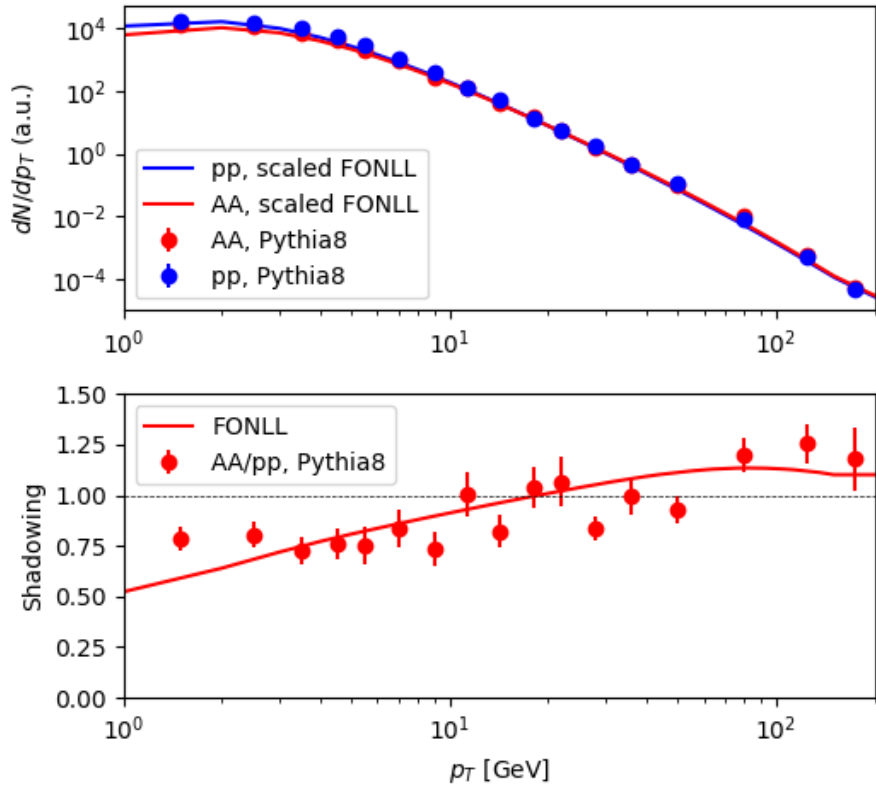


Figure 4.3: Top plot: a comparison of D -meson production in proton-proton collisions (blue) and in Pb-Pb collisions (red) with cold nuclear matter effect only. FONLL calculations are shown as lines and Pythia8 simulations are shown as symbols. Bottom plot: the ratio between the production in Pb-Pb collision (cold nuclear matter effect only) to the proton-proton baseline shows the nuclear shadowing effect.

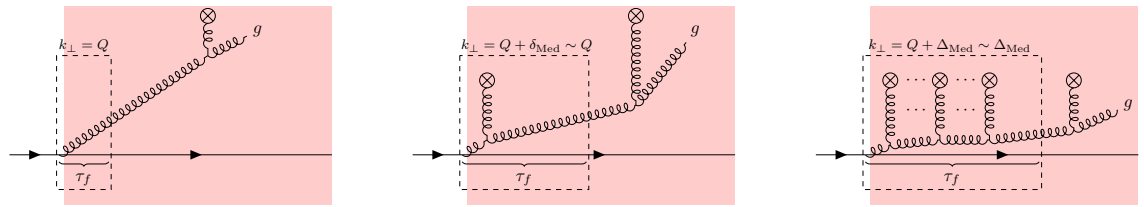


Figure 4.4: Demonstration of the medium corrections to vacuum-like radiation with different formation time. The energy of the gluon is hold fixed, while the virtuality is decreasing from left to right.

the “vacuum-like” splitting follows the same argument as before. Scatterings that are well separated from the formation processes $\tau_f \ll t_i$ are treated as independent, and only broaden the transverse momentum distribution without changing the probability of the process. For $t_i \lesssim \tau_f$, the branching probability of the vacuum-like radiation also gets modified, in addition to broadening. Now classifying the radiations using the average “number” of scatterings $N = \tau_f/\lambda$ (for the case of a static medium),

- For a branching with large virtuality (left of figure 4.4) so that $N \ll 1$ or equivalently $Q^2 \gg g^2 x(1-x)ET$. The chance for a medium modification of the vacuum branching probability is negligible.
- Hold the energy of the radiation and decrease its virtuality (middle of figure 4.4) so that $N = \tau_f/\lambda \sim 1$ ($Q^2 \sim g^2 x(1-x)ET$). Now, there is an order one probability of scatterings within τ_f , but the transverse momentum of the gluon is still dominated by the initial virtuality. The probability for the branching should also be modified accordingly, for example, using the higher-twist formula that expands in terms of $1/Q^2$.
- Further decrease the initial virtuality of the branching (right of figure 4.4) until $N \gg 1$. Eventually, the medium broadening of the transverse momentum is large compared to the parton’s virtuality from initial production. It is proper to associate this parton an in-medium virtuality $Q^2 \sim g^2 \sqrt{x(1-x)ET^3}$. When this happens, the branching probability is heavily modified by the medium and should be replaced by a medium-induced splitting calculation.

Summarizing the two extreme regions: The unmodified DGLAP evolution is applied to the high-virtuality part of the shower ($Q^2 \gg \alpha_s \omega T$), while medium-induced calculations should be applied to the low-virtuality shower $Q^2 \sim \sqrt{\hat{q}\omega}$ (relation obtained in a static medium) via transport equations. It is therefore natural to use the comparative relation between the parton’s initial virtuality Q^2 and the transverse momentum change contributed by medium broadening $\Delta k_\perp^2 = (\mathbf{k}_\perp(\tau = \tau_f) - \mathbf{k}_\perp(\tau = 0))^2$ to separate the medium-induced radiation from the vacuum-like radiation. The matching prescription is then to simply cut-out the vacuum branchings generated by Pythia in the region $\Delta k_\perp^2 \gtrsim Q^2$, the cut region is referred as the “vetoed” region in the literature [CIMS18]). For a dynamical and fluctuating medium, there is no simple relation as $\Delta k_\perp^2 \sim \sqrt{\hat{q}\omega}$ in the static medium, but the “preformed parton” technique can be used to determine Δk_\perp^2 self-consistently for each vacuum branching (to be explained in the next paragraph). In a finite medium, certain vacuum-like branchings may have a long formation time that they form outside of the medium. Due to the uncertainty principle, these branchings do not resolve the details of the medium and their branching probability will not be modified in our model. This separate treatment of different regions of phase-space still depends on the detailed choice of the separation scale, so in the future, it would be desirable to develop a unified theoretical treatment for both vacuum and medium-induced showers in the time evolution picture.

Focusing only on the vacuum-like radiation generated by heavy quarks, one traces back a heavy quark line in the Pythia event recorder to find all the gluons from

its final state radiation (FSR) and the original four momentum of the heavy quark at the initial production vertex. These FSR gluons are first treated as “unformed” by the transport models, and they are allowed to undergo elastic broadening with the medium. In this way, by the time these gluons reaches their formation times ($t - t_0 > \tau_f$), one knows both the initial virtuality of the splitting Q^2 , as well as how much medium broadening Δk_\perp^2 has been acquired. Then, applying our previous approximation, vacuum-like branching with $\Delta k_\perp^2 < R_v Q^2$ remains unmodified, but $\Delta k_\perp^2 > R_v Q^2$ vacuum branchings are rejected because their contribution is already taken care by the medium-induced rate in the transport model. The order one R_v parameter is introduced to parametrize the uncertainty in this matching scale.

4.2.2 Visualizing the matching on the Lund diagram

The Lund diagram is a useful tool to visualize the phase-space for high energy parton splitting. There are many different choice of kinematic variables, but here we choose the vertical axis to be $Y = \ln(1/x) = \ln(E/\omega)$, and the horizontal axis to be $X = \ln(1/\theta^2) = \ln(\omega^2/k_\perp^2)$. Here x is the energy fraction carried by the daughter parton in a particular splitting, and θ is the daughter’s emission angle relative to the mother parton. This arrangement is inspired by the soft and collinear limit of the QCD splitting function (for example $q \rightarrow q + g$),

$$dP_{qg}^q \sim \frac{\alpha_s C_F}{\pi} \frac{dx}{x} \frac{d\theta^2}{\theta^2} = \frac{\alpha_s C_F}{\pi} d\ln \frac{1}{x} d\ln \frac{1}{\theta^2}. \quad (4.2)$$

Therefore, the probability distribution of a vacuum-like splitting vertex should be uniform, apart from the running coupling effect. The closer a point lies towards the origin, the higher its virtuality. The soft and collinear radiations reside at large X and Y . Also, constant-formation-time contours are simply straight lines $Y + X = \ln(E\tau_f/2)$.

On the left of figure 4.5, we show the phase space occupied by the vacuum branching without medium (left); on the right, it is medium-modified vacuum splitting (blue color map) and the medium induced radiation (red contour) from our simulation. The simulation first identifies charm quarks with transverse momentum $90 < p_T < 110$ GeV at the production vertex in Pythia, and then propagate them and their vacuum radiated gluons in a static medium with $T = 0.3$ GeV with $\alpha_s = 0.3$ for a path length L . We see that without the medium effect, the vacuum radiations fills the region bounded by the time-evolution limit $\tau_f < L$ (dash-dotted line) and the default non-perturbative bounds $k_\perp > 0.4$ GeV (dotted line) of Pythia. Inside the medium, the medium-induced radiations are distributed around the line $\tau_f \hat{q} = k_\perp^2$ which is $\theta^4 \omega^3 = 2\hat{q}$ (dashed line) in the soft limit. But this line is only an averaged estimation of the relation between k_\perp, ω and \hat{q} , since the actually outcome of the simulation has huge fluctuations. The triangle area bounded by the line $\tau_f < L$ and the line $\theta^4 \omega^3 = 2\hat{q}$ is where the vacuum-like radiation receives large modification from medium interactions. The rejection program introduced before suppresses the vacuum-like radiation in this region compared to the case without a medium. Again,

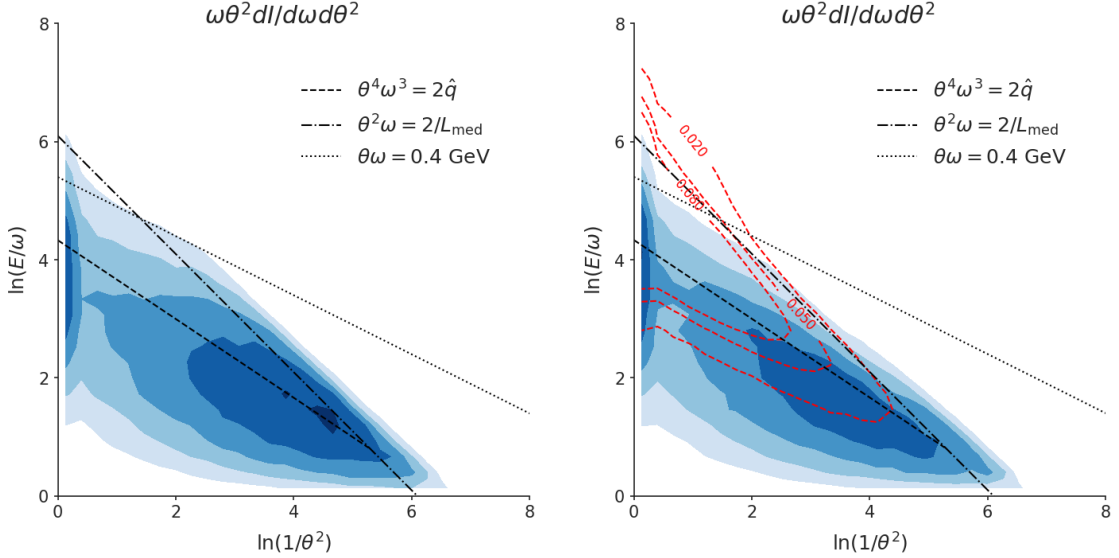


Figure 4.5: Plotting the gluon radiations from a charm quark on the Lund diagram. The gluon emission has an energy ω with angle θ with respect to the heavy quark. The blue heat map in the left plot shows the distribution of vacuum-like emissions without medium effects. The heat map in right left plot shows the distribution of vacuum-like emissions with medium effects; while the red contour stands for the medium induced emissions. Emissions on the black dashed lines have $k_{\perp}^2 = \sqrt{2}\omega\hat{q}$. Emissions on the dashed-dotted lines have a formation time equals to the medium path-length. Finally, the dotted lines is the non-perturbative cut-off in Pythia $k_{\perp} = 0.4$ GeV.

due to fluctuations, the triangular region is not entirely vetoed as the one demonstrated in [CIMS18].

Concluding this section, the realm of the transport equation and the DGLAP evolution is separated when the parton virtuality is comparable to the acquired transverse momentum broadening within the formation time. High virtuality evolution is approximated as unmodified, while low virtuality evolution is terminated and replaced by the medium-induced processes via the transport evolution. This procedure is, of course, only viable if we initialize the simulation with a parton shower event generator. We are not able to do such a separation using heavy quark spectra obtained from FONLL.

4.3 Particles coupled to an evolving medium

The coupling between hydrodynamics and hard parton transport often requires a switching of the reference frame, as the velocity of the medium local-rest-frame relative to the lab frame is a function of space-time.

For diffusion dynamics The diffusion equations are most easily written in the local-rest-frame of the medium. Given a particle's four momentum in the lab frame (p_L^μ), one first boost it into the medium local-rest-frame (p_M^μ),

$$p_M^\mu = L_\nu^\mu(\vec{\beta}) p_L^\nu \quad (4.3)$$

$$L_\nu^\mu = \begin{bmatrix} \gamma & -\gamma\vec{\beta} \\ -\gamma\vec{\beta} & \mathbb{1} + \frac{\gamma^2}{\gamma+1}\vec{\beta}\vec{\beta} \end{bmatrix} \quad (4.4)$$

where $\vec{\beta}$ is the velocity of the fluid cell relative to the lab frame, and L_ν^μ is the Lorentz transformation. One needs to be careful with that since the time step in the fluid rest frame Δt_M is different from the one in the lab frame Δt_L . Consider the particle trajectory Δx_L^μ within Δt_L observed in the lab frame and boost it into the medium frame,

$$\Delta x_L^\mu = \frac{p_L^\mu}{E_L} \Delta t_L \xrightarrow{\text{boost}} \Delta x_M^\mu = \frac{L_\nu^\mu(\mathbf{v}_M) p_L^\nu}{E_L} \Delta t_L = \frac{p_M^\mu}{E_L} \Delta t_L \quad (4.5)$$

Comparing the time-component of the equations, one finds the time step in the medium frame being related to the lab frame step by the ratio between the energy of the particle in the two reference frames,

$$\Delta t_M = \frac{E_M}{E_L} \Delta t_L \quad (4.6)$$

Once the momentum is updated in the medium frame to p'_M , it is boosted back to the lab frame,

$$x'^\mu = x^\mu + \frac{p_L^\mu}{E_L} \Delta t_L \quad (4.7)$$

$$p_L'^\mu = L_\nu^\mu(-\vec{\beta}) p_M'^\nu \quad (4.8)$$

where we have chosen to update position before the update of the momentum.

The choice of Δt_L is also tricky. A most straightforward uniform time step for all the particles is not the optimal choice. This is due to relativistic hydrodynamics for heavy-ion collision often being solved in (τ, x, y, η_s) coordinates and the hydrodynamic field being propagated from one constant proper time $\tau = \sqrt{t^2 - z^2}$ to the next. There are two consequences if we choose the same Δt_L for all particles:

1. Different particles will be at different proper times τ at a constant t . It requires the program to load the entire hydrodynamic temperature and velocity history into the memory, which can be a memory storage problem for 3+1 D hydro simulation (the memory consumption for boost-invariant hydrodynamics is not critical).
2. The time step in the medium-rest-frame for particles at large space-time rapidity would be too small.

For these practical reasons, we choose to propagate particles with a constant proper-time step $\Delta\tau$. As a result, the time step in the lab frame is different for each particle, depending on its location and momentum, and is solved by,

$$\Delta\tau = \sqrt{(t + \Delta t_L)^2 - (z + v_z \Delta t_L)^2} - \sqrt{t^2 - z^2}. \quad (4.9)$$

This is (keeping the positive solution),

$$\Delta t_L(p, x) = \frac{-(t - zv_z) + \sqrt{(t - zv_z)^2 - (1 - v_z^2)(\Delta\tau^2 + 2\sqrt{t^2 - z^2}\Delta\tau)}}{2(1 - v_z^2)} \quad (4.10)$$

This adaptive time step propagates a particle between constant proper-time hypersurfaces, therefore only two steps of hydrodynamic information needs to be loaded into memory at any given time. Also Δt_L becomes larger for forward/backward particles.

For matrix-element scattering The situation for matrix-element scatterings is more complicated. Because the initial state of scattering is straightforwardly sampled in the medium local-rest-frame, but the full final state is most efficiently sampled in the center-of-mass frame of the few-body collisions. The center-of-mass velocity relative to the local-rest-frame is,

$$\vec{\beta}_C = \frac{\sum_{i \in IS} \vec{p}_i}{\sum_{i \in IS} E_i} \quad (4.11)$$

where “IS” stands for the initial state.

1. For each hard parton, determine Δt_L with equation 4.10.
2. Boost the particle to the medium rest-frame and sample the scattering rate $\Delta t_M R$ channel, and then sample the medium parton(s) that forms the scattering initial state with the hard parton.
3. In the CoM frame of the initial state, sample the final state particles.
4. Boost back the final state particles to the medium rest frame.
5. Boost back to the lab frame.

4.4 Heavy-flavor hadronization and hadronic stage

At a temperature around T_c , light hadrons can be sampled from the hydrodynamics energy momentum tensor statistically. For hard partons that may be off equilibrium, a microscopic hadronization model is in need. The final hadronic system is also dense enough for the heavy hadron to interact. Though the hadronic interactions are not analyzed as extensively as the QGP interaction, studies have shown hadronic rescatterings contribute to finite low- p_T v_2 of D-mesons [CQB15]. Therefore we also includes the afterburner stage for the heavy flavors.

4.4.1 The instantaneous approximation of hadronization

The hadronization implementation is described in [CQB13a]. It combines the fragmentation of heavy quarks at high momentum and the recombination with medium partons into hadrons at low momentum. The hadronization is treated to be instantaneous on an isothermal hypersurface. This instantaneous approximation has certain drawbacks. First, hadronization is a long distance process. In the rest frame of the heavy flavor, it takes time on a scale of $1/\Lambda_{QCD}$. With a large boost factor $E/M_H \sim E/M_Q$, the formation time of the heavy hadron can be comparable to macroscopic length scales. For example, for a moderate $E = 10$ GeV charm quark with $M_Q = 1.3$ GeV, this time is estimated to be 8 fm/c, which is certainly not instantaneous considering the hydrodynamic stage only last for $O(10)$ fm/c. Second, an instantaneous recombination process breaks energy conservation and detailed balance. In order to solve all of these problems, one may need to consider using a dynamical hadronization model [HR19].

Fragmentation In high energy electron-positron collisions and proton-proton collisions, high momentum heavy quarks hadronize through the fragmentation mechanism. The energetic heavy quark produces a bunch of hadrons with a heavy hadron that carries a certain fraction of the origin quark momentum $z = p_H/p_Q$. The probability distribution of z is known as the fragmentation function $D(z)$, and can be measured in, e.g., electron-positron colliders. There are different parametrizations for $D(z)$ and the Peterson fragmentation function [PSSZ83] is used in the present study,

$$D(z) \propto \frac{1}{z(1 - \frac{1}{z} - \frac{\epsilon}{1-z})^2} \quad (4.12)$$

where ϵ is a parameter that scales as m_Q^{-2} ($\epsilon_c \approx 0.05, \epsilon_b \approx 0.006$).

Recombination It was already known in proton-proton collisions that heavy quarks can hadronize into mesons by the recombination with a light quark in the proton remnant [Meh04]. In a heavy-ion collision, the recombination mechanism can play an important role for low p_T heavy flavors, given the abundance of medium thermal partons. Early studies in nuclear collisions [OKLY09] assumed that the recombination probability can be computed from the wave function overlap between initial state partons and final state mesons or baryons, with the momentum of the medium parton integrated over the thermal distribution.

$$\frac{dP_M(p', p)}{dp'^3} = \int dk^3 n_{\bar{q}}(k) W_M(p, k) \delta^{(3)}(\vec{p}' - \vec{p} - \vec{k}), \quad (4.13)$$

$$\frac{dP_B(p', p)}{dp'^3} = \int dk_1^3 dk_2^3 n_{\bar{q}}(k_1) n_{\bar{q}}(k_2) W_B(p, k_1, k_2) \delta^{(3)}(\vec{p}' - \vec{p} - \vec{k}_1 - \vec{k}_2), \quad (4.14)$$

On the left are the differential probability for a heavy quark with momentum p to hadronize into a heavy meson (first line) or a heavy baryon (second line) with momentum p' through recombination. They are equal to an integration of light quark(s)

/ anti-quark(s) momenta of the produced baryon / meson Wigner function W times the thermal distribution function, subjected to three-momentum conservation. It is evident that the energy conservation is not imposed in the instantaneous $2 \rightarrow 1$ coalescence approach. The quark / anti-quark distribution function is the Fermi-Dirac one, neglecting chemical potential,

$$n = \frac{g_q V}{e^{\beta p \cdot u} + 1} \quad (4.15)$$

with u the fluid velocity and p the four momentum of the light quark / anti-quark. g is the degeneracy factor of the quark, and V is a test volume that will eventually be canceled by the normalization factor in the the Wigner function. As a remark, we have assumed in the transport model that medium partons are massless because the thermal masses are higher order effects for energy loss; but for recombination into bound states near T_c , it is important to use non-perturbative constituent masses of light quarks $m_u = m_d = 300$ MeV and $m_s = 475$ MeV.

Regarding the meson wave-function, there has been efforts using the Dirac equation to obtain a more realistic wave-function for different states of heavy mesons. The current model uses a parametrized Gaussian wave-function for simplicity,

$$\phi_M(\vec{r}) = \left(\frac{1}{\pi\sigma^2} \right)^{3/4} e^{-\frac{r^2}{2\sigma^2}} \quad (4.16)$$

The σ s are related to the reduced mass of the two body system $\mu = m_1 m_2 / (m_1 + m_2)$ and the frequency of the two-body potential ω by $\sigma = 1/\sqrt{\mu\omega}$. These frequencies are estimated from the charge radius of different heavy mesons: 0.106 GeV for charmed mesons and 0.059 GeV for the bottom mesons. The Wigner function is defined in terms of the relative distance \vec{r} and relative momentum \vec{q} between the quark and anti-quark,

$$W_M(\vec{r}, q^2) = g_M \int d^3 \vec{a} e^{-i\vec{q}\cdot\vec{a}} \phi_M(\vec{r} + \vec{a}/2) \phi_M^*(\vec{r} - \vec{a}/2) \quad (4.17)$$

$$\vec{q} = \frac{E_2 \vec{p}_1 - E_1 \vec{p}_2}{E_1 + E_2}. \quad (4.18)$$

Averaging over the light quark's positions,

$$W_M(q^2) = \frac{g_M}{V} (2\sqrt{\pi}\sigma)^3 e^{-\sigma^2 q^2}, \quad (4.19)$$

which is the quantity needed in equation 4.13,

$$\frac{dP_M(p', p)}{dp'^3} = \int dk^3 \frac{g_q g_M}{e^{\beta p \cdot u} + 1} (2\sqrt{\pi}\sigma)^3 e^{-\sigma^2 q^2} \delta^{(3)}(\vec{p}' - \vec{p} - \vec{k}), \quad (4.20)$$

where the test volume in the distribution function has been canceled by the one in the Wigner function.

The same procedure applies to heavy baryons, with the three-body Wigner function in the Gaussian approximation as,

$$f_B^W(q_1^2, q_2^2) = \frac{N g_B}{V^2} (2\sqrt{\pi}\sigma_{1,2}\sigma_{12,3})^6 e^{-q_{1,2}^2 \sigma_{1,2}^2 - q_{12,3}^2 \sigma_{12,3}^2}. \quad (4.21)$$

The relative momenta are defined as,

$$\vec{q}_{1,2} = \frac{E_2 \vec{p}_1 - E_1 \vec{p}_2}{E_1 + E_2}, \quad (4.22)$$

$$\vec{q}_{12,3} = \frac{E_3 (\vec{p}_1 + \vec{p}_2) - (E_1 + E_2) \vec{p}_3}{E_1 + E_2 + E_3}, \quad (4.23)$$

and the σ related to the frequency and masses by,

$$\sigma_{1,2}^{-1} = \sqrt{\omega \frac{m_1 m_2}{m_1 + m_2}} \quad (4.24)$$

$$\sigma_{12,3}^{-1} = \sqrt{\omega \frac{(m_1 + m_2)m_3}{m_1 + m_2 + m_3}} \quad (4.25)$$

To synthesize these two competing mechanisms of hadronization, one first samples the recombination probability in equations 4.13 and 4.14 and determines whether the heavy quark coalesces with medium partons. If not, its hadronization will be handled by the Pythia fragmentation routine with the Peterson fragmentation function.

4.4.2 Hadronic rescattering

Currently, hadronic rescattering of charmed mesons with π and ρ mesons is included in the UrQMD framework. These cross-sections are obtained from [LDK01]. Hadronic cross-section of the charmed baryons and bottom hadrons are not included.

One modification made to the UrQMD heavy-flavor sector is that the kinematic effect of back reaction from heavy flavor mesons on the light sector is turned-off. This is done by resetting the light scattering partner's four momentum back to its initial value. This is done to retain the same level of approximation of the linearized transport equation in the QGP phase, and allows for an easy oversampling of the number of heavy flavor particles to obtain better statistics.

4.5 Benchmark calculation of observables

In the last section of this chapter, we provide a benchmark calculation of this open-heavy flavor simulation framework by comparing to experimental data. A systematic calibration of model parameters and uncertainties will be discussed in the next two chapters.

4.5.1 Open heavy flavor observables

Experimentally, the ground states mesons $D^0, \bar{D}^0, D^\pm, B^\pm, D_s^\pm, B_s^\pm$ and the excited states $D^{*\pm}$ can be measured. Their nuclear modification factor and momentum anisotropy have been measured at both LHC and RHIC. Currently, we focus on comparing to non-strange D and B mesons data. Though strange heavy mesons D_s, B_s

are also very interested as they contain the strangeness enhancement information, but the strangeness physics is not the main focus of this work.

The nuclear modification factor has already been introduced in the chapter 1. Here we summarize how the momentum anisotropy observables are computed. A list of the measurements and references can be find in table 4.1 and table 4.2.

Table 4.1: ALICE dataset

Observables	Centrality	Reference
D -meson v_2	30-50%	[A ⁺ 18a]
Event-engineered meson v_2	D - 30-50%	[Gro17]
D -meson R_{AA}	0-10, 30-50, 50-80%	[A ⁺ 18b]

Table 4.2: CMS dataset

Observables	Centrality	Reference
D^0 -meson v_2	0-10, 10-30, 30-50%	[S ⁺ 18b]
D^0 -meson R_{AA}	0-10%, 0-100%	[S ⁺ 18c]
B^\pm -meson R_{AA}	0-100%	[S ⁺ 17]

Momentum anisotropy Heavy flavor momentum anisotropy at high- p_T is thought to be the result of anisotropic energy loss, because on average, hard partons emitted along the short axis lose less energy than those emitted along the long axis. At low momentum, the momentum anisotropy is related to collective flow since the heavy quark interacts so frequently with the medium and tends to catch up with the flow velocity of the medium. Both mechanisms produce v_2 relative to the common reference frame of the bulk geometry / bulk flow. The p_T differential v_2 is usually measured in a two-particle correlation approach,

$$v_n\{2\}(p_T) = \frac{\Re e \langle d_n\{2\} \rangle}{\langle c_n\{2\} \rangle}. \quad (4.26)$$

c_n is the event-wise two particle correlation of N reference particles (REF, the bulk medium) within a certain kinematic range,

$$c_n = \frac{|Q_n|^2 - N}{N(N-1)}, \quad (4.27)$$

$$Q_n = \sum_{i=1}^N e^{in\phi}, \quad (4.28)$$

and the event average ($\langle \cdots \rangle$) is weighted by $N(N-1)$. d_n is the correlation between the M particles of interest (POI, in this case the heavy flavors) and the N reference

particles,

$$d_n = \frac{q_n Q_n^* - m}{MN - m}, \quad (4.29)$$

$$q_n = \sum_{j=1}^M e^{in\phi} \quad (4.30)$$

m is the number of POI that is also counted as REF to subtract auto-correlations. The event average is weighted by the number of pairs $MN - m$.

Event-shape engineering on heavy-flavor v_2 Event-shape engineering is a more recent idea to look at the detailed response of the hard sector to the medium geometry. Experimentally, an ensemble of events belonging a certain centrality class is further classified according to its “event shape”, measured by q_2 ,

$$q_2 = \frac{|Q_2|}{\sqrt{N}}. \quad (4.31)$$

Due to event-by-event geometry fluctuations, the event shape in a given centrality class can vary dramatically. The ALICE experiment then measures the D meson v_2 with events having the 20% largest q_2 and events with the 60% smallest q_2 . They found a large separation between the resulting v_2 of bias selected events compared to the v_2 calculated from unbiased events. This measurement quantifies the response of the hard probe to the event geometry fluctuation while controlling multiplicity.

4.5.2 A first comparison to data

We do not intend to optimize all the parameters in the model in this first comparison to data, but use a reasonable estimate of the parameters to understand the model. The TRENTo parameters and the hydrodynamic transport coefficients are obtained from the high likelihood parameters in [Ber18]. The heavy quarks start to lose energy from $0.6 \text{ fm}/c$, and the matching condition between the vacuum-like radiation and the medium-induced radiation is $\Delta k_\perp^2 = R_v Q^2$ with $R_v = 1$. We used only leading order contributions from the weakly coupled theory, and try both fixed coupling and running coupling. The default switching scale between a large- Q scattering small- Q is $Q_{\text{cut}}^2 = 4m_D^2$.

Fixed coupling First, we compute with a fixed coupling constant. It should be understood as an effective in-medium coupling for both elastic and radiative processes. In figure 4.6, we present the results (lines and bands) with data points measured at $\sqrt{s_{\text{NN}}}s = 5.02 \text{ TeV}$ for D mesons (symbol with errorbars and boxes). Different line shapes corresponds to different coupling $\alpha = 0.2$ (dashed), 0.3 (solid), and 0.4 (dash-dotted). The types of observables are shown within each subplots, indicating the experimental collaboration, the collision system and the centrality.

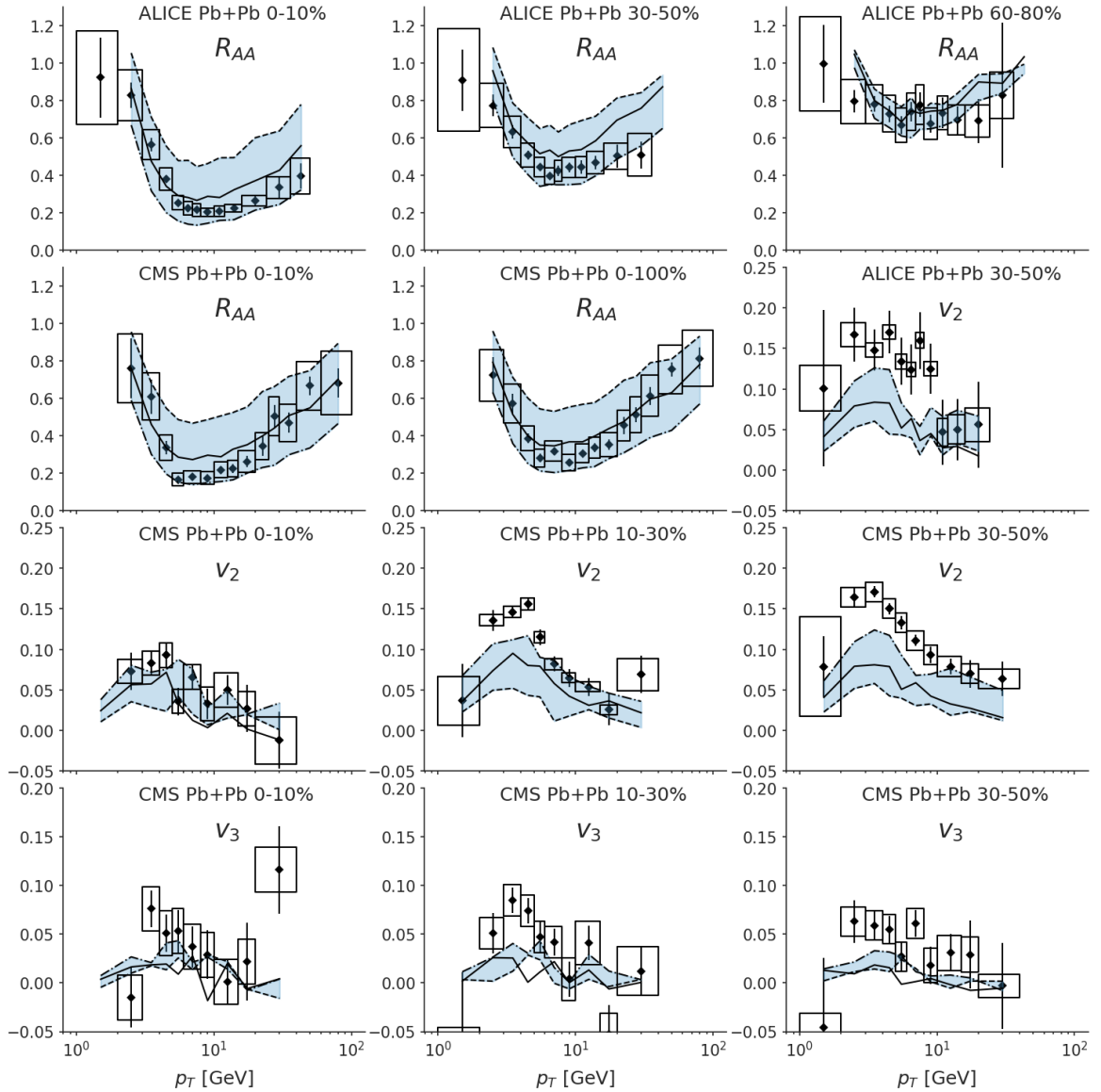


Figure 4.6: Benchmark results using a fixed coupling constant $\alpha_s = 0.2$ (dashed), 0.3 (solid), and 0.4 (dash-dotted). The blue bands fill between the results using $\alpha_s = 0.2$ and 0.4. They are compared to the experimental data (black symbols) obtained by the ALICE Collaboration [A⁺18a, A⁺18b] and the CMS Collaboration [S⁺18c, S⁺18b].

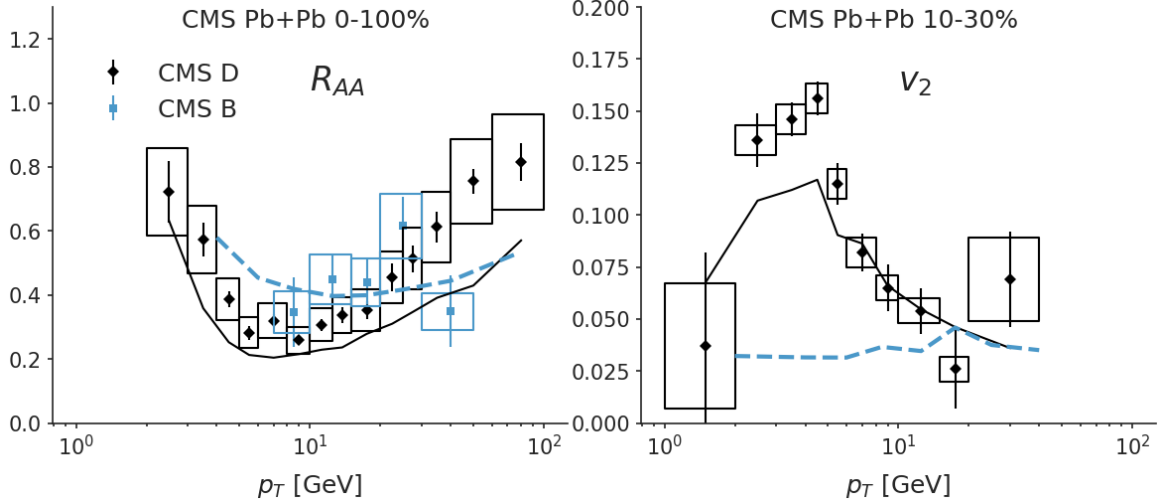


Figure 4.7: Demonstrating the mass dependence of the observables using $\alpha_s = 0.4$. The D meson and B meson results are labeled by color black and blue respectively. Left plot: R_{AA} for 0-100% centrality. Right plot: v_2 for 10-30% centrality.

Looking at the experimental measurements, R_{AA} increases with the centrality classes and displays a minimum around $8 < p_T < 10$ GeV. At high- p_T , the R_{AA} increases towards the baseline around one. This increase is slow, noticing the p_T is plotted on a log scale. At low- p_T , the R_{AA} quickly rises. There are many reasons for this, for example, the feed down from higher- p_T particles due to energy loss; the feeding from low- p_T particles that are pushed outward by the strong medium radial flow. In addition, the recombination hadronization mechanism also plays a part, as the D meson is gaining momentum (on average) in the recombination process. Based on the comparison to R_{AA} , a phenomenological value for a fixed α_s is around 0.3–0.4. However, such values cannot explain the large momentum anisotropy in mid-central collisions, e.g. centrality 30–50%. This is known as the D meson R_{AA} – v_2 puzzle, which also appears for leading light hadrons. There have been different solutions proposed to this problem, such as a sudden increase of the interaction strength near T_c , fine tuning the general temperature-momentum dependence of the transport coefficients, etc [SDP⁺16, XBB⁺18, SLG19]. In the next two chapters, we will see if this discrepancy can be overcome by a fine tuning of parameters in the current model. A non-zero v_3 of D mesons is an evidence of heavy-flavor coupling to detailed event-by-event nuclear geometry fluctuations. The calculation of v_3 is systematically below the data, despite the large statistical and systematic uncertainty,

In figure 4.7, we compare the calculation with $\alpha_s = 0.4$ for charmed meson R_{AA}^D and bottom meson R_{AA}^B at 0 – 100% centrality and D meson and B meson flow at 10–30% centrality. The mass effect of bottom quarks is much stronger than for charm quarks, therefore, R_{AA}^B at intermediate p_T is higher than R_{AA}^D . At very high p_T , the “dead cone” of bottom quark becomes insignificant, and the B and D meson R_{AA} converge. Unlike the sudden increase of v_2^D at low p_T , v_2^B is always small, meaning that the bottom quarks do not catch up to the medium flow as the charm quarks do

and remains far from equilibrium.

Running coupling Moving to a running coupling constant, the uncertainty of the in-medium coupling strength is transferred to the uncertainty of the medium scale in the running α_s ,

$$\alpha_s(Q) = \frac{2\pi}{9} \frac{1}{\ln(\max\{Q, \mu\pi T\}/\Lambda)}. \quad (4.32)$$

Due to the running, heavy quark radiation at high energy will be reduced compared to low energy and the interaction strength with the medium is enhanced at low temperature relative to high temperature.

In the comparison shown in figure 4.8, we choose $\mu = 1, 2, 4$, terminating the low- Q running of α_s at $Q = \pi T$ (dashed), $2\pi T$ (solid), $4\pi T$ (dash-dotted). We use πT as a natural unit because it is the typical thermal scale in the finite-temperature field theory calculations. Given that the entire heavy-flavor coupled-to hydrodynamic model is only an approximation, one should not think of the appearance of π so seriously. The $\mu = 2\pi T$ choice explains the nuclear modification factor for all centralities very well, but underestimates v_2 by 50%. The $\mu = \pi T$ case achieves a better agreement with v_n , but R_{AA} is systematically off. Therefore, going from fixed coupling to running coupling, the v_2 puzzle still remains.

Switching scale dependence By construction, the energy loss should be insensitive to the switching scale between the small- Q diffusion and the large- Q scattering in the high energy, weakly coupled limit. We check if this argument holds for phenomenological application. In figure 4.9, in addition to the default $Q_{\text{cut}}^2 = 4m_D^2$ (red solid lines), we also use $Q_{\text{cut}}^2 = 16m_D^2$ (blue dashed lines) to model an increase amount of probe-medium interaction by diffusion compared to scattering. We find that the effect on high- p_T observable is small. Because the high- p_T dynamics is dominated by the radiative energy loss, whose Q_{cut} is indeed small as checked in chapter 3. Larger differences of R_{AA} and v_2 is observed at low- p_T . One reason for this is that the Q_{cut} independence argument obtained for high energy partons does not work very well for low velocity partons. Another reason is that despite the scattering dynamics and the diffusion dynamics having a matched diffusion constant (second moment of the momentum transfer), they are differed in all other higher moments, in particular the drag (first moment). Remember that the drag coefficient in the diffusion dynamics is not a direct input from the weakly coupled theory, but is determined by the Einstein relation. The Einstein relation only guarantees that the diffusion dynamics evolves the system to the same equilibrium as the scattering dynamics, but the non-equilibrium path it takes can be very different from that of the scattering dynamics.

This Q_{cut} dependence may be bad at first sight, but one knows that the weakly coupled scattering picture does not necessarily work for the phenomenological coupling regime ($g \sim 2$), while the diffusion dynamics can be extended to the strongly coupled regime. The Q_{cut} actually parametrizes an important source of theoretical uncertainty in our modeling.

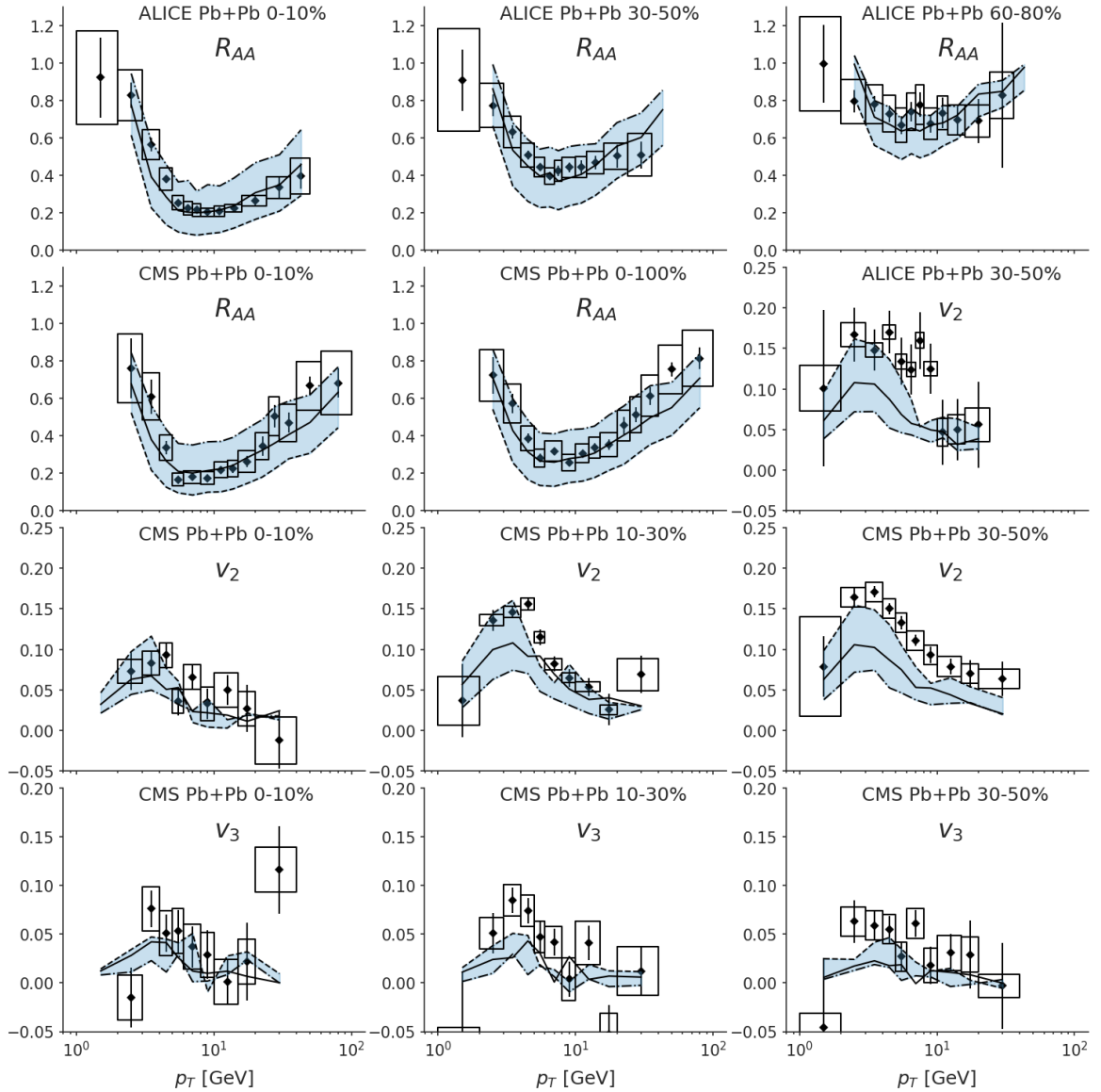


Figure 4.8: Benchmark results using a running coupling constant. The medium scale that stops the low- Q running is chosen at $Q_{\text{med}} = \mu\pi T = \pi T$ (dashed), $2\pi T$ (solid), and $4\pi T$ (dash-dotted). They are compared to the experimental data (black symbols) obtained by the ALICE Collaboration and the CMS Collaboration.

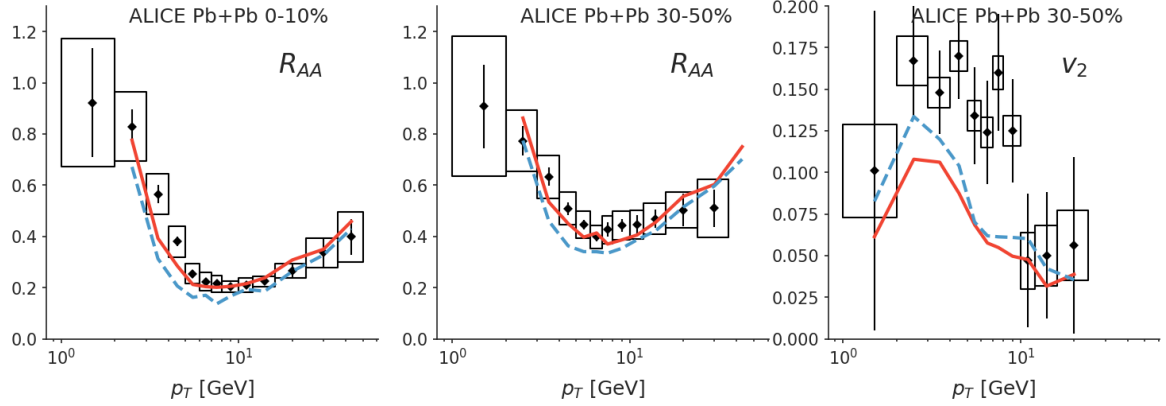


Figure 4.9: Effect of changing the switch scale between small- Q diffusion modeling and large- Q scattering modeling. $\mu = 2$ is used. The red solid lines used a switching scale at $Q_{\text{switch}}^2 = 4m_D^2$, and the blue dashed lines uses $16m_D^2$.

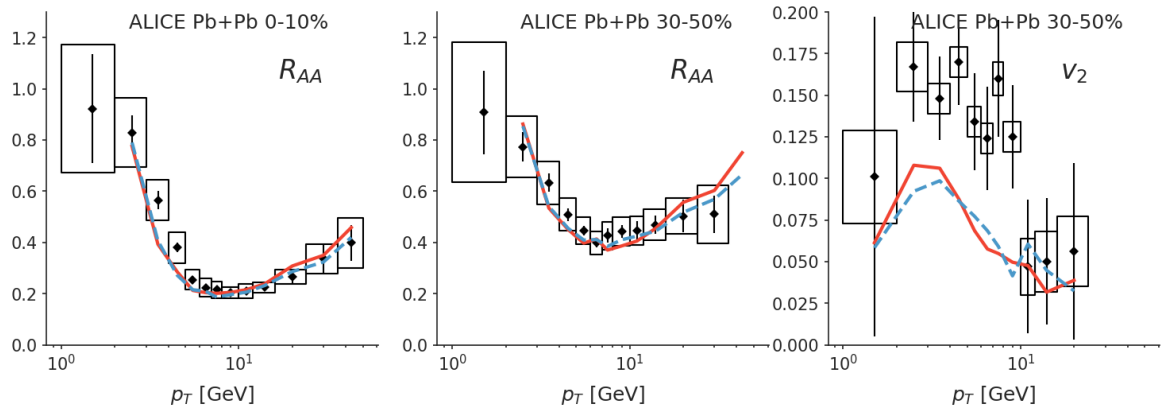


Figure 4.10: Effect of changing the matching scale parameter R_v ($\Delta k_\perp^2 = R_v Q^2$) between the vacuum-like shower and the medium-induced shower. $\mu = 2$ is used. The red solid lines use $R_v = 1$, while the blue dashed lines use $R_v = 1000$, which leave the vacuum-like shower largely unmodified.

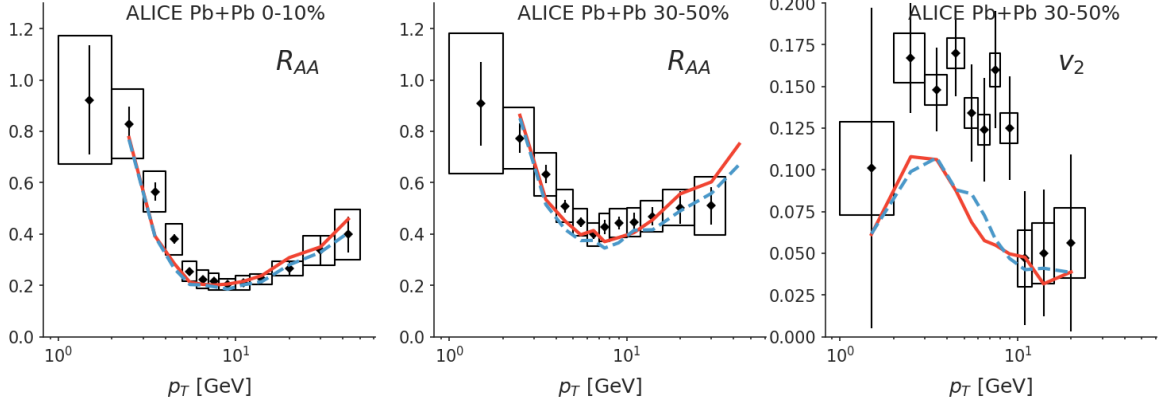


Figure 4.11: The impact of using the “local rate” approximation. The red solid lines use the default implementation; while the blue dashed lines perform the rescatterings in an imaginary infinite box using locally defined temperatures to mimic the “local rate” approximation.

Vacuum / medium-induced radiation matching scale dependence As explained, there is a separation of the treatment of radiation that lives in different regions of phase-space on the Lund-diagram. Accordingly, we need to subtract the vacuum radiation that overlaps with the medium-induced region in the Pythia event generator. In our earlier transport study of heavy flavor [KXB18], this subtraction was not included, therefore, we would like to demonstrate the impact of this mistreatment here.

In figure 4.10, two calculations are shown. The red dashed lines stand for the case where we removed vacuum-like radiations that satisfy $\Delta k_\perp^2 > Q^2$. The blue solid lines are calculations without this subtraction. The two calculations for R_{AA} only differ for $p_T \gtrsim 20$ GeV, because only high- p_T heavy quarks can undergo splittings that take long enough time to receive large medium corrections. Also the difference is larger for central collisions than for peripheral collisions, because medium the effect for the latter is weaker. No significant difference is observed for v_n .

Performance of the “local rate” approximation Finally, it is interesting to examine the effect of an “local rate” approximation of the radiative processes on the observables. It approximates the radiation probability in a medium with slowly varying temperature by the integration of radiation rates defined in an infinite static box with the local temperature at each point. One can also refer to it as the “adiabatic” approximation, because it really assumes the temperature variation is slow compared to the formation time.

We know this approximation can be broken by the fast expansion of the QGP fireball, and would like to quantify the impact. It is easy to mimic the “local” approximation in our model, one can simply let the preformed-gluon rescattering procedure be done in an imaginary medium with the same temperature and flow velocity as those at the point of its production, instead of those in the evolving medium. The resulting comparison is shown in figure 4.11. The local approximation is good except

at very high- p_T ($p_T > 30$ GeV).

Chapter 5

Bayesian model-to-data comparison

We have discussed the modeling details of the heavy flavor transport in relativistic heavy-ion collisions, and have shown a first comparison to data with rather a “naïve” guess of multiple parameters. Till now we have only varied a small subset of them to qualitatively understand the model. In this section, we introduce the advanced statistical tool known as Bayesian analysis that can calibrate all parameters simultaneously to the experimental data. For the full details of such an analysis, we refer the readers to this excellent dissertation on this subject [Ber18] in the context of heavy-ion collisions.

To facilitate the discussion, I define problem for this chapter and introduce a few notations and terminologies. We formulate the general task of a model-to-data comparison into the following form,

- A complex model M , with n input parameters organized as a n -dimensional vector \mathbf{p} .
- There exists a prior belief on the reasonable range of each parameter, known as the prior probability distribution, and for short “Prior”.
- n experimental measurements are organized as an observation vector \mathbf{y}_{exp} of dimension m , with given statistical and systematic uncertainties $\delta\mathbf{y}_{\text{stat}}, \delta\mathbf{y}_{\text{sys}}$.
- The task is to infer the posterior probability distribution of p (Posterior), given the model M , the measurements $\delta\mathbf{y}_{\text{exp}} \pm \delta\mathbf{y}$, and the Prior.

The analysis proceeds in the following steps that are explained in each section.

5.1 Model evaluation

First, we need a fast evaluation of model M at any point in the considered region of parameter space. This is done by sampling the high-dimensional input parameter space at N carefully designed points and then interpolates. This N set of parameter vectors of length n forms a so-called design matrix \mathbf{D} ,

$$\mathbf{D}_{N \times n} = \begin{bmatrix} p_{11} & p_{12} & \cdots & p_{1n} \\ p_{21} & p_{22} & \cdots & p_{2n} \\ \vdots & \vdots & \ddots & \vdots \\ p_{N1} & p_{N2} & \cdots & p_{Nn} \end{bmatrix} \quad (5.1)$$

where the first index is the label of different parameter set, and the second index labels different parameters.

We use the so-called Latin-Hyper-Cube sampling method to determine the location of these points in parameter space. It generates a semi-random design subject to the following constraints:

- The marginalized distribution on any parameter is a uniform distribution. This is different from a grid design, where the marginalized distribution are spiky delta functions on the grid points.
- The minimum distance between any two points in the parameter space is maximized. This is different from a completely random design in which points may form tight clusters or leave sparsely occupied regions.

Usually, for a well behaved model, the number of design points needed for a good interpolation increases linearly with the number of parameters n . This is in contrast to an exponential increasing with n in a grid design.

The actually model evaluation on these points is the most time consuming part in this analysis. The outputs are organized into the observation matrix,

$$\mathbf{Y}_{N \times m} = \begin{bmatrix} y_{11} & y_{12} & \cdots & y_{1m} \\ y_{21} & y_{22} & \cdots & y_{2m} \\ \vdots & \vdots & \ddots & \vdots \\ y_{N1} & y_{N2} & \cdots & y_{Nm} \end{bmatrix} \quad (5.2)$$

where the first index is the label of different parameter set, and the second index labels different observables. The design matrix \mathbf{D} and the observations matrix \mathbf{Y} help to train a general interpolator to infer the calculated observables at any given parameter value.

5.2 Data reduction

The model M is a mapping of an n -dimesional vector to an m -dimensional vector. One can certainly construct an array of independent m scalar mappings, and interpolate each of them. However, this naïve construction does not make use of the intrinsic correlations / structures that are already present in the training data, and can be very inefficient for practice usage. Considering an observation with two values of R_{AA} and v_2 . Usually the larger the R_{AA} the model predicts, the smaller the v_2 , and thus an anti-correlation is expected. If one build interpolators for them independently, their uncertainties are also going to be independent, and the true covariance is omitted. However, if one interpolates the linearly combinations $aR_{AA} \pm bv_2$; then a wise choice of a, b can largely reduces the correlation between these two “newly” constructed observables.

The principal component analysis (PCA) is a systematic way to implement this idea. The original vectors of observables are transformed into the principal-component (PC) space, with each PC a specific linear combination of the original observables, so that the covariances between the newly defined observables (the PCs) vanish.

Mathematically, this is the same as finding the singular value decomposition (SVD) of $\tilde{\mathbf{Y}}$. $\tilde{\mathbf{Y}}$ is the standardized observation matrix \mathbf{Y} ,

$$\tilde{y}_{ij} = \frac{y_{ij} - \mu_j}{\sigma_j} \quad (5.3)$$

with μ_j and σ_j the mean and the standard deviation of column j . Then the SVD proceeds as,

$$\tilde{\mathbf{Y}}_{N \times m} = \mathbf{U}_{N \times N} \boldsymbol{\Sigma}_{N \times m} \mathbf{V}_{m \times m}. \quad (5.4)$$

Here $\boldsymbol{\Sigma}$ only contains the variance of each PCs on its diagonal. The PCs are defined as the components after the V transformation.

$$z = \mathbf{V}y \quad (5.5)$$

It is evident that the covariance matrix of the z observables is diagonalized,

$$\text{Var}(z_i, z_j) = \frac{1}{N} V_{ii'} \tilde{Y}_{ki'} V_{jj'} \tilde{Y}_{kj'} = \frac{1}{N} V \tilde{Y}^T \tilde{Y} V^T = \frac{1}{N} \boldsymbol{\Sigma}. \quad (5.6)$$

So different PCs are orthogonalized. Another benefit is data reduction. Suppose the variance in $\boldsymbol{\Sigma}$ has been ordered from maximum to minimum. For data with pronounced structures, often the first few PCs take into account the majority of the data variance. Practically, a truncated set of PCs already gives a good representation of the original data, and this greatly reduces the computations necessary for interpolating a large number of observables. Certainly, one can always go back from the PC space to the original space by the inverse transformation $y = V^{-1}z$.

5.3 Model emulator

With limited information on a finite number of design points contained in the matrices D and M , the original mapping is approximated by a model emulator (a surrogate model) using a Gaussian Process (GP). The Gaussian Process provides a non-parametric interpolation for scalar function with one or high dimensional input. We shall let the readers refer to [RW06] for the technical details and only summarize the basic of the Gaussian Process.

Gaussian Process Taking a uni-variate case as an example, given an array of input and an array of output, the common way to interpolate the data is, e.g., polynomial interpolation. However, polynomials only uses local information of the grid, and its performance can be sensitive to the error of the output (e.g. statistical fluctuation in the simulation). Moreover, it is hard to work with a Latin-hypercube design because the design points are not arranged on a grid. In contrary, a GP does not make any assumption on the functional form of the interpolation, but infers the output at a certain input based on how the output at the present point correlates with those

given outputs at other input points. Mathematically, one assumes that elements of the predicted output \mathbf{y}^* at input \mathbf{x}^* and the known outputs $\mathbf{y}_{\text{train}}$ at the training points $\mathbf{x}_{\text{train}}$ form a multi-variate normal distribution,

$$\begin{bmatrix} \mathbf{y}^* \\ \mathbf{y}_{\text{train}} \end{bmatrix} \sim \mathcal{N} \left(\begin{bmatrix} \mu^* \\ \mu_{\text{train}} \end{bmatrix}, \begin{bmatrix} \Sigma(\mathbf{x}^*, \mathbf{x}^*) & \Sigma(\mathbf{x}^*, \mathbf{x}_{\text{train}}) \\ \Sigma(\mathbf{x}_{\text{train}}, \mathbf{x}^*) & \Sigma(\mathbf{x}_{\text{train}}, \mathbf{x}_{\text{train}}) \end{bmatrix} \right) \quad (5.7)$$

μ^* and μ_{train} are the mean values and can be often set to zero after standardizing the training data. The Σ s form the co-variance matrix, and each of them has the same shape of the outer product of its two arguments. Its matrix-element (the kernel function) are parametric, and one often takes a squared exponential form,

$$\Sigma_{ij} = k(x_i, x_j) = \sigma^2 \exp \left(-\frac{(x_i - x_j)^2}{2l^2} \right). \quad (5.8)$$

σ^2 is the auto correlation. The co-variance decays exponentially with the squared separation of the two input points. In such a way, points that are close in inputs will also be close in outputs, and points that are far apart are effectively uncorrelated.

Conditioning a Gaussian Process The outputs at training points are known. Therefore, the probability distribution of \mathbf{y}^* is obtained by conditioning the training outputs on their actual values,

$$\begin{aligned} \mathbf{y}^* \sim & \quad \mathcal{N} \left(\Sigma(\mathbf{x}^*, \mathbf{x}_{\text{train}}) \Sigma^{-1}(\mathbf{x}_{\text{train}}, \mathbf{x}_{\text{train}}) \mathbf{y}_{\text{train}}, \right. \\ & \quad \left. \Sigma(\mathbf{x}^*, \mathbf{x}^*) - \Sigma(\mathbf{x}^*, \mathbf{x}_{\text{train}}) \Sigma^{-1}(\mathbf{x}_{\text{train}}, \mathbf{x}_{\text{train}}) \Sigma(\mathbf{x}_{\text{train}}, \mathbf{x}^*) \right) \end{aligned} \quad (5.9)$$

Note that the conditional multivariate normal distribution is still a normal distribution, with modified mean and co-variance matrix. One can easily check that if the predicted input approaches one of the training inputs, the distribution of the output approaches an delta function (as the limit of a narrow Gaussian) at the training output.

Hyperparameters and training We have not discussed the parameters in the kernel function $k(x, x')$ too much yet. They are the auto-correlation σ^2 and the correlation length l . The squared exponential form is not the only possible kernel function, more sophisticated choices with more parameters are designed for various problems. They are known as hyper-parameters (denoted as a vector θ), and should in principle, also be treated as unknown parameters in the calibration. But a common practice to reduce the complexity is to fix the hyper-parameters at a set of “optimal values” by minimizing the loss function \mathcal{L} ,

$$\mathcal{L} = -\ln p(\mathbf{y}|\theta) = \frac{1}{2} \ln \det \Sigma(\theta) + \frac{1}{2} \mathbf{y}^T \Sigma(\theta)^{-1} \mathbf{y} + \frac{N}{2} \ln(2\pi) \quad (5.10)$$

where \mathbf{y} is the (PCA transformed) training data, and N is the number of training points. The minimization process is referred as “training” a Gaussian Process emulator.

Inference with uncertainty quantification Unlike the polynomial interpolation, a GP does not provide a single estimation of the output, but infers the probability distribution of the predicted outputs by giving both the mean and the co-variance matrix. This is a huge advantage of the Gaussian Process as it quantifies its own interpolation uncertainty.

Validation Though the training process includes a penalty for over-fitting the data, whether the trained GP has over-fitting problem can only be checked by validation. A validation is done by performing the model calculation at novel points in the parameter space that the GP was not trained on, then comparing the trained GP's prediction $y_i \pm \sigma_i$ to the model calculation $y_{\text{validate},i}$. If an emulator is trained to work properly, then the standardized deviation $(y_i - y_{\text{validate},i})/\sigma_i$ should follow approximately a standard normal distribution.

Multivariate inputs and outputs The GP formulation can be easily generalized to higher dimensional inputs by specifying a multidimensional kernel function. For high dimensional outputs, one first applies the PCA analysis introduced in the previous section and the build individual GPs for each of the first N_{PC} principal components that take most of the data's variance.

5.4 Bayes' theorem and Markov chain Monte Carlo

With the model emulator M (we are using the same symbol as the model, but one should always remember that the emulator is only a fast surrogate of the original model and comes with uncertainty), we apply Bayes' theorem, the essence of the statistical analysis. Bayes' theorem provides a quantitative way to update the knowledge of model parameters with empirical observations,

$$\text{Posterior}(\mathbf{p}|M, \mathbf{y}_{\text{exp}}) \propto \text{Likelihood}(\mathbf{y}_{\text{exp}}|M, \mathbf{p}) \times \text{Prior}(\mathbf{p}). \quad (5.11)$$

It states that the posterior probability distribution of parameters, given model and experimental measurements, is proportional to the likelihood of describing the experiments with the model using this set of parameters, times the prior belief of the distribution of the parameters. The likelihood function is often assumed to be a multivariate Gaussian,

$$\text{Likelihood}(\mathbf{p}) = (2\pi)^{-\frac{m}{2}} (\det |\Sigma|)^{-\frac{1}{2}} \exp \left\{ -\frac{1}{2} \Delta \mathbf{y}^T \Sigma^{-1} \Delta \mathbf{y} \right\}, \quad (5.12)$$

$$\Delta \mathbf{y} = \mathbf{y}(\mathbf{p}) - \mathbf{y}_{\text{exp}} \quad (5.13)$$

where the $\mathbf{y}(\mathbf{p})$ is the model emulators' prediction at parameter point \mathbf{p} , m is the number of observables. The prior distribution is often a multi-dimensional uniform distribution within a reasonable range. The co-variance matrix contains various sources of uncertainties from both theory and experimental side.

A model dependent statement The posterior is always defined with a given model, and therefore even the extraction of theoretically well defined quantities can be affected by the use of different dynamical modeling assumptions and approximations. The ultimate solution is of course the improvement of model's physical accuracy. Using a flexible model or models with different (but reasonable) assumptions to extract the same quantity can help estimate the level of theoretical uncertainty.

The covariance matrix covariance matrix is decomposed into different contributions,

$$\Sigma = \Sigma_{\text{stat}} + \Sigma_{\text{sys}} + \Sigma_{\text{emulator}} + \Sigma_{\text{truncation}} + \Sigma_{\text{model, sys}} \quad (5.14)$$

- The statistical co-variance takes the diagonal form, $\Sigma_{\text{stat}} = \delta_{ij}\delta\mathbf{y}_{\text{stat},i}^2$. $\delta\mathbf{y}_{\text{stat},i}$ is the experimental statistical uncertainty.
- The experimental systematic uncertainties Σ_{sys} can be correlated for different observations, so generally its off-diagonal elements are non-zero,
- The emulator covariance Σ_{emulator} is the prediction covariance of the GPs in the PC space and then transformed into the physical space.
- The truncation covariance $\Sigma_{\text{truncation}}$ take those less important principal components that are not being emulated by GPs into account. Its variance is first computed in the PC space and then transformed back to the physical space.
- Finally, $\Sigma_{\text{model, sys}}$ stands for the model uncertainty. It is always present but is hard to quantify using the model itself. Therefore, the previous study [Ber18] assign a variable model systematic uncertainty parameter σ and this parameter will be treated as uncertainty in the calibration as well. The σ stands for a uniform model uncertainty fraction on each principal component, and is added to the emulator prediction covariance. The σ parameter is given an information prior distribution $P(\sigma) \propto \sigma^2 e^{-\sigma/0.05}$. Meaning an expectation of 15% model uncertainty. The exact origin of this model uncertainty is unknown, but it plays a role as a “regulator” in the fitting process to prevent the model trying to explaining feature that can never be described better than at the σ level precision.

Marginalize the posterior distribution The resultant posterior distribution is a function of n parameters. To answer what is the probability distribution of one parameter folded with the uncertainty from other parameters, one looks at the marginalized distribution with the other $n - 1$ parameters integrated out. This is done by a Markov chain Monte Carlo (MCMC) sampling of the posterior function using an ensemble of n -dimensional walkers whose distribution thermalizes into the target posterior distribution function. The marginalized distribution is then the distribution of the projected ensemble onto one dimension. Similarly, a marginalization of the joint distribution of two or more parameters can be obtained similarly.

Chapter 6

Results

In this chapter, we apply the advanced statistical tools to the heavy-flavor transport model and extract the heavy quark transport coefficients. I would like to present this in a two step processes to show the improvements of the latest extraction.

A list of experimental data

6.1 Lessons from earlier extractions of \hat{q}_Q

In an earlier publication [KXB18], we used a linearized Boltzmann model with the coherence factor approach to implement the LPM effect. The heavy quark initial momentum distribution was obtained from the FONLL calculation. We have already commented on the advantages and disadvantages of these choices. Two different sets of nuclear PDF–EPPS and nCTEQ15–were used to represent the uncertainty from the cold nuclear matter effect in the \hat{q} extraction.

Regarding model parameters, the one parameter for the perturbative elastic and inelastic scatterings was controlled by $1/3 < \mu < 4$ in the running coupling. There was an additional pure diffusion process with a diffusion constant κ_{NP} parametrized to peak at low temperature and low energy, in order to mimic the non-perturbative coupling between a low energy probe and the medium near T_c ,

$$\kappa_{NP} = T^3 \kappa_D \left(x_D + (1 - x_D) \frac{1 \text{ GeV}^2}{ET} \right). \quad (6.1)$$

The $0 < \kappa_D < 8$ parameter was the overall strength of the diffusion, and the $0 < x_D < 1$ controlled the degree of energy-temperature dependence. One can see that in the heavy quark limit $M \rightarrow \infty$, this parametrization becomes independent of mass. An additional parameter was the in-medium energy loss starting time τ_0 that was allowed to be tuned between $0.1 \text{ fm}/c$ to $1.0 \text{ fm}/c$ (before the onset of hydrodynamics). The reason is our lack of a quantitative description of the production of color charge in the initial stages. This starting time is a simple approximation that interactions was only turned on after τ_0 when the color carries was assumed to approach a Boltzmann distribution.

The design of the four dimensional parameter space $(\tau_0, \mu, \kappa_D, x_D)$ had 80 design points. The computation was carried on the distributed computing system Open Science Grid [PKO⁺07, SBH⁺09] using about a million CPU hours. The observables on which we calibrated are listed in tables 4.1 and 4.2. Including, p_T dependent D -meson nuclear modification factor R_{AA} and p_T dependent (event-shape-engineered) azimuthal anisotropy v_2 . CMS measurements of the B^\pm -meson R_{AA} were also included to constrain the mass dependence of the transport coefficients.

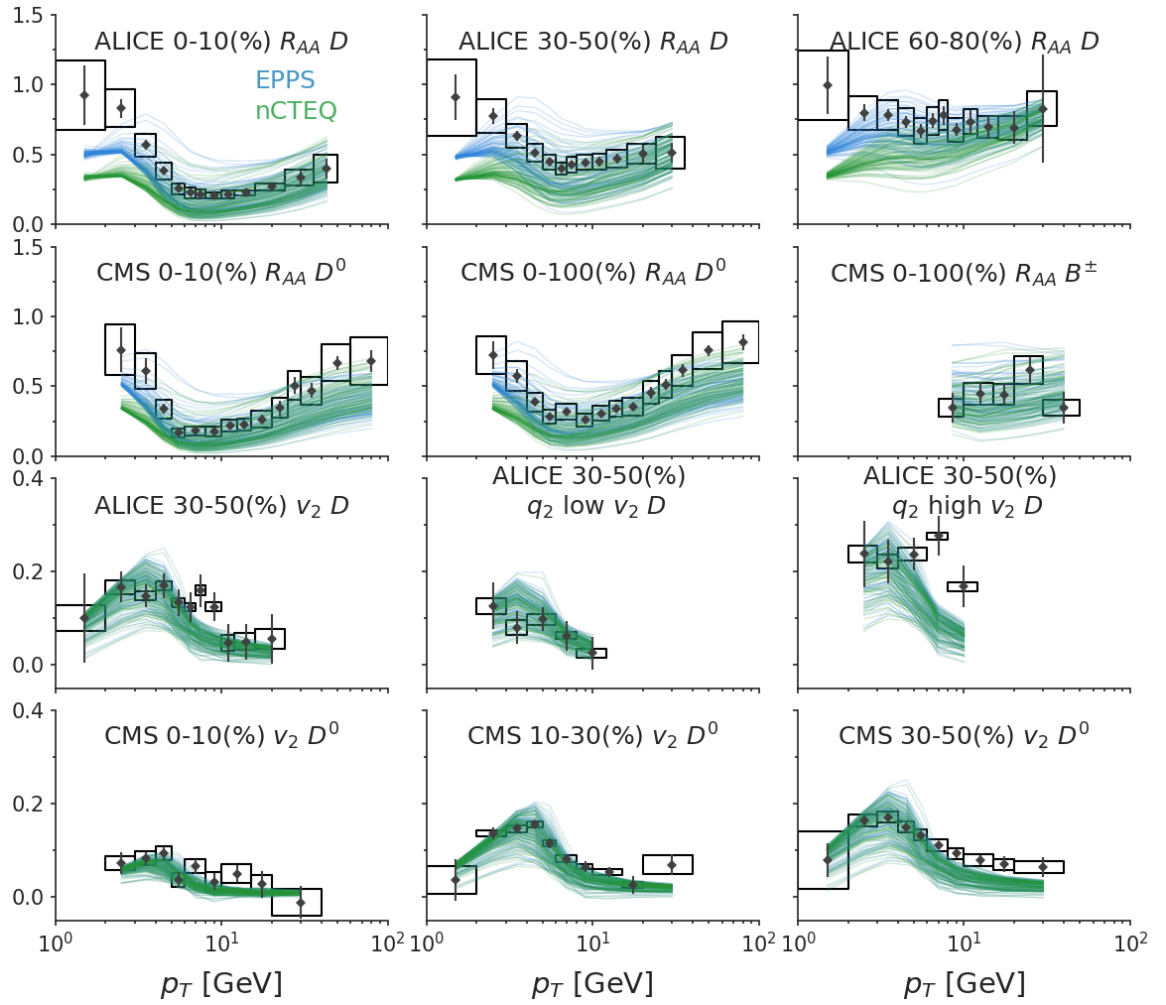


Figure 6.1: The prior distribution of calculated observables compared to data. The colors labeled the use of EPPS (blue) and nCTEQ15np (green) nuclear PDF.

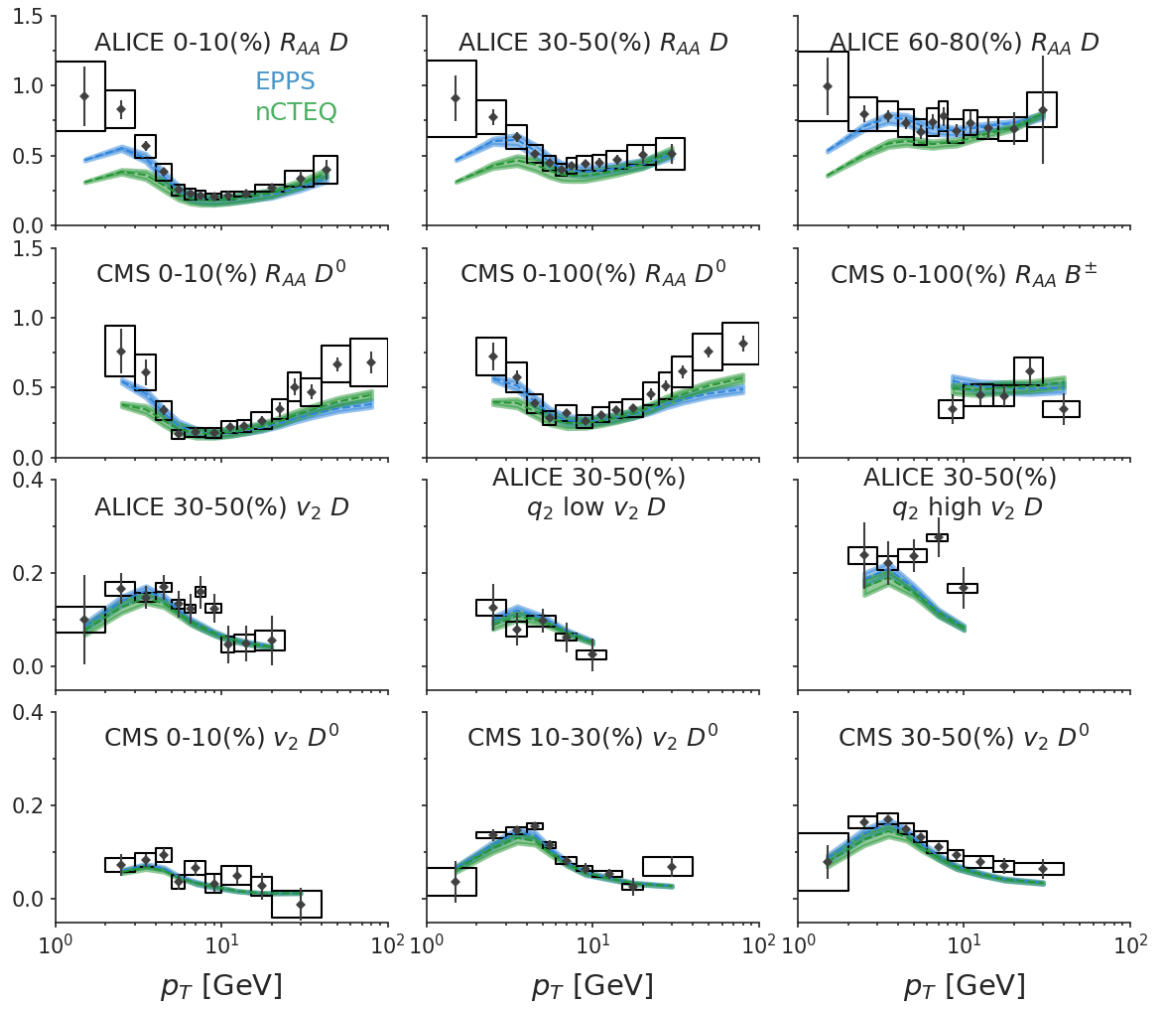


Figure 6.2: The 90% credible region of the posterior distribution of observables compared to data. The colors labeled the use of EPPS (blue) and nCTEQ15np (green) nuclear PDF.

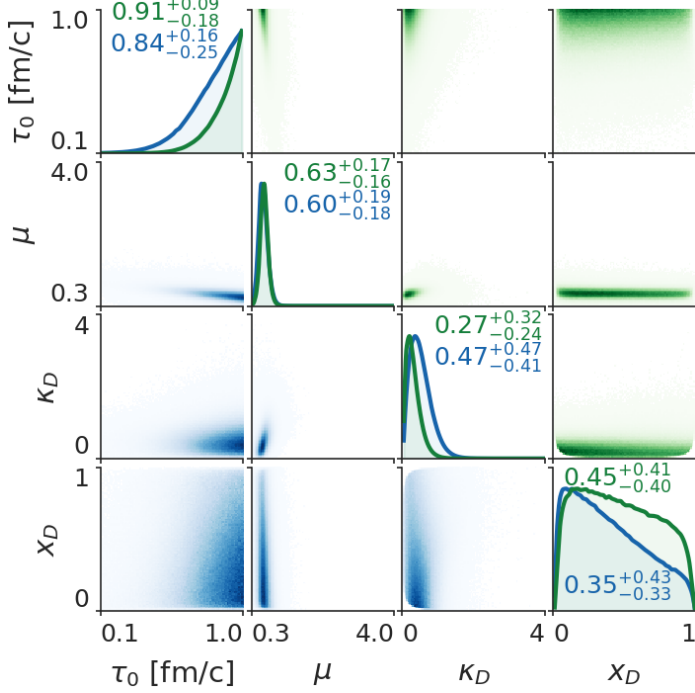


Figure 6.3: Posteriors of single-parameter distributions (diagonal plots) and two-parameter joint distributions (off-diagonal plots). The colors labeled the use of EPPS (blue) and nCTEQ15np (green) nuclear PDF.

The prior and the posterior of the observables before and after the calibration is shown in figures 6.1 and 6.2. blue stands for using EPPS nuclear PDF and green stands for using the nCTEQnp nuclear PDF. We found that the model after the calibration provided a good description of R_{AA} and v_2 at the intermediate p_T of the ALICE experiments. But it did not reproduce the fast uprising shape of R_{AA} at high- p_T of the CMS experiment. In addition, the model seemed to underestimate the high- p_T v_2 of the 30 – 50% centrality bin measured by CMS. The model is able to explain the correlation between the D-meson v_2 and the event-shape, though there are still large fluctuation in the data. The use of different nuclear PDFs had a negligible effect on v_2 , but did affect the R_{AA} at small and large p_T . Another thing worth noting is that the D and B meson R_{AA} were described at the same time.

The inferred posterior probability distribution of the parameters is shown in the figure 6.3. The diagonal plots show single parameterized distributions, and the off-diagonal ones displays the two-parameter correlations. We split the results that use different nuclear PDFs into the upper (EPPS, green heat map and lines) and lower (nCTEQ15np, blue heat maps and lines) triangles. One notices that the results from different nuclear PDF are consistent within the uncertainty; therefore, from now on I shall not stress on any differences between these two sets of results, but combine them into a single distribution to fold in the PDF uncertainty. The favored parameters are $\mu \sim 0.6$ and $\kappa_D \sim 0.4$, indicating a large in-medium α_s and a small amount of additional diffusion. The typical value of α_s is, in fact, so large that one is

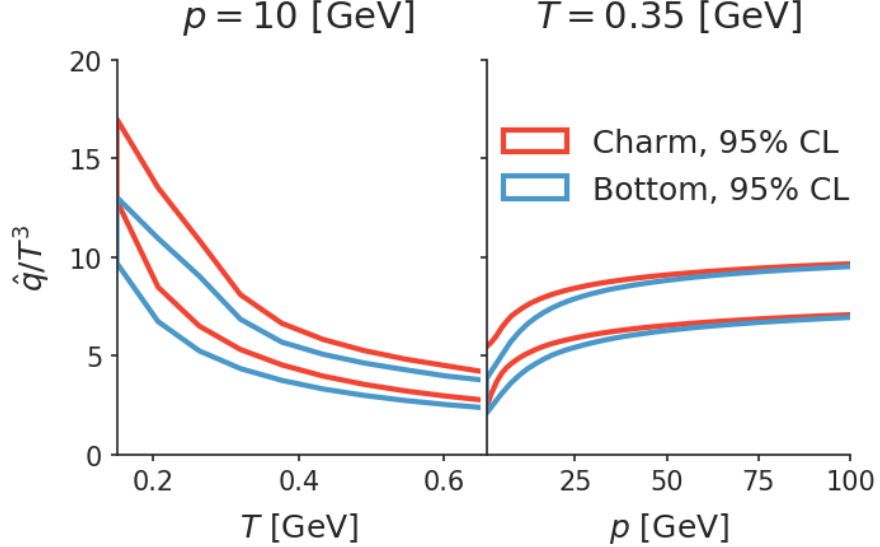


Figure 6.4: The 95% credible region of the heavy quark transverse momentum broadening parameter \hat{q} extracted using the model described in [KXB18]. The charm quark results are shown in red, and bottom results in blue. The difference coming from using different nuclear PDF has been marginalized into the uncertainty bands. Left plot: the temperature dependence at $p = 10$ GeV. Right plot: the momentum dependence at $T = 0.35$ GeV.

let to worry about the use of weakly-coupled approaches. For example, $\alpha_s(0.6\pi T)$ at $T = 300$ MeV is 0.67, corresponding to $g \approx 3$. And the screening mass $m_D \sim 3.6T$ is even larger than the average energy of the thermal partons $3T$. In the discussion of the next section, we will see that this problem can be somewhat alleviated, once we use the improved implementation of the LPM effect and implement a separation of soft-modes into the diffusion constant, though g is still large.

Transport coefficients In this analysis, the heavy quark transport coefficient \hat{q} is computed by adding up the momentum broadening from both the scattering and the parametric diffusion,

$$\hat{q} = 2T^3\kappa_D \left(x_D + (1 - x_D) \frac{\text{GeV}^2}{ET} \right) + \hat{q}_{\text{el}}. \quad (6.2)$$

In a perturbative definition of the transport coefficients, the inelastic process does not contribute to heavy quark transport coefficient at leading order. In figure 6.4, the 95% credible region of \hat{q} is shown as a function of temperature at a fixed energy (left), and as function of energy at a fixed temperature (right). Results for charm (red) and bottom (blue) quarks are labeled by different colors. The mass difference only causes a small difference in \hat{q} .

Comparison to results from an improved-Langevin model The same transport coefficient is also extracted using the improved-Langevin model [CQB13a]. It

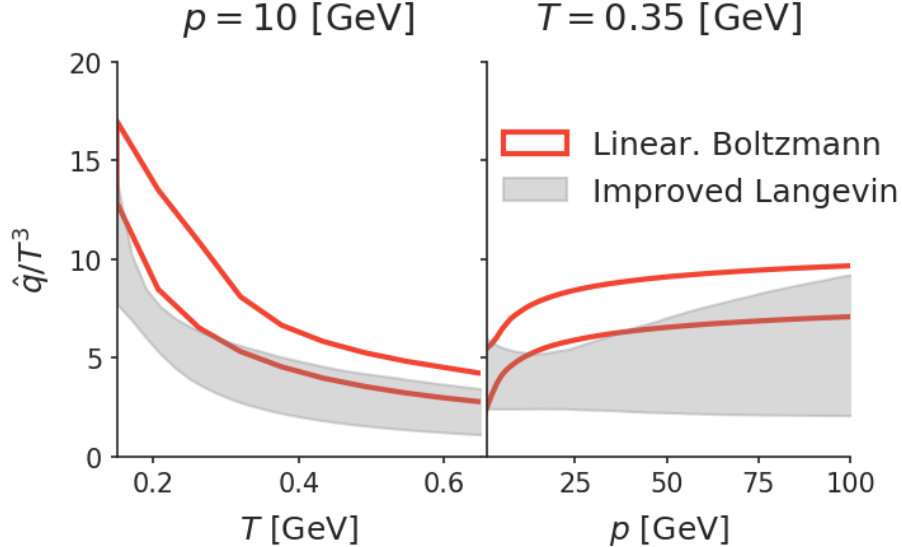


Figure 6.5: Comparison of the 95% credible region of the charm \hat{q} using different models. The red regions use the model described in [KXB18], while the shaded regions are obtained using the improved-Langevin model [CQB13a].

includes a diffusion modeling of the elastic interaction, a higher-twist single gluon emission rate, and a similar routine to implement multiple radiations. This model is then coupled to the same medium as the one used here and compared to the same set of observables as this work does. The resultant posterior (for charm quarks only) is shown as the shaded region in figure 6.5. We see that the \hat{q} extracted using the two models only overlap at the boundary of the credible region. Their difference is comparable to the uncertainty band of either model, while both models provide a reasonable description of the data. This suggests that the theoretical uncertainty that comes from the assumption made about the probe-medium is a significant one. The ability to tune a switching scale parameter in the new model intends to include this type of theoretical uncertainty.

6.2 Calibration using the improved transport model

Finally, we apply the improved model to the extraction of the heavy quark transport coefficients. Here we summarize the improvements:

- A more sophisticated implementation of the LPM effect to reduce modeling uncertainty of the radiative processes;
- An interpolation between the diffusion picture and the scattering picture to take into account modeling uncertainty.
- Separation of the high-virtuality evolution and the low-virtuality transport equation at a medium scale.

Table 6.1: Prior range of parameters

Symbol	Description	Range
$\xi = \frac{\tau_0}{\tau_{\text{hydro}}}$	Energy loss starting time	(.1, .9)
$c = \frac{Q_{\text{cut}}^2}{m_D^2}$	Soft / hard switching scale	(.1, 10.)
R_v	Vacuum / Medium matching scale	(0, 7)
μ	Running α_s stops at $Q = \mu\pi T$	(.6, 10)
K	Magnitude of $\Delta\hat{q}/T^3$	(0, 15)
p	E -dependence of $\Delta\hat{q}/T^3$	(-2, 2)
a		(-1, 1)
q	T -dependence of $\Delta\hat{q}/T^3$	(-.5, 3)
b		(-.5, 3)
γ	$\Delta\hat{q}_L = (E/M)^\gamma \Delta\hat{q}_L$	(-1, 1)

Model parameters In the new analysis, we try to include as many theoretical uncertainties as possible, so we have more parameters than in the two previous studies. They are listed in table 6.1.

- The first parameter is again the energy loss starting time τ_i . In this analysis, we are comparing to data at two collision energies and the hydrodynamic starting time τ_0 varies from 1.2 fm/ c to 0.6 fm/ c . To account for this differences, we use the ratio $\xi = \tau_i/\tau_0$ as the single parameter for both energies. It means that after ξ fraction of the hydrodynamization time, the color density is assumed to be large enough to apply the linearized transport model.
- The second parameter is switching scale parameter $1.0 < c < 10.0$ in $Q_{\text{cut}}^2 = cm_D^2$. For a typical coupling $g \sim 2$, Q_{cut} is then varied from about $2T$ to $7T$.
- The third parameter $0 < R_v < 7$ controls the matching condition between the vacuum-like radiation and the medium-induce radiation $\Delta k_\perp^2 = R_v Q^2$. At $R_v = 0$, the vacuum-like radiation is completely forbidden once the daughter parton interacts with the medium; for $R_v \gg 1$, the vacuum-like radiation is effectively unmodified.
- The $0.6 < \mu < 10$ parameter controls the in-medium strong coupling constant $\alpha_s(\max\{Q, \mu\pi T\})$.
- The remaining six numbers K, a, b, p, q, γ parametrize a correction to the weakly coupled transport coefficient $\hat{q} + \Delta\hat{q}$, $\hat{q}_L + \Delta\hat{q}_L$,

$$\Delta\hat{q} = \frac{KT^3}{\left[1 + \left(a\frac{T}{T_c}\right)^p\right] \left[1 + \left(b\frac{E}{T}\right)^q\right]}, \quad (6.3)$$

$$\Delta\hat{q}_L = \left(\frac{E}{M}\right)^\gamma \frac{\Delta\hat{q}}{2} \quad (6.4)$$

$0 < K < 15$ is the overall magnitude of the correction. The deviation from the T^3 dependence and the energy dependence are parametrized using two dimensionless combinations T/T_c , and E/T . The γ parameter varies from -1 to 1

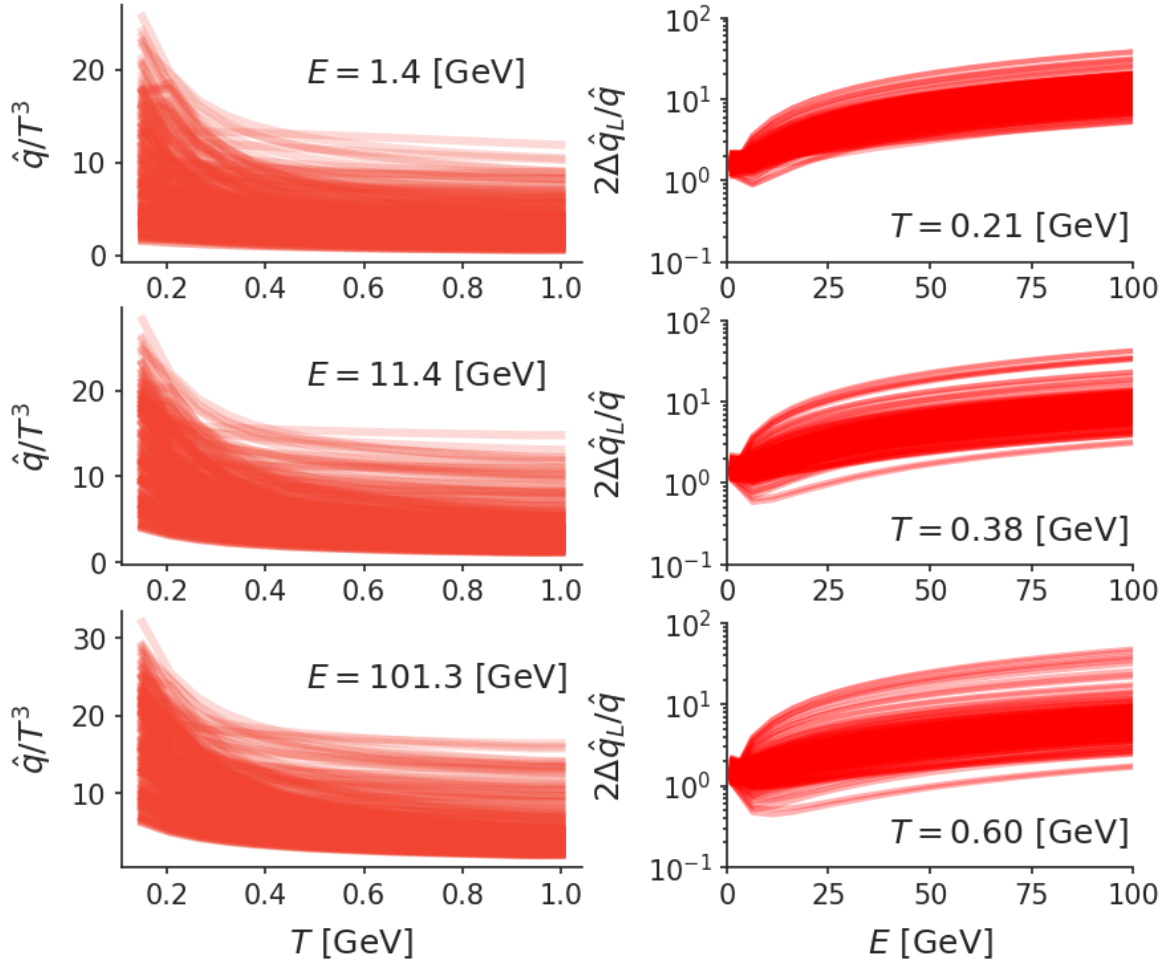


Figure 6.6: Left: the prior range of the transport parameter \hat{q} as function of temperature at different heavy quark energy. Right: the prior range of the longitudinal diffusion parameter \hat{q}_L , plotted as ratio $2\hat{q}_L/\hat{q}$.

allow the correction to be anisotropic. Note that such a construction reverts back to an isotropic diffusion when velocity approaches zero ($E \rightarrow M$).

Design and prior We choose to give $\ln c$, $\ln R_v$, $\ln \mu$, $\ln a$ and $\ln b$ a uniform design and a uniform prior. Therefore, the original parameter will have a non-uniform design and prior distribution. The reason is that these parameters either cause a logarithmically slow change of the model prediction or their prior uncertainty is large that they are allowed to vary by orders of magnitude. For example, the μ parameter enters the logarithmic running of α_s and we can rewrite the maximum possible α_s as,

$$\alpha_{s,\max}(T) = \frac{2\pi}{9} \frac{1}{\ln(\mu) + \ln(\pi T / \Lambda_{\text{QCD}})} \quad (6.5)$$

Therefore, we assign a uniform prior to $\ln(\mu)$ so that α_s also varies notably within the prior range. For the c and R_v parameter, we have seen in the previous benchmark

calculation that the R_{AA} and v_2 predictions depend fairly weakly on the choice of these parameters, therefore they are also given a logarithm prior. For the a and b parameters, one notices that asymptotic largeness or smallness of these numbers do not change the value of $\Delta\hat{q}$ notably. By applying the logarithmic prior, we can explore both the large and small limits of these numbers while still having enough design points to control the interpolation uncertainty in the physically interesting regions (a and b are of order one).

We sample 250 design points and 50 validation points. Combining μ, K, p, q, a, b and γ , the prior region of the heavy quark transport parameters are plotted as a function of temperature and energy in figure 6.6. On the left, the 250 design \hat{q} 's as function of temperatures are shown (using charm mass for demonstration). Each subplot shows a quark energy at 1.4 GeV, 11.4 GeV and 101.3 GeV. The prior range of \hat{q} varies over an order of magnitude. On the right of the figure, we show the ratio $2\hat{q}_L/\hat{q}$ to indicate the degree of anisotropy of the transport parameters.

The computations of the model on both the design points and the validation points are performed on the NERSC super-computing platform using over two million CPU hours. The observables calculated on the prior are shown in figure 6.7 at LHC energy $\sqrt{s} = 5.02$ TeV and in figure 6.8 at RHIC energy $\sqrt{s} = 200$ GeV. In addition to the LHC dataset used in the last calibration, we also include a dataset at RHIC energy measured by the STAR Collaboration [A^{+17b}, A⁺¹⁹]. We choose two observables at RHIC, namely D meson R_{CP} and v_2 . The new one, R_{CP} , is defined as the N_{bin} normalized ratio between the D meson yield in a smaller centrality class C to a larger centrality class P ,

$$R_{CP} = \frac{dN_C/dp_T N_{\text{bin},P}}{dN_P/dp_T N_{\text{bin},C}}. \quad (6.6)$$

Using the nuclear data as a reference has the advantage of canceling certain theoretical uncertainties, such as the nuclear PDF (if its impact-parameter dependence is neglected) and possible modifications to the initial production mechanism in the nuclear environment. A problem we found at RHIC energy is that even exploring a broad parameter range, the very low- p_T R_{CP} is not well covered by the calculation. This indicates the model will have to be improved in this region of p_T , possibly by a more up-to-date dynamical hadronization model. Our temporary solution is to only include the STAR R_{CP} data above 5 GeV in the calibration.

Emulator validation The validation is performed by comparing the emulator trained on the 250 design points to the actual calculation on the 50 validation points. We visualize the validation in figure 6.9. In the top row, the emulated v_2 (left) and emulated R_{AA} (right) are compared with the model calculations, and the data from different experiments and centrality has been labeled by different colors. The emulated values strongly correlates with the true calculations around the the $y = x$ line. Most points slightly miss the line, meaning the emulator is not 100% accurate. To see if the uncertainty is accounted for, we scatter plot the emulator's prediction uncertainty (1σ , y axis) versus the absolute deviation between the prediction and the

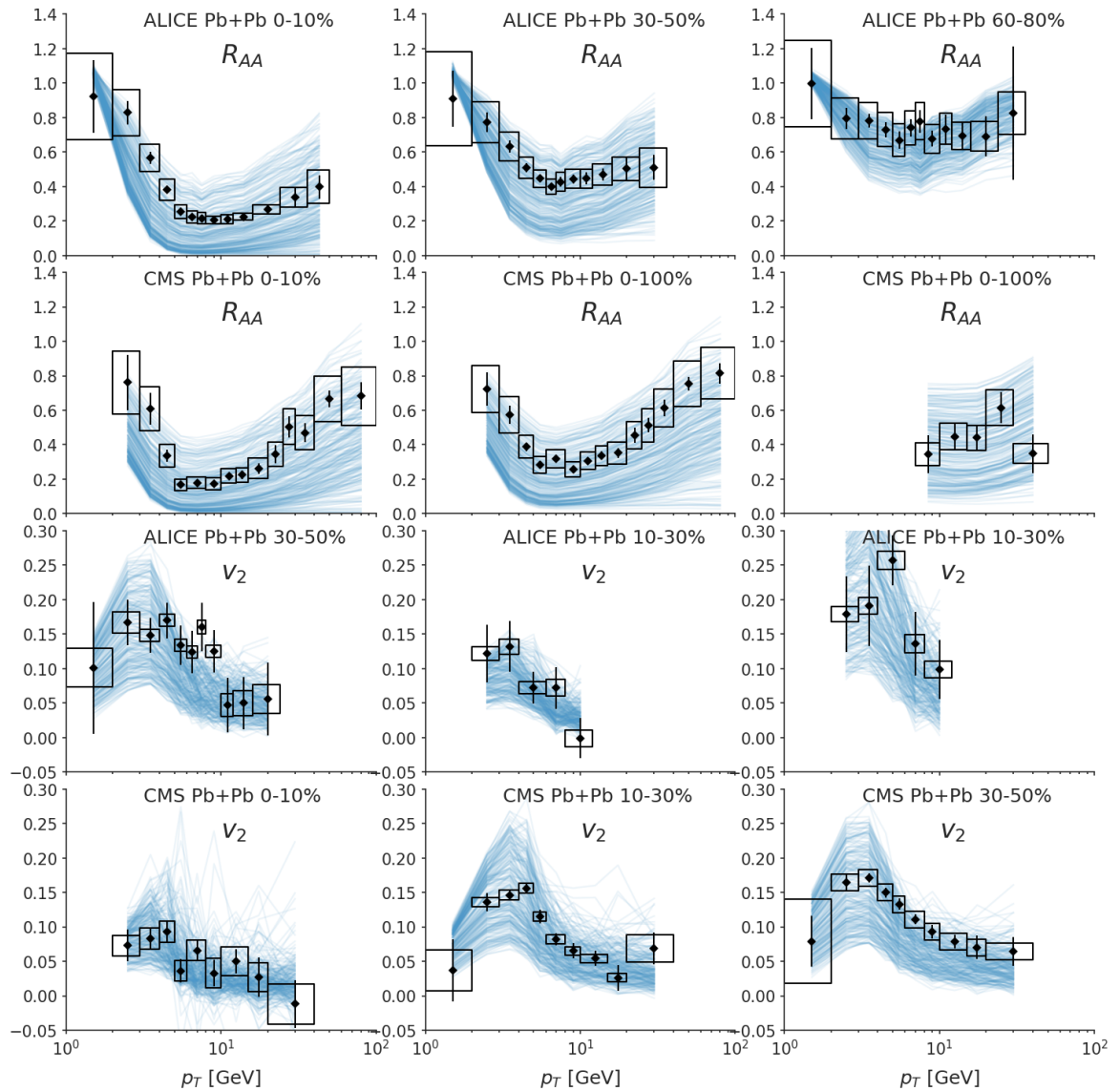


Figure 6.7: The prior distribution of the calculated observables at LHC energy compared to data.

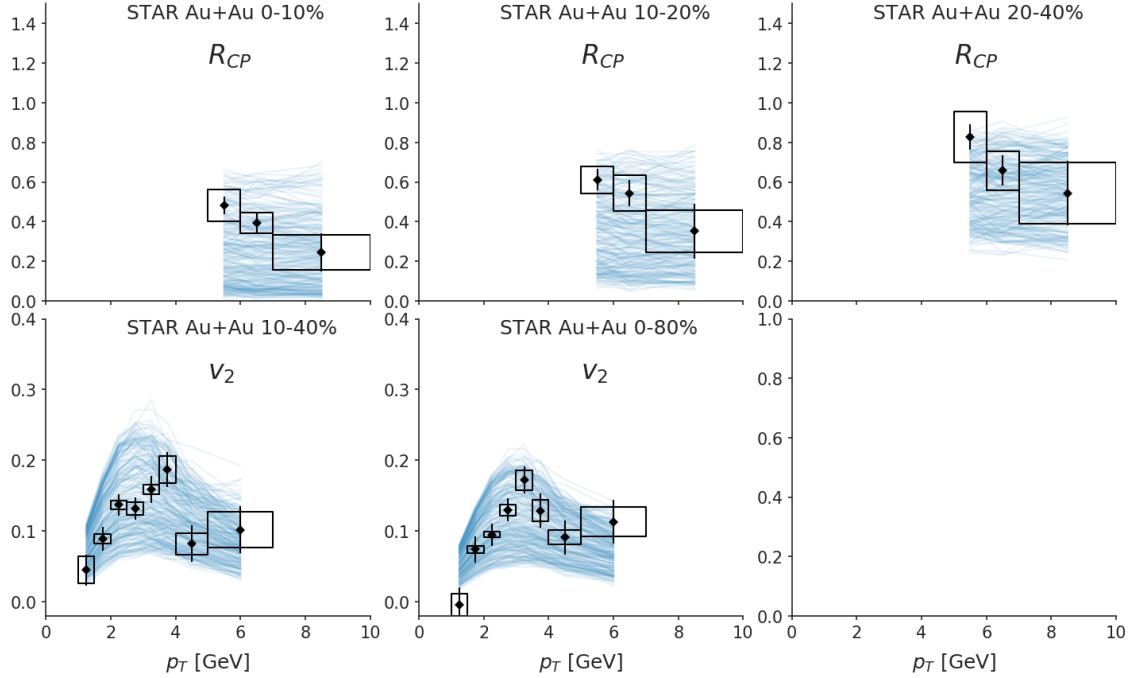


Figure 6.8: The prior distribution of the calculated observables at RHIC energy compared to data.

calculation (the x axis). The dashed line defines the shaded region where the true deviation is larger than $\pm 3\sigma$. We found that over 99% of the prediction are within the 3σ region. Therefore, for most cases the emulator correctly estimates its uncertainty and therefore prevents over-fitting.

Covariance matrix From chapter 5, the covariance matrix has the structure

$$\Sigma = \Sigma_{\text{emulator}} + \Sigma_{\text{truncation}} + \Sigma_{\text{stat}} + \Sigma_{\text{sys}} + \Sigma_{\text{model, sys}} \quad (6.7)$$

The construction of these terms is straight forward, except for the systematic covariance Σ_{sys} of the experimental data. Usually, experiments publish the marginalized uncertainty on each observable point δy_{sys} (for example, R_{AA} of a certain centrality at a single p_T bin), and may specify the nature of the uncertainty as “correlated” or “uncorrelated”. The correlation among uncertainties is important as it directly affects the interpretation of the quality of fit. For instance: a fit with $+5\%$ deviations on each of the N data points will be penalized by a factor $e^{-N(0.05y)^2/\delta y^2}$, assuming uncorrelated uncertainty; while it will only be penalized by $e^{-(0.05y)^2/\delta y^2}$ if one assumes fully correlated uncertainty. This is because fully correlated uncertainty allows data to systematically deviate from a trend.

However, we lack the information to construct the full covariance matrix from δy_{sys} . In this study, we simply parametrize the correlation as function of observables (labeled by $\alpha, \beta \in \{R_{AA}, v_2, R_{CP}\}$), centrality labeled by m, n and transverse

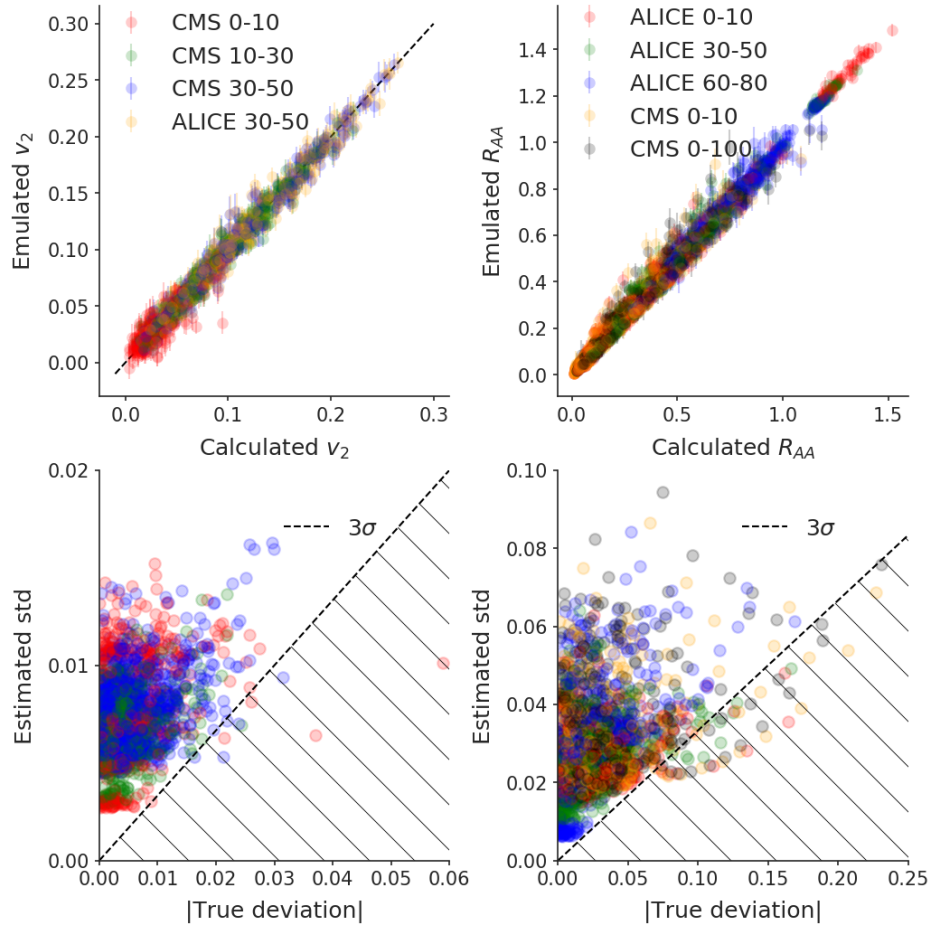


Figure 6.9: Validation of the emulators performance. The top two plots shows the correlation between the calculated quantities (x variable) versus the emulated quantities (y variable). The bottom two plots compare the GP's estimated standard deviation σ of the prediction to the true deviation from the actual calculation. The dashed regions indicates where the true deviations have a larger than 3σ difference from the emulator's prediction.

momentum (labeled by i, j),

$$\boldsymbol{\Sigma}_{\text{sys}} = \delta_{\alpha\beta} C_{mn} \exp \left\{ -\frac{1}{2L_{\text{corr}}^2} \left(\ln \frac{p_{T,i}}{p_{T,j}} \right)^2 \right\} \times \sigma_{\text{sys},i}^{\alpha m} \sigma_{\text{sys},j}^{\beta n}. \quad (6.8)$$

So, the covariance is zero if there are different observables or measurements from different experiments or different particle species. The centrality correlation C_{mn} is only applied to R_{AA} and R_{CP} as these quantities share the same baseline reference across different centrality, so a fraction of their uncertainty must be correlated across-centrality. By default, $C_{m=n} = 1$ and $C_{m \neq n} = 0.3$. The correlation in the p_T dimension is assumed to be a Gaussian in the $\ln p_T$ space with correlation length L_{corr} . We use $\ln p_T$ based on the consideration that the original uncertainty should not be sensitive to the linear change of p_T as there is no other scale present. The default correlation length is 1, meaning the uncertainty is effectively uncorrelated with measurements at a p_T 2.7 times larger or smaller. Finally, this correlation modulation is applied to the completely correlation case of the systematic uncertainty $\sigma_{\text{sys},i}^{\alpha m} \sigma_{\text{sys},j}^{\beta n}$. This construction is entirely parametric, except for the direct experimental inputs $\sigma_{\text{sys},i}^{\alpha m}$. We hope that future measurements will provide more information on the co-variance structure of the published systematic uncertainties.

What we have done is to parametrize the unknown experimental covariance matrix by a reasonable ansatz using two parameters C and L_{corr} . One may try selecting different values C and L_{corr} to do a Bayesian analysis to investigate whether the calibrated parameters are sensitive to these choices. However, since neither of these values is superior than the rest due to the lack of knowledge, the uncertainty from different choices should be considered as another uncertainty to the model-to-data comparison. In the language of the Bayesian analysis, we treat L_{corr} (the C parameter is fixed to the default values for simplicity) as a hyperparameter that appears in the definition of the likelihood function, and use the MCMC to marginalize this parameter when focusing on other parameters. It is given a uniform prior probability distribution within $0.2 < L_{\text{corr}} < 2.0$. This range corresponds to 1σ reduction of the correlation once p_T is multiplied a factor of 1.2–7.4. Meanwhile, the posterior distribution also infers the probability distribution of L_{corr} . We can compare this inference to future experimental estimations of the uncertainty correlation for a consistency check.

Posterior observables The global level of agreement between the calibrated model and the data is shown in figure 6.10 at the LHC energy, and figure 6.11 at the RHIC energy. The black dashed lines show the median prediction, while the blue bands stand for 90% credible region. We remind the reader that because the model predicts anti-correlation between R_{AA} and v_2 , the lower and upper bounds of the uncertainty bands are also anti-correlated. For example, a line that is close to the higher bounds in R_{AA} is likely to be close to the lower bounds in v_2 .

The shape of the D -meson and the B -meson R_{AA} and D -meson v_2 at the LHC energy are described by the calibrated model, while the absolute values of R_{AA} are systematically below the data, so the R_{AA} - v_2 is not entirely solved in the current level

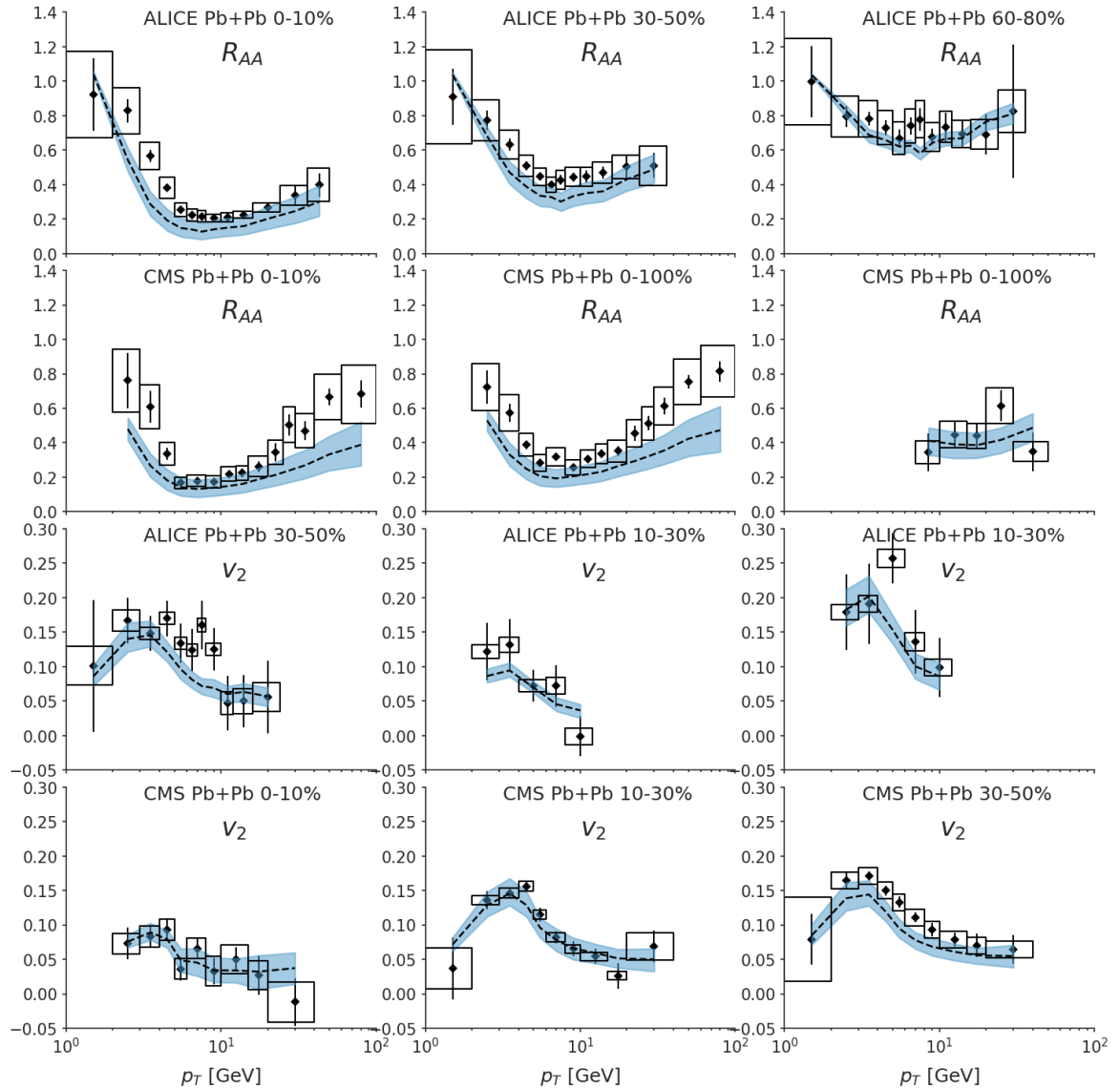


Figure 6.10: The 90% credible region (blue bands) of the posterior distribution of the observables at the LHC energy. Black dashed lines are the median prediction.

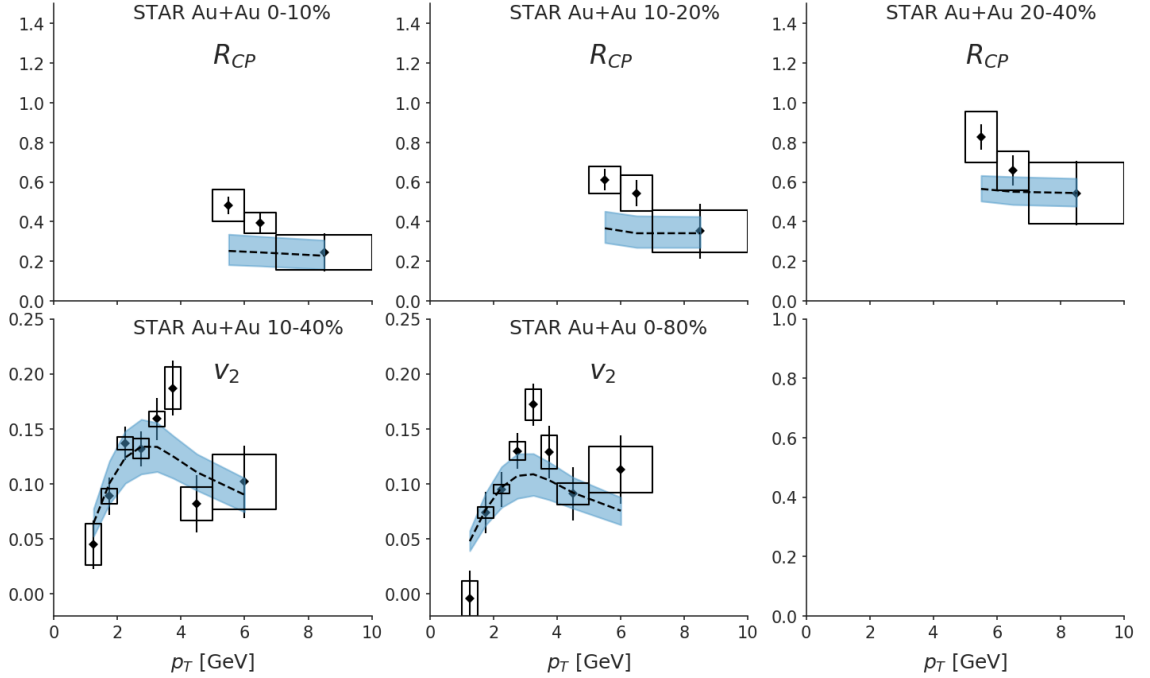


Figure 6.11: The 90% credible region (blue bands) of the posterior distribution of the observables at the RHIC energy. Black dashed lines are the median prediction.

of modeling. A large separation between the event-engineered v_2 is observed and is in a good agreement with data. This means our model correctly accounts for the heavy-flavor response on the event-by-event geometry fluctuation of the medium. At RHIC energy, v_2 is well described. The magnitude of R_{CP} at $p_T > 5$ GeV¹ and its centrality dependences are correctly reflected, though the p_T -shape is too flat compared to the data.

Posterior distribution of parameters Figure 6.12 shows the single parameter posterior (diagonal plots) and two-parameter-joint posterior distributions (off-diagonal plots) of the 10 model parameters, plus the model systematic uncertainty parameter (σ_m). Both the $\ln \mu$ parameter which controls the perturbative coupling and the K parameter which controls the magnitude of parametric diffusion have rather broad distributions. But looking at the correlation between these two parameters, we find that the high-likelihood parameter values can either be around $\mu \sim 1.5, K \sim 0$ or around $\mu \sim 8, K \sim 15$. So that a similar level agreement with data can either be achieved with a more perturbative-driven physics or a more parametric modeling using diffusion. Note that since the origin of this parametric diffusion can also be coming a high-order correction to \hat{q} from a weakly-coupled theory, we cannot immediately interpret a large K value as a large non-perturbative effect.

The resulting posterior of α_s is plotted in figure 6.13, the median value of α_s at $Q = \mu\pi T$ varies from 0.3 to 0.22 for the relevant temperature range $0.15 < T < 0.5$

¹Remember that the model is calibrated on the three data points above $p_T = 5$ GeV

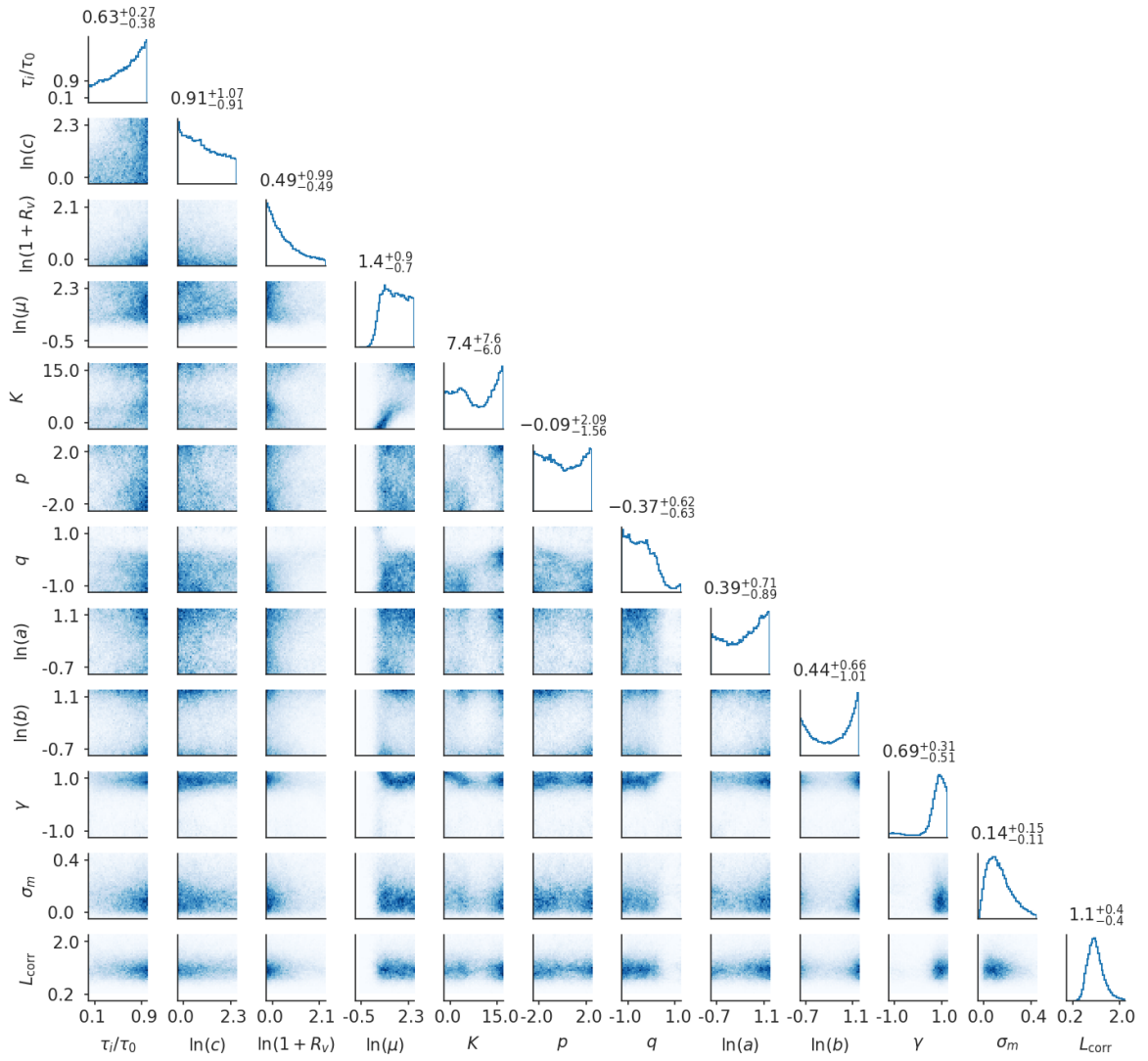


Figure 6.12: The single-parameter posterior distributions (diagonal plots) and two-parameter joint posterior distributions (off-diagonal plots).

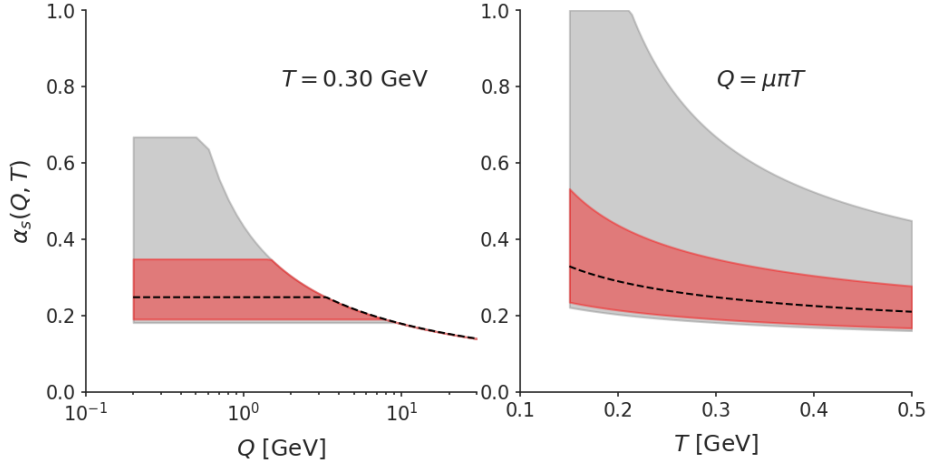


Figure 6.13: Left plot: the scale dependence of the running coupling constant at $T = 0.3$ GeV. Right plot: the temperature dependence of running coupling evaluated at the cut-off scale $Q = \mu\pi T$. The red bands are generated using 90% credible region of the μ parameter; the gray bands are the prior distributions; and the black dashed lines are median predictions.

GeV, corresponding to $g \sim 2$. Compared to the previous extraction, the preferred in-medium coupling strength is smaller and is closer to the phenomenological values used by other studies [B⁺14b]. However, the coupling is still large compared to the weakly coupled assumption $g \ll 1$. This α_s does not stand for the strength of all the probe-medium interaction, recalling that there is a significant parametric diffusion contribution to the elastic energy loss. For radiative processes, though the $1 \rightarrow 2$ splitting vertex explicitly uses this α_s , the strength of the LPM effect is again controlled by the elastic broadening.

The calibration suggests a late energy loss starting time with a medium value around 0.6 of the τ_{hydro} . The switching scale parameter does not have a strong preference as long as it is not too large, which is consistent with our model construction that physical processes should only weakly depend on this switching scale between diffusion and scattering modeling. The posterior matching parameter R_v tends a small value, with a median value 0.6, meaning a matching between vacuum-like and medium-induced showers around $\Delta k_\perp^2 \sim 0.6Q^2$.

The posteriors of p, q, a, b, γ cannot be easily explained individually. It is more instructive to directly look at the posteriors of the transport coefficients \hat{q}, \hat{q}_L . We plot the 90% credible range (red bands) of charm quark \hat{q}, \hat{q}_L on top of their prior range (gray band) in figure 6.14. The values of \hat{q} at $E = 10.4$ GeV are found to be comparable to earlier extractions of the light quark \hat{q} by the JET Collaboration [B⁺14b]². We also present a first extraction of the longitudinal transport parameter \hat{q}_L . The longitudinal transport is quite anisotropic when compared to \hat{q} .

For the heavy quark spatial diffusion constant, since it is related to \hat{q} in the zero

²Note that the JET Collaboration extracts the light quark \hat{q} . However, at $p_T = 10$ GeV, the mass effect of the charm is small and these two numbers should be comparable.

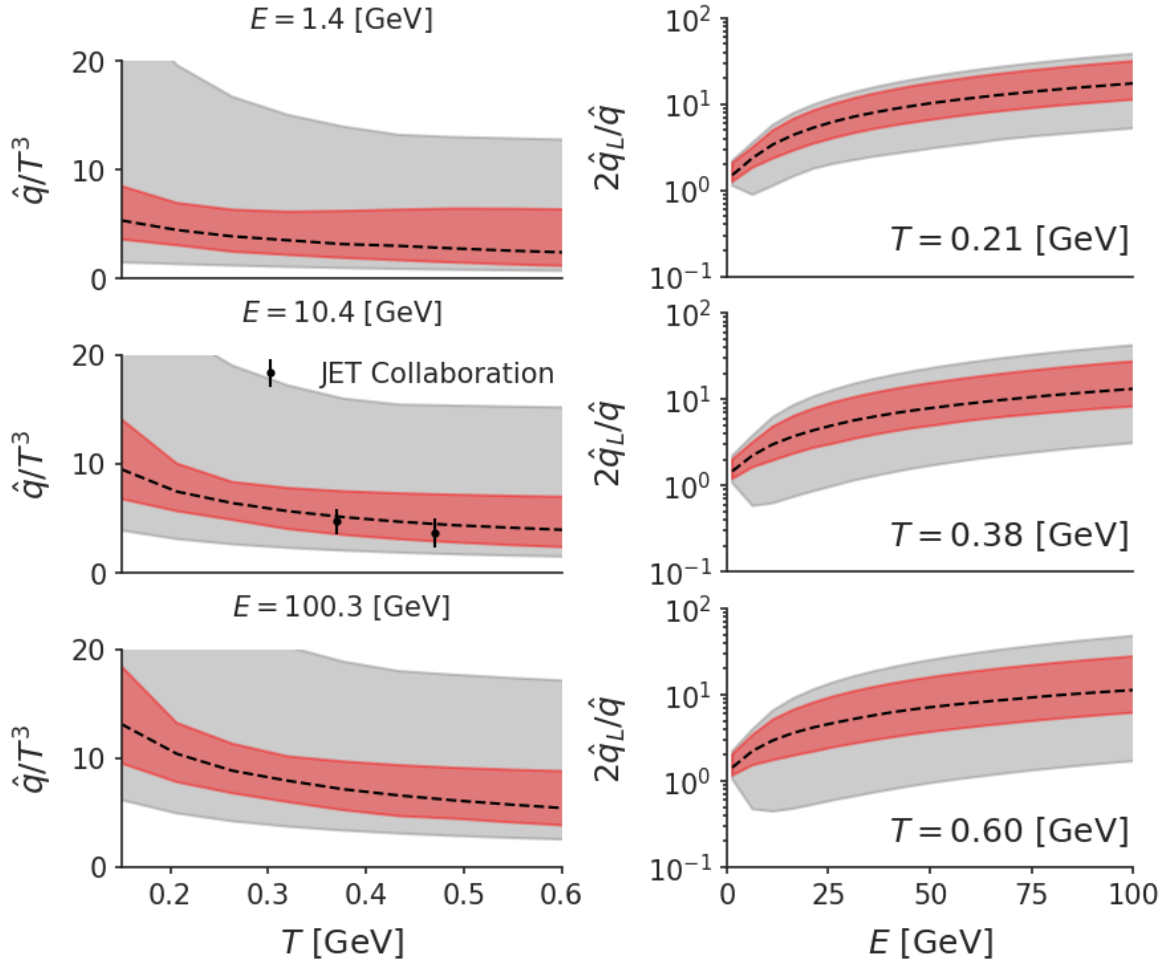


Figure 6.14: The 90% credible region of the charm quark transport coefficients (left plot) and of the longitudinal transport parameter (right plot) are shown in red. The prior range are shown in gray. The results are also compared to the previous JET Collaboration extraction of the light quark transport parameters at $p = 10$ GeV (black symbols).

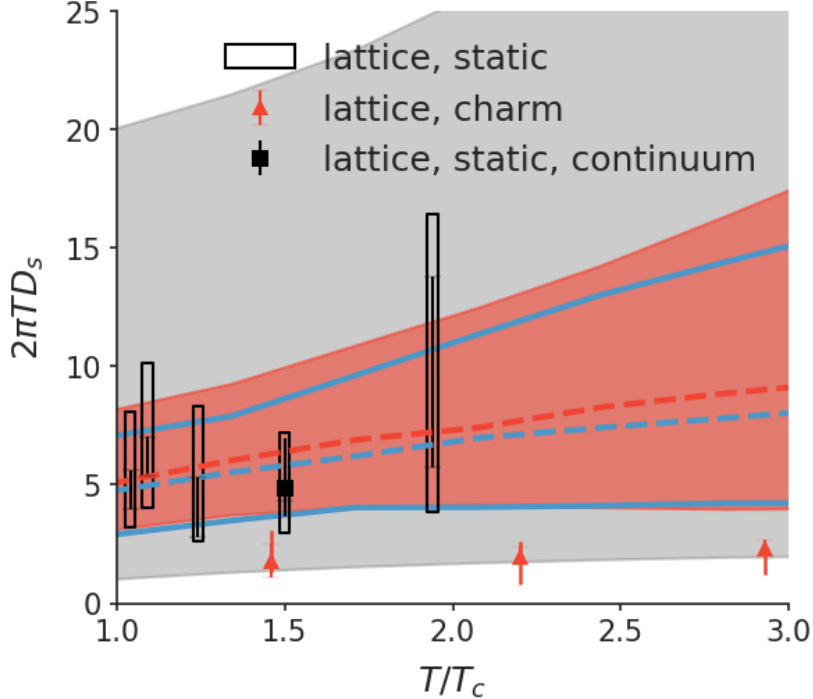


Figure 6.15: The 90% credible region of the spatial diffusion constant defined in the zero momentum limit. Prior range is indicated by the gray band. The posterior of charm and bottom flavor are shown as red band and blue boundary receptively. It is compared to lattice QCD evaluation in references [BDGM12] (black boxes), [FKL⁺¹⁵] (the black dot) and [DFK⁺¹²] (red triangles).

momentum limit, our extraction is essentially an extrapolation of the parametrization and can be sensitive to the detailed choice of the ansatz. Nevertheless, the extraction (red band for 90% credible region) is compared to various lattice calculations [BDGM12, DFK⁺¹², FKL⁺¹⁵] in figure 6.15. Our extraction for both the charm and bottom quark spatial diffusion constants is similar, and is consistent with lattice calculations in the static / infinitely heavy limit of the heavy quark. While the lattice calculation of dynamical charm quarks gives a much lower value of D_s . One may expect that our phenomenological extraction should give a similar separation between bottom and charm flavor, as the bottom is more than three times heavier. However, we found that the mass dependence in the elastic part of our model is relatively weak. First, the mass only affects the phase-space integration of t -channel exchange perturbative scattering. Second, we are using the heavy-quark limit that it does not depend on mass for the diffusion parameter of the weakly coupled theory. Finally, mass only enters the parametric diffusion part through a combination E/T , which is approximately M/T at low momentum, since both charm and bottom mass are already much higher than the typical temperature, therefore the parametric part also introduces only a weak flavor dependence. In the future, one may seek a more physically motivated flavor dependence parametrization of the transport parameters.

Chapter 7

Conclusion

In this dissertation, I have focused on understanding the transport properties of heavy flavor in the strongly coupled quark-gluon plasma applying model-to-data comparison methodology, aiming for model improvements and uncertainty quantification.

A prerequisite for the study is an “accurate” modeling of the physical ingredients to be tested. It is not so trivial to model the heavy quark transport that is coupled to an event-by-event fluctuating and evolving medium. On the one hand, this is because the finite medium-induced radiation formation time at high energy is much greater than the mean-free-path in semi-classical transport equations, and can be comparable to the medium evolution time scales. On the other hand, there are two competing pictures regarding the heavy-quark-to-medium coupling: a weakly coupled picture modeled by scatterings, and a strongly coupled picture whose dynamics is often modeled by diffusion equations. We developed a transport model for hard parton propagation in a near equilibrium plasma. An improved treatment of the LPM effect is implemented and it is shown to reduce to theoretical baseline calculations in idealized infinite static medium limit, and capture qualitative features in a finite and evolving medium. The model also treats the large and small momentum transfer processes with different strategies of few-body scattering and diffusion (plus diffusion-induced radiation), which grants a flexible parametrization of diffusion-like deviations from the leading order weakly coupled approach.

The transport in a hot QGP stage is embedded in a more general “transport” picture including the initial production and high-virtuality evolution, hadronization near the transition temperature and hadronic dynamics and decay. We identify a matching problem between the high-virtuality evolution and medium-induced evolution. Currently, a unified formulation that smoothly connects the virtuality shower and the in-medium shower is still missing, and we use a separation of phase-space to terminate vacuum showers at a scale (Q^2) where they are likely to receive similar amounts of medium modification to the transverse momentum ($\Delta k_\perp^2 \sim Q^2$). The exact location of the separation scale is then treated as an uncertainty of the model.

Finally, we apply a Bayesian analysis to infer the model parameter distribution by comparing to heavy flavor measurements at both RHIC and the LHC. The model parameters include uncertainties such as the in-medium coupling strength, energy loss starting time, matching scale between vacuum and medium-induced shower, diffusion versus scattering model, as well as parametrized deviations from weakly coupled calculations.

We highlight the progress of this work in the conclusion figure 7.1. It visualizes the 90% credible region of the energy and momentum dependence of the heavy quark momentum diffusion transport parameter \hat{q} scaled by T^3 . We found \hat{q}/T^3 gradually increases with $\ln E$ and displays an enhancement near the critical temperature.

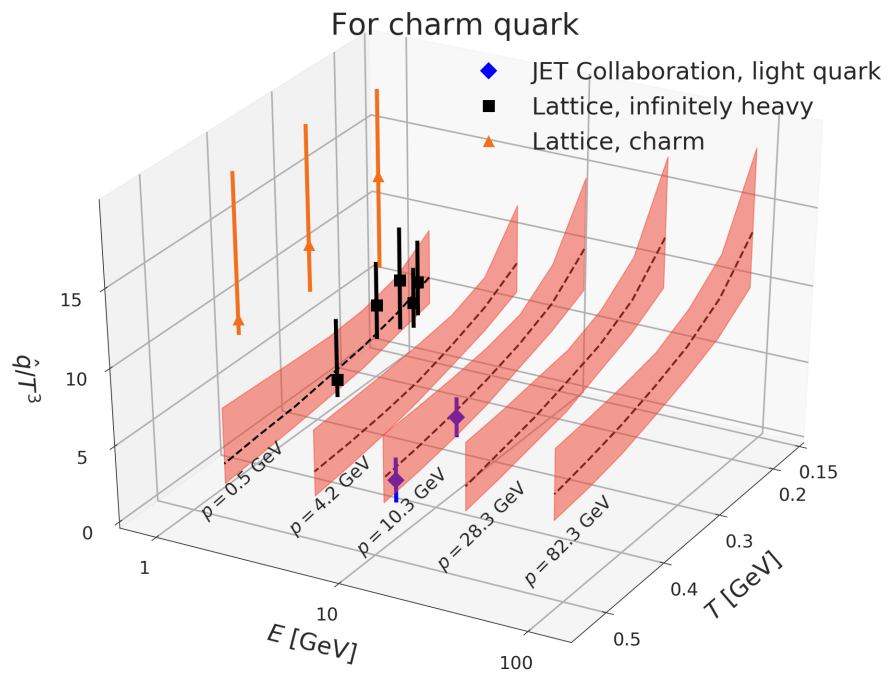


Figure 7.1: This figure shows the main result of this dissertation. The 90% credible transport coefficient \hat{q}/T^3 extracted for the charm flavor is displayed on the two dimensional landscape of energy and temperature. The JET Collaboraton extraction of light quark transport coefficients at $p = 10$ GeV [B⁺14b] (blue diamonds) and two lattice calculations of the momentum diffusion coefficient κ ($\hat{q} = 2\kappa$) [DFK⁺12, BDGM12] are plotted for comparison.

Studying heavy flavor helps to connect the knowledge of in-medium transport properties at very high momentum (light quark limit) and very low momentum (static sources limit). At relatively high momentum $p \sim 10$ GeV, it is consistent with the light quark transport parameter extracted by the JET Collaboration (blue). At low momentum, it is consistent with lattice calculations in the heavy quark limit (black). Future study with improved flavor dependence may be needed to understand the impact of using the “heavy” limit in a dynamical model. In the present calibration, the effective in-medium strong coupling constant is about 0.3, and only contributes to a small fraction of the extracted \hat{q} parameter. The rest comes from the parametric contribution whose origin can be either perturbative or non-perturbative; either way, it suggests the necessity to model beyond leading order physics.

In conclusion, a transport model with perturbative parton evolution with a parametric probe-medium interaction term provides reasonable description to the open-heavy flavor observables measured at RHIC and LHC, while the level of accuracy needs to be improved. Extracted heavy quark transport coefficients as function of energy and temperature are consistent with early phenomenological studies and lattice calculations.

The present model accuracy is still not enough to make the best use of future high-precision hard probe measurements in heavy-ion collisions. We therefore list a few necessary points of improvements which may help to reduce or estimate the theoretical and modeling uncertainties.

- An interpolation formula between vacuum and medium-induced radiation: a calculation that connects virtuality evolution with in-medium time evolution will help to eliminate the matching scale uncertainty. Even though its effect is not strong for the present observables and p_T range, it may impact more delicate jet observables.
- Correlations among multiple emissions in the presence of a medium. We have been neglecting the correlation among subsequent emissions in the “modified transport model”. In the infinite medium limit, this is because the probability of overlapping emissions scales as $\tau_{1,f}R(\omega_2) \sim \tau_{1,f}\alpha_s/\tau_{2,f}$ which is suppressed by α_s . But this higher order effect can be important since the phenomenological α_s is not small. There are ongoing studies on this topic [AI15, ACI16a, ACI16c, ACI16b].
- Off equilibrium corrections to the linearized transport equation. One essential assumption in the linearized transport model is that medium partons follow a local thermal distributions, even though the hydrodynamics used includes viscous corrections. In fact, the viscous correction and the momentum space anisotropy can be very large at early times of the hydrodynamic evolution. One needs to understand how these off-equilibrium effects change the interpretation of the transport coefficients one extracts assuming full thermal equilibrium of partons.
- Dynamical hadronization model and improved treatment of energy loss in the

hadronic stage. Our current hadronization model has the problem of pinching long distance physics into a sudden process. At low- p_T , the sudden recombination model breaks the detailed balance of the transport model and treating the recombination model in a dynamical way would be desirable. At high- p_T , the problem is more severe, as the hadronization time scale is dilated by the large boost. Moreover, the hadronic system near T_c is still very dense, and it is inconsistent to apply the vacuum fragmentation function at $T \sim T_c$. One possible solution for those high- p_T heavy quarks (the recombination process is negligible) is to continue their partonic transport into the hadronic phase, and finally apply the vacuum fragmentation function when the system is dilute enough. Meanwhile, one can also study the energy loss in the dense hadronic system to extend the extracted transport parameter to the region below T_c .

- A calibration with simultaneous tuning of the bulk and hard sectors. The bulk medium calibration is performed by a separate analysis. With future high precision hard probe measurements, a simultaneous calibration of both soft and hard sector would be interesting. For example, we found that the number of binary collision as a function of centrality is quite sensitive to the proton shape modeling in the Monte-Carlo Glauber model. The sensitivity of hard probe production to the number of binary collision may help to improve the proton shape modeling in the soft sector. In turn, a better calibrated medium may help to reduce the uncertainty in the hard parton energy loss study.

Appendix A

Few-Body Matrix-Elements

This section provides the detailed $2 \leftrightarrow 2$ and $2 \leftrightarrow 3$ matrix-elements we used in the transport model. The $2 \leftrightarrow 2$ results are standard and we do not re-derive them here. The $2 \leftrightarrow 3$ cross-sections are more complicated and a detailed derivation is attached to show the approximations we made for readers reference.

A.0.1 $2 \leftrightarrow 2$ processes

The two-body scatterings between quarks, anti-quarks and gluons are standard and we quote the results from existing references [Owe87]. For a light parton scattering, we keep only \hat{t} -channel contribution, the \hat{s} and \hat{u} channel contribution are suppressed at high energy.

$$\overline{|M_{q_1 q_2 \rightarrow q_1 q_2}|^2} = \frac{64\pi^2 \alpha_s^2}{9} \frac{s^2 + u^2}{t^2} \quad (\text{A.1})$$

$$\overline{|M_{gg \rightarrow gg}|^2} \approx 72\pi^2 \alpha_s^2 \frac{-su}{t^2} \quad (\text{A.2})$$

$$\overline{|M_{qg \rightarrow qg}|^2} \approx 16\pi^2 \alpha_s^2 \frac{s^2 + u^2}{t^2} \quad (\text{A.3})$$

For the heavy quark, since we are interested in its diffusion dynamics at low p_T , we uses the exact leading order matrix-element in the vacuum.

$$\begin{aligned} \overline{|M_{Qq \rightarrow Qq}|^2} &= \frac{64\pi^2 \alpha_s^2}{9} \frac{(M^2 - u)^2 + (s - M^2)^2 + 2M^2 t}{t^2} \\ \overline{|M_{Qq \rightarrow Qq}|^2} &= \pi^2 \left\{ 32\alpha_s^2 \frac{(s - M^2)(M^2 - u)}{t^2} \right. \\ &\quad + \frac{64}{9} \alpha_s^2 \frac{(s - M^2)(M^2 - u) + 2M^2(s + M^2)}{(s - M^2)^2} \\ &\quad + \frac{64}{9} \alpha_s^2 \frac{(s - M^2)(M^2 - u) + 2M^2(u + M^2)}{(M^2 - u)^2} \\ &\quad + \frac{16}{9} \alpha_s^2 \frac{M^2(4M^2 - t)}{(M^2 - u)(s - M^2)} \\ &\quad + 16\alpha_s^2 \frac{(s - M^2)(M^2 - u) + M^2(s - u)}{t(s - M^2)} \\ &\quad \left. - 16\alpha_s^2 \frac{(s - M^2)(M^2 - u) - M^2(s - u)}{t(M^2 - u)} \right\} \end{aligned} \quad (\text{A.4})$$

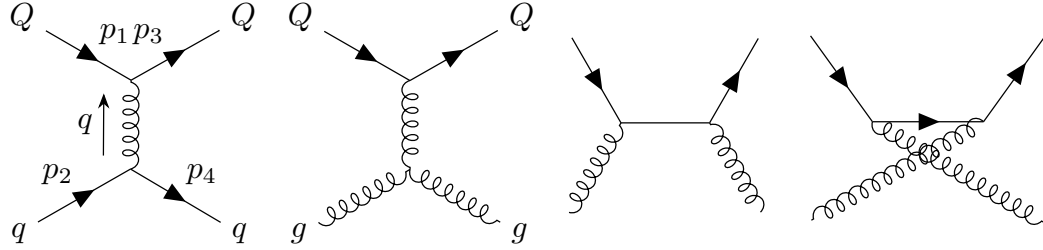


Figure A.1: Elastic processes: The first diagram corresponds to heavy quark (Q) - light quark (q, \bar{q}) scattering. The last three diagrams contribute to heavy quark (Q) - gluon (g) scattering.

A.0.2 $2 \rightarrow 3$ matrix-elements

Large- Q $2 \rightarrow 3$ inelastic processes are $g + i \rightarrow q + \bar{q} + i$, $q + i \rightarrow q + g + i$ and $g + i \rightarrow g + g + i$, where i stands for a medium parton, and the other symbols stands for hard partons. In the medium frame, the hard parton has an energy $E \gg T$, while the medium thermal parton has $E \sim T$, and the typical center-of-mass energy is therefore $\sqrt{6ET}$. We perform the calculation in the the center-of-mass frame of the two incoming partons and let the hard parton move towards the $+z$ direction with momentum p_1 , and the medium parton moving to the $-z$ direction with p_2 . The hard parton then splits into two daughter partons with momenta k and $p_1 + q - k$. The momentum transfer q between the hard parton and the medium parton is thought to be large enough $|q| > Q_{\text{cut}}$ so we neglect the thermal correction to its propagator.

Our derivation largely follows the work of [FUXG13] while relaxing the soft approximation $xq_\perp \ll k_\perp$ in [FUXG13], and we only use the collinear approximation $k_\perp^2, q_\perp^2 \ll x(1-x)\hat{s}$ with $x = k^+/\sqrt{s} = k_\perp e_k^y/\sqrt{s}$. Also, we only include the contributions with a \hat{t} -channel momentum exchange between the medium and the hard partons. The collinear approximation requires $y_k \gg \ln(k_\perp/\sqrt{s})$ so that y_k cannot be arbitrarily small and $y_k > 0 \gg -\ln(\sqrt{s}/k_\perp)$ is a reasonable range of application. Because $\hat{s} \sim 6ET$, we expect this approximation to break down when either the typical values of q_\perp^2 becomes comparable to $x(1-x)6ET$ or when $y_k < 0$ ($x < k_\perp/\sqrt{s} \sim k_\perp/\sqrt{6ET}$). We shall briefly mention the treatment of the $y_k < 0$ region in the end.

The light-cone momentum for p_1 , p_2 and k can written down directly using \sqrt{s} , x and k_\perp , then applying the above collinear condition, the expression for q (and therefore p_3 and p_4) is obtained by kinematic constraint up to corrections of order $\{k_\perp, q_\perp^2\}/x(1-x)\hat{s}$.

$$p_1 = (\sqrt{s}, 0, \vec{0}) \quad (\text{A.5})$$

$$p_2 = (0, \sqrt{s}, \vec{0}) \quad (\text{A.6})$$

$$k = (x\sqrt{s}, \frac{k_\perp^2}{x\sqrt{s}}, \vec{k}_\perp) \quad (\text{A.7})$$

$$q \sim \left(-\frac{q_\perp^2}{\sqrt{s}}, \frac{q_\perp^2 + k_\perp^2/x - 2\vec{q}_\perp \cdot \vec{k}_\perp}{(1-x)\sqrt{s}}, \vec{q}_\perp \right) \quad (\text{A.8})$$

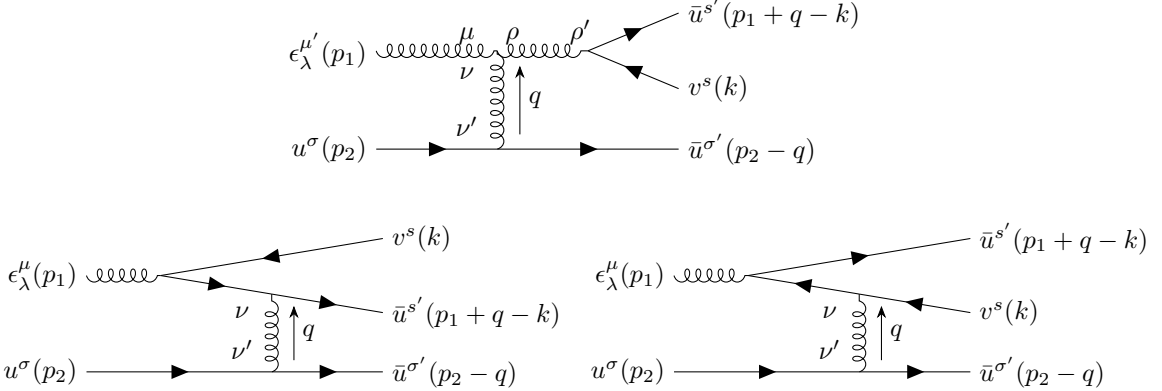


Figure A.2: Three diagrams A (Top), B (Bottom left), C (Bottom right) that contribute to the large angle scattering induced gluon splitting into quark-anti-quark pair in the forward region of the center-of-mass frame.

Using the light-cone gauge with a light-like vector $n = (0, 1, 0)$, the gauge fixing condition $n \cdot A = 0$ eliminates the "+" component in the gluon (with momentum p) polarization vector, and is obtained by applying the transverse condition $\epsilon \cdot p = 0$ (up to a higher order correction to its normalization)

$$\epsilon(p) \sim (0, \frac{2\vec{\epsilon}_\perp \cdot \vec{p}_\perp}{p^+}, \vec{\epsilon}_\perp). \quad (\text{A.9})$$

With these preparations, the matrix-element is factorized into an amplitude for the splitting process (approximated in the collinear limit) times the amplitude for two-body collision with the medium parton. We shall only derive explicitly the cases where the medium parton is a quark, for colliding with medium anti-quark and gluon, it is sufficient to replace the $H + q \xrightarrow{\hat{t}} H + q$ amplitude by $H + \bar{q} \xrightarrow{\hat{t}} H + \bar{q}$ and $H + g \xrightarrow{\hat{t}} H + g$. The connection of these results to the Bethe-Heitler limit of the AMY integral equation will be elucidated in the end.

Gluon splitting to quark-anti-quark pair Three Feynman diagrams contribute to the kinematic region $y_k > 0$ in the current approximation, as shown in figure A.2. We start from the amplitude for diagram A .

$$\begin{aligned} iM_A &= (-ig)^2 (-g) f^{abc} (t^b)_{j'i} (t^c)_{i'j} \epsilon_\lambda^\mu(p_1) \\ &\quad \frac{-i}{(p_1 + q)^2} \left(g^{\rho\rho'} - \frac{n^\rho(p_1 + q)^{\rho'} + n^{\rho'}(p_1 + q)^\rho}{n \cdot (p_1 + q)} \right) \bar{u}^s(p_1 + q - k) \gamma_{\rho'} v^{s'}(k) \\ &\quad \frac{-i}{q^2} \left(g^{\nu\nu'} - \frac{n^\nu q^{\nu'} + n^{\nu'} q^\nu}{n \cdot q} \right) \bar{u}^\sigma(p_4) \gamma_{\nu'} u^{\sigma'}(p_2) \\ &\quad [g_{\mu\nu}(p_1 - q)_\rho + g_{\nu\rho}(2q + p_1)_\rho + g_{\rho\mu}(-2p_1 - q)_\nu] \end{aligned} \quad (\text{A.10})$$

Next, express the projection matrix of the gluon propagator with momentum $p_1 + q$ by the sum of tensor products of its polarization vectors, and identify the amplitude

$iP_{A,\lambda'}^{ss'}$ for a gluon with polarization λ' to split into the quark and anti-quark pair with spin s and s' . Also, use the high energy approximation to replace $\bar{u}^i(a)\gamma^\alpha u^j(b)$ by $(a+b)^\alpha \delta^{ij}$, then

$$iM_A \approx -g^3 f^{abc} (t^b)_{j'j} (t^c)_{i'i} \delta^{\sigma\sigma'} \epsilon^\mu(p_1) \quad (\text{A.11})$$

$$\frac{1}{(p_1+q)^2} \sum_{\lambda'=\pm} \epsilon_{\lambda'}^\rho(p_1+q) \underbrace{\epsilon_{\lambda'}^{*,\rho'}(p_1+q) \bar{u}^s(p_1+q-k) \gamma_{\rho'} v^{s'}(k)}_{iP_{A,\lambda'}^{ss'}} \quad (\text{A.11})$$

$$\begin{aligned} & \frac{1}{q_\perp^2} \left(g^{\nu\nu'} - \frac{n^\nu q^{\nu'} + n^{\nu'} q^\nu}{n \cdot q} \right) (2p_2 - q)_\nu \\ & [g_{\mu\nu}(p_1 - q)_\rho + g_{\nu\rho}(2q + p_1)_\rho + g_{\rho\mu}(-2p_1 - q)_\nu] \\ = & -g^3 f^{abc} (t^b)_{j'j} (t^c)_{i'i} \frac{1}{(p_1+q)^2} \frac{1}{q_\perp^2} \sum_{\lambda'=\pm} iP_{A,\lambda'}^{ss'} \delta^{\sigma\sigma'} \\ & \epsilon_\lambda^\mu(p_1) 2p_2^\nu \epsilon_{\lambda'}^\rho(p_1+q) [g_{\mu\nu}(p_1 - q)_\rho + g_{\nu\rho}(2q + p_1)_\rho + g_{\rho\mu}(-2p_1 - q)_\nu]. \end{aligned} \quad (\text{A.12})$$

Finally, we evaluate the contraction in the second line using the expression for p_1, q and ϵ , and keep only terms that is leading in q_\perp^2/s to get,

$$iM_A \approx -g^3 f^{abc} (t^b)_{j'j} (t^c)_{i'i} \delta^{\sigma\sigma'} \frac{2s}{q_\perp^2} \frac{x(1-x)}{(\vec{k}_\perp - x\vec{q}_\perp)^2} iP_{A,\lambda'}^{ss'}. \quad (\text{A.13})$$

Diagram B and C are similar and we only write down diagram B in detail.

$$\begin{aligned} iM_B = & (-ig)^3 (t^b t^a)_{i'i} (t^b)_{j'j} \epsilon_\lambda^\mu(p_1) \quad (\text{A.14}) \\ & \frac{-i}{q_\perp^2} \left(g^{\nu\nu'} - \frac{n^\nu q^{\nu'} + n^{\nu'} q^\nu}{n \cdot q} \right) \\ & \bar{u}^s(p_1 + q - k) \gamma_\nu \frac{i(p'_1 - \not{k})}{(p_1 - k)^2} \gamma^\mu v^{s'}(k) \\ & \bar{u}^\sigma(p_4) \gamma_{\nu'} u^{\sigma'}(p_2) \end{aligned}$$

Again, we represent the tensor structure of the fermion propagator by the sum of tensor products of the spinors, identify the splitting amplitude $iP_{B,\lambda'}^{ss'}$ and use the high energy limit of the current,

$$\begin{aligned} iM_B \approx & ig^3 (t^b t^a)_{i'i} (t^b)_{j'j} \quad (\text{A.15}) \\ & \frac{-i}{q_\perp^2} \left(g^{\nu\nu'} - \frac{n^\nu q^{\nu'} + n^{\nu'} q^\nu}{n \cdot q} \right) (2p_2 - q)'_\nu \\ & \frac{1}{2p_1 \cdot k} \sum_\sigma \bar{u}^s(p_1 + q - k) \gamma_\nu u^\sigma(p_1 - k) \underbrace{\epsilon_\lambda^\mu(p_1) \bar{u}^\sigma(p_1 - k) \gamma^\mu v^{s'}(k)}_{iP_{B,\lambda}^{\sigma s'}} \end{aligned}$$

$$\begin{aligned} \approx & ig^3 (t^b t^a)_{i'i} (t^b)_{j'j} \frac{-i}{q_\perp^2} \frac{1}{2p_1 \cdot k} iP_{B,\lambda}^{ss'} \quad (\text{A.16}) \\ & \left(g^{\nu\nu'} - \frac{n^\nu q^{\nu'} + n^{\nu'} q^\nu}{n \cdot q} \right) (2p_2 - q)_{\nu'} (2p_1 - q + 2k)_\nu \end{aligned}$$

Note that iP_B is different from iP_A as the initial splitting parton has a different transverse momentum from diagram A . Finally, we evaluate the contraction and get,

$$iM_B = ig^3(t^b t^a) i' i t^b j' j \delta^{\sigma\sigma'} \frac{2s}{q_\perp^2} \frac{x(1-x)}{k_\perp^2} iP_{B,\lambda}^{ss'} \quad (\text{A.17})$$

Diagram C can be obtained similarly,

$$iM_C = -ig^3(t^a t^b) i' i t^b j' j \delta^{\sigma\sigma'} \frac{2s}{q_\perp^2} \frac{x(1-x)}{(\vec{k}_\perp - \vec{q}_\perp)^2} iP_{C,\lambda}^{ss'} \quad (\text{A.18})$$

To sum the contributions from all three diagrams, applying $f^{abc}t^c = -i[t^a, t^b]$ to iM_A and the result is,

$$\begin{aligned} i(M_A + M_B + M_C) &= ig^3 \frac{2s}{q_\perp^2} (t^b)_{j'j} x(1-x) \\ &\quad \left\{ (t^a t^b)_{i'i} \left(\frac{iP_{A,\lambda}^{ss'}}{(\vec{k}_\perp - x\vec{q}_\perp)^2} - \frac{iP_{C,\lambda}^{ss'}}{(\vec{k}_\perp - \vec{q}_\perp)^2} \right) \right. \\ &\quad \left. - (t^a t^b)_{i'i} \left(\frac{iP_{A,\lambda}^{ss'}}{(\vec{k}_\perp - x\vec{q}_\perp)^2} - \frac{iP_{B,\lambda}^{ss'}}{k_\perp^2} \right) \right\} \end{aligned} \quad (\text{A.19})$$

Now we have to address what those splitting amplitudes are. Label the four momenta as $p_g = c$, $p_q = a$, $p_{\bar{q}} = b$. And use the following representation for the spinors,

$$u^s(p) = (\sqrt{p \cdot \sigma} \xi^s, \sqrt{p \cdot \bar{\sigma}} \xi^s)^T v^s(p) = (\sqrt{p \cdot \sigma} \eta^s, -\sqrt{p \cdot \bar{\sigma}} \eta^s)^T \quad (\text{A.20})$$

where $\sigma_{i=\{1,2,3\}}$ are Pauli matrices, $\sigma = (1_{2 \times 2}, \vec{\sigma})$, and $\bar{\sigma} = (1_{2 \times 2}, -\vec{\sigma})$. The square root of the matrix is,

$$\sqrt{p \cdot \sigma} = \begin{bmatrix} p^- & -p_L^\perp \\ -p_R^\perp & p^+ \end{bmatrix}^{1/2} = \frac{1}{\sqrt{2(E \pm M)}} (p \cdot \sigma \pm \mathbf{1}M) \quad (\text{A.21})$$

$$\sqrt{p \cdot \bar{\sigma}} = \begin{bmatrix} p^+ & p_\perp^- \\ p_R^\perp & p^- \end{bmatrix}^{1/2} = \frac{1}{\sqrt{2(E \pm M)}} (p \cdot \bar{\sigma} \pm \mathbf{1}M) \quad (\text{A.22})$$

(A.23)

where M is the mass of the particle, $p^\pm = E \pm p_z$, and $p_{R,L}^\perp = p_x \pm ip_y$. Currently, we only consider the massless case, because the mass effect is not implemented in the few-body matrix-elements in our model. Neglecting the mass, the splitting amplitude

is,

$$\epsilon_{\lambda,\mu}(c)\bar{u}_s(a)\gamma^\mu v_{s'}(b) \quad (\text{A.24})$$

$$= \frac{1}{\sqrt{2a}\sqrt{2b}}(\xi_s^T a \cdot \sigma, \xi_s^T a \cdot \bar{\sigma}) \begin{bmatrix} \epsilon \cdot \bar{\sigma} & 0 \\ 0 & \epsilon \cdot \sigma \end{bmatrix} \begin{bmatrix} b \cdot \sigma \eta_{s'} \\ b \cdot \bar{\sigma} \eta_{s'} \end{bmatrix} \quad (\text{A.25})$$

$$= \frac{1}{2\sqrt{ab}}\xi_s^T \begin{bmatrix} a^- & -a_L^\perp \\ -a_R^\perp & a^+ \end{bmatrix} \begin{bmatrix} 0 & \sqrt{2}\delta_{\lambda R} \\ \sqrt{2}\delta_{\lambda L} & \frac{\sqrt{2}c_\lambda^\perp}{c^+} \end{bmatrix} \begin{bmatrix} b^- & -b_L^\perp \\ -b_R^\perp & b^- \end{bmatrix} \eta_{s'} \quad (\text{A.26})$$

$$\begin{aligned} & - \frac{1}{2\sqrt{ab}}\xi_s^T \begin{bmatrix} a^+ & a_L^\perp \\ a_R^\perp & a^- \end{bmatrix} \begin{bmatrix} \frac{\sqrt{2}c_\lambda^\perp}{c^+} & -\sqrt{2}\delta_{\lambda R} \\ -\sqrt{2}\delta_{\lambda L} & 0 \end{bmatrix} \begin{bmatrix} b^+ & b_L^\perp \\ b_R^\perp & b^- \end{bmatrix} \eta_{s'} \\ & = \frac{1}{\sqrt{2ab}}\xi_s^T \begin{bmatrix} -a_L^\perp b^- \delta_{\lambda L} - a^- b_L^\perp \delta_{\lambda R} + a_L^\perp b_R^\perp \frac{c_\lambda^\perp}{c^+} & a_L^\perp b_L^\perp \delta_{\lambda L} + a^- b^+ \delta_{\lambda R} - a_L^\perp b^+ \frac{c_\lambda^\perp}{c^+} \\ a^+ b^- \delta_{\lambda L} + a_R^\perp b_R^\perp \delta_{\lambda R} - a^+ b_R^\perp \frac{c_\lambda^\perp}{c^+} & -a^+ b_L^\perp \delta_{\lambda L} - a_R^\perp b^+ \delta_{\lambda R} + a^+ b^+ \frac{c_\lambda^\perp}{c^+} \end{bmatrix} 2\eta_s \\ & - \frac{1}{\sqrt{2ab}}\xi_s^T \begin{bmatrix} -a_L^\perp b^+ \delta_{\lambda L} - a^+ b_R^\perp \delta_{\lambda R} + a^+ b^+ \frac{c_\lambda^\perp}{c^+} & -a_L^\perp b_L^\perp \delta_{\lambda L} - a^+ b^- \delta_{\lambda R} + a^+ b_L^\perp \frac{c_\lambda^\perp}{c^+} \\ -a^- b^+ \delta_{\lambda L} - a_R^\perp b_R^\perp \delta_{\lambda R} + a_R^\perp b^+ \frac{c_\lambda^\perp}{c^+} & -a^- b_L^\perp \delta_{\lambda L} - a_R^\perp b^- \delta_{\lambda R} + a_R^\perp b_L^\perp \frac{c_\lambda^\perp}{c^+} \end{bmatrix} \eta_{s'} \end{aligned}$$

Keep the leading terms in the collinear limit which are products of (+)(+) or (+)(\perp) components of the momenta, and drop terms that are of order (+)(-), (\perp)(\perp) and (\perp)(-),

$$\epsilon_{\lambda,\mu}\bar{u}_s(a)\gamma^\mu v_{s'}(b) \quad (\text{A.28})$$

$$= \frac{1}{\sqrt{2ab}}\xi_s^T \begin{bmatrix} a_L^\perp b^+ \delta_{\lambda L} + a^+ b_R^\perp \delta_{\lambda R} - a^+ b^+ \frac{c_\lambda^\perp}{c^+} & 0 \\ 0 & -a^+ b_L^\perp \delta_{\lambda L} - a_R^\perp b^+ \delta_{\lambda R} + a^+ b^+ \frac{c_\lambda^\perp}{c^+} \end{bmatrix} \quad (\text{A.29})$$

There are four combinations for the possible initial state polarization and final state spins

$$\epsilon_{\lambda,\mu}\bar{u}_s(a)\gamma^\mu v_{s'}(b) = \frac{x\vec{a} - (1-x)\vec{b}}{\sqrt{2x(1-x)}} \begin{cases} x, & \lambda = L, s = \uparrow \\ -(1-x), & \lambda = L, s = \downarrow \\ (1-x), & \lambda = R, s = \uparrow \\ -x, & \lambda = R, s = \downarrow \end{cases} \quad (\text{A.30})$$

Where we have used $a^+ = (1-x)c^+$, $b^+ = xc^+$ and $c_\perp = a_\perp + b_\perp$. Sum over the spins and average over polarization for the squared amplitude,

$$\frac{1}{2} \sum_{\pm} |P|^2 = \frac{2(x^2 + (1-x)^2)}{x(1-x)} \left((1-x)\vec{a}_\perp - x\vec{b}_\perp \right)^2. \quad (\text{A.31})$$

This result goes back to the standard splitting function if it is computed in the frame where $a_\perp = -b_\perp$. However, there is no such frame that $a_\perp = -b_\perp$ satisfies simultaneously for the splitting in diagram A, B and C. Therefore different amplitude needs to be inserted for each diagram and we find,

$$\begin{aligned} \frac{\sum_{\lambda,s,s',\sigma,\sigma',a,b} |M^2|_{g+q \rightarrow q+\bar{q}+q}}{2d_F 2d_A} &= g^4 \frac{2C_F}{d_A} \frac{4s^2 x(1-x)}{q_\perp^4} \\ &\times g^2 \frac{(x^2 + (1-x)^2)}{2} \left(C_F \vec{A}^2 + C_F \vec{B}^2 - (2C_F - C_A) \vec{A} \cdot \vec{B} \right) \end{aligned} \quad (\text{A.32})$$

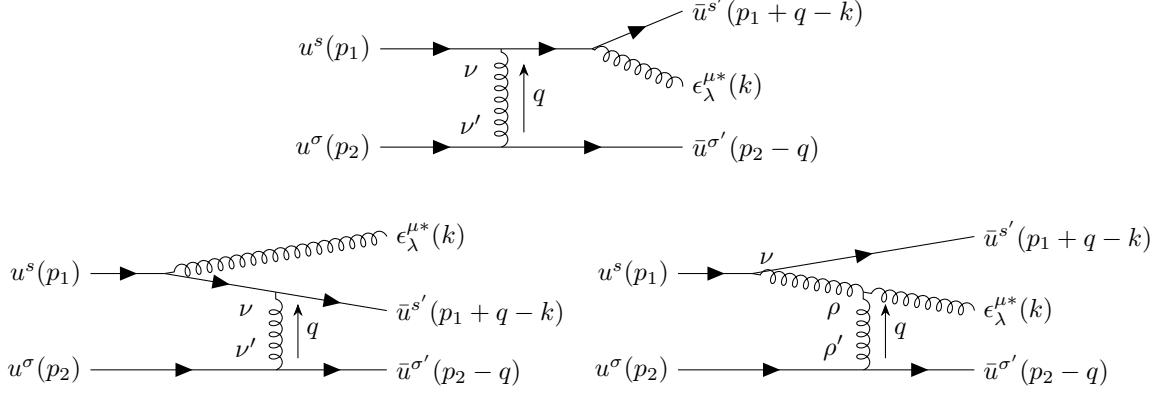


Figure A.3: Three diagrams A (Top), B (Bottom left), C (Bottom right) that contribute to the large angle scattering induced a quark splitting into a quark and a gluon in the forward region of the center-of-mass frame.

Where the \vec{A} and \vec{B} are,

$$\vec{A} = \frac{\vec{k}_\perp - x\vec{q}_\perp}{(\vec{k}_\perp - x\vec{q}_\perp)^2} - \frac{\vec{k}_\perp - \vec{q}_\perp}{(\vec{k}_\perp - \vec{q}_\perp)^2}, \quad (\text{A.33})$$

$$\vec{B} = \frac{\vec{k}_\perp - x\vec{q}_\perp}{(\vec{k}_\perp - x\vec{q}_\perp)^2} - \frac{\vec{k}_\perp}{\vec{k}_\perp^2}. \quad (\text{A.34})$$

The final squared matrix-element has been factorized into the two body scattering part (first line) and the collinear splitting part (second line) with the desired leading order QCD splitting function.

Quark splits to quark and gluon The Feynman diagrams to be included for $q + q \rightarrow q + g + q$ are shown in Figure A.3. The calculation uses exactly the same technique we used for the gluon splitting channel, and we present the result directly,

$$|\overline{M^2}|_{g+q \rightarrow g+g+q} = g^4 \frac{C_F}{d_F} \frac{4s^2}{q_\perp^4} x(1-x) \quad (\text{A.35})$$

$$\times g^2 \frac{1 + (1-x)^2}{x} (C_F \vec{A}^2 + C_F \vec{B}^2 - (2C_F - C_A) \vec{A} \cdot \vec{B})$$

$$\vec{A} = \frac{\vec{k}_\perp - \vec{q}_\perp}{(\vec{k}_\perp - \vec{q}_\perp)^2} - \frac{\vec{k}_\perp - x\vec{q}_\perp}{(\vec{k}_\perp - x\vec{q}_\perp)^2} \quad (\text{A.36})$$

$$\vec{B} = \frac{\vec{k}_\perp - \vec{q}_\perp}{(\vec{k}_\perp - \vec{q}_\perp)^2} - \frac{\vec{k}_\perp}{\vec{k}_\perp^2} \quad (\text{A.37})$$

Gluon splitting to two gluons Finally, for $g+q \rightarrow g+q+g$, the Feynman diagrams are shown in Figure A.4. The simplification of the two body collision amplitude can be done in a similar manner as the previous two channels. We only write down the

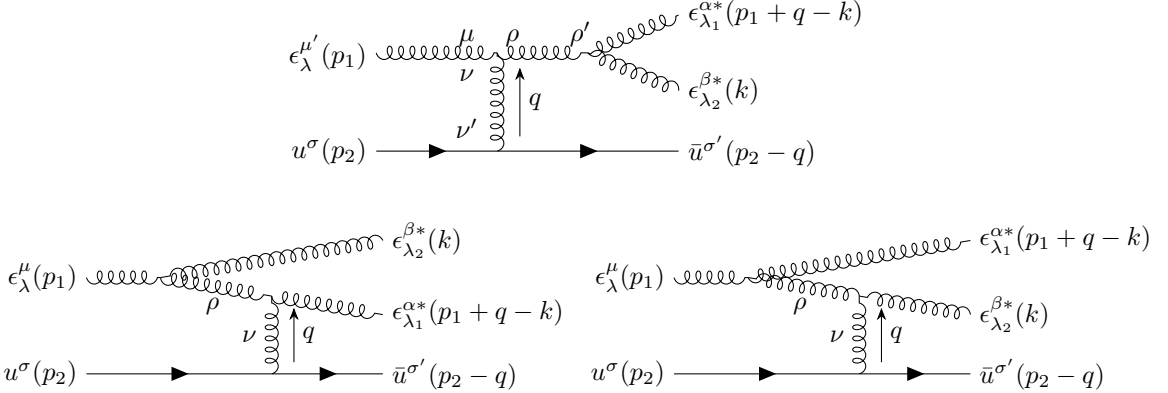


Figure A.4: Three diagrams A (Top), B (Bottom left), C (Bottom right) that contribute to the large angle scattering induced gluon splitting into two gluons in the forward region of the center-of-mass frame.

splitting amplitude $g \rightarrow g + g$ in detail. Suppressing the color index, we label the initial gluon with $\epsilon_1^\mu(p)$, and the two daughter gluons with $\epsilon_2^\nu(k)$ and $\epsilon_3^\rho(q)$. The splitting amplitudes are then (omitting the factor $-gf^{abc}$)

$$iP = \epsilon_1^\mu \epsilon_2^\nu \epsilon_3^\rho [g_{\mu\nu}(p+k)_\rho + g_{\nu\rho}(p+k)_\mu + g_{\rho\mu}(-q-p)_\nu] \quad (\text{A.38})$$

$$= -\vec{\epsilon}_{1,\perp} \cdot \vec{\epsilon}_{2,\perp} \left[(p+k)^+ \frac{\vec{\epsilon}_{3,\perp} \cdot \vec{q}_\perp}{q^+} - \vec{\epsilon}_{3,\perp} \cdot (\vec{p}_\perp + \vec{k}_\perp) \right] \quad (\text{A.39})$$

$$-\vec{\epsilon}_{2,\perp} \cdot \vec{\epsilon}_{3,\perp} \left[(-k+q)^+ \frac{\vec{\epsilon}_{1,\perp} \cdot \vec{p}_\perp}{p^+} - \vec{\epsilon}_{1,\perp} \cdot (-\vec{k}_\perp + \vec{q}_\perp) \right]$$

$$-\vec{\epsilon}_{3,\perp} \cdot \vec{\epsilon}_{1,\perp} \left[(-q-p)^+ \frac{\vec{\epsilon}_{2,\perp} \cdot \vec{k}_\perp}{k^+} - \vec{\epsilon}_{2,\perp} \cdot (-\vec{q}_\perp - \vec{p}_\perp) \right]$$

There are four possible combinations of the polarization vectors, and their respective amplitude is computed as,

$$iP = \sqrt{2} \left[x\vec{q}_\perp - (1-x)\vec{k}_\perp \right] \times \begin{cases} \frac{1-x+x^2}{x(1-x)}, & \lambda_1 = \lambda_2 = \lambda_3 \\ -1, & \lambda_1 \neq \lambda_2 = \lambda_3 \\ \frac{1}{x}, & \lambda_1 = \lambda_3 \neq \lambda_2 \\ \frac{1}{1-x}, & \lambda_1 = \lambda_2 \neq \lambda_3 \end{cases} \quad (\text{A.40})$$

Summing over the squared amplitude of all four cases and averaging over the initial gluon polarization, one gets the desired leading order QCD splitting function,

$$2 \frac{1+x^2+(1-x)^4}{x^2(1-x)^2} \left[x\vec{q}_\perp - (1-x)\vec{k}_\perp \right]^2. \quad (\text{A.41})$$

Substituting the amplitude in each diagram, the final squared matrix-element is

$$\overline{|M^2|}_{g+q \rightarrow g+g+q} = g^4 \frac{C_A}{d_F} \frac{4s^2x(1-x)}{q_\perp^4} \quad (\text{A.42})$$

$$\times g^2 \frac{1+x^4+(1-x)^4}{x(1-x)} (C_A \vec{A}^2 + C_A \vec{B}^2 - C_A \vec{A} \cdot \vec{B})$$

$$\vec{A} = \frac{\vec{k}_\perp - x\vec{q}_\perp}{(\vec{k}_\perp - x\vec{q}_\perp)^2} - \frac{\vec{k}_\perp - \vec{q}_\perp}{(\vec{k}_\perp - \vec{q}_\perp)^2} \quad (\text{A.43})$$

$$\vec{B} = \frac{\vec{k}_\perp - x\vec{q}_\perp}{(\vec{k}_\perp - x\vec{q}_\perp)^2} - \frac{\vec{k}_\perp}{\vec{k}_\perp^2} \quad (\text{A.44})$$

Regulating the $2 \rightarrow 3$ squared matrix-elements The divergence in the q integration is removed by the requirement that this few-body matrix-element only applies to processes with $q > Q_{\text{cut}}$. The collinear divergence when k approaches q or xq is regulated by including a gluon thermal mass. In practice, the collinear region will be further suppressed by the LPM effect. The cross-section is obtained by integrating over the final state phase-space, where we have chosen to parameterize the three particle final state in terms of k_\perp^2 , the rapidity of k in the center-of-mass frame y_k , and the solid angle of the recoil medium particle.

Soft limit: the Gunion-Bertsch approximation The result we obtained for the $g \rightarrow g + g$ and $q \rightarrow q + g$ channel have a soft limit that goes back to the well known Gunion-Bertsch form. In the soft limit, we require the radiated gluon energy to be small enough such that $xq_\perp \ll k_\perp$. Then, the splitting amplitudes for both $g \rightarrow g + g$ and $q \rightarrow q + g$ are simplified into the same form,

$$\overline{|M|}_{22}^2 x(1-x) g^2 \frac{2(1-x+O(x^2))}{x} C_A \left(\frac{\vec{k}_\perp}{k_\perp^2} - \frac{\vec{k}_\perp - \vec{q}_\perp}{(\vec{k}_\perp - \vec{q}_\perp)^2} \right)^2 \quad (\text{A.45})$$

Neglecting the $O(x^2)$ terms in the splitting function, the result is the same as the improved verison of the Gunion-Bertsch cross-section [FUXG13] used in the full Boltzmann partonic transport model BAMPS [XG05],

$$\overline{|M|}_{22}^2 8\pi C_A \alpha_s (1-x)^2 \left(\frac{\vec{k}_\perp}{k_\perp^2} - \frac{\vec{k}_\perp - \vec{q}_\perp}{(\vec{k}_\perp - \vec{q}_\perp)^2} \right)^2 \quad (\text{A.46})$$

The backward ($y_k < 0$) region We have mentioned in the beginning of the derivation that the condition $k_\perp^2 < x(1-x)\hat{s}$ restricts the splitting to be happen only for the parton moving in the $+z$ direction in the center-of-mass frame ($y_k > 0$). For splittings that happen in the backward region, another set of diagrams contribute, where the splitting comes from the parton that moves in the $-z$ direction in the center-of-mass frame. Also one needs a different gauge $A^- = 0$. The derivation is

similar to the previous ones, but with the definition of x and q changed to $x = k^-/\sqrt{s}$, and $q = p_1 - p_3$.

To combine the results that are obtained in different regions of phase space ($y_k > 0$ and $y_k < 0$), we follow [FUXG13] and defines,

$$\bar{x} = \frac{(k + |k_z|)}{\sqrt{s}} = \frac{k_\perp e^{|y_k|}}{\sqrt{s}} \quad (\text{A.47})$$

$$\bar{q} = \Theta(y_k)(p_2 - p_4) + \Theta(-y_k)(p_1 - p_3) \quad (\text{A.48})$$

which replaces the original x and q in our formula, and the resultant matrix-elements can be used for both forward and backward regions.

Relation to the Bethe-Heitler limit of the AMY formalism Now we show the connection between the $2 \rightarrow 3$ cross section obtained here and the Bethe-Heitler limit of the AMY equation. In the Bethe-Heitler limit, the AMY integral equation can be solved approximately by treating $1/\tau_f$ as the leading factor. One obtains the splitting rate for each different channels (denoting \vec{a}/a^2 as $\vec{\phi}_a$),

$$R_{q \rightarrow q+g}^{BH} \propto g^2 P_{qg}^{q(0)}(x) \int dk^2 dq^2 \mathcal{A}(q^2) \left\{ C_A \vec{\phi}_k \cdot (\vec{\phi}_k - \vec{\phi}_{k-q}) + (2C_F - C_A) \vec{\phi}_k \cdot (\vec{\phi}_k - \vec{\phi}_{k+xq}) + C_A \vec{\phi}_k \cdot (\vec{\phi}_k - \vec{\phi}_{k+(1-x)q}) \right\} \quad (\text{A.49})$$

$$R_{g \rightarrow g+g}^{BH} \propto g^2 P_{gg}^{g(0)}(x) \int dk^2 dq^2 \mathcal{A}(q^2) \left\{ C_A \vec{\phi}_k \cdot (\vec{\phi}_k - \vec{\phi}_{k-q}) + C_A \vec{\phi}_k \cdot (\vec{\phi}_k - \vec{\phi}_{k+xq}) + C_A \vec{\phi}_k \cdot (\vec{\phi}_k - \vec{\phi}_{k+(1-x)q}) \right\} \quad (\text{A.50})$$

$$R_{g \rightarrow q+\bar{q}}^{BH} \propto g^2 P_{q\bar{q}}^{g(0)}(x) \int dk^2 dq^2 \mathcal{A}(q^2) \left\{ (2C_F - C_A) \vec{\phi}_k \cdot (\vec{\phi}_k - \vec{\phi}_{k-q}) + C_A \vec{\phi}_k \cdot (\vec{\phi}_k - \vec{\phi}_{k+xq}) + C_A \vec{\phi}_k \cdot (\vec{\phi}_k - \vec{\phi}_{k+(1-x)q}) \right\} \quad (\text{A.51})$$

with the collision kernel $\mathcal{A} = g^2 T m_D^2 / q^2 (q^2 + m_D^2)$. These expressions look drastically different from the incoherent rate computed using the cross-section derived in the previous section, however, we would like to show that they are the same once integration over dk^2 is performed. Therefore, the incoherent rate we used in the Boltzmann equation indeed recovers the Bethe-Heitler limit of the AMY integral equation.

To show this, we start from the $2 \rightarrow 3$ rate formula using the matrix-elements from equations A.32, A.35 and A.42. For the $q \rightarrow q + g$ channel, the rate in our Boltzmann equation is,

$$R_{q \rightarrow q+g} \propto g^2 P_{qg}^{q(0)}(x) \int \frac{f(p_2) dp_2^3}{2E_2(2\pi)^3} dq^2 \frac{g^4}{q^4} \int dk^2 \left\{ C_F (\vec{\phi}_{k-q} - \vec{\phi}_{k-xq})^2 + C_F (\vec{\phi}_{k-q} - \vec{\phi}_k)^2 - (2C_F - C_A) (\vec{\phi}_{k-q} - \vec{\phi}_{k-xq}) \cdot (\vec{\phi}_{k-q} - \vec{\phi}_k) \right\} \quad (\text{A.52})$$

Focusing on the three products (squares) of $\vec{\phi}$ s under the dk^2 integration, we are going to expand the first term in each product and then shift the argument of the first $\vec{\phi}$ to

k ,

$$\begin{aligned}
R_{q \rightarrow q+g} &\propto g^2 P_{qg}^{q(0)}(x) \int \frac{f(p_2) dp_2^3}{2E_2(2\pi)^3} dq^2 \frac{g^4}{q^4} \\
&\quad \int dk^2 \left\{ C_F \vec{\phi}_k \left(\vec{\phi}_k - \vec{\phi}_{k+(1-x)q} \right) - C_F \vec{\phi}_k \left(\vec{\phi}_{k-(1-x)q} - \vec{\phi}_k \right) \right. \\
&\quad + C_F \vec{\phi}_k \left(\vec{\phi}_k - \vec{\phi}_{k+q} \right) - C_F \vec{\phi}_k \left(\vec{\phi}_{k-q} - \vec{\phi}_k \right) \\
&\quad \left. - (2C_F - C_A) \vec{\phi}_k \cdot \left(\vec{\phi}_k - \vec{\phi}_{k+q} \right) + (2C_F - C_A) \vec{\phi}_k \cdot \left(\vec{\phi}_{k-(1-x)q} - \vec{\phi}_{k+xq} \right) \right\}
\end{aligned} \tag{A.53}$$

Next, flip the sign of q under the integration, and meanwhile, insert a $-\vec{\phi}_k + \vec{\phi}_k$ in the brackets of the last term,

$$\begin{aligned}
R_{q \rightarrow q+g} &\propto g^2 P_{qg}^{q(0)}(x) \int \frac{f(p_2) dp_2^3}{2E_2(2\pi)^3} dq^2 \frac{g^4}{q^4} \\
&\quad \int dk^2 \left\{ 2C_F \vec{\phi}_k \left(\vec{\phi}_k - \vec{\phi}_{k+(1-x)q} \right) + 2C_F \vec{\phi}_k \left(\vec{\phi}_k - \vec{\phi}_{k+q} \right) \right. \\
&\quad - (2C_F - C_A) \vec{\phi}_k \cdot \left(\vec{\phi}_k - \vec{\phi}_{k+q} \right) + (2C_F - C_A) \vec{\phi}_k \cdot \left(\vec{\phi}_{k+(1-x)q} - \vec{\phi}_k \right) \\
&\quad \left. + (2C_F - C_A) \vec{\phi}_k \cdot \left(\vec{\phi}_k - \vec{\phi}_{k+xq} \right) \right\}
\end{aligned} \tag{A.54}$$

After this manipulation, the first (second) term cancels the C_F part of the fourth (third) term,

$$\begin{aligned}
R_{q \rightarrow q+g} &\propto g^2 P_{qg}^{q(0)}(x) \int \frac{f(p_2) dp_2^3}{2E_2(2\pi)^3} dq^2 \frac{g^4}{q^4} \\
&\quad \int dk^2 \left\{ C_A \vec{\phi}_k \cdot \left(\vec{\phi}_k - \vec{\phi}_{k+q} \right) + C_A \vec{\phi}_k \cdot \left(\vec{\phi}_k - \vec{\phi}_{k+(1-x)q} \right) \right. \\
&\quad \left. + (2C_F - C_A) \vec{\phi}_k \cdot \left(\vec{\phi}_k - \vec{\phi}_{k+xq} \right) \right\}
\end{aligned} \tag{A.55}$$

which is the same integration as the one obtained from the Bethe-Heitler limit of the AMY equation (neglecting the screen mass in \mathcal{A} when $q^2 \gg m_D^2$) The equivalence between these two expressions for the $g \rightarrow g + g$ channel and the $g \rightarrow q + \bar{q}$ channel can also be shown similarly.

Mass effect in the $2 \rightarrow 3$ squared matrix-elements For completeness, we briefly outline the derivation of $2 \rightarrow 3$ cross-section with mass effect. As a remark, putting the heavy flavor mass directly into the these matrix-elements is certainly legitimate if one only focus on $2 \rightarrow 3$ processes. But once we want to approximate the effect of multiple scatterings: $(n \rightarrow n+1) \approx (2 \rightarrow 3)(2 \rightarrow 2) \cdots (2 \rightarrow 2) \times$ corrections, it is not advantageous to put the mass effect into the $(2 \rightarrow 3)$ part, but better to be included into the last step of corrections, which is the approach we used.

First, we still work under the assumption that $M \ll E$, and will only keep terms

when M is making direct comparison to k_\perp, q_\perp . The kinematics are now changed to,

$$p_1 = (\sqrt{s}, 0, \vec{0}) \quad (\text{A.56})$$

$$p_2 = (0, \sqrt{s}, \vec{0}) \quad (\text{A.57})$$

$$k = (x\sqrt{s}, \frac{k_\perp^2}{x\sqrt{s}}, \vec{k}_\perp) \quad (\text{A.58})$$

$$q \sim \left(-\frac{q_\perp^2 \sqrt{s}}{s - M^2}, \frac{x(\vec{q}_\perp - \vec{k}_\perp)^2 + (1-x)k_\perp^2 + x^2 M^2}{x(1-x)\sqrt{s}}, \vec{k}_\perp \right) \quad (\text{A.59})$$

For the splitting amplitude, off diagonal elements of $\epsilon_{\lambda,\mu}(c)\bar{u}_s(a)\gamma^\mu v_{s'}(b)$ also need to be included for helicity flipping process. Moreover,

$$\sqrt{p \cdot \sigma} = \frac{p \cdot \sigma + M}{\sqrt{2(E + M)}} \approx \frac{p \cdot \sigma + M}{\sqrt{2E}} \quad (\text{A.60})$$

$$\sqrt{p \cdot \bar{\sigma}} = \frac{p \cdot \bar{\sigma} + M}{\sqrt{2(E + M)}} \approx \frac{p \cdot \bar{\sigma} + M}{\sqrt{2E}} \quad (\text{A.61})$$

where we have omitted the mass in the denominator since it only involves corrections of order M/E . From this one can see that the previous calculation can be used for the massive case with the substitution $a^\pm \rightarrow a^\pm + M$ and $b^\pm \rightarrow b^\pm + M$. Then, the splitting amplitude becomes,

$$\epsilon_{\lambda,\mu}\bar{u}_s(a)\gamma^\mu v_{s'}(b) = \frac{1}{\sqrt{2ab}}\xi_s^T A_{ss'}\eta_{s'} \quad (\text{A.62})$$

$$A_{\uparrow\uparrow} = \delta_{\lambda L} 2b_z a_L^\perp + \delta_{\lambda R} 2a_z b_R^\perp + \frac{c_\lambda^\perp}{c^+} (a_L^\perp b_R^\perp - a^+ b^+) \quad (\text{A.63})$$

$$A_{\downarrow\downarrow} = -\delta_{\lambda L} 2a_z b_L^\perp - \delta_{\lambda R} 2b_z a_R^\perp - \frac{c_\lambda^\perp}{c^+} (a_R^\perp b_L^\perp - a^+ b^+) \quad (\text{A.64})$$

$$A_{\uparrow\downarrow} = \delta_{\lambda L} 2a_L^\perp b_L^\perp + \delta_{\lambda R} (a^+ b^- + a^- b^+) - \frac{c_\lambda^\perp}{c^+} (a^+ b^\perp + a^\perp b^+) \quad (\text{A.65})$$

$$A_{\downarrow\uparrow} = \delta_{\lambda L} (a^+ b^- + a^- b^+) + \delta_{\lambda R} 2a_R^\perp b_R^\perp - \frac{c_\lambda^\perp}{c^+} (a^+ b^\perp + a^\perp b^+) \quad (\text{A.66})$$

Bibliography

- [A⁺⁰⁸] A. Adare et al. Suppression pattern of neutral pions at high transverse momentum in Au+Au collisions at $s_{NN}^{1/2} = 200$ GeV and constraints on medium transport coefficients. *Phys. Rev. Lett.*, 101:232301, 2008.
- [A⁺¹⁰] K Aamodt et al. Elliptic flow of charged particles in Pb-Pb collisions at 2.76 TeV. *Phys. Rev. Lett.*, 105:252302, 2010.
- [A⁺¹¹] K. Aamodt et al. Higher harmonic anisotropic flow measurements of charged particles in Pb-Pb collisions at $\sqrt{s_{NN}}=2.76$ TeV. *Phys. Rev. Lett.*, 107:032301, 2011.
- [A^{+12a}] S. Afanasiev et al. Measurement of Direct Photons in Au+Au Collisions at $\sqrt{s_{NN}} = 200$ GeV. *Phys. Rev. Lett.*, 109:152302, 2012.
- [A^{+12b}] Nestor Armesto et al. Comparison of Jet Quenching Formalisms for a Quark-Gluon Plasma 'Brick'. *Phys. Rev.*, C86:064904, 2012.
- [A^{+13a}] Georges Aad et al. Measurement of Z boson Production in Pb+Pb Collisions at $\sqrt{s_{NN}} = 2.76$ TeV with the ATLAS Detector. *Phys. Rev. Lett.*, 110(2):022301, 2013.
- [A^{+13b}] Georges Aad et al. Measurement with the ATLAS detector of multi-particle azimuthal correlations in p+Pb collisions at $\sqrt{s_{NN}} = 5.02$ TeV. *Phys. Lett.*, B725:60–78, 2013.
- [A^{+13c}] Ehab Abbas et al. Centrality dependence of the pseudorapidity density distribution for charged particles in Pb-Pb collisions at $\sqrt{s_{NN}} = 2.76$ TeV. *Phys. Lett.*, B726:610–622, 2013.
- [A^{+13d}] Betty Abelev et al. Directed Flow of Charged Particles at Midrapidity Relative to the Spectator Plane in Pb-Pb Collisions at $\sqrt{s_{NN}}=2.76$ TeV. *Phys. Rev. Lett.*, 111(23):232302, 2013.
- [A^{+14a}] Georges Aad et al. Measurement of long-range pseudorapidity correlations and azimuthal harmonics in $\sqrt{s_{NN}} = 5.02$ TeV proton-lead collisions with the ATLAS detector. *Phys. Rev.*, C90(4):044906, 2014.
- [A^{+14b}] Georges Aad et al. Measurement of the centrality and pseudorapidity dependence of the integrated elliptic flow in lead-lead collisions at $\sqrt{s_{NN}} = 2.76$ TeV with the ATLAS detector. *Eur. Phys. J.*, C74(8):2982, 2014.
- [A^{+14c}] B Abelev et al. Technical Design Report for the Upgrade of the ALICE Inner Tracking System. *J. Phys.*, G41:087002, 2014.

- [A^{+14d}] Betty Bezverkhny Abelev et al. Measurement of prompt D -meson production in $p - Pb$ collisions at $\sqrt{s_{NN}} = 5.02$ TeV. *Phys. Rev. Lett.*, 113(23):232301, 2014.
- [A^{+14e}] Betty Bezverkhny Abelev et al. Multiparticle azimuthal correlations in p-Pb and Pb-Pb collisions at the CERN Large Hadron Collider. *Phys. Rev.*, C90(5):054901, 2014.
- [A^{+14f}] Betty Bezverkhny Abelev et al. Multiparticle azimuthal correlations in p-Pb and Pb-Pb collisions at the CERN Large Hadron Collider. *Phys. Rev.*, C90(5):054901, 2014.
- [A^{+15a}] Georges Aad et al. Measurement of the centrality dependence of the charged-particle pseudorapidity distribution in proton-lead collisions at $\sqrt{s_{NN}} = 5.02$ TeV with the ATLAS detector. 2015.
- [A^{+15b}] Georges Aad et al. Measurement of the correlation between flow harmonics of different order in lead-lead collisions at $\sqrt{s_{NN}} = 2.76$ TeV with the ATLAS detector. *Phys. Rev.*, C92(3):034903, 2015.
- [A^{+15c}] A. Adare et al. An Upgrade Proposal from the PHENIX Collaboration. 2015.
- [A^{+15d}] A. Adare et al. Measurement of long-range angular correlation and quadrupole anisotropy of pions and (anti)protons in central $d + Au$ collisions at $\sqrt{s_{NN}} = 200$ GeV. *Phys. Rev. Lett.*, 114(19):192301, 2015.
- [A^{+15e}] A. Adare et al. Measurements of directed, elliptic, and triangular flow in Cu+Au collisions at $\sqrt{s_{NN}} = 200$ GeV. 2015.
- [A^{+15f}] A. Adare et al. Measurements of elliptic and triangular flow in high-multiplicity $^3He + Au$ collisions at $\sqrt{s_{NN}} = 200$ GeV. *Phys. Rev. Lett.*, 115(14):142301, 2015.
- [A^{+15g}] Ani Aprahamian et al. Reaching for the horizon: The 2015 long range plan for nuclear science. 2015.
- [A^{+16a}] Georges Aad et al. Centrality, rapidity and transverse momentum dependence of isolated prompt photon production in lead-lead collisions at $\sqrt{s_{NN}} = 2.76$ TeV measured with the ATLAS detector. *Phys. Rev.*, C93(3):034914, 2016.
- [A^{+16b}] Jaroslav Adam et al. Anisotropic flow of charged particles in Pb-Pb collisions at $\sqrt{s_{NN}} = 5.02$ TeV. *Phys. Rev. Lett.*, 116(13):132302, 2016.
- [A^{+16c}] Jaroslav Adam et al. Centrality dependence of the charged-particle multiplicity density at midrapidity in Pb-Pb collisions at $\sqrt{s_{NN}} = 5.02$ TeV. *Phys. Rev. Lett.*, 116(22):222302, 2016.

- [A^{+16d}] Jaroslav Adam et al. Centrality evolution of the charged-particle pseudorapidity density over a broad pseudorapidity range in Pb-Pb collisions at $\sqrt{s_{NN}} = 2.76$ TeV. *Phys. Lett.*, B754:373–385, 2016.
- [A^{+16e}] Jaroslav Adam et al. Correlated event-by-event fluctuations of flow harmonics in Pb-Pb collisions at $\sqrt{s_{NN}} = 2.76$ TeV. 2016.
- [A^{+16f}] Jaroslav Adam et al. Direct photon production in Pb-Pb collisions at $\sqrt{s_{NN}} = 2.76$ TeV. *Phys. Lett.*, B754:235–248, 2016.
- [A^{+16g}] Jaroslav Adam et al. Pseudorapidity dependence of the anisotropic flow of charged particles in Pb-Pb collisions at $\sqrt{s_{NN}} = 2.76$ TeV. *Phys. Lett.*, B762:376–388, 2016.
- [A^{+17a}] B. P. Abbott et al. GW170817: Observation of Gravitational Waves from a Binary Neutron Star Inspiral. *Phys. Rev. Lett.*, 119(16):161101, 2017.
- [A^{+17b}] L. Adamczyk et al. Measurement of D^0 Azimuthal Anisotropy at Midrapidity in Au+Au Collisions at $\sqrt{s_{NN}}=200$ GeV. *Phys. Rev. Lett.*, 118(21):212301, 2017.
- [A^{+18a}] Shreyasi Acharya et al. D -meson azimuthal anisotropy in midcentral Pb-Pb collisions at $\sqrt{s_{NN}} = \mathbf{5.02}$ TeV. *Phys. Rev. Lett.*, 120(10):102301, 2018.
- [A^{+18b}] Shreyasi Acharya et al. Measurement of D^0 , D^+ , D^{*+} and D_s^+ production in Pb-Pb collisions at $\sqrt{s_{NN}} = 5.02$ TeV. 2018.
- [A^{+18c}] A. Adare et al. Pseudorapidity Dependence of Particle Production and Elliptic Flow in Asymmetric Nuclear Collisions of $p+\text{Al}$, $p+\text{Au}$, $d+\text{Au}$, and ${}^3\text{He}+\text{Au}$ at $\sqrt{s_{NN}} = 200$ GeV. *Phys. Rev. Lett.*, 121(22):222301, 2018.
- [A⁺¹⁹] Jaroslav Adam et al. Centrality and transverse momentum dependence of D^0 meson production at mid-rapidity in Au+Au collisions at $\sqrt{s_{NN}} = 200$ GeV. *Phys. Rev.*, C99(3):034908, 2019.
- [ACI16a] Peter Arnold, Han-Chih Chang, and Shahin Iqbal. The LPM effect in sequential bremsstrahlung 2: factorization. *JHEP*, 09:078, 2016.
- [ACI16b] Peter Arnold, Han-Chih Chang, and Shahin Iqbal. The LPM effect in sequential bremsstrahlung: 4-gluon vertices. *JHEP*, 10:124, 2016.
- [ACI16c] Peter Arnold, Han-Chih Chang, and Shahin Iqbal. The LPM effect in sequential bremsstrahlung: dimensional regularization. *JHEP*, 10:100, 2016.

- [AD08] Peter Brockway Arnold and Caglar Dogan. QCD Splitting/Joining Functions at Finite Temperature in the Deep LPM Regime. *Phys. Rev.*, D78:065008, 2008.
- [AER10] Jussi Auvinen, Kari J. Eskola, and Thorsten Renk. A Monte-Carlo model for elastic energy loss in a hydrodynamical background. *Phys. Rev.*, C82:024906, 2010.
- [AFG⁺14] S. Ambikasaran, D. Foreman-Mackey, L. Greengard, D. W. Hogg, and M. O’Neil. Fast Direct Methods for Gaussian Processes. *ArXiv e-prints*, March 2014.
- [AFMG⁺14] S. Ambikasaran, D. Foreman-Mackey, L. Greengard, D. W. Hogg, and M. O’Neil. Fast direct methods for gaussian processes and the analysis of nasa kepler mission data. mar 2014.
- [AGG14] Joerg Aichelin, Pol Bernard Gossiaux, and Thierry Gousset. Gluon radiation by heavy quarks at intermediate energies. *Phys. Rev.*, D89(7):074018, 2014.
- [AGZ02] P. Aurenche, F. Gelis, and H. Zaraket. A Simple sum rule for the thermal gluon spectral function and applications. *JHEP*, 05:043, 2002.
- [AI15] Peter Arnold and Shahin Iqbal. The LPM effect in sequential bremsstrahlung. *JHEP*, 04:070, 2015. [Erratum: JHEP09,072(2016)].
- [AJMS12] Raktim Abir, Umme Jamil, Munshi G. Mustafa, and Dinesh K. Srivastava. Heavy quark energy loss and D-mesons in RHIC and LHC energies. *Phys. Lett.*, B715:183–189, 2012.
- [AKBB18] Jussi Auvinen, Iurii Karpenko, Jonah E. Bernhard, and Steffen A. Bass. Investigating the collision energy dependence of η/s in RHIC beam energy scan using Bayesian statistics. *Phys. Rev.*, C97(4):044905, 2018.
- [AMSS18] Liliana ApolinÃ¡rio, JosÃ£o Guilherme Milhano, Gavin P. Salam, and Carlos A. Salgado. Probing the time structure of the quark-gluon plasma with top quarks. *Phys. Rev. Lett.*, 120(23):232301, 2018.
- [AMY02] Peter Brockway Arnold, Guy D. Moore, and Laurence G. Yaffe. Photon and gluon emission in relativistic plasmas. *JHEP*, 06:030, 2002.
- [AMY03a] Peter Brockway Arnold, Guy D. Moore, and Laurence G. Yaffe. Effective kinetic theory for high temperature gauge theories. *JHEP*, 01:030, 2003.
- [AMY03b] Peter Brockway Arnold, Guy D. Moore, and Laurence G. Yaffe. Transport coefficients in high temperature gauge theories. 2. Beyond leading log. *JHEP*, 05:051, 2003.

- [AP77] Guido Altarelli and G. Parisi. Asymptotic Freedom in Parton Language. *Nucl. Phys.*, B126:298–318, 1977.
- [AR10] B. Alver and G. Roland. Collision geometry fluctuations and triangular flow in heavy-ion collisions. *Phys. Rev.*, C81:054905, 2010. [Erratum: Phys. Rev.C82,039903(2010)].
- [Arn09] Peter Brockway Arnold. High-energy gluon bremsstrahlung in a finite medium: harmonic oscillator versus single scattering approximation. *Phys. Rev.*, D80:025004, 2009.
- [ASW04] Nestor Armesto, Carlos A. Salgado, and Urs Achim Wiedemann. Medium induced gluon radiation off massive quarks fills the dead cone. *Phys. Rev.*, D69:114003, 2004.
- [B⁺98] S. A. Bass et al. Microscopic models for ultrarelativistic heavy ion collisions. *Prog. Part. Nucl. Phys.*, 41:255–369, 1998. [Prog. Part. Nucl. Phys.41,225(1998)].
- [B⁺99] M. Bleicher et al. Relativistic hadron hadron collisions in the ultrarelativistic quantum molecular dynamics model. *J. Phys.*, G25:1859–1896, 1999.
- [B⁺05] B. B. Back et al. Scaling of charged particle production in d + Au collisions at s(NN)**(1/2) = 200-GeV. *Phys. Rev.*, C72:031901, 2005.
- [B⁺14a] A. Bazavov et al. Equation of state in (2+1)-flavor QCD. *Phys. Rev.*, D90:094503, 2014.
- [B⁺14b] Karen M. Burke et al. Extracting the jet transport coefficient from jet quenching in high-energy heavy-ion collisions. *Phys. Rev.*, C90(1):014909, 2014.
- [B⁺17] A. Bazavov et al. The QCD Equation of State to $\mathcal{O}(\mu_B^6)$ from Lattice QCD. *Phys. Rev.*, D95(5):054504, 2017.
- [B⁺18] A. Beraudo et al. Extraction of Heavy-Flavor Transport Coefficients in QCD Matter. *Nucl. Phys.*, A979:21–86, 2018.
- [BB13] Piotr Bozek and Wojciech Broniowski. Collective dynamics in high-energy proton-nucleus collisions. *Phys. Rev.*, C88(1):014903, 2013.
- [BB16a] Piotr Bozek and Wojciech Broniowski. The torque effect and fluctuations of entropy deposition in rapidity in ultra-relativistic nuclear collisions. *Phys. Lett.*, B752:206–211, 2016.
- [BB16b] Wojciech Broniowski and Piotr BoÅijek. Simple model for rapidity fluctuations in the initial state of ultrarelativistic heavy-ion collisions. *Phys. Rev.*, C93(6):064910, 2016.

- [BBO15] Piotr Bozek, Wojciech Broniowski, and Adam Olszewski. Hydrodynamic modeling of pseudorapidity flow correlations in relativistic heavy-ion collisions and the torque effect. *Phys. Rev.*, C91:054912, 2015.
- [BCG⁺14] Ante Bilandzic, Christian Holm Christensen, Kristjan Gulbrandsen, Alexander Hansen, and You Zhou. Generic framework for anisotropic flow analyses with multiparticle azimuthal correlations. *Phys. Rev.*, C89(6):064904, 2014.
- [BDGM12] Debasish Banerjee, Saumen Datta, Rajiv Gavai, and Pushan Majumdar. Heavy Quark Momentum Diffusion Coefficient from Lattice QCD. *Phys. Rev.*, D85:014510, 2012.
- [BDH⁺12] A. Bazavov, H.-T. Ding, P. Hegde, O. Kaczmarek, F. Karsch, E. Laermann, Swagato Mukherjee, P. Petreczky, C. Schmidt, D. Smith, W. Soeldner, and M. Wagner. Freeze-out conditions in heavy ion collisions from qcd thermodynamics. *Phys. Rev. Lett.*, 109:192302, Nov 2012.
- [BDM⁺97a] R. Baier, Yuri L. Dokshitzer, Alfred H. Mueller, S. Peigne, and D. Schiff. Radiative energy loss and p(T) broadening of high-energy partons in nuclei. *Nucl. Phys.*, B484:265–282, 1997.
- [BDM⁺97b] R. Baier, Yuri L. Dokshitzer, Alfred H. Mueller, S. Peigne, and D. Schiff. Radiative energy loss of high-energy quarks and gluons in a finite volume quark - gluon plasma. *Nucl. Phys.*, B483:291–320, 1997.
- [BDMS98] R. Baier, Yuri L. Dokshitzer, Alfred H. Mueller, and D. Schiff. Radiative energy loss of high-energy partons traversing an expanding QCD plasma. *Phys. Rev.*, C58:1706–1713, 1998.
- [Ber18] Jonah E. Bernhard. *Bayesian parameter estimation for relativistic heavy-ion collisions*. PhD thesis, 2018.
- [BGM⁺09] Steffen A. Bass, Charles Gale, Abhijit Majumder, Chiho Nonaka, Guang-You Qin, Thorsten Renk, and Jorg Ruppert. Systematic Comparison of Jet Energy-Loss Schemes in a realistic hydrodynamic medium. *Phys. Rev.*, C79:024901, 2009.
- [BHS16] Dennis Bazow, Ulrich W. Heinz, and Michael Strickland. Massively parallel simulations of relativistic fluid dynamics on graphics processing units with CUDA. 2016.
- [BIR01] J. P. Blaizot, Edmond Iancu, and A. Rebhan. Approximately selfconsistent resummations for the thermodynamics of the quark gluon plasma. 1. Entropy and density. *Phys. Rev.*, D63:065003, 2001.
- [Bjo83] J. D. Bjorken. Highly relativistic nucleus-nucleus collisions: The central rapidity region. *Phys. Rev. D*, 27:140–151, Jan 1983.

- [BJP15] Rajeev S. Bhalerao, Amaresh Jaiswal, and Subrata Pal. Collective flow in event-by-event partonic transport plus hydrodynamics hybrid approach. *Phys. Rev.*, C92(1):014903, 2015.
- [BMB⁺16] Jonah E. Bernhard, J. Scott Moreland, Steffen A. Bass, Jia Liu, and Ulrich Heinz. Applying Bayesian parameter estimation to relativistic heavy-ion collisions: simultaneous characterization of the initial state and quark-gluon plasma medium. *Phys. Rev.*, C94(2):024907, 2016.
- [BMCS⁺15] Jonah E. Bernhard, Peter W. Marcy, Christopher E. Coleman-Smith, Snehalata Huzurbazar, Robert L. Wolpert, and Steffen A. Bass. Quantifying properties of hot and dense QCD matter through systematic model-to-data comparison. *Phys. Rev.*, C91(5):054910, 2015.
- [BOP15] Rajeev S. Bhalerao, Jean-Yves Ollitrault, and Subrata Pal. Characterizing flow fluctuations with moments. *Phys. Lett.*, B742:94–98, 2015.
- [BSTV13] Adam Bzdak, Bjoern Schenke, Prithwish Tribedy, and Raju Venugopalan. Initial state geometry and the role of hydrodynamics in proton-proton, proton-nucleus and deuteron-nucleus collisions. *Phys. Rev.*, C87(6):064906, 2013.
- [BSV11] Ante Bilandzic, Raimond Snellings, and Sergei Voloshin. Flow analysis with cumulants: Direct calculations. *Phys. Rev.*, C83:044913, 2011.
- [BT91] Eric Braaten and Markus H. Thoma. Energy loss of a heavy fermion in a hot qed plasma. *Phys. Rev. D*, 44:1298–1310, Aug 1991.
- [BT13] Adam Bzdak and Derek Teaney. Longitudinal fluctuations of the fireball density in heavy-ion collisions. *Phys. Rev.*, C87(2):024906, 2013.
- [BW09] Piotr Bozek and Iwona Wyskiel. Rapid hydrodynamic expansion in relativistic heavy-ion collisions. *Phys. Rev.*, C79:044916, 2009.
- [BW10] Piotr Bozek and Iwona Wyskiel. Directed flow in ultrarelativistic heavy-ion collisions. *Phys. Rev.*, C81:054902, 2010.
- [C⁺11] Serguei Chatrchyan et al. Study of Z boson production in PbPb collisions at $\sqrt{s_{NN}} = 2.76$ TeV. *Phys. Rev. Lett.*, 106:212301, 2011.
- [C⁺13a] Serguei Chatrchyan et al. Multiplicity and transverse momentum dependence of two- and four-particle correlations in pPb and PbPb collisions. *Phys. Lett.*, B724:213–240, 2013.
- [C⁺13b] Serguei Chatrchyan et al. Observation of long-range near-side angular correlations in proton-lead collisions at the LHC. *Phys. Lett.*, B718:795–814, 2013.

- [C⁺17] S. Cao et al. Multistage Monte-Carlo simulation of jet modification in a static medium. *Phys. Rev.*, C96(2):024909, 2017.
- [C⁺18] Shanshan Cao et al. Towards the determination of heavy-quark transport coefficients in quark-gluon plasma. 2018.
- [CBOP18] Chandrodoy ChattoPadhyay, Rajeev S. Bhalerao, Jean-Yves Ollitrault, and Subrata Pal. Effects of initial-state dynamics on collective flow within a coupled transport and viscous hydrodynamic approach. *Phys. Rev. C*, 97:034915, Mar 2018.
- [CF74] Fred Cooper and Graham Frye. Single-particle distribution in the hydrodynamic and statistical thermodynamic models of multiparticle production. *Phys. Rev. D*, 10:186–189, Jul 1974.
- [CGN98] Matteo Cacciari, Mario Greco, and Paolo Nason. The P(T) spectrum in heavy flavor hadroproduction. *JHEP*, 05:007, 1998.
- [Cha06] A. K. Chaudhuri. Dissipative hydrodynamics in 2+1 dimension. *Phys. Rev.*, C74:044904, 2006.
- [CHG10] Simon Caron-Huot and Charles Gale. Finite-size effects on the radiative energy loss of a fast parton in hot and dense strongly interacting matter. *Phys. Rev.*, C82:064902, 2010.
- [CHM08] Simon Caron-Huot and Guy D. Moore. Heavy quark diffusion in QCD and N=4 SYM at next-to-leading order. *JHEP*, 02:081, 2008.
- [CIMS18] P. Caucal, E. Iancu, A. H. Mueller, and G. Soyez. Vacuumlike jet fragmentation in a dense qcd medium. *Phys. Rev. Lett.*, 120:232001, Jun 2018.
- [CIMS19] Paul Caucal, Edmond Iancu, Alfred H. Mueller, and Gregory Soyez. A new pQCD based Monte Carlo event generator for jets in the quark-gluon plasma. *PoS*, HardProbes2018:028, 2019.
- [CLQW16] Shanshan Cao, Tan Luo, Guang-You Qin, and Xin-Nian Wang. Linearized Boltzmann transport model for jet propagation in the quark-gluon plasma: Heavy quark evolution. *Phys. Rev.*, C94(1):014909, 2016.
- [CLQW18] Shanshan Cao, Tan Luo, Guang-You Qin, and Xin-Nian Wang. Heavy and light flavor jet quenching at RHIC and LHC energies. *Phys. Lett.*, B777:255–259, 2018.
- [CM17] Shanshan Cao and Abhijit Majumder. Nuclear modification of single hadron and jet production within a virtuality-ordered (MATTER) parton shower. 2017.
- [Col12] ATLAS Collaboration. Future of the ATLAS heavy ion program. 2012.

- [col15] The ATLAS collaboration. Measurement of two-particle pseudorapidity correlations in lead-lead collisions at $\sqrt{s_{NN}} = 2.76$ TeV with the ATLAS detector. 2015.
- [Col17a] CMS Collaboration. Projected Heavy Ion Physics Performance at the High Luminosity LHC Era with the CMS Detector. 2017.
- [col17b] The ATLAS collaboration. Z boson production in Pb+Pb collisions at $\sqrt{s_{NN}} = 5.02$ TeV with the ATLAS detector at the LHC. 2017.
- [CQB13a] Shanshan Cao, Guang-You Qin, and Steffen A. Bass. Heavy-quark dynamics and hadronization in ultrarelativistic heavy-ion collisions: Collisional versus radiative energy loss. *Phys. Rev.*, C88:044907, 2013.
- [CQB13b] Shanshan Cao, Guang-You Qin, and Steffen A. Bass. Model and parameter dependence of heavy quark energy loss in a hot and dense medium. *J. Phys.*, G40:085103, 2013.
- [CQB15] Shanshan Cao, Guang-You Qin, and Steffen A. Bass. Energy loss, hadronization and hadronic interactions of heavy flavors in relativistic heavy-ion collisions. *Phys. Rev.*, C92(2):024907, 2015.
- [CSG⁺16] Sandeep Chatterjee, Sushant Kumar Singh, Snigdha Ghosh, Md Hasanujjaman, Jane Alam, and Sourav Sarkar. Initial condition from the shadowed Glauber model. *Phys. Lett.*, B758:269–273, 2016.
- [CSM12] Christopher E Coleman-Smith and Berndt Muller. Results of a systematic study of dijet suppression measured at the BNL Relativistic Heavy Ion Collider. *Phys. Rev.*, C86:054901, 2012.
- [CSS07] Jorge Casalderrey-Solana and Carlos A. Salgado. Introductory lectures on jet quenching in heavy ion collisions. *Acta Phys. Polon.*, B38:3731–3794, 2007.
- [DBPT19] Tianyu Dai, Steffen A. Bass, Jean-FranÃ§ois Paquet, and Derek Teaney. Parton energy loss in the reformulated weakly-coupled kinetic approach. *PoS*, HardProbes2018:063, 2019.
- [DFK⁺12] H. T. Ding, A. Francis, O. Kaczmarek, F. Karsch, H. Satz, and W. Soeldner. Charmonium properties in hot quenched lattice QCD. *Phys. Rev.*, D86:014509, 2012.
- [DGW05] Magdalena Djordjevic, Miklos Gyulassy, and Simon Wicks. The Charm and beauty of RHIC and LHC. *Phys. Rev. Lett.*, 94:112301, 2005.
- [DH08] Magdalena Djordjevic and Ulrich W. Heinz. Radiative energy loss in a finite dynamical QCD medium. *Phys. Rev. Lett.*, 101:022302, 2008.

- [DK01] Yuri L. Dokshitzer and D. E. Kharzeev. Heavy quark colorimetry of QCD matter. *Phys. Lett.*, B519:199–206, 2001.
- [DKLN12] Adrian Dumitru, Dmitri E. Kharzeev, Eugene M. Levin, and Yasushi Nara. Gluon Saturation in pA Collisions at the LHC: KLN Model Predictions For Hadron Multiplicities. *Phys. Rev.*, C85:044920, 2012.
- [DKT91] Yu L Dokshitzer, V A Khoze, and S I Troyan. On specific QCD properties of heavy quark fragmentation (dead cone). *Journal of Physics G: Nuclear and Particle Physics*, 17(10):1602–1604, oct 1991.
- [DMRS15] Gabriel Denicol, Akihiko Monnai, Sangwook Ryu, and Bjoern Schenke. New insights from 3D simulations of heavy ion collisions. In *25th International Conference on Ultra-Relativistic Nucleus-Nucleus Collisions (Quark Matter 2015) Kobe, Japan, September 27-October 3, 2015*, 2015.
- [DN07] H. J. Drescher and Y. Nara. Effects of fluctuations on the initial eccentricity from the Color Glass Condensate in heavy ion collisions. *Phys. Rev.*, C75:034905, 2007.
- [Dok77] Yuri L. Dokshitzer. Calculation of the Structure Functions for Deep Inelastic Scattering and e+ e- Annihilation by Perturbation Theory in Quantum Chromodynamics. *Sov. Phys. JETP*, 46:641–653, 1977. [Zh. Eksp. Teor. Fiz. 73, 1216(1977)].
- [DT08] K. Dusling and D. Teaney. Simulating elliptic flow with viscous hydrodynamics. *Phys. Rev.*, C77:034905, 2008.
- [EKRT00] K. J. Eskola, K. Kajantie, P. V. Ruuskanen, and Kimmo Tuominen. Scaling of transverse energies and multiplicities with atomic number and energy in ultrarelativistic nuclear collisions. *Nucl. Phys.*, B570:379–389, 2000.
- [EPPS17] Kari J. Eskola, Petja Paakkinen, Hannu Paukkunen, and Carlos A. Salgado. EPPS16: Nuclear parton distributions with LHC data. *Eur. Phys. J.*, C77(3):163, 2017.
- [EPS09] K. J. Eskola, H. Paukkunen, and C. A. Salgado. EPS09: A New Generation of NLO and LO Nuclear Parton Distribution Functions. *JHEP*, 04:065, 2009.
- [FH11] Kenji Fukushima and Tetsuo Hatsuda. The phase diagram of dense QCD. *Rept. Prog. Phys.*, 74:014001, 2011.
- [Fie89] R. D. Field. Applications of Perturbative QCD. *Front. Phys.*, 77:1–366, 1989.

- [FKL⁺15] A. Francis, O. Kaczmarek, M. Laine, T. Neuhaus, and H. Ohno. Nonperturbative estimate of the heavy quark momentum diffusion coefficient. *Phys. Rev.*, D92(11):116003, 2015.
- [FMHLG13] Daniel Foreman-Mackey, David W. Hogg, Dustin Lang, and Jonathan Goodman. emcee: The mcmc hammer. *Publications of the Astronomical Society of the Pacific*, 125(925):306, 2013.
- [FUXG13] Oliver Fochler, Jan Uphoff, Zhe Xu, and Carsten Greiner. Radiative parton processes in perturbative QCD: An improved version of the Gunion and Bertsch cross section from comparisons to the exact result. *Phys. Rev.*, D88(1):014018, 2013.
- [GA08] P. B. Gossiaux and J. Aichelin. Towards an understanding of the RHIC single electron data. *Phys. Rev.*, C78:014904, 2008.
- [GA09] Pol B. Gossiaux and Joerg Aichelin. Energy Loss of Heavy Quarks in a QGP with a Running Coupling Constant Approach. *Nucl. Phys.*, A830:203C–206C, 2009.
- [GB82] J. F. Gunion and G. Bertsch. Hadronization by color bremsstrahlung. *Phys. Rev. D*, 25:746–753, Feb 1982.
- [GBB⁺17] J. N. Guenther, R. Bellwied, S. Borsanyi, Z. Fodor, S. D. Katz, A. Pasztor, C. Ratti, and K. K. Szabó. The QCD equation of state at finite density from analytical continuation. *Nucl. Phys.*, A967:720–723, 2017.
- [GGLNH17] Fernando G. Gardim, Frederique Grassi, Matthew Luzum, and Jacqueline Noronha-Hostler. Hydrodynamic Predictions for Mixed Harmonic Correlations in 200 GeV Au+Au Collisions. *Phys. Rev.*, C95(3):034901, 2017.
- [GJS⁺13] Charles Gale, Sangyong Jeon, Björn Schenke, Prithwish Tribedy, and Raju Venugopalan. Event-by-event anisotropic flow in heavy-ion collisions from combined Yang-Mills and viscous fluid dynamics. *Phys. Rev. Lett.*, 110(1):012302, 2013.
- [GL72] V. N. Gribov and L. N. Lipatov. Deep inelastic e p scattering in perturbation theory. *Sov. J. Nucl. Phys.*, 15:438–450, 1972. [Yad. Fiz.15,781(1972)].
- [GLV00] Miklos Gyulassy, Peter Levai, and Ivan Vitev. Jet quenching in thin quark gluon plasmas. 1. Formalism. *Nucl. Phys.*, B571:197–233, 2000.
- [GMT16] Jacopo Ghiglieri, Guy D. Moore, and Derek Teaney. Jet-Medium Interactions at NLO in a Weakly-Coupled Quark-Gluon Plasma. *JHEP*, 03:095, 2016.

- [Gos13] Pol Bernard Gossiaux. Recent results on heavy quark quenching in ultrarelativistic heavy ion collisions: the impact of coherent gluon radiation. *Nucl. Phys.*, A910-911:301–305, 2013.
- [Gro17] Fabrizio Grosa. Measurement of the D-meson nuclear modification factor and elliptic flow in Pb-Pb collisions at $\sqrt{s_{NN}} = 5.02$ TeV with ALICE at the LHC. In *17th International Conference on Strangeness in Quark Matter (SQM 2017) Utrecht, the Netherlands, July 10-15, 2017*, 2017.
- [GVWZ03] Miklos Gyulassy, Ivan Vitev, Xin-Nian Wang, and Ben-Wei Zhang. Jet quenching and radiative energy loss in dense nuclear matter. pages 123–191, 2003.
- [GW73] David J. Gross and Frank Wilczek. Ultraviolet Behavior of Nonabelian Gauge Theories. *Phys. Rev. Lett.*, 30:1343–1346, 1973. [,271(1973)].
- [GYNHO16] Giuliano Giacalone, Li Yan, Jacquelyn Noronha-Hostler, and Jean-Yves Ollitrault. Symmetric cumulants and event-plane correlations in Pb + Pb collisions. *Phys. Rev.*, C94(1):014906, 2016.
- [HCC⁺19] Yayun He, Shanshan Cao, Wei Chen, Tan Luo, Long-Gang Pang, and Xin-Nian Wang. Interplaying mechanisms behind single inclusive jet suppression in heavy-ion collisions. *Phys. Rev. C*, 99:054911, May 2019.
- [HFR11] Min He, Rainer J. Fries, and Ralf Rapp. Thermal Relaxation of Charm in Hadronic Matter. *Phys. Lett.*, B701:445–450, 2011.
- [HFR13] Min He, Rainer J. Fries, and Ralf Rapp. D_s -Meson as Quantitative Probe of Diffusion and Hadronization in Nuclear Collisions. *Phys. Rev. Lett.*, 110(11):112301, 2013.
- [HGWR08] Dave Higdon, James Gattiker, Brian Williams, and Maria Rightley. Computer model calibration using high-dimensional output. *Journal of the American Statistical Association*, 103(482):570–583, 2008.
- [HHMN13] Tetsufumi Hirano, Pasi Huovinen, Koichi Murase, and Yasushi Nara. Integrated Dynamical Approach to Relativistic Heavy Ion Collisions. *Prog. Part. Nucl. Phys.*, 70:108–158, 2013.
- [HMS⁺15] Dave Higdon, Jordan D. McDonnell, Nicolas Schunck, Jason Sarich, and Stefan M Wild. A Bayesian Approach for Parameter Estimation and Prediction using a Computationally Intensive Model. *J.Phys.*, G42(3):034009, 2015.
- [HR19] Min He and Ralf Rapp. Hadronization and Charm-Hadron Ratios in Heavy-Ion Collisions. 2019.

- [HS13] Ulrich Heinz and Raimond Snellings. Collective flow and viscosity in relativistic heavy-ion collisions. *Ann. Rev. Nucl. Part. Sci.*, 63:123–151, 2013.
- [HSC06] Ulrich W. Heinz, Huichao Song, and Asis K. Chaudhuri. Dissipative hydrodynamics for viscous relativistic fluids. *Phys. Rev.*, C73:034904, 2006.
- [HvHG⁺13] Min He, Hendrik van Hees, Pol B. Gossiaux, Rainer J. Fries, and Ralf Rapp. Relativistic Langevin Dynamics in Expanding Media. *Phys. Rev.*, E88:032138, 2013.
- [Isr76] Werner Israel. Nonstationary irreversible thermodynamics: A causal relativistic theory. *Annals of Physics*, 100(1):310 – 331, 1976.
- [Jef61] Harold Jeffreys. *The Theory of Probability*. The International series of monographs on physics. Oxford, 3rd ed edition, 1961.
- [JH14] Jiangyong Jia and Peng Huo. Forward-backward eccentricity and participant-plane angle fluctuations and their influences on longitudinal dynamics of collective flow. *Phys. Rev.*, C90(3):034915, 2014.
- [Jia16] Jiangyong Jia. Forward-backward multiplicity correlations in pp, pPb and Pb+Pb collisions with the ATLAS detector. In *25th International Conference on Ultra-Relativistic Nucleus-Nucleus Collisions (Quark Matter 2015) Kobe, Japan, September 27-October 3, 2015*, 2016.
- [JM05] Sangyong Jeon and Guy D. Moore. Energy loss of leading partons in a thermal QCD medium. *Phys. Rev.*, C71:034901, 2005.
- [JRZ16] Jiangyong Jia, Sooraj Radhakrishnan, and Mingliang Zhou. Forward-backward multiplicity fluctuation and longitudinal harmonics in high-energy nuclear collisions. *Phys. Rev.*, C93(4):044905, 2016.
- [K⁺15a] Vardan Khachatryan et al. Evidence for Collective Multiparticle Correlations in p-Pb Collisions. *Phys. Rev. Lett.*, 115(1):012301, 2015.
- [K⁺15b] Vardan Khachatryan et al. Evidence for Collective Multiparticle Correlations in p-Pb Collisions. *Phys. Rev. Lett.*, 115(1):012301, 2015.
- [K⁺15c] Vardan Khachatryan et al. Evidence for transverse momentum and pseudorapidity dependent event plane fluctuations in PbPb and pPb collisions. *Phys. Rev.*, C92(3):034911, 2015.
- [K⁺15d] Vardan Khachatryan et al. Evidence for transverse momentum and pseudorapidity dependent event plane fluctuations in PbPb and pPb collisions. *Phys. Rev.*, C92(3):034911, 2015.

- [K⁺16a] Vardan Khachatryan et al. Pseudorapidity dependence of long-range two-particle correlations in $p\text{Pb}$ collisions at $\sqrt{s_{NN}} = 5.02$ TeV. *Submitted to: Phys. Rev. C*, 2016.
- [K⁺16b] K. Kovarik et al. nCTEQ15 - Global analysis of nuclear parton distributions with uncertainties in the CTEQ framework. *Phys. Rev.*, D93(8):085037, 2016.
- [K⁺17a] Vardan Khachatryan et al. Charged-particle nuclear modification factors in PbPb and pPb collisions at $\sqrt{s_{NN}} = 5.02$ TeV. *JHEP*, 04:039, 2017.
- [K⁺17b] Vardan Khachatryan et al. Suppression and azimuthal anisotropy of prompt and nonprompt J/ψ production in PbPb collisions at $\sqrt{s_{NN}} = 2.76$ TeV. *Eur. Phys. J.*, C77(4):252, 2017.
- [Kau18] Kolja Kauder. JETSCAPE v1.0 Quickstart Guide. In *27th International Conference on Ultrarelativistic Nucleus-Nucleus Collisions (Quark Matter 2018) Venice, Italy, May 14-19, 2018*, 2018.
- [KHB14] Iu. Karpenko, P. Huovinen, and M. Bleicher. A 3+1 dimensional viscous hydrodynamic code for relativistic heavy ion collisions. *Comput. Phys. Commun.*, 185:3016–3027, 2014.
- [KLRO⁺15] Zhong-Bo Kang, Robin Lashof-Regas, Grigory Ovanesyan, Philip Saad, and Ivan Vitev. Jet quenching phenomenology from soft-collinear effective theory with Glauber gluons. *Phys. Rev. Lett.*, 114(9):092002, 2015.
- [KMBB17] Weiyao Ke, J. Scott Moreland, Jonah E. Bernhard, and Steffen A. Bass. Constraints on rapidity-dependent initial conditions from charged-particle pseudorapidity densities and two-particle correlations. *Phys. Rev. C*, 96:044912, Oct 2017.
- [KMP⁺19] Aleksi Kurkela, Aleksas Mazeliauskas, Jean-François Paquet, Sören Schlichting, and Derek Teaney. Matching the Nonequilibrium Initial Stage of Heavy Ion Collisions to Hydrodynamics with QCD Kinetic Theory. *Phys. Rev. Lett.*, 122(12):122302, 2019.
- [KRV17] Zhong-Bo Kang, Felix Ringer, and Ivan Vitev. Effective field theory approach to open heavy flavor production in heavy-ion collisions. *JHEP*, 03:146, 2017.
- [KW03] Alexander Kovner and Urs Achim Wiedemann. Gluon radiation and parton energy loss. pages 192–248, 2003.
- [KXB18] Weiyao Ke, Yingru Xu, and Steffen A. Bass. A linearized Boltzmann–Langevin model for heavy quark transport in hot and dense QCD matter. 2018.

- [LDK01] Zi-wei Lin, T. G. Di, and C. M. Ko. Charm meson scattering cross-sections by pion and rho meson. *Nucl. Phys.*, A689:965–979, 2001.
- [LGH⁺10] Hung-Liang Lai, Marco Guzzi, Joey Huston, Zhao Li, Pavel M. Nadolsky, Jon Pumplin, and C. P. Yuan. New parton distributions for collider physics. *Phys. Rev.*, D82:074024, 2010.
- [Loi16] Constantin Loizides. Experimental overview on small collision systems at the LHC. In *25th International Conference on Ultra-Relativistic Nucleus-Nucleus Collisions (Quark Matter 2015) Kobe, Japan, September 27-October 3, 2015*, 2016.
- [LR08] Matthew Luzum and Paul Romatschke. Conformal Relativistic Viscous Hydrodynamics: Applications to RHIC results at $s(\text{NN})^{**}(1/2) = 200\text{-GeV}$. *Phys. Rev.*, C78:034915, 2008. [Erratum: *Phys. Rev.*C79,039903(2009)].
- [LSH15] Jia Liu, Chun Shen, and Ulrich Heinz. Pre-equilibrium evolution effects on heavy-ion collision observables. *Phys. Rev.*, C91(6):064906, 2015. [Erratum: *Phys. Rev.*C92,no.4,049904(2015)].
- [Maj09] A. Majumder. The In-medium scale evolution in jet modification. 2009.
- [Maj12] Abhijit Majumder. Hard collinear gluon radiation and multiple scattering in a medium. *Phys. Rev.*, D85:014023, 2012.
- [MBB15] J. Scott Moreland, Jonah E. Bernhard, and Steffen A. Bass. Alternative ansatz to wounded nucleon and binary collision scaling in high-energy nuclear collisions. *Phys. Rev.*, C92(1):011901, 2015.
- [MBB18] J. Scott Moreland, Jonah E. Bernhard, and Steffen A. Bass. Estimating initial state and quark-gluon plasma medium properties using a hybrid model with nucleon substructure calibrated to $p\text{-Pb}$ and Pb-Pb collisions at $\sqrt{s_{NN}} = 5.02 \text{ TeV}$. 2018.
- [Meh04] Thomas Mehen. Charm production asymmetries from heavy quark recombination. *AIP Conf. Proc.*, 698(1):508–512, 2004.
- [Mig56] A. B. Migdal. Bremsstrahlung and pair production in condensed media at high energies. *Phys. Rev.*, 103:1811–1820, Sep 1956.
- [MM08] A. Majumder and Berndt Muller. Higher twist jet broadening and classical propagation. *Phys. Rev.*, C77:054903, 2008.
- [MP15] Larry McLerran and Michal Praszalowicz. Fluctuations and the Participant Number Dependence of pA Collisions. 2015.
- [MR04] Azwinndini Muronga and Dirk H. Rischke. Evolution of hot, dissipative quark matter in relativistic nuclear collisions. 2004.

- [MRSS07] Michael L. Miller, Klaus Reygers, Stephen J. Sanders, and Peter Steinberg. Glauber modeling in high energy nuclear collisions. *Ann. Rev. Nucl. Part. Sci.*, 57:205–243, 2007.
- [MS13] Denes Molnar and Deke Sun. High-pT suppression and elliptic flow from radiative energy loss with realistic bulk medium expansion. 2013.
- [MS16a] Akihiko Monnai and Bjoern Schenke. Pseudorapidity correlations in heavy ion collisions from viscous fluid dynamics. *Phys. Lett.*, B752:317–321, 2016.
- [MS16b] J. Scott Moreland and Ron A. Soltz. Hydrodynamic simulations of relativistic heavy-ion collisions with different lattice quantum chromodynamics calculations of the equation of state. *Phys. Rev.*, C93(4):044913, 2016.
- [MSST17] Heikki MÄntysaari, Björn Schenke, Chun Shen, and Prithwish Tripathy. Imprints of fluctuating proton shapes on flow in proton-lead collisions at the LHC. *Phys. Lett.*, B772:681–686, 2017.
- [MT05] Guy D. Moore and Derek Teaney. How much do heavy quarks thermalize in a heavy ion collision? *Phys. Rev.*, C71:064904, 2005.
- [MT19] Yacine Mehtar-Tani. Gluon bremsstrahlung in finite media beyond multiple soft scattering approximation. 2019.
- [MTST12] Yacine Mehtar-Tani, Carlos A. Salgado, and Konrad Tywoniuk. The Radiation pattern of a QCD antenna in a dense medium. *JHEP*, 10:197, 2012.
- [MTT18] Yacine Mehtar-Tani and Konrad Tywoniuk. Radiative energy loss of neighboring subjects. *Nucl. Phys.*, A979:165–203, 2018.
- [MVL11] A. Majumder and M. Van Leeuwen. The Theory and Phenomenology of Perturbative QCD Based Jet Quenching. *Prog. Part. Nucl. Phys.*, 66:41–92, 2011.
- [NAGW14] Marlène Nahrgang, Joerg Aichelin, Pol Bernard Gossiaux, and Klaus Werner. Azimuthal correlations of heavy quarks in Pb + Pb collisions at $\sqrt{s} = 2.76$ TeV at the CERN Large Hadron Collider. *Phys. Rev.*, C90(2):024907, 2014.
- [NDHH13] H. Niemi, G. S. Denicol, H. Holopainen, and P. Huovinen. Event-by-event distributions of azimuthal asymmetries in ultrarelativistic heavy-ion collisions. *Phys. Rev.*, C87(5):054901, 2013.
- [NEP16] H. Niemi, K. J. Eskola, and R. Paatelainen. Event-by-event fluctuations in a perturbative QCD + saturation + hydrodynamics model: Determining QCD matter shear viscosity in ultrarelativistic heavy-ion collisions. *Phys. Rev.*, C93(2):024907, 2016.

- [NEPT16] H. Niemi, K. J. Eskola, R. Paatelainen, and K. Tuominen. Predictions for 5.023 TeV Pb + Pb collisions at the CERN Large Hadron Collider. *Phys. Rev.*, C93(1):014912, 2016.
- [NHLO16] Jacquelyn Noronha-Hostler, Matthew Luzum, and Jean-Yves Ollitrault. Hydrodynamic predictions for 5.02 TeV Pb-Pb collisions. *Phys. Rev.*, C93(3):034912, 2016.
- [NNP⁺14] John Novak, Kevin Novak, Scott Pratt, Joshua Vredevoogd, Chris Coleman-Smith, and Robert Wolpert. Determining Fundamental Properties of Matter Created in Ultrarelativistic Heavy-Ion Collisions. *Phys. Rev.*, C89(3):034917, 2014.
- [OKLY09] Yongseok Oh, Che Ming Ko, Su Houng Lee, and Shigehiro Yasui. Heavy baryon/meson ratios in relativistic heavy ion collisions. *Phys. Rev.*, C79:044905, 2009.
- [OV11] Grigory Ovanesyan and Ivan Vitev. An effective theory for jet propagation in dense QCD matter: jet broadening and medium-induced bremsstrahlung. *JHEP*, 06:080, 2011.
- [Owe87] J. F. Owens. Large-momentum-transfer production of direct photons, jets, and particles. *Rev. Mod. Phys.*, 59:465–503, Apr 1987.
- [OâŽ06] Anthony OâŽHagan. Bayesian analysis of computer code outputs: a tutorial. *Rel. Engin. Sys. Safety*, 91(10âŠ11):1290–1300, 2006.
- [P⁺19] J. H. Putschke et al. The JETSCAPE framework. 2019.
- [Par15] Chanwook Park. Jet energy loss with finite-size effects and running coupling in MARTINI. Master’s thesis, McGill University, Montréal, Québec, 2015.
- [Phy15] Hydrodynamics beyond the gradient expansion: Resurgence and resummation. *Phys. Rev. Lett.*, 115:072501, Aug 2015.
- [PKO⁺07] Ruth Pordes, Bill Kramer, Doug Olson, Miron Livny, Alain Roy, et al. The Open Science Grid. *J.Phys.Conf.Ser.*, 78:012057, 2007.
- [Pol73] H. David Politzer. Reliable Perturbative Results for Strong Interactions? *Phys. Rev. Lett.*, 30:1346–1349, 1973. [,274(1973)].
- [PPQ⁺16] Long-Gang Pang, Hannah Petersen, Guang-You Qin, Victor Roy, and Xin-Nian Wang. Decorrelation of anisotropic flow along the longitudinal direction. *Eur. Phys. J.*, A52(4):97, 2016.
- [Pra14] Scott Pratt. Accounting for backflow in hydrodynamic-Boltzmann interfaces. *Phys. Rev.*, C89(2):024910, 2014.

- [PSB⁺08] Hannah Petersen, Jan Steinheimer, Gerhard Burau, Marcus Bleicher, and Horst Stocker. A Fully Integrated Transport Approach to Heavy Ion Reactions with an Intermediate Hydrodynamic Stage. *Phys. Rev.*, C78:044901, 2008.
- [PSJG17] Chanwook Park, Chun Shen, Sangyong Jeon, and Charles Gale. Rapidity-dependent jet energy loss in small systems with finite-size effects and running coupling. *Nucl. Part. Phys. Proc.*, 289-290:289–292, 2017.
- [PSSW15] Scott Pratt, Evan Sangaline, Paul Sorensen, and Hui Wang. Constraining the Eq. of State of Super-Hadronic Matter from Heavy-Ion Collisions. *Phys. Rev. Lett.*, 114:202301, 2015.
- [PSSZ83] C. Peterson, D. Schlatter, I. Schmitt, and P. M. Zerwas. Scaling violations in inclusive e^+e^- annihilation spectra. *Phys. Rev. D*, 27:105–111, Jan 1983.
- [PST98] Andre Peshier, Klaus Schertler, and Markus H. Thoma. One loop self-energies at finite temperature. *Annals Phys.*, 266:162–177, 1998.
- [PT10] Scott Pratt and Giorgio Torrieri. Coupling Relativistic Viscous Hydrodynamics to Boltzmann Descriptions. *Phys. Rev.*, C82:044901, 2010.
- [QHL16] Jing Qian, Ulrich W. Heinz, and Jia Liu. Mode-coupling effects in anisotropic flow in heavy-ion collisions. *Phys. Rev.*, C93(6):064901, 2016.
- [Rad16] Sooraj Radhakrishnan. Measurement of two particle pseudorapidity correlations in Pb+Pb collisions at $\sqrt{s_{NN}} = 2.76$ TeV with the ATLAS detector. In *Proceedings, 7th International Conference on Hard and Electromagnetic Probes of High-Energy Nuclear Collisions (Hard Probes 2015): Montréal, Québec, Canada, June 29-July 3, 2015*, 2016.
- [Rom18] Paul Romatschke. Relativistic Fluid Dynamics Far From Local Equilibrium. *Phys. Rev. Lett.*, 120(1):012301, 2018.
- [RPS⁺15] S. Ryu, J. F. Paquet, C. Shen, G. S. Denicol, B. Schenke, S. Jeon, and C. Gale. Importance of the Bulk Viscosity of QCD in Ultrarelativistic Heavy-Ion Collisions. *Phys. Rev. Lett.*, 115(13):132301, 2015.
- [RR07] Paul Romatschke and Ulrike Romatschke. Viscosity Information from Relativistic Nuclear Collisions: How Perfect is the Fluid Observed at RHIC? *Phys. Rev. Lett.*, 99:172301, 2007.
- [RR10] F. Riek and R. Rapp. Quarkonia and Heavy-Quark Relaxation Times in the Quark-Gluon Plasma. *Phys. Rev.*, C82:035201, 2010.

- [RSBB14] Maciej Rybczynski, Grzegorz Stefanek, Wojciech Broniowski, and Piotr Bozek. GLISSANDO 2 : GLauber Initial-State Simulation AND mOreâ€, ver. 2. *Comput. Phys. Commun.*, 185:1759–1772, 2014.
- [RvH10] Ralf Rapp and Hendrik van Hees. Heavy Quarks in the Quark-Gluon Plasma. In *Quark-gluon plasma 4*, pages 111–206, 2010.
- [RW06] C.E. Rasmussen and C.K.I. Williams. *Gaussian Processes for Machine Learning*. Adaptative computation and machine learning series. University Press Group Limited, 2006.
- [S⁺17] Albert M Sirunyan et al. Measurement of the B^\pm Meson Nuclear Modification Factor in Pb-Pb Collisions at $\sqrt{s_{NN}} = 5.02$ TeV. *Phys. Rev. Lett.*, 119(15):152301, 2017.
- [S⁺18a] Albert M Sirunyan et al. Measurement of prompt and nonprompt charmonium suppression in PbPb collisions at 5.02 TeV. *Eur. Phys. J.*, C78(6):509, 2018.
- [S⁺18b] Albert M Sirunyan et al. Measurement of prompt D^0 meson azimuthal anisotropy in Pb-Pb collisions at $\sqrt{s_{NN}} = 5.02$ TeV. *Phys. Rev. Lett.*, 120(20):202301, 2018.
- [S⁺18c] Albert M Sirunyan et al. Nuclear modification factor of D^0 mesons in PbPb collisions at $\sqrt{s_{NN}} = 5.02$ TeV. *Phys. Lett.*, B782:474–496, 2018.
- [SAC⁺15] TorbjÃ¤rn SjÃ¤strand, Stefan Ask, Jesper R. Christiansen, Richard Corke, Nishita Desai, Philip Ilten, Stephen Mrenna, Stefan Prestel, Christine O. Rasmussen, and Peter Z. Skands. An Introduction to PYTHIA 8.2. *Comput. Phys. Commun.*, 191:159–177, 2015.
- [SALS11] Michael Strickland, Jens O. Andersen, Lars E. Leganger, and Nan Su. Hard-thermal-loop QCD Thermodynamics. *Prog. Theor. Phys. Suppl.*, 187:106–114, 2011.
- [SBC⁺16] Taesoo Song, Hamza Berrehrah, Daniel Cabrera, Wolfgang Cassing, and Elena Bratkovskaya. Charm production in Pb + Pb collisions at energies available at the CERN Large Hadron Collider. *Phys. Rev.*, C93(3):034906, 2016.
- [SBC17] Dinesh K. Srivastava, Steffen A. Bass, and Rupa Chatterjee. Production of charm quarks in a parton cascade model for relativistic heavy ion collisions at $\sqrt{s_{NN}} = 200$ GeV. *Phys. Rev.*, C96(6):064906, 2017.
- [SBH⁺09] Igor Sfiligoi, Daniel C. Bradley, Burt Holzman, Parag Mhashilkar, Sanjay Padhi, et al. The pilot way to Grid resources using glideinWMS. *WRI World Congress*, 2:428–432, 2009.

- [SDM⁺17] Francesco Scardina, Santosh K. Das, Vincenzo Minissale, Salvatore Plumari, and Vincenzo Greco. Estimating the charm quark diffusion coefficient and thermalization time from D meson spectra at energies available at the BNL Relativistic Heavy Ion Collider and the CERN Large Hadron Collider. *Phys. Rev.*, C96(4):044905, 2017.
- [SPP⁺16] F. Scardina, S.K. Das, S. Plumari, J.I. Bellone, and V. Greco. Toward an understanding of the raa and v2 puzzle for heavy quarks. *Nuclear and Particle Physics Proceedings*, 276-278:329 – 332, 2016. 7th International Conference on Hard and Electromagnetic Probes of High Energy Nuclear Collisions.
- [SGJ09] Bjoern Schenke, Charles Gale, and Sangyong Jeon. MARTINI: An Event generator for relativistic heavy-ion collisions. *Phys. Rev.*, C80:054913, 2009.
- [SH08a] Huichao Song and Ulrich W. Heinz. Causal viscous hydrodynamics in 2+1 dimensions for relativistic heavy-ion collisions. *Phys. Rev.*, C77:064901, 2008.
- [SH08b] Huichao Song and Ulrich W. Heinz. Multiplicity scaling in ideal and viscous hydrodynamics. *Phys. Rev.*, C78:024902, 2008.
- [SH15] Chun Shen and Ulrich Heinz. The road to precision: Extraction of the specific shear viscosity of the quark-gluon plasma. 2015.
- [SJG10] Bjoern Schenke, Sangyong Jeon, and Charles Gale. (3+1)D hydrodynamic simulation of relativistic heavy-ion collisions. *Phys. Rev.*, C82:014903, 2010.
- [SLG19] Shuzhe Shi, Jinfeng Liao, and Miklos Gyulassy. Global constraints from RHIC and LHC on transport properties of QCD fluids in CUJET/CIBJET framework. *Chin. Phys.*, C43(4):044101, 2019.
- [SMS06] Torbjorn Sjostrand, Stephen Mrenna, and Peter Z. Skands. PYTHIA 6.4 Physics and Manual. *JHEP*, 05:026, 2006.
- [SP16] Evan Sangaline and Scott Pratt. Toward a deeper understanding of how experiments constrain the underlying physics of heavy-ion collisions. *Phys. Rev.*, C93(2):024908, 2016.
- [SQS⁺16] Chun Shen, Zhi Qiu, Huichao Song, Jonah Bernhard, Steffen Bass, and Ulrich Heinz. The iEBE-VISHNU code package for relativistic heavy-ion collisions. *Comput. Phys. Commun.*, 199:61–85, 2016.
- [SS16] Bjoern Schenke and Soeren Schlichting. 3-D Glasma initial state for relativistic heavy ion collisions. 2016.

- [ST09] Thomas Schäfer and Derek Teaney. Nearly Perfect Fluidity: From Cold Atomic Gases to Hot Quark Gluon Plasmas. *Rept. Prog. Phys.*, 72:126001, 2009.
- [Str19] Michael Strickland. The non-equilibrium attractor: Beyond hydrodynamics. In *25th Cracow Epiphany Conference on Advances in Heavy Flavour Physics (Epiphany 2019) Cracow, Poland, January 8-11, 2019*, 2019.
- [STV12] Bjoern Schenke, Prithwish Tripathy, and Raju Venugopalan. Fluctuating Glasma initial conditions and flow in heavy ion collisions. *Phys. Rev. Lett.*, 108:252301, 2012.
- [STV13] Jurgen Schukraft, Anthony Timmins, and Sergei A. Voloshin. Ultra-relativistic nuclear collisions: event shape engineering. *Phys. Lett.*, B719:394–398, 2013.
- [Su15] Nan Su. Recent progress in hard-thermal-loop QCD thermodynamics and collective excitations. *Int. J. Mod. Phys.*, A30:1530025, 2015.
- [Sve88] Benjamin Svetitsky. Diffusion of charmed quarks in the quark-gluon plasma. *Phys. Rev. D*, 37:2484–2491, May 1988.
- [SVZ09] Rishi Sharma, Ivan Vitev, and Ben-Wei Zhang. Light-cone wave function approach to open heavy flavor dynamics in QCD matter. *Phys. Rev.*, C80:054902, 2009.
- [TLS01] D. Teaney, J. Lauret, and E. V. Shuryak. A Hydrodynamic description of heavy ion collisions at the SPS and RHIC. 2001.
- [UFXG10] Jan Uphoff, Oliver Fochler, Zhe Xu, and Carsten Greiner. Heavy quark production at RHIC and LHC within a partonic transport model. *Phys. Rev.*, C82:044906, 2010.
- [UFXG15] Jan Uphoff, Oliver Fochler, Zhe Xu, and Carsten Greiner. Elastic and radiative heavy quark interactions in ultra-relativistic heavy-ion collisions. *J. Phys.*, G42(11):115106, 2015.
- [vdSS15] Wilke van der Schee and Bjoern Schenke. Rapidity dependence in holographic heavy ion collisions. *Phys. Rev.*, C92(6):064907, 2015.
- [vHMGR08] H. van Hees, M. Mannarelli, V. Greco, and R. Rapp. Nonperturbative heavy-quark diffusion in the quark-gluon plasma. *Phys. Rev. Lett.*, 100:192301, 2008.
- [Wan02] Xin-Nian Wang. Modified fragmentation function and jet quenching at RHIC. *Nucl. Phys.*, A702:238, 2002.

- [WG91] Xin-Nian Wang and Miklos Gyulassy. HIJING: A Monte Carlo model for multiple jet production in p p, p A and A A collisions. *Phys. Rev.*, D44:3501–3516, 1991.
- [WG01] Xin-Nian Wang and Xiao-feng Guo. Multiple parton scattering in nuclei: Parton energy loss. *Nucl. Phys.*, A696:788–832, 2001.
- [WGP95] Xin-Nian Wang, Miklos Gyulassy, and Michael Plumer. The LPM effect in QCD and radiative energy loss in a quark gluon plasma. *Phys. Rev.*, D51:3436–3446, 1995.
- [WHDG07] Simon Wicks, William Horowitz, Magdalena Djordjevic, and Miklos Gyulassy. Heavy quark jet quenching with collisional plus radiative energy loss and path length fluctuations. *Nucl. Phys.*, A783:493–496, 2007.
- [Wie00] Urs Achim Wiedemann. Gluon radiation off hard quarks in a nuclear environment: Opacity expansion. *Nucl. Phys.*, B588:303–344, 2000.
- [WKF⁺15] S. Wesolowski, N. Klco, R. J. Furnstahl, D. R. Phillips, and A. Thapaliya. Bayesian parameter estimation for effective field theories. 2015.
- [WKP⁺10] K. Werner, Iu. Karpenko, T. Pierog, M. Bleicher, and K. Mikhailov. Event-by-Event Simulation of the Three-Dimensional Hydrodynamic Evolution from Flux Tube Initial Conditions in Ultrarelativistic Heavy Ion Collisions. *Phys. Rev.*, C82:044904, 2010.
- [WtSC14] Yaping Wang and the Star Collaboration. Star upgrade program and future physics. *Journal of Physics: Conference Series*, 535(1):012022, 2014.
- [XBB⁺18] Yingru Xu, Jonah E. Bernhard, Steffen A. Bass, Marlene Nahrgang, and Shanshan Cao. Data-driven analysis for the temperature and momentum dependence of the heavy-quark diffusion coefficient in relativistic heavy-ion collisions. *Phys. Rev.*, C97(1):014907, 2018.
- [XBM⁺19] Yingru Xu, Steffen A. Bass, Pierre Moreau, Taesoo Song, Marlene Nahrgang, Elena Bratkovskaya, Pol Gossiaux, Jorg Aichelin, Shanshan Cao, Vincenzo Greco, Gabriele Coci, and Klaus Werner. Resolving discrepancies in the estimation of heavy quark transport coefficients in relativistic heavy-ion collisions. *Phys. Rev. C*, 99:014902, Jan 2019.
- [XG05] Zhe Xu and Carsten Greiner. Thermalization of gluons in ultrarelativistic heavy ion collisions by including three-body interactions in a parton cascade. *Phys. Rev.*, C71:064901, 2005.
- [Xie16] Guannan Xie. Nuclear Modification Factor of D^0 Meson in Au+Au Collisions at $\sqrt{s_{NN}}=200$ GeV. *Nucl. Phys.*, A956:473–476, 2016.

- [XLG15] Jiechen Xu, Jinfeng Liao, and Miklos Gyulassy. Consistency of Perfect Fluidity and Jet Quenching in semi-Quark-Gluon Monopole Plasmas. *Chin. Phys. Lett.*, 32(9):092501, 2015.
- [XLW13] Kai Xiao, Feng Liu, and Fuqiang Wang. Event-plane decorrelation over pseudorapidity and its effect on azimuthal anisotropy measurements in relativistic heavy-ion collisions. *Phys. Rev.*, C87(1):011901, 2013.
- [Zak96] B. G. Zakharov. Fully quantum treatment of the Landau-Pomeranchuk-Migdal effect in QED and QCD. *JETP Lett.*, 63:952–957, 1996.
- [Zak97] B. G. Zakharov. Radiative energy loss of high-energy quarks in finite size nuclear matter and quark - gluon plasma. *JETP Lett.*, 65:615–620, 1997.
- [ZCGZ16] Kai Zhou, Zhengyu Chen, Carsten Greiner, and Pengfei Zhuang. Thermal Charm and Charmonium Production in Quark Gluon Plasma. *Phys. Lett.*, B758:434–439, 2016.
- [Zho16a] You Zhou. Measurements of correlations of anisotropic flow harmonics in Pb–Pb Collisions with ALICE. *Nucl. Phys.*, A956:296–299, 2016.
- [Zho16b] You Zhou. Review of anisotropic flow correlations in ultrarelativistic heavy-ion collisions. *Adv. High Energy Phys.*, 2016:9365637, 2016.
- [ZKLL00] Bin Zhang, C. M. Ko, Bao-An Li, and Zi-Wei Lin. A multiphase transport model for nuclear collisions at RHIC. *Phys. Rev.*, C61:067901, 2000.
- [ZSW11] Korinna Christine Zapp, Johanna Stachel, and Urs Achim Wiedemann. A local Monte Carlo framework for coherent QCD parton energy loss. *JHEP*, 07:118, 2011.
- [ZWW04] Ben-Wei Zhang, Enke Wang, and Xin-Nian Wang. Heavy quark energy loss in nuclear medium. *Phys. Rev. Lett.*, 93:072301, 2004.
- [ZXF⁺16] You Zhou, Kai Xiao, Zhao Feng, Feng Liu, and Raimond Snellings. Anisotropic distributions in a multiphase transport model. *Phys. Rev.*, C93(3):034909, 2016.
- [ZZXS16] Xiangrong Zhu, You Zhou, Haojie Xu, and Huichao Song. Investigating the correlations of flow harmonics in 2.76A TeV Pb–Pb collisions. 2016.
- [ZZXS17] Xiangrong Zhu, You Zhou, Haojie Xu, and Huichao Song. Correlations of flow harmonics in 2.76A TeV Pb–Pb collisions. *Phys. Rev.*, C95(4):044902, 2017.

Biography

Weiyao Ke was born in Beijing, China in 1991. He received a B.S. in Physics from Peking University in 2014. His published or currently in preparation works during his PhD include:

Weiyao Ke, Yingru Xu, and Steffen A. Bass Modeling of quantum-coherence effects in parton radiative energy loss. arXiv:1810.08177.

Weiyao Ke, Yingru Xu, and Steffen A. Bass A linearized Boltzmann-Langevin transport model for heavy quark transport in hot and dense QCD matter. Phys. Rev. C **98**, 064901 (2018).

Weiyao Ke, J. Scott Moreland, Jonah E. Bernhard, and Steffen A. Bass Constraints on rapidity-dependent initial conditions from charged-particle pseudorapidity densities and two-particle correlations. Phys. Rev. C **96**, 044912 (2017).